THE ROLE OF THE CATALYST IN THE GROWTH OF ONE-DIMENSIONAL NANOSTRUCTURES

A Dissertation
Presented to
The Academic Faculty

By

Melanie Kirkham

In Partial Fulfillment
Of the Requirements for the Degree
Doctor of Philosophy in Materials Science and Engineering

Georgia Institute of Technology

December 2009

THE ROLE OF THE CATALYST IN THE GROWTH OF ONE-DIMENSIONAL NANOSTRUCTURES

Approved by:

Dr. Robert L. Snyder, Advisor
School of Materials Science and Engineering
Georgia Institute of Technology

Dr. Zhong Lin Wang, Advisor
School of Materials Science and Engineering
Georgia Institute of Technology

Dr. Hamid Garmestani
School of Materials Science and Engineering
Georgia Institute of Technology

Dr. Christopher Summers
School of Materials Science and Engineering
Georgia Institute of Technology

Dr. Angus Wilkinson
School of Chemistry and Biochemistry
Georgia Institute of Technology

Date Approved:
2 November 2009

ACKNOWLEDGEMENTS

I would like to thank my advisors, Dr. Zhong Lin Wang and Dr. Robert L. Snyder, whose guidance was vital throughout my studies. I would also like to thank Dr. Hamid Garmestani, Dr. Christopher Summers and Dr. Angus Wilkinson for serving on my committee. I would like to thank my fellow group members, who gave helpful discussion, advice and assistance. Dr. Yong Ding aided with HRTEM measurements, and Dr. Xudong Wang, Dr. Puxian Gao and Dr. J.R. Morber provided samples to characterize. I especially would like to thank Dr. Jung-Il Hong for serving as a mentor for me.

Outside of Georgia Tech, I would like to thank my friends at Second Ponce de Leon Baptist Church for providing a welcoming retreat and sustaining faith. Finally, and most importantly, I want to thank my family, especially my parents, Glenn and Nancy Kirkham, for always supporting and encouraging me, even if they do not always understand what exactly I am doing.

TABLE OF CONTENTS

LIST OF TABLES

LIST OF FIGURES

LIST OF SYMBOLS AND ABBREVIATIONS

1D	(quasi) one-dimensional
α-1	Panalytical X'Pert PRO Alpha-1 Diffractometer
CBE	chemical beam epitaxy
CNT	carbon nanotube
CVD	chemical vapor deposition
EDS	energy dispersive X-ray spectroscopy
FCC	face-centered cubic
FFT	fast Fourier transformation
FWHM	full width at half maximum
GIXRD	grazing incidence X-ray diffraction
HCP	hexagonal close-packed
HRTEM	high-resolution transmission electron microscopy
ICSD	Inorganic Crystal Structure Database
ITO	indium tin oxide
LED	light-emitting diode
LPA	Panalytical Line Profile Analysis software
MBE	molecular beam epitaxy
MPD	Panalytical X'Pert PRO Multi-Purpose Diffractometer
MRD	Panalytical X'Pert PRO Materials Research Diffractometer
MSDS	Material Safety Data Sheet
NIST	National Institute of Standards and Technology
NNI	National Nanotechnology Initiative
OAG	oxide-assisted growth
ODF	orientation distribution function
PDF	powder diffraction file
PLD	pulsed laser deposition
PSD	position-sensitive detector
QLL	quasi-liquid layer
SEM	scanning electron microscopy
SRM	standard reference material
TEM	transmission electron microscopy
UV	ultraviolet
VLS	vapor-liquid-solid
VS	vapor-solid
VSS	vapor-solid-solid
XRD	X-ray diffraction

SUMMARY

Quasi one-dimensional (1D) nanostructures show great promise for many applications, including in solar cells, nanogenerators and chemical sensors, due to the high surface-to-volume ratio and unique properties of nanostructures. The growth of these nanostructures is commonly catalyzed by metal nanoparticles and generally attributed to the vapor-liquid-solid (VLS) mechanism. The purpose of this research is to better understand the role of the catalyst nanoparticles in the growth of 1D nanostructures, in order to allow improved control of the synthesis process. To this end, nanostructures were grown with a variety of compositions, including Au- and Sn-catalyzed ZnO, Au-catalyzed Fe_xO_y and Au-catalyzed Si nanostructures. The morphology of the nanostructures was characterized with electron microscopy, and the crystallographic orientation with X-ray texture analysis. The catalyst particles were further characterized with both *in-situ* and post-growth X-ray diffraction. The types of bonding in the source material and catalyst play a significant role in the diffusion path of the source material to the growth front and in the catalyst particle state during growth. Dissimilar bonding types in the source material and catalyst prevent bulk diffusion of the source material through the catalyst, thereby preventing eutectic melting of the catalyst. These results bring new insight into the catalyzed growth of 1D nanostructures and assist the informed choice of appropriate catalyst materials, which may aid the utilization of 1D nanostructures in energy-related and other applications.

CHAPTER 1

INTRODUCTION AND BACKGROUND

1.1 Introduction

1.1.1 The Promise of Nanoscience and Nanotechnology

Nanoscience and nanotechnology are research areas of great interest at this time. The U.S. National Nanotechnology Initiative (NNI), will provide $1.64 billion for nanotechnology research in 2010, for a total of approximately $12 billion since its inception in 2001 [1]. This level of interest is due to the promise of nanoscience and nanotechnology to revolutionize the technological capabilities of the world. In the words of J. Storrs Hall, "Nanotechnology has the potential for increasing our physical capabilities more than did the industrial revolution." [2]

From a materials science point of view, nanoscale science is promising because of surface effects. As the diameter of a particle decreases, the surface-to-volume ratio increases, and the fraction of atoms on the surface decreases. Assuming a spherical particle with a surface thickness of 0.3 nm, approximately 0.0001% of the atoms are on the surface of a particle with a diameter of 1 mm, 0.1% with a diameter of 1 μm, 1% with a diameter of 100 nm and fully 10% of the atoms are on the surface of a particle with a diameter of 10 nm. The behavior of a surface is altered from that of the bulk due to the broken bonds of the surface atoms. Therefore nanoscale materials, with a high fraction of surface atoms, will have altered properties. For example, the melting temperature of metallic nanoparticles decreases with decreasing diameter [3, 4], the emission wavelength

of CdS, CdSe and CdTe quantum dots blue-shifts with decreasing diameter [5], and the elastic modulus of quasi-one-dimensional ZnO nanostructures increases with decreasing diameter [6, 7].

A significant amount of research, including this work, has been directed towards quasi-one-dimensional (1D) nanostructures. These 1D nanostructures have large aspect ratios with diameters on the order of 100 nm or less [8, 9]. They are often classified according to the cross-section shape. Nanowires and nanorods have approximately circular cross-sections, nanobelts and nanoribbons have rectangular cross-sections, and nanotubes are hollow. (The term 'nanowire' is also often used as a general term for all 1D nanostructures.)

1.1.2 Potential Applications of One-Dimensional Nanostructures

The progress of application of nanostructures to real-world, in-the-store products has been divided into four generations by Roco [10]. The first generation consists of passive uses of nanostructures, typically as additives to improve materials properties. The second generation consists of active uses of nanostructures, such as sensors, transistors and actuators. The third generation will consist of systems of nanosystems, and the fourth of molecular nanosystems.

Many examples of first generation, passive nanotechnology are already in the marketplace. For example, ZnO and TiO_2 nanoparticles are added to some sunscreens to improve light scattering. Nanowhiskers are attached to clothing fibers to produce "stain-free" fabric. Platinum nanoparticles in automotive catalytic converters make use of the large surface-to-volume ratio of nanoparticles. [11, 12]

Furthermore, the nanotechnology market is increasing. Lux Research, a nanotechnology business research firm, estimates that $13 billion worth of nanotechnology-enabled products were produced in 2005 [11], which quickly grew to $147 billion in 2007 [12]. By 2015, the market is expected to be $3.1 trillion [12], a growth of more than 2000% in eight years. A large part of this growth will likely be in second-generation, active nanotechnology.

Many potential second generation, active applications of 1D nanostructures have been demonstrated, as seen in Figure 1.1. Metal oxide nanowires and nanobelts have been fashioned into chemical sensors, based on the phenomenon that their conductivity changes appreciably when exposed to different chemicals due to the high surface-to-volume ratio [13-19]. The same principle can be used to detect biomolecules when the nanostructure is suitably functionalized [20, 21]. 1D nanostructures with photonic properties have been used as photosensors [22-25], nano-lasers [26, 27], light-emitting diodes (LEDs) [28, 29] and wave-guides [30]. 1D nanostructures also show promise for improved solar cell performance [31-36]. Carbon nanotube (CNT) films have been fashioned into flexible, transparent speakers [37].

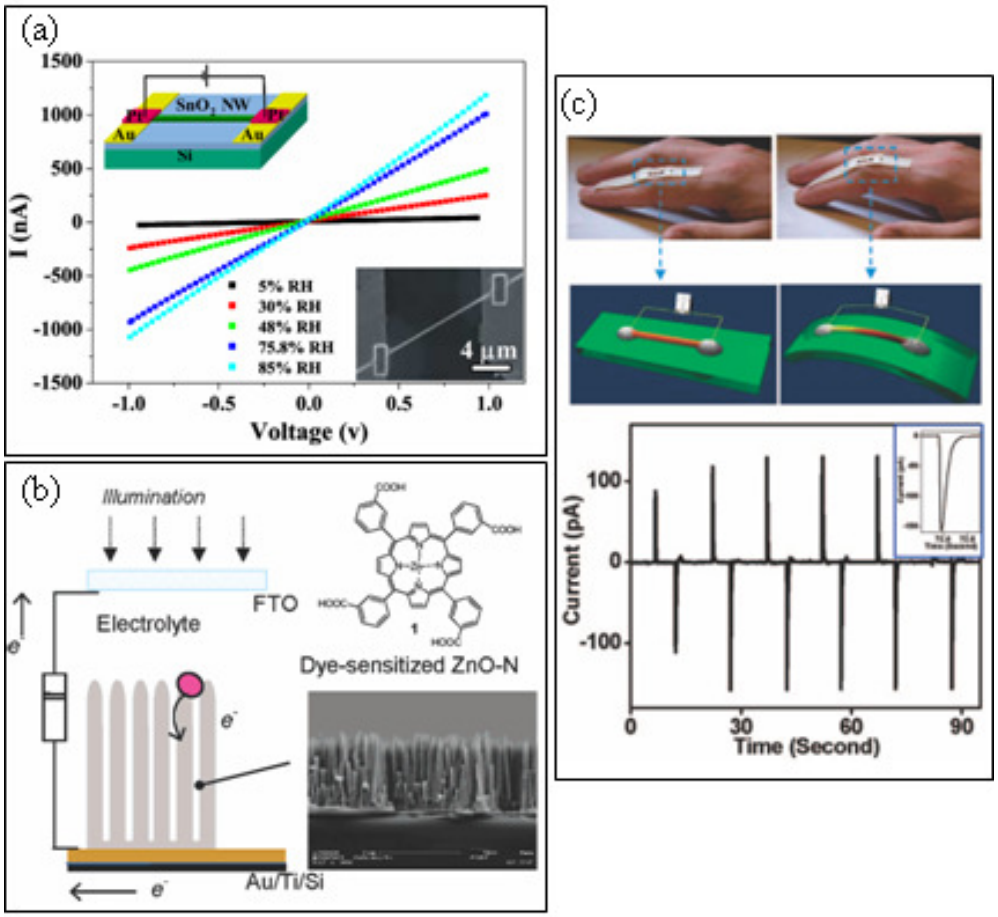

Figure 1.1 Applications of 1D nanostructures, including (a) humidity sensor with SnO_2 nanowire [15], (b) dye-sensitized solar cell with ZnO nanowires [31] and (c) nanogenerator with ZnO nanowire [38]. Reproduced by permission from the American Chemical Society.

The piezoelectric properties (i.e. displaying an electrical response to a mechanical stimulus, and vice versa) of some 1D nanostructures, most commonly of ZnO, also allow many potential active applications. These applications include nanogenerators [39-43], capable of generating electric power from environmental vibrations or oscillations, and outputting either alternating- [38, 44] or direct-current [45-48] (AC or DC, respectively) depending on the device design. Piezoelectric 1D nanostructures have also been demonstrated in force sensors [49-52], in which charge carriers become trapped due to bending of the nanostructure, causing a measurable change in conductivity.

Other uses of 1D nanostructures include as field emitters [53-55], mass balances [56], and temperature sensors [57]. Silicon nanowires have been found to improve the performance of Li-ion battery anodes [58-61]. In the medical field, besides biosensor as discussed above, 1D nanostructures have been used for tumor imaging [62] and for detecting electrical signals from neurons [63] and hearts [64].

1.1.3 Motivation of This Work

Central to realizing these near- and long-term applications, as described in section 1.1.2 above, will be the ability to control the self-aligned growth of arrays of 1D nanostructures. Manipulation of nanostructures into desirable configurations is a significant problem. Individual nanostructures can be moved using the probe of an atomic force microscope (AFM) [65], but the procedure cannot easily be scaled up for commercial production.

A solution is to self-assemble the nanostructures by growing them in the desired arrangement. Toward this end, patterned arrays of aligned nanostructures have been grown by a vapor deposition method. The nanostructures are patterned by patterning the

metal catalyst necessary for growth [66]. Much of the research into the catalyzed growth of 1D nanostructures has concentrated on the empirical effect of varying the processing parameters, such as temperature, pressure and time. A better understanding of the underlying science behind the mechanisms of formation of these nanostructures would allow controlled production and tailoring of the nanostructures via the synthesis process.

This research addresses the synthesis mechanism for the catalyzed growth of 1D nanostructures. The growth of silicon and several metal oxide nanostructures is examined. Special attention is placed on the role of the catalyst during growth.

1.2 Background

1.2.1 Morphologies and Compositions of One-Dimensional Nanostructures

Quasi-one-dimensional (1D) nanostructures have widths on the order of 100 nm or smaller and lengths on the order of 1 μm or larger. These nanostructures are generally classified according to their morphology and composition. A wide variety of both morphologies and compositions have been synthesized.

The most commonly grown morphology of 1D nanostructures, as seen in Figure 1.2, have nearly circular cross-sections. These nanostructures are generally known as nanowires, or as nanorods when the aspect ratio is relatively low. Nanotubes are also circular in cross-section, but with a hollow core. 1D nanostructures are also often grown with rectangular cross-sections, which are known as nanobelts or nanoribbons. Related morphologies built on nanobelts of polar materials, such as ZnO, include nanorings and nanosprings. More complex heterostructures of branched 1D nanostructures have also been grown. [13, 67, 68]

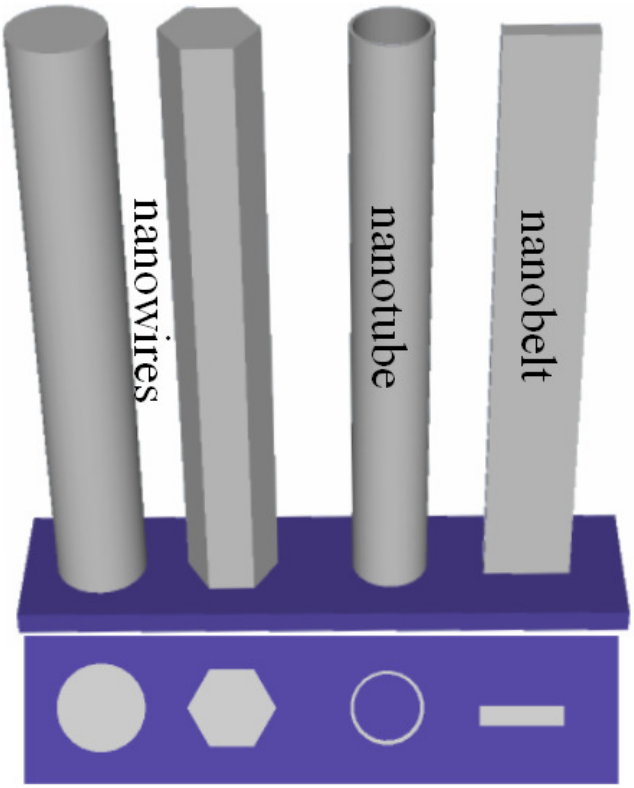

Figure 1.2 Types of 1D nanostructures commonly observed, including nanowires with circular and hexagonal cross-sections, nanotubes and nanobelts.

One-dimensional nanostructures are commonly grown of semiconductors, due to their functionality and potential for applications. Nanostructures have been grown of elemental semiconductors, including silicon [69-92] and germanium [71, 84, 93-101], III-V semiconductors, including GaAs [102-111], GaN [112-114], GaP [102, 104, 115-117], InAs [102, 104, 105, 118-121] and InP [102, 104, 122, 123], and II-VI semiconductors, including ZnO [66, 124-148], ZnS [149-152], CdS [153, 154], CdSe [155], ZnSe [156, 157], ZnTe [158] [159] and GaSe [160]. Besides semiconductors, 1D nanostructures have been grown of oxides, including MgO [161-168], CdO [169-171], Fe_xO_y [172], SnO_2 [173-177], In_2O_3 [173, 178, 179], Ga_2O_3 [173, 180-183] and Bi_2O_3 [184]. 1D nanostructures have also been grown of various metals [185-188], and, of course, carbon nanotubes have long been a subject of much research interest [189-198]. From the wide range of compositions of 1D nanostructures, it is evident that the formation of 1D nanostructures is a common phenomenon, and that understanding the synthesis process behind these nanostructures will have wide application in many areas.

1.2.2 Catalyzed Growth of One-Dimensional Nanostructures

1.2.2.1 Growth Techniques

The growth of 1D nanostructures is commonly accomplished using catalyst particles [199]. The source materials are generally supplied to the catalyst in the vapor form, although solutions [200, 201] and supercritical fluids [92, 202, 203] have also been used. A wide variety of techniques may be used to supply the source material vapor, as will be discussed in section 1.2.2.1.1 below. The catalyst particles are generally deposited on a substrate, where they serve as collection sites for the source material. Growth occurs at the interface between the catalyst particle and nanostructure. A wide

variety of materials and techniques may be used for the catalyst, as will be discussed in section 1.2.2.1.2 below.

1.2.2.1.1 Source Material Supply

The source material vapor may be supplied in several different ways, which can be divided into two broad categories: techniques that supply the source materials in the form of the individual elements or the desired species for the nanostructure composition, and techniques that supply the source materials in the form of compounds that must be decomposed at the catalyst particle.

For the first category, thermal vaporization is the simplest method, involving the heating of source material of the same composition as desired for the nanostructure to a sufficient temperature to vaporize the source material. The vapor is then driven by a carrier gas flow to the catalyst particles in a lower temperature region, where the nanostructures grow. Thermal vaporization has been used for the growth of a wide variety of nanostructure compositions, primarily, but not limited to, II-VI semiconductors including ZnS [149-152] and many oxides including ZnO [124-140]. A related technique is molecular beam epitaxy (MBE), where each element is supplied in separate molecular beams generated by heating elemental sources in Knudsen cells. For example, MBE has been used for the growth of ZnSe [156, 157] and ZnTe [158]nanostructures. A laser can also be used to vaporize the source material from a solid target, a technique known as pulsed laser deposition (PLD). For example, PLD has been used for the growth of GaP [117], Fe_xO_y [172] and MgO [165, 166] nanostructures.

For the second category, which decomposes molecules on the surface of the catalyst to supply the source material, chemical vapor deposition (CVD) is common. In

CVD, the vapor is simply flowed over a heated substrate. An example is the growth of silicon nanowires via the decomposition of silane (SiH_4) over gold catalysts [71-79]. A subset of CVD is metal-organic chemical phase deposition (MOCVD), in which one or more components are supplied in the form of an organic complex. MOCVD is commonly used for the growth of 1D nanostructures of III-V semiconductors, such as InP nanostructures from trimethylindium ($In(CH_3)_3$) and phosphine (PH_3) [102, 104, 123]or tertiarybutylphosphine ($P(C_4H_9)_3$) [122]. The CVD process can also be enhanced through the use of a plasma, a process called plasma-enhanced chemical vapor deposition (PECVD). PECVD is commonly used for the growth of carbon nanotubes [189, 194, 195]. Chemical beam epitaxy (CBE) supplies each chemical species in separate beams, in a manner similar to MBE. CBE has been used for the growth of InAs nanostructures from trimethylindium ($In(CH_3)_3$) and arsine (AsH_3) [102, 104, 118, 119] or tertiarybutylarsine ($As(C_4H_9)_3$) [105, 120].

1.2.2.1.2 Catalysts

The vapor deposition techniques discussed above, in the absence of catalysts, generally result in thin film deposition. Catalysts promote the growth 1D nanostructures. The catalysts are in the form of metallic nanoparticles. The most common catalyst material is gold, which has been used to catalyze the growth of almost every type of 1D nanostructure. (See, for example, Au-catalyzed Si [72], Ga_2O_3 [180], GaP [117], CdS [153] and In_2Se_3 [204] nanostructures.) The exception is carbon nanotubes, which are generally catalyzed by iron, cobalt or nickel. (See, for example, references [190, 193], [194] and [189], respectively.) These and other transitional metals have also been used to catalyze other nanomaterials. To a lesser extent, non-transition elements have also been

used as catalysts, for example Sn-catalyzed ZnO [66], Al-catalyzed CdO [171] and In- and Ga-catalyzed Si nanostructures [85].

The catalyst particles may be deposited on the substrate via several different methods. Colloidal nanoparticles of the catalyst material may be dispersed in a solution and deposited on the substrate. (See, for example, their use in the growth of Au-catalyzed In_2Se_3 [204], SnO_2 [173], ZnO [146, 147] and InAs [121] nanostructures.) The most common technique is to deposit a thin film of the catalyst material, which separates into nanoparticles upon heating. (See, for example, their use in the growth of Ag-, Ni-, and Au-catalyzed ZnO nanostructures [139, 140]; Au-catalyzed Ge and Si nanostructures [100]; Au-, Ag-, Al-, Ni-, Pd- and Pt-catalyzed CdO [171]; and Au-, Al-, W-, Ta-, Ag-, Pd-, Mo-, Nb-, Cu-, Ti-, Cr-, Fe-, Co- and Ni-catalyzed SnO_2 [174].) Less commonly, the metal catalyst may be reduced from an oxide, as in the Sn-catalyzed growth of ZnO nanostructures where SnO_2 is vaporized with the source material and a reducing agent [66, 142, 143], or the metal catalyst may be precipitated from solution, as in Ni-catalyzed Ga_2O_3 nanostructures, where the nickel is precipitated from a $Ni(NO_3)_2$ solution [181].

1.2.2.2 Growth Theories

Research into the growth of 1D nanostructures grew out of earlier investigations of the growth of larger whiskers, with diameters on the order of 100 μm or larger. One prominent early explanation for whisker growth was put forth by F. C. Frank and co-workers around 1949 [205-207]. In this theory the growth of high aspect ratio crystals is due to crystal defects, in particular, the presence of a screw dislocation parallel to the long axis. The intersection of the screw dislocation axis and the top surface of the whisker results in a perpetual step on that surface, as seen in Figure 1.3. The perpetual

step provides a more favorable place for the attachment of atoms, as compared to the sides of the whisker, which do not have steps. Therefore, the growth is faster along the axis of the screw dislocation than on the sides, leading to a high aspect ratio. The Frank screw dislocation mechanism was cited in the growth of copper [208] and mercury [209] whiskers.

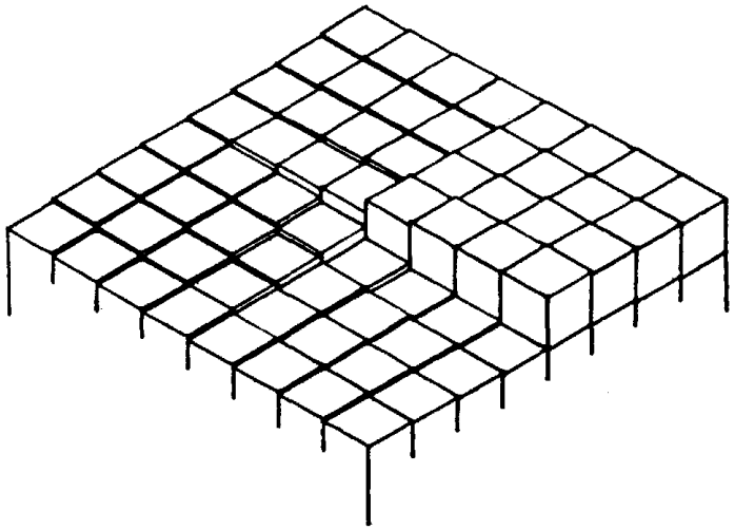

Figure 1.3 Intersection of screw dislocation with top surface of growing whisker, showing perpetual step, as in the Frank screw dislocation growth theory [205]. Reproduced by permission of The Royal Society of Chemistry.

However, in detailed investigations of the growth of silicon whiskers via the disproportionation of SiI_2, Wagner and Ellis found that the Frank screw dislocation mechanism did not apply [210]. This conclusion arose because there was no sign of axial screw dislocations in the silicon whiskers. Additionally, Wagner and Ellis found that impurities, or catalysts, such as gold, nickel or platinum particles, were required for whisker growth, and that small globules were present at the tips of the whiskers.

From these results, Wagner and Ellis formulated in 1964 the vapor-liquid-solid (VLS) mechanism of whisker growth [86, 210]. In the VLS mechanism, the source material, supplied in vapor form, is decomposed on the surface of and absorbed into the catalyst particle. The catalyst particle melts to the liquid state due to a eutectic reaction with the source material. Source material continues to dissolve into the liquid catalyst particle until it becomes supersaturated, at which point a solid particle nucleates on the surface. Continued growth at the interface between the liquid catalyst and solid particle leads to one-dimensional growth. The VLS mechanism was generally accepted for the growth of whiskers and later applied to the catalyzed growth of 1D nanostructures of silicon and other materials, including compound semiconductors and oxides.

Despite the general acceptance of the VLS mechanism, the Frank screw dislocation mechanism has still found some limited application. In a 2008 study, PbS 1D nanostructures were grown with side branches spiraling up the main trunk, which had an axial "screwlike" dislocation, as seen in Figure 1.4a [211]. Also recently, the growth of chiral single-walled carbon nanotubes (CNTs) has been envisioned as involving a theoretical axial screw dislocation, which results in perpetual steps along the edge of the CNT, the number of which depends on the chiral angle, as seen in Figure 1.4b [212]. The authors successfully correlated the growth rate of the nanotubes with the number of steps on the growth front, as measured by the chiral angle.

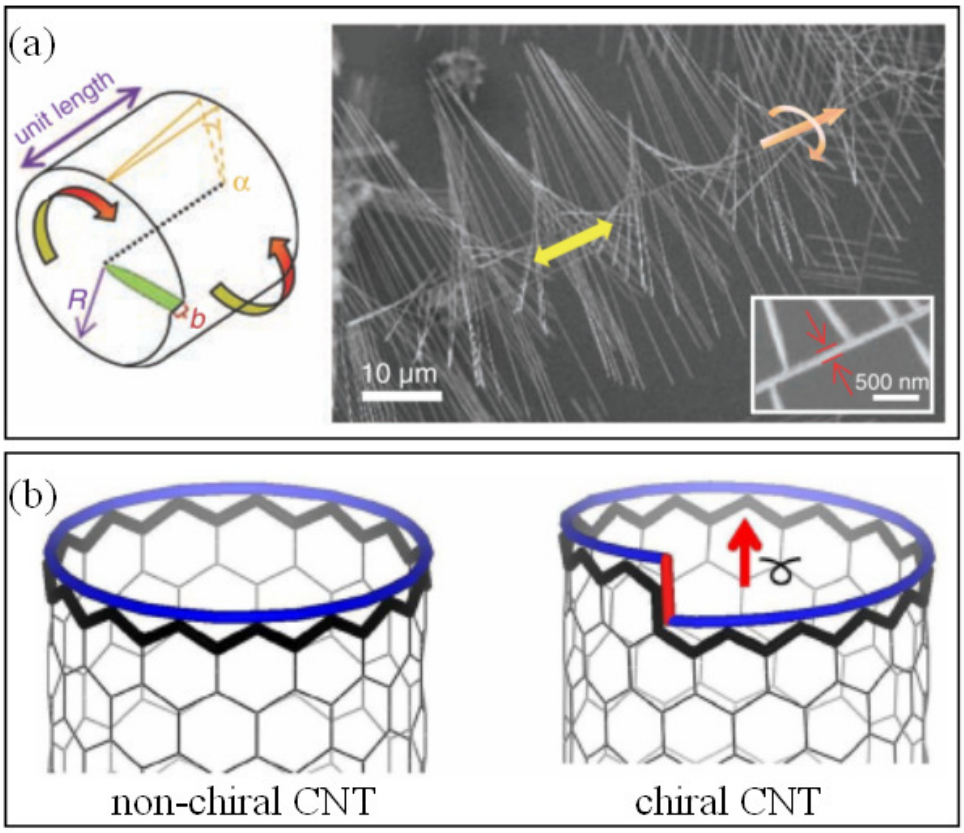

Figure 1.4 (a) PbS nanowire with axial screw dislocation leading to spiraling branches [211]. Reprinted with permission from AAAS. (b) The mechanism for screw dislocation-like atom displacement leading to perpetual steps for carbon nanotube synthesis [212]. Reproduced by permission, ©2009 National Academy of Sciences, U.S.A.

1.2.3 Open Questions

Despite three decades of research into the catalyzed growth of 1D whiskers and nanostructures, much about the synthesis mechanism is still not fully understood, including the nucleation process, the driving force for supersaturation of the catalyst particle and the growth rate dependence on diameter. However, the two main open questions, which will be addressed in this thesis, are as follows. First, what is the state of the catalyst particle during growth, liquid or solid? Second, what is the diffusion path of source material to the growth front, bulk diffusion through the catalyst or surface diffusion around it?

1.2.3.1 Catalyst Particle State

The early studies of the Au-catalyzed growth of Si whiskers reported that the gold catalyst was liquid during growth, giving rise to the vapor-liquid-solid (VLS) mechanism [86, 210, 213, 214]. This VLS mechanism was then applied to the catalyzed growth of 1D nanostructures of many different materials. However, as early as 1971, Bootsma and Gassen raised the possibility that growth could occur from solid catalyst particles [71]. Not until 2001 was a solid catalyst positively reported [82], for the growth of Ti-catalyzed Si nanowires. Growth with a solid catalyst particle has become known as the vapor-solid-solid (VSS) mechanism. Since then, the question of the state of the catalyst particles during growth has been under debate, with some reports that they must be liquid [193] and other reports that solid catalyst particles are possible [71, 82, 92, 106, 186, 203, 215], or even required [118].

1.2.3.2 Diffusion Path

The earliest formulations of the mechanism of catalyzed growth of 1D structures stated that bulk diffusion of the source material into the catalyst particles was necessary to cause eutectic melting and that supersaturation of the catalyst particle then leads to nucleation of the whisker or 1D nanostructure. Bootsma and Gassen again in 1971 first raised the possibility of diffusion around the catalyst particle surface [71]. Surface diffusion of the source material was treated more fully in 1994 by Wang and Fischmann [216] and later by Hofman, Csányi, Ferrari, Payne and Robertson [194]. However, other studies continue to point to a bulk diffusion pathway [109, 127]. The diffusion path of the source material to the growth front is still uncertain.

1.3 References

1. *The National Nanotechnology Initiative Supplement to the President's FY2010 Budget*. 2009, National Science and Technology Council: Washington, D.C. p. 36.

2. Hall, J.S., *Nanofuture*. 2005, Amherst, New York: Prometheus Books. p. 333.

3. Buffat, P. and J.P. Borel, *Size Effect on the Melting Temperature of Gold Particles.* Physical Review A, 1976. **13**(6): p. 2287-2298.

4. Qi, W.H., *Size Effect on Melting Temperature of Nanosolids.* Physica B, 2005. **368**: p. 46-50.

5. Murray, C.B., D.J. Norris, and M.G. Bawendi, *Synthesis and Characterization of Nearly Monodisperse CdE (E = S, Se, Te) Semiconductor Nanoscrystals.* Journal of the American Chemical Society, 1993. **115**: p. 8706-8715.

6. Agrawal, R., B. Peng, E.E. Gdoutos, and H.D. Espinosa, *Elasticity Size Effects in ZnO Nanowires - A Combined Experimental-Computational Approach.* Nano Letters, 2008. **8**(11): p. 3668-3674.

7. Stan, G., C.V. Ciobanu, P.M. Parthangal, and R.F. Cook, *Diameter-Dependent Radial and Tangential Elastic Moduli of ZnO Nanowires.* Nano Letters, 2007. **7**(12): p. 3691-3697.

8. Lieber, C.M., *One-Dimensional Nanostructures: Chemistry, Physics & Applications.* Solid State Communiations, 1998. **107**(11): p. 607-616.

9. Xia, Y., P. Yang, Y. Sun, Y. Wu, B. Mayers, B. Gates, Y. Yin, F. Kim, and H. Yan, *One-Dimensional Nanostructures: Synthesis, Characterization, and Applications.* Advanced Materials, 2003. **15**(5): p. 353-389.

10. Roco, M.C., *Nanoscale Science and Engineering: Unifying and Transforming Tools.* AIChE Journal, 2004. **50**(5): p. 890-897.

11. Booker, R. and E. Boysen, *Nanotechnology for Dummies*. 2005, Indianapolis: Wiley Publishing, Inc. p. 384.

12. *Lux Research Report Finds Nanotechnology on the Rise*, 24 July 2008, Ceramics Industry, http://www.ceramicindustry.com, accessed 22 August 2009.

13. Comini, E., C. Baratto, G. Faglia, M. Ferroni, A. Vomiero, and G. Sberveglieri, *Quasi-One Dimensional Metal Oxide Semiconductors: Preparation,*

Characterization and Application as Chemical Sensors. Progress in Materials Science, 2009. **54**: p. 1-67.

14. Fields, L.L., J.P. Zheng, Y. Cheng, and P. Xiong, *Room-Temperature Low-Power Hydrogen Sensor Based on a Single Tin Dioxide Nanobelt.* Applied Physics Letters, 2006. **88**: p. 263102.

15. Kuang, Q., C. Lao, Z.L. Wang, Z. Xie, and L. Zheng, *High-Sensitivity Humidity Sensor Based on Single SnO_2 Nanowire.* Journal of the American Chemical Society, 2007. **129**: p. 6070-6071.

16. Lao, C.S., Q. Kuang, Z.L. Wang, M.-C. Park, and Y. Deng, *Polymer Functionalized Piezoelectric-FET as Humidity/Chemical Nanosensors.* Applied Physics Letters, 2007. **90**(26): p. 262107.

17. Sysoev, V.V., B.K. Button, K. Wepsiec, S. Dmitriev, and A. Kolmakov, *Toward the Nanoscopic "Electronic Nose": Hydrogran vs Carbon Monoxide Discrimination with an Array of Individual Metal Oxide Nano- and Mesowire Sensors.* Nano Letters, 2006. **6**(8): p. 1584-1588.

18. Al-Hilli, S.M., R.T. Al-Mofarji, and M. Willander, *Zinc Oxide Nanorod for Intracellular pH Sensing.* Applied Physics Letters, 2006. **89**: p. 173119.

19. Cheng, Y., P. Xiong, C.S. Yun, G.F. Strouse, J.P. Zheng, R.S. Yang, and Z.L. Wang, *Mechanism and Optimization of pH Sensing Using SnO_2 Nanobelt Field Effect Transistors.* Nano Letters, 2008. **8**(12): p. 4179-4184.

20. Tang, X., S. Bansaruntip, N. Nakayama, E. Yenilmez, Y.-l. Chang, and Q. Wang, *Carbon Nanotube DNA Sensor and Sensing Mechanism.* Nano Letters, 2006. **6**(8): p. 1632-1636.

21. Roy, S. and Z. Gao, *Nanostructure-Based Electrical Biosensors.* Nano Today, 2009. **4**: p. 318-334.

22. Fan, Z., J.C. Ho, Z.A. Jacobson, H. Razavi, and A. Javey, *Large-Scale, Heterogeneous Integration of Nanowire Arrays for Image Sensor Circuitry.* Proceedings of the National Academy of Sciences, 2008. **105**(32): p. 11066-11070.

23. Hsu, C.L., S.J. Chang, Y.R. Lin, P.C. Li, T.S. Lin, S.Y. Tsai, T.H. Lu, and I.C. Chen, *Ultraviolet Photodetectors with Low Temperature Synthesized Vertical ZnO Nanowires.* Chemical Physics Letters, 2005. **416**(1-3): p. 75-78.

24. Lao, C., M.-C. Park, Q. Kuang, Y. Deng, A.K. Sood, D.L. Polla, and Z.L. Wang, *Giant Enhancement in UV Response of ZnO Nanobelts by Polymer Surface-Functionalization.* Journal of the American Chemical Society, 2007. **129**: p. 12096-12097.

25. He, J.H., S.T. Ho, T.B. Wu, L.J. Chen, and Z.L. Wang, *Nano-Photodiode Based on ZnO Nanowires.* Chemical Physics Letters, 2006. **435**: p. 119-122.

26. Huang, M.H., S. Mao, H. Feick, H.Q. Yan, Y.Y. Wu, H. Kind, E. Weber, R. Russo, and P.D. Yang, *Room-Temperature Ultraviolet Nanowire Nanolasers.* Science, 2001. **292**(5523): p. 1897-1899.

27. Yang, H.Y., S.P. Lau, S.F. Yu, A.P. Abiyasa, M. Tanemura, T. Okita, and H. Hatano, *High-Temperature Random Lasing in ZnO Nanoneedles.* Applied Physics Letters, 2006. **89**: p. 011103.

28. Bao, J., M.A. Zimmler, F. Capasso, X. Wang, and Z.F. Ren, *Broadband ZnO Single-Nanowire Light-Emitting Diode.* Nano Letters, 2006. **6**(8): p. 1719-1722.

29. Sun, J.C., J.Z. Zhao, H.W. Liang, J.M. Bian, L.Z. Hu, H.Q. Zhang, X.P. Liang, W.F. Liu, and G.T. Du, *Realization of Ultraviolet Electroluminescence from ZnO Homojunction with n-ZnO/p-ZnO:As/GaAS Structure.* Applied Physics Letters, 2007. **90**: p. 121128.

30. Voss, T., G.T. Svacha, E. Mazur, S. Müller, C. Ronning, D. Konjhodzic, and F. Marlow, *High-Order Waveguide Modes in ZnO Nanowires.* Nano Letters, 2007. **7**(12): p. 3675-3680.

31. Galoppini, E., J. Rochford, H. Chen, G. Saraf, Y. Lu, A. Hagfeldt, and G. Boschloo, *Fast Electron Transport in Metal Organic Vapor Deposition Grown Dye-Sensitized ZnO Nanorod Solar Cells.* Journal of Physical Chemistry B Letters, 2006. **110**: p. 16159-16161.

32. Fang, H., X. Li, S. Song, Y. Xu, and J. Zhu, *Fabrication of Slantingly-Aligned Silicon Nanowire Arrays for Solar Cell Applications.* Nanotechnology, 2008. **19**: p. 255703.

33. Peng, K., X. Wang, and S.-T. Lee, *Silicon Nanowire Array Photoelectrochemical Solar Cells.* Applied Physics Letters, 2008. **92**(16): p. 163103.

34. Stelzner, T., M. Pietsch, G. Andrä, F. Falk, E. Ose, and S. Christiansen, *Silicon Nanowire-Based Solar Cells.* Nanotechnology, 2008. **19**: p. 295203.

35. Tsakalakos, L., J. Balch, J. Fronheiser, B.A. Korevaar, O. Sulima, and J. Rand, *Silicon Nanowire Solar Cells.* Applied Physics Letters, 2007. **91**: p. 233117.

36. Liu, J., Y.-T. Kuo, K.J. Klabunde, C. Rochford, J. Wu, and J. Li, *Novel Dye-Sensitized Solar Cell Architecture Using TiO_2-Coated Vertically Aligned Carbon Nanofiber Arrays.* Applied Materials & Interfaces, 2009. **1**(8): p. 1645-1649.

37. Xiao, L., Z. Chen, C. Feng, L. Liu, Z.-Q. Bai, Y. Wang, L. Qian, Y. Zhang, Q. Li, K. Jiang, and S. Fan, *Flexible, Stretchable, Transparent Carbon Nanotube Thin Film.* Nano Letters, 2008. **8**(12): p. 4539-4545.

38. Yang, R., Y. Qin, C. Li, G. Zhu, and Z.L. Wang, *Converting Biomechanical Energy into Electricity by a Muscle-Movement-Driven Nanogenerator.* Nano Letters, 2009. **9**(3): p. 1201-1205.

39. Gao, P.X., J. Song, J. Liu, and Z.L. Wang, *Nanowire Piezoelectric Nanogenerators on Plastic Substrates as Flexible Power Sources for Nanodevices.* Advanced Materials, 2006. **19**(1): p. 67-72.

40. Lin, Y.-F., J. Song, Y. Ding, Z.L. Wang, and S.-Y. Lu, *Piezoelectric Nanogenerator using CdS Nanowires.* Applied Physics Letters, 2007. **92**: p. 022105.

41. Song, J., J. Zhou, and Z.L. Wang, *Piezoelectric and Semiconducting Coupled Power Generating Process of a Single ZnO Belt/Wire. A Technology for Harvesting Electricity from the Environment.* Nano Letters, 2006. **6**(8): p. 1656-1662.

42. Wang, Z.L. and J.H. Song, *Piezoelectric nanogenerators based on zinc oxide nanowire arrays.* Science, 2006. **312**(5771): p. 242-246.

43. Qin, Y., X. Wang, and Z.L. Wang, *Microfibre-nanowire hybrid structure for energy scavenging.* Nature, 2008. **451**: p. 809-813.

44. Yang, R., Y. Qin, L. Dai, and Z.L. Wang, *Power generation with laterally packaged piezoelectric fine wires.* Nature Nanotechnology, 2008. **4**: p. 34-39.

45. Liu, J., P. Fei, J. Zhou, R. Tummala, and Z.L. Wang, *Toward High Output-Power Nanogenerator.* Applied Physics Letters, 2008. **92**: p. 173105.

46. Wang, X., J. Song, J. Liu, and Z.L. Wang, *Direct-Current Nanogenerator Driven by Ultrasonic Waves.* Science, 2007. **316**: p. 102-105.

47. Wang, X., J. Liu, J. Song, and Z.L. Wang, *Integrated Nanogenerators in Bio-Fluid.* Nano Letters, 2007. **7**(8): p. 2475-2479.

48. Wang, X., Y. Gao, Y. Wei, and Z.L. Wang, *The Output of Ultrasonic-Wave Driven Nanogenerator in a Confined Tube.* Nano Research, 2009. **2**: p. 177-182.

49. Wang, X., J. Zhou, J. Song, J. Liu, N. Xu, and Z.L. Wang, *Piezoelectric-Field Effect Transistor and Nano-Force-Sensor Based on a Single ZnO Nanowire.* Nano Letters, 2006. **6**(12): p. 2768-2772.

50. Zhou, J., P. Fei, Y. Gao, Y. Gu, J. Liu, G. Bao, and Z.L. Wang, *Mechanical-Electrical Triggers and Sensors Using Piezoelectric Microwires/Nanowires.* Nano Letters, 2008. **8**(9): p. 2725-2730.

51. He, J.H., C.L. Hsin, J. Liu, L.J. Chen, and Z.L. Wang, *Piezoelectric Gated Diode of a Single ZnO Nanowire.* Advanced Materials, 2007. **19**: p. 781-784.

52. Yang, Y., J. Qi, Q. Liao, H. Li, Y. Wang, L. Tang, and Y. Zhang, *High-Performance Piezoelectric Gate Diode of a Single Polar-Surface Dominated ZnO Nanobelt.* Nanotechnology, 2009. **20**: p. 125201.

53. Chueh, Y.-L., M.-T. Ko, L.-J. Chou, L.-J. Chen, C.-S. Wu, and C.-D. Chen, *$TaSi_2$ nanowires: A potential field emitter and interconnect.* Nano Letters, 2006. **6**(8): p. 1637-1644.

54. Givargizov, E.I., *Ultrasharp tips for field emission applications prepared by the vapor-liquid-solid growth technique.* Journal of Vacuum Science and Technology B, 1993. **11**(2): p. 449-453.

55. Wang, X., J. Zhou, C. Lao, J. Song, N. Xu, and Z.L. Wang, *In-situ field emission of density controlled ZnO nanowire arrays.* Applied Physics Letters, 2007. **19**: p. 1627-1631.

56. Zhou, J., C.S. Lao, P. Gao, W. Mai, W.L. Hughes, S.Z. Deng, N.S. Xu, and Z.L. Wang, *Nanowire as pico-gram balance at workplace atmosphere.* Solid State Communiations, 2006. **139**: p. 222-226.

57. He, J.-H., S. Singamaneni, C.H. Ho, Y.-H. Lin, M.E. McConney, and V.V. Tsukruk, *A Thermal Sensor and Switch Based on a Plasma Polymer/ZnO Suspended Nanobelt Bimorph Structure.* Nanotechnology, 2009. **20**: p. 065502.

58. Chan, C.K., H. Peng, G. Liu, K. McIlwrath, X.F. Zhang, R.A. Huggins, and Y. Cui, *High-Performance Lithium Battery Anodes Using Silicon Nanowires.* Nature Nanotechnology, 2008. **3**: p. 31-35.

59. Chan, C.K., R. Ruffo, S.S. Hong, R.A. Huggins, and Y. Cui, *Structural and Electrochemical Study of the Reaction of Lithium with Silicon Nanowires.* Journal of Power Sources, 2009. **189**: p. 34-39.

60. Peng, K., J. Jie, W. Zhang, and S.-T. Lee, *Silicon Nanowires for Rechargeable Litium-Ion Battery Anodes.* Applied Physics Letters, 2008. **93**: p. 033105.

61. Ruffo, R., S.S. Hong, C.K. Chan, R.A. Huggins, and Y. Cui, *Impedance Analysis of Silicon Nanowire Lithium Ion Battery Anodes.* Journal of Physical Chemistry C, 2009. **113**: p. 11390-11398.

62. Park, J.-H., G. von Maltzahn, L. Zhang, M.P. Schwartz, E. Ruoslahti, S.N. Bhatia, and M.J. Sailor, *Magnetic Iron Oxide Nanoworms for Tumor Targeting and Imaging.* Advanced Materials, 2008. **20**: p. 1630-1635.

63. Patolsky, F., B.P. Timko, G. Yu, Y. Fang, A.B. Greytak, G. Zheng, and C.M. Lieber, *Detection, Stimulations, and Inhibition of Neuronal Signals with High-Density Nanowire Transistor Arrays.* Science, 2006. **313**: p. 1100-1104.

64. Timko, B.P., T. Cohen-Karni, G. Yu, Q. Qing, B. Tian, and C.M. Lieber, *Electrical Recording from Hearts with Flexible Nanowire Device Arrays.* Nano Letters, 2009. **9**(2): p. 914-918.

65. Rubio-Sierra, F.J., W.M. Heckl, and R.W. Stark, *Nanomanipulation by atomic force microscopy.* Advanced Engineering Materials, 2005. **7**(4): p. 193-196.

66. Gao, P.X., Y. Ding, and I.L. Wang, *Crystallographic orientation-aligned ZnO nanorods grown by a tin catalyst.* Nano Letters, 2003. **3**(9): p. 1315-1320.

67. Wang, N., Y. Cai, and R.Q. Zhang, *Growth of nanowires.* Materials Science and Engineering R, 2008. **60**: p. 1-51.

68. Wang, Z.L., *ZnO nanowire and nanobelt platform for nanotechnology.* Materials Science and Engineering R, 2009. **64**: p. 33-71.

69. Hourlier-Bahloul, D. and P. Perrot, *Comprehension of the S(V)LS Mechanism Growth of the Silicon-Based Nanowires.* Comptes Rendus Chimie, 2007. **10**: p. 658-665.

70. Sunkara, M.K., S. Sharma, R. Miranda, G. Lian, and E.C. Dickey, *Bulk synthesis of silicon nanowires using a low-temperature vapor-liquid-solid method.* Applied Physics Letters, 2001. **79**(10): p. 1546-1548.

71. Bootsma, G.A. and H.J. Gassen, *A Quantitative Study on the Growth of Silicon Whiskers from Silane and Germanium Whiskers from Germane.* Journal of Crystal Growth, 1971. **10**: p. 223-234.

72. Allen, J.E., E.R. Hemesath, D.E. Perea, J.L. Lensch-Falk, Z.Y. Li, F. Yin, M.H. Gass, P. Wang, A.L. Bleloch, R.E. Palmer, and L.J. Lauhon, *High-Resolution Detection of Au Catalyst Atoms in Si Nanowires.* Nature Nanotechnology, 2008. **3**: p. 168-173.

73. Cao, L., B. Garipcan, J.S. Atchison, C. Ni, B. Nabet, and J.E. Spanier, *Instability and Transport of Metal Catalyst in the Growth of Tapered Silicon Nanowires.* Nano Letters, 2006. **6**(9): p. 1852-1857.

74. Hannon, J.B., S. Kodambaka, F.M. Ross, and R.M. Tromp, *The influence of the surface migration of gold on the growth of silicon nanowires.* Nature, 2006. **440**(7080): p. 69-71.

75. Kalache, B., P.R. Cabarrocas, and A.F. Morral, *Observation of incubation times in the nucleation of silicon nanowires obtained by the vapor-liquid-solid method.* Japanese Journal of Applied Physics Part 2-Letters & Express Letters, 2006. **45**(7): p. L190-L193.

76. Kim, B.J., J. Tersoff, S. Kodambaka, M.C. Reuter, E.A. Stach, and F.M. Ross, *Kinetics of Individual Nucleation Events Observed in Nanoscale Vapor-Liquid-Solid Growth.* Science, 2008. **322**: p. 1070-1073.

77. Kodambaka, S., J. Tersoff, M.C. Reuter, and F.M. Ross, *Diameter-independent kinetics in the vapor-liquid-solid growth of Si nanowires.* Physical Review Letters, 2006. **96**(9): p. 096105.

78. Westwater, J., D.P. Gossain, S. Tomiya, and S. Usui, *Growth of silicon nanowires via gold/silane vapor-liquid-solid reaction.* Journal of Vacuum Science and Technology B, 1997. **15**(3): p. 554-557.

79. Wu, Y., Y. Cui, L. Huynh, C.J. Barrelet, D.C. Bell, and C.M. Lieber, *Controlled Growth and Structures of Molecular-Scale Silicon Nanowires.* Nano Letters, 2004. **4**(3): p. 433-436.

80. Xing, Y.-J., D.-P. Yu, Z.-H. Xi, and Z.-Q. Xue, *Investigation of the growth process of Si nanowires using the vapour-liquid-solid mechanism.* Chinese Physics, 2002. **11**(10): p. 1047-1050.

81. Kamins, T.I., R.S. Williams, T. Hesjedal, and J.S. Harris, *Chemically vapor deposited Si nanowires nucleated by self-assembled Ti islands on patterned and unpatterned Si substrates.* Physica E, 2002. **13**: p. 995-998.

82. Kamins, T.I., R.S. Williams, D.P. Basile, T. Hesjedal, and J.S. Harris, *Ti-catalyzed Si nanowires by chemical vapor deposition: Microscopy and growth mechanisms.* Journal of Applied Physics, 2001. **89**(2): p. 1008-1016.

83. Wang, Y., V. Schmidt, S. Senz, and U. Gösele, *Epitaxial growth of silicon nanowires using an aluminium catalyst.* Nature Nanotechnology, 2006. **1**: p. 186-189.

84. Givargizov, E.I., *Periodic Instability in Whisker Growth.* Journal of Crystal Growth, 1973. **20**: p. 219-226.

85. Givargizov, E.I. and N.N. Sheftal, *Morphology of silicon whiskers grown by the VLS-technique.* Journal of Crystal Growth, 1971. **9**: p. 326-9.

86. Wagner, R.S. and W.C. Ellis, *Vapor-Liquid-Solid Mechanism of Single Crystal Growth.* Applied Physics Letters, 1964. **4**(5): p. 89-90.

87. Weyher, J. and M. Surowiec, *Structure of VLS Silicon-Crystals Grown with Platinum and Gold.* Journal of Crystal Growth, 1978. **43**(2): p. 245-249.

88. Weyher, J., *Some Notes on Growth Kinetics and Morphology of VLS Silicon-Crystals Grown with Platinum and Gold as Liquid-Forming Agents.* Journal of Crystal Growth, 1978. **43**(2): p. 235-244.

89. Nebol'sin, V.A., A.A. Shchetinin, A.A. Dolgachev, and V.V. Korneeva, *Effect of the Nature of the Metal Solvent on the Vapor-Liquid-Solid Growth Rate of Silicon Whiskers.* Inorganic Materials, 2005. **41**(12): p. 1256-1259.

90. Schubert, L., P. Werner, N.D. Zakharov, G. Gerth, F.M. Kolb, L. Long, U. Gösele, and T.Y. Tan, *Silicon nanowhiskers grown on <111>Si substrates by molecular-beam epitaxy.* Applied Physics Letters, 2004. **84**(24): p. 4968-4970.

91. Dubrovskii, V.G., N.V. Sibirev, G.E. Cirlin, J.C. Harmand, and V.M. Ustinov, *Theoretical analysis of the vapor-liquid-solid mechanism of nanowire growth during molecular beam epitaxy.* Physical Review E, 2006. **73**: p. 021603.

92. Tuan, H.-Y., D.C. Lee, T. Hanrath, and B.A. Korgel, *Catalytic Solid-Phase Seeding of Silicon Nanowires by Nickel Nanocrystals in Organic Solvents.* Nano Letters, 2005. **5**(4): p. 681-684.

93. Dailey, J.W., J. Taraci, T. Clement, D.J. Smith, J. Drucker, and S.T. Picraux, *Vapor-liquid-solid growth of germanium nanostructures on silicon.* Journal of Applied Physics, 2004. **96**(12): p. 7556-7567.

94. Sutter, E. and P. Sutter, *Phase Diagram of Nanoscale Alloy Particles Used for Vapor-Liquid-Solid Growth of Semiconductor Nanowires.* Nano Letters, 2008. **8**(2): p. 411-414.

95. Greytak, A.B., L.J. Lauhon, M.S. Gudiksen, and C.M. Lieber, *Growth and Transport Properties of Complementary Germanium Nanowire Field-Effect Transistors.* Applied Physics Letters, 2004. **84**(21): p. 4176-4178.

96. Kodambaka, S., J. Tersoff, M.C. Reuter, and F.M. Ross, *Germanium Nanowire Growth Below the Eutectic Temperature.* Science, 2007. **316**: p. 729-732.

97. Adhikari, H., A.F. Marshall, C.E.D. Chidsey, and P.C. McIntyre, *Germanium Nanowire Epitaxy: Shape and Orientation Control.* Nano Letters, 2006. **6**(2): p. 318-323.

98. Wu, Y. and P. Yang, *Germanium Nanowire Growth via Simple Vapor Transport.* Chemistry of Materials, 2000. **12**: p. 605-607.

99. Wu, Y. and P. Yang, *Direct Observation of Vapor-Liquid-Solid Nanowire Growth.* Journal of the American Chemical Society, 2001. **123**: p. 3165-3166.

100. Colli, A., S. Hofmann, A. Fasoli, A.C. Ferrari, C. Ducati, R.E. Dunin-Borkowski, and J. Robertson, *Synthesis and Optical Properties of Silicon Nanowires Grown by Different Methods.* Applied Physics A, 2006. **85**: p. 247-253.

101. Chandrasekaran, H., G.U. Sumanasekara, and M.K. Sunkara, *Rationalization of Nanowire Synthesis Using Low-Melting Point Metals.* Journal of Physical Chemistry B, 2006. **110**: p. 18351-18357.

102. Seifert, W., M. Borgström, K. Deppert, K.A. Dick, J. Johansson, M.W. Larsson, T. Mårtensson, N. Sköld, C.P.T. Svensson, B.A. Wacaser, L.R. Wallenberg, and L. Samuelson, *Growth of one-dimensional nanostructures in MOVPE.* Journal of Crystal Growth, 2004. **272**: p. 211-220.

103. Borgström, M., K. Deppert, L. Samuelson, and W. Seifert, *Size- and shape-controlled GaAs nano-whiskers grown by MOVPE: a growth study.* Journal of Crystal Growth, 2004. **260**: p. 18-22.

104. Dick, K.A., K. Deppert, L.S. Karlsson, L.R. Wallenberg, L. Samuelson, and W. Seifert, *A New Understanding of Au-Assisted Growth of III-V Semiconductor Nanowires.* Advanced Functional Materials, 2005. **15**: p. 1603-1610.

105. Ohlsson, B.J., M.T. Björk, A.I. Persson, C. Thelander, L.R. Wallenberg, M.H. Magnusson, K. Deppert, and L. Samuelson, *Growth and characterization of GaAs and InAs nano-whiskers and InAs/GaAs heterostructures.* Physica E, 2002. **13**: p. 1126-1130.

106. Persson, A.I., M.W. Larsson, S. Stenström, B.J. Ohlsson, L. Samuelson, and L.R. Wallenberg, *Solid-phase diffusion mechanism for GaAs nanowire growth.* Nature Materials, 2004. **3**: p. 677-681.

107. Persson, A.I., B.J. Ohlsson, S. Jeppesen, and L. Samuelson, *Growth mechanisms for GaAs nanowires grown in CBE.* Journal of Crystal Growth, 2004. **272**: p. 167-174.

108. Harmand, J.C., G. Patriarche, N. Péré-Laperne, M.-N. Mérat-Combes, L. Travers, and F. Glas, *Analysis of vapor-liquid-solid mechanism in Au-assisted GaAs nanowire growth.* Applied Physics Letters, 2005. **87**: p. 203101.

109. Plante, M.C. and R.R. LaPierre, *Growth mechanisms of GaAs nanowires by gas source molecular beam epitaxy.* Journal of Crystal Growth, 2006. **286**: p. 394-399.

110. Wu, Z.H., X. Mei, D. Kim, M. Blumin, H.E. Ruda, J.Q. Liu, and K.L. Kavanagh, *Growth, branching, and kinking of molecular-beam epitaxial <110> GaAs nanowires.* Applied Physics Letters, 2003. **83**(16): p. 3368-3370.

111. Tchernycheva, M., J.C. Harmand, G. Patriarche, L. Travers, and G.E. Cirlin, *Temperature conditions for GaAs nanowire formation by Au-assisted molecular beam epitaxy.* Nanotechnology, 2006. **17**: p. 4025-4030.

112. Chen, C.-C., C.-C. Yeh, C.-H. Chen, M.-Y. Yu, H.-L. Liu, J.-J. Wu, K.-H. Chen, L.-C. Chen, J.-Y. Peng, and Y.-F. Chen, *Catalytic Growth and Characterization of Gallium Nitride Nanowires.* Journal of the American Chemical Society, 2001. **123**(12): p. 2791-2798.

113. Chen, C.-C. and C.-C. Yeh, *Large-Scale Catalytic Synthesis of Crystalline Gallium Nitride Nanowires.* Advanced Materials, 2000. **12**(10): p. 738-740.

114. Kuykendall, T., P. Pauzauskie, S. Lee, Y. Zhang, J. Goldberger, and P. Yang, *Metalorganic Chemical Vapor Deposition Route to GaN Nanowires with Triangular Cross Sections.* Nano Letters, 2003. **3**(8): p. 1063-1066.

115. Borgström, M.T., G. Immink, B. Ketelaars, R. Algra, and E.P.A.M. Bakkers, *Synergetic nanowire growth.* Nature Nanotechnology, 2007. **2**: p. 541-544.

116. Dick, K.A., K. Deppert, T. Mårtensson, W. Seifert, and L. Samuelson, *Growth of GaP nanotree structures by sequential seeding of 1D nanowires.* Journal of Crystal Growth, 2004. **272**: p. 131-137.

117. Gudiksen, M.S. and C.M. Lieber, *Diameter-Selective Synthesis of Semiconductor Nanowires.* Journal of the American Chemical Society, 2000. **122**: p. 8801-8802.

118. Dick, K.A., K. Deppert, T. Mårtensson, B. Mandl, L. Samuelson, and W. Seifert, *Failure of the Vapor-Liquid-Solid Mechanism in Au-Assisted MOVPE Growth of InAs Nanowires.* Nano Letters, 2005. **5**(4): p. 761-4.

119. Caroff, P., K.A. Dick, J. Johansson, M.E. Messing, K. Deppert, and L. Samuelson, *Controlled polytypic and two-plane superlattices in III-V nanowires.* Nature Nanotechnology, 2009. **4**: p. 50-55.

120. Fröberg, L.E., W. Seifert, and J. Johansson, *Diameter-dependent growth rate of InAs nanowires.* Physical Review B, 2007. **76**: p. 153401.

121. Park, H.D., A.-C. Gaillot, S.M. Prokes, and R.C. Cammarata, *Observation of size dependent liquid depression in the growth of InAs nanowires.* Journal of Crystal Growth, 2006. **296**: p. 159-164.

122. Bhunia, S., T. Kawamura, S. Fujikawa, and Y. Watanabe, *Systematic investigation of growth of InP nanowires by metalorganic vapor-phase epitaxy.* Physica E, 2004. **24**: p. 138-142.

123. Algra, R.E., M.A. Verheijen, M.T. Borgström, L.-F. Feiner, G. Immink, W.J.P.v. Enckevort, E. Vlieg, and E.P.A.M. Bakkers, *Twinning superlattices in indium phosphide nanowires.* Nature, 2008. **456**: p. 369-372.

124. Borchers, C., S. Müller, D. Stichtenoth, D. Schwen, and C. Ronning, *Catalyst-Nanostructrue Interaction in the Growth of 1-D ZnO Nanostructures.* Journal of Physical Chemistry B, 2006. **110**: p. 1656-1660.

125. Chen, Y.X., M. Lewis, and W.L. Zhou, *ZnO nanostructure fabricated through a double-tube vapor-phase transport synthesis.* Journal of Crystal Growth, 2005. **282**: p. 85-93.

126. Fan, H.J., B. Fuhrmann, R. Scholz, F. Syrowatka, A. Dadgar, A. Krost, and M. Zacharias, *Well-ordered ZnO nanowire arrays on GaN substrate fabricated via nanosphere lithography.* Journal of Crystal Growth, 2006. **287**(1): p. 34-38.

127. Hejazi, S.R. and H.R. Hosseini, *A Diffusion-Controlled Kinetic Model for Growth of Au-Catalyzed ZnO Nanorods: Theory and Experiment.* Journal of Crystal Growth, 2007. **309**: p. 70-75.

128. Li, Y.J., M. Feneberg, A. Reiser, M. Schirra, R. Enchelmaier, A. Ladenburger, A. Langlois, R. Sauer, K. Thonke, J. Cai, and H. Rauscher, *Au-catalyzed growth processes and luminescence properties of ZnO nanopillars on Si.* Journal of Applied Physics, 2006. **99**(5): p. 054307.

129. Philipose, U., S.V. Nair, S. Trudel, C.F.d. Souza, S. Aouba, R.H. Hill, and H.E. Ruda, *High-temperature ferromagnetism in Mn-doped ZnO nanowires.* Applied Physics Letters, 2006. **88**: p. 263101.

130. Tseng, Y.-K., I.-N. Lin, K.-S. Liu, T.-S. Lin, and I.-C. Chen, *Low-temperature growth of ZnO nanowires.* Journal of Materials Research, 2003. **18**(3): p. 714-718.

131. Wang, X.D., C.J. Summers, and Z.L. Wang, *Large-scale hexagonal-patterned growth of aligned ZnO nanorods for nano-optoelectronics and nanosensor arrays.* Nano Letters, 2004. **4**(3): p. 423-426.

132. Wang, X.D., J.H. Song, P. Li, J.H. Ryou, R.D. Dupuis, C.J. Summers, and Z.L. Wang, *Growth of uniformly aligned ZnO nanowire heterojunction arrays on GaN, AIN, and Al0.5Ga0.5N substrates.* Journal of the American Chemical Society, 2005. **127**(21): p. 7920-7923.

133. Wang, X.D., J.H. Song, C.J. Summers, J.H. Ryou, P. Li, R.D. Dupuis, and Z.L. Wang, *Density-controlled growth of aligned ZnO nanowires sharing a common contact: A simple, low-cost, and mask-free technique for large-scale applications.* Journal of Physical Chemistry B, 2006. **110**(15): p. 7720-7724.

134. Yang, P., H. Yan, S. Mao, R. Russo, J. Johnson, R. Saykally, N. Morris, J. Pham, R. He, and H.-J. Choi, *Controlled Growth of ZnO Nanowires and Their Optical Properties.* Advanced Functional Materials, 2002. **12**(5): p. 323-331.

135. He, J.H., J.H. Hsu, C.W. Wang, H.N. Lin, L.J. Chen, and Z.L. Wang, *Pattern and feature designed growth of ZnO nanowire arrays for vertical devices.* Journal of Physical Chemistry B, 2006. **110**(1): p. 50-53.

136. Hejazi, S.R., H.R.M. Hosseini, and M.S. Ghamsari, *The Role of Reactants and Droplet Interfaces on Nucleation and Growth of ZnO Nanorods Synthesized by Vapor-Liquid-Solid (VLS) Mechanism.* Journal of Alloys and Compounds, 2008. **455**: p. 353-357.

137. Mai, W., P. Gao, C. Lao, Z.L. Wang, A.K. Sood, D.L. Polla, and M.B. Soprano, *Vertically Aligned ZnO Nanowire Arrays on GaN and SiC Substrates.* Chemical Physics Letters, 2008. **460**: p. 253-256.

138. Huang, M.H., Y. Wu, H. Feick, N. Tran, E. Weber, and P. Yang, *Catalytic Growth of Zinc Oxide Nanowires by Vapor Transport.* Advanced Materials, 2001. **13**(2): p. 113-116.

139. Zhu, Z., T.-L. Chen, Y. Gu, J. Warren, and R.M. Osgood, Jr., *Zinc Oxide Nanowires Grown by Vapor-Phase Transport Using Selected Metal Catalysts: A Comparative Study.* Chemistry of Materials, 2005. **17**: p. 4227-4234.

140. Kong, X., X. Sun, X. Li, and Y. Li, *Catalytic growth of ZnO nanotubes.* Materials Chemistry and Physics, 2003. **82**: p. 997-1001.

141. Iwanga, H., N. Shibata, M. Hirose, and K. Suzuki, *Growth Mechanism of ZnO Ribbon Crystals from ZnS.* Journal of Crystal Growth, 1976. **35**: p. 159-164.

142. Gao, P.X. and Z.L. Wang, *Substrate atomic-termination-induced anisotropic growth of ZnO nanowires/nanorods by the VLS process.* Journal of Physical Chemistry B, 2004. **108**(23): p. 7534-7537.

143. Yang, R.S. and Z.L. Wang, *Growth of Self-Assembled ZnO Nanowire Arrays.* Philosophical Magazine, 2006. **87**(14-15): p. 2097-2104.

144. Ding, Y., P.X. Gao, and Z.L. Wang, *Catalyst-Nanostructure Interfacial Lattice Mismatch in Determining the Shape of VLS Grown Nanowires and Nanobelts: A Case of Sn/ZnO.* Journal of the American Chemical Society, 2004. **126**: p. 2066-72.

145. Zhuang, H., D. Wang, J. Shen, C. Xue, X. Zhang, and H. Liu, *Fabrication and Characterization of Novel Bicrystalline ZnO Nanowires.* Journal of Materials Research, 2009. **24**(8): p. 2536-2540.

146. Wang, Y.W., L.D. Zhang, G.Z. Wang, X.S. Peng, Z.Q. Chu, and C.H. Liang, *Catalytic growth of semiconducting zinc oxide nanowires and their photoluminescence properties.* Journal of Crystal Growth, 2002. **234**: p. 171-175.

147. Wang, X., Q. Li, Z. Liu, J. Zhang, Z. Liu, and R. Wang, *Low-temperature growth and properties of ZnO nanowires.* Applied Physics Letters, 2004. **84**(24): p. 4941-4943.

148. Iwanga, H., N. Shibata, O. Nittono, and M. Kasuga, *Crystal Growth in c Direction and Crystallographic Polarity in ZnO Crystals.* Journal of Crystal Growth, 1978. **45**: p. 228-232.

149. Hao, Y., G. Meng, Z.L. Wang, C. Ye, and L. Zhang, *Periodically Twinned Nanowires and Polytypic Nanobelts of ZnS: The Role of Mass Diffusion in Vapor-Liquid-Solid Growth.* Nano Letters, 2006. **6**(8): p. 1650-1655.

150. Lin, M., T. Sudhiranjan, C. Boothroyd, and K.P. Loh, *Influence of Au catalyst on the growth of ZnS nanowires.* Chemical Physics Letters, 2004. **400**: p. 175-178.

151. Moore, D., J.R. Morber, R.L. Snyder, and Z.L. Wang, *Growth of Ultralong ZnS/SiO2 Core-Shell Nanowires by Volume and Surface Diffusion VLS process.* Journal of Physical Chemistry C, 2008. **112**: p. 2895-2903.

152. Wang, Y., L. Zhang, C. Liang, G. Wang, and X. Peng, *Catalystic growth and photoluminescence properties of semiconductor single-crystal ZnS nanowires.* Chemical Physics Letters, 2002. **357**: p. 314-318.

153. Wang, Y., G. Meng, L. Zhang, C. Liang, and J. Zhang, *Catalytic Growth of Large-Scale Single-Crystal CdS Nanowires by Physical Evaporation and Their Photoluminescence.* Chemistry of Materials, 2002. **14**: p. 1773-1777.

154. Zhang, J., Y. Yang, F. Jiang, J. Li, B. Xu, S. Wang, and X. Wang, *Fabrication of semiconductor CdS hierarchial nanostructures.* Journal of Crystal Growth, 2006. **293**: p. 236-241.

155. Dai, G., Q. Zhang, Z. Peng, W. Zhou, M. Xia, Q. Wan, A. Pan, and B. Zou, *One-step synthesis of low-dimensional CdSe nanostructures and optical waveguide of CdSe nanowires.* Journal of Physics D, 2008. **41**: p. 135301.

156. López-López, M., A. Guillén-Cervantes, Z. Rivera-Alvarez, and I. Hernández-Calderón, *Hillocks formation during the molecular beam epitaxial growth of ZnSe on GaAs substrates.* Journal of Crystal Growth, 1998. **193**: p. 528-534.

157. Cai, Y., S.K. Chan, I.K. Sou, Y.F. Chan, D.S. Su, and N. Wang, *The Size-Dependent Growth Direction of ZnSe Nanowires.* Advanced Materials, 2006. **18**: p. 109-114.

158. Janik, E., J. Sadowski, P. Dluzewski, S. Kret, L.T. Baczewski, A. Petroutchik, E. Lusakowska, J. Wróbel, W. Zaleszczyk, G. Karczewski, T. Wojtowicz, and A. Presz, *ZnTe nanowires grown on GaAs(100) substrates by molecular beam epitaxy.* Applied Physics Letters, 2006. **89**: p. 133114.

159. Meng, Q., C. Jiang, and S.X. Mao, *Temperature-dependent growth of zinc-blende-structured ZnTe nanostructures.* Journal of Crystal Growth, 2008. **310**: p. 4481-4486.

160. Peng, H., S. Meister, C.K. Chan, X.F. Zhang, and Y. Cui, *Morphology Control of Layer-Structured Gallium Selenide Nanowires.* Nano Letters, 2007. **7**(1): p. 199-203.

161. Kalyanikutty, K.P., F.L. Deepak, C. Edem, A. Govindaraj, and C.N.R. Rao, *Carbon-Assisted Synthesis of Nanowires and Related Nanostructures of MgO.* Materials Research Bulletin, 2005. **40**: p. 831-839.

162. Kar, S. and S. Chaudhuri, *Synthesis and Characterization of One-Dimensional MgO Nanostructures.* Journal of Nanoscience and Nanotechnology, 2006. **6**: p. 1447-1452.

163. Kim, G., R.L. Martens, G.B. Thompson, B.C. Kim, and A. Gupta, *Selective Area Synthesis of Magnesium Oxide Nanowires.* Journal of Applied Physics, 2007. **102**: p. 104906.

164. Han, S., C. Li, Z. Liu, B. Lei, D. Zhang, W. Jin, X. Liu, T. Tang, and C. Zhou, *Transition Metal Oxide Core-Shell Nanowires: Generic Synthesis and Transport Studies.* Nano Letters, 2004. **4**(7): p. 1241-1246.

165. Nagashima, K., T. Yanagida, H. Tanaka, and T. Kawai, *Control of Magnesium Oxide Nanowire Morphologies by Ambient Temperature.* Applied Physics Letters, 2007. **90**: p. 233103.

166. Yanagida, T., K. Nagashima, H. Tanaka, and T. Kawai, *Mechanism of catalyst diffusion on magnesium oxide nanowire growth.* Applied Physics Letters, 2007. **91**: p. 061502.

167. Zhan, J., Y. Bando, J. Hu, and D. Goldberg, *Bulk Synthesis of Single-Crystalline Magnesium Oxide Nanotubes.* Inorganic Chemistry, 2004. **43**: p. 2462-2464.

168. Kim, H.W., S.H. Shim, and J.W. Lee, *Sn-catalyzed growth of MgO nanowires.* Journal of Nanoscience and Nanotechnology, 2007. **7**(12): p. 4434-4438.

169. Liu, X., C. Li, S. Han, J. Han, and C. Zhou, *Synthesis and electronic transport studies of CdO nanoneedles.* Applied Physics Letters, 2003. **82**(12): p. 1950-1952.

170. Kuo, T.-J. and M.H. Huang, *Gold-Catalyzed Low-Temperature Growth of Cadmium Oxide Nanowires by Vapor Transport.* Journal of Physical Chemistry B, 2006. **110**: p. 13717-13721.

171. Koparanova, N., Z. Zlatev, D. Genchev, and G. Popovich, *Cadmium oxide whisker crystals grown by the vapour-liquid-solid mechanism using various elements as growth initiators.* Journal of Materials Science, 1994. **29**: p. 103-109.

172. Morber, J.R., Y. Ding, M.S. Haluska, Y. Li, J.P. Liu, Z.L. Wang, and R.L. Snyder, *PLD-Assisted VLS Growth of Aligned Ferrite Nanorods, Nanowires, and Nanobelts-Synthesis, and Properties.* Journal of Physical Chemistry B, 2006. **110**(43): p. 21672-21679.

173. Johnson, M.C., S. Aloni, D.E. McCready, and E.D. Bourret-Courchesne, *Controlled Vapor-Liquid-Solid Growth of Indium, Gallium, and Tin Oxide Nanowires via Chemical Vapor Transport.* Crystal Growth & Design, 2006. **6**(8): p. 1936-1941.

174. Nguyen, P., H.T. Ng, and M. Meyyappan, *Catalyst Metal Selection for Synthesis of Inorganic Nanowires.* Advanced Materials, 2005. **17**: p. 1773-1777.

175. Nguyen, P., H.T. Ng, J. Kong, A.M. Cassell, R. Quinn, J. Li, J. Han, M. McNeil, and M. Meyyappan, *Epitaxial Directional Growth of Indium-Doped Tin Oxide Nanowire Arrays.* Nano Letters, 2003. **3**(7): p. 925-928.

176. Liu, Z., D. Zhang, S. Han, C. Li, T. Tang, W. Jin, X. Liu, B. Lei, and C. Zhou, *Laser Ablation Synthesis and Electron Transport Studies of Tin Oxide Nanowires.* Advanced Materials, 2003. **15**(20): p. 1754-1757.

177. He, J.H., T.H. Wu, C.L. Hsin, K.M. Li, L.J. Chen, Y.L. Chueh, L.J. Chou, and Z.L. Wang, *Beaklike SnO_2 Nanorods with Strong Photoluminescent and Field-Emission Properties.* Small, 2006. **2**(1): p. 116-120.

178. Li, C., D. Zhang, S. Han, X. Liu, T. Tang, and C. Zhou, *Diameter-Controlled Growth of Single-Crystalline In_2O_3 Nanowires and Their Electronic Properties.* Advanced Materials, 2003. **15**(2): p. 143-146.

179. Zhang, J., X. Qing, F. Jiang, and Z. Dai, *A route to Ag-catalyzed growth of the semiconducting In_2O_3 nanowires.* Chemical Physics Letters, 2003. **371**(3): p. 311-316.

180. Choi, Y.J., S.Y. Moon, J.H. Park, J.G. Park, and S. Nahm, *Synthesis of gallium oxide nanostructures and their structural properties.* Journal of the Korean Physical Society, 2006. **49**(3): p. 1152-1155.

181. Chang, K.-W. and J.-J. Wu, *Catalytic growth and characterization of Ga_2O_3 nanowires.* Applied Physics A, 2003. **76**: p. 629-631.

182. Chang, K.W. and J.J. Wu, *One-dimensional β-Ga_2O_3 nanostructures on sapphire (0001): Low-temperature epitaxial nanowires and high-temperature nanorod bundles.* Journal of Materials Research, 2005. **20**(12): p. 3397-3403.

183. Zhang, J., F. Jiang, Y. Yang, and J. Li, *Catalyst-Assisted Vapor-Liquid-Solid Growth of Single-Crystal Ga_2O_3 Nanobelts.* Journal of Physical Chemistry B, 2005. **109**: p. 13143-13147.

184. Park, S., H. Kim, C. Lee, D.H. Lee, and S.S. Hong, *Synthesis of Very Straight Bismuth Oxide Nanowires by Using Thermal Evaporation of Bismuth Powders.* Journal of the Korean Physical Society, 2008. **53**(4): p. 1965-1970.

185. Wang, S., Y. He, J. Zou, Y. Jiang, J. Xu, B. Huang, C.T. Liu, and P.K. Liaw, *Synthesis of single-crystalline tungsten nanowires by nickel-catalyzed vapor-phase method at 850°C.* Journal of Crystal Growth, 2007. **306**: p. 433-436.

186. Wang, S.L., Y.H. He, J. Zou, Y. Wang, H. Huang, B.Y. Huang, C.T. Liu, and P.K. Liaw, *Catalytic growth of metallic tungsten whiskers based on the vapor-solid-solid mechanism.* Nanotechnology, 2008. **19**: p. 345604.

187. Hulteen, J.C. and C.R. Martin, *A General Template-Based Method for the Preparation of Nanomaterials.* Journal of Materials Chemistry, 1997. **7**(7): p. 1075-1787.

188. Huczko, A., *Template-Based Synthesis of Nanomaterials.* Applied Physics A, 2000. **70**: p. 365-376.

189. Lin, C.C., I.C. Leu, J.H. Yen, and M.H. Hon, *A possible approach exploring the melting state of catalysts during the low-temperature growth of carbon nanotubes.* Diamond and Related Materials, 2005. **14**(11-12): p. 1901-1905.

190. Homma, Y., Y. Kobayachi, T. Ogino, D. Takagi, R. Ito, Y.J. Jung, and P.M. Ajayan, *Role of Transition Metal Catalysts in Single-Walled Carbon Nanotube Growth in Chemical Vapor Depostion.* Journal of Physical Chemistry B, 2003. **107**: p. 12161.

191. Kukovitsky, E.F., S.G. L'vov, and N.A. Sainov, *VLS-growth of carbon nanotubes from the vapor.* Chemical Physics Letters, 2000. **317**: p. 65-70.

192. Lin, M., J.P.Y. Tan, C. Boothroyd, K.P. Loh, E.S. Tok, and Y.-L. Foo, *Dynamical Observation of Bamboo-like Carbon Nanotube Growth.* Nano Letters, 2007. **7**(8): p. 2234-2238.

193. Harutyunyan, A.R., T. Tokune, and E. Mora, *Liquid as a required catalyst phase for carbon single-walled nanotube growth.* Applied Physics Letters, 2005. **87**: p. 051919.

194. Hofmann, S., G. Csnyi, A.C. Ferrari, M.C. Payne, and J. Robertson, *Surface Diffusion: The Low Activation Energy Path for Nanotube Growth.* Physical Review Letters, 2005. **95**: p. 036101.

195. Hofmann, S., C. Ducati, J. Robertson, and B. Kleinsorge, *Low-temperature growth of carbon nanotubes by plasma-enhanced chemical vapor deposition.* Applied Physics Letters, 2003. **83**(1): p. 135-137.

196. Chen, M., C.-M. Chen, S.-C. Shi, and C.-F. Chen, *Low-Temperature Synthesis Multiwalled Carbon Nanotubes by Microwave Plasma Chemical Vapor Deposition Using CH_4-CO_2 Gas Mixture.* Japanese Journal of Applied Physics, 2003. **42**: p. 614-619.

197. Seidel, R., G.S. Duesberg, E. Unger, A.P. Graham, M. Liebau, and F. Kreupl, *Chemical Vapor Deposition Growth of Single-Walled Carbon Nanotubes at 600ºC and a Simple Growth Model.* Journal of Physical Chemistry B, 2004. **108**: p. 1888-1893.

198. Helveg, S., C. López-Cartes, J. Sehested, P.L. Hansen, B.S. Clausen, J.R. Rostrup-Nielsen, F. Abild-Pedersen, and J.K. Norskov, *Atomic-scale imaging of carbon nanofibre growth.* Nature, 2004. **427**: p. 426-429.

199. Kolasinski, K.W., *Catalytic growth of nanowires: Vapor-liquid-solid, vapor-solid-solid, solution-liquid-solid and solid-liquid-solid growth.* Current Opinion in Solid State and Materials Science, 2006. **10**: p. 182-191.

200. Yong, K.-T., Y. Sahoo, M.T. Swihart, and P.N. Prasad, *Growth of CdSe Quantum Rods and Multipods Seeded by Noble-Metal Nanoparticles.* Advanced Materials, 2006. **18**: p. 1978-1982.

201. Wang, F., A. Dong, J. Sun, R. Tang, H. Yu, and W.E. Buhro, *Solution-Liquid-Solid Growth of Semiconductor Nanowires.* Inorganic Chemistry, 2006. **45**: p. 7511-7521.

202. Holmes, J.D., K.P. Johnston, R.C. Doty, and B.A. Korgel, *Control of Thickness and Orientation of Solution-Grown Silicon Nanowires.* Science, 2000. **287**: p. 1471-1473.

203. Tuan, H.-Y., D.C. Lee, T. Hanrath, and B.A. Korgel, *Germanium Nanowire Synthesis: An Example of Solid-Phase Seeded Growth with Nickel Nanocrystals.* Chemistry of Materials, 2005. **17**: p. 5705-5711.

204. Sun, X., B. Yu, G. Ng, T.D. Nguyen, and M. Meyyappan, *III-VI compound semiconductor indium selenide (In_2Se_3) nanowires: Synthesis and characterization.* Applied Physics Letters, 2006. **89**: p. 233121.

205. Frank, F.C., *The Influence of Dislocations on Crystal Growth.* Discussions of the Faraday Society, 1949. **5**: p. 48-54.

206. Burton, W.K., N. Cabrera, and F.C. Frank, *The Growth of Crystals and the Equilibrium Structure of their Surfaces.* Philosophical Transactions of the Royal Society of London A, 1951. **243**(866): p. 299-358.

207. Burton, W.K., N. Cabrera, and F.C. Frank, *Role of Dislocations in Crystal Growth.* Nature, 1949. **163**: p. 398-399.

208. Morelock, C.R. and G.W. Sears, *Growth Mechanism of Copper Whiskers by Hydrogen Reduction of Cuprous Iodide.* Journal of Chemical Physics, 1959. **31**(4): p. 926-928.

209. Sears, G.W., *Mercury Whiskers.* Acta Metallurgica, 1953. **1**: p. 457-459.

210. Wagner, R.S. and W.C. Ellis, *The Vapor-Liquid-Solid Mechanism of Crystal Growth and Its Application to Silicon.* Transactions of the Metallurgical Society of AIME, 1965. **233**: p. 1053-1064.

211. Bierman, M.J., Y.K.A. Lau, A.V. Kvit, A.L. Schmitt, and S. Jin, *Dislocation-Driven Nanowire Growth and Eshelby Twist.* Science, 2008. **320**: p. 1060-1063.

212. Ding, F., A.R. Harutyunyan, and B.I. Yakobson, *Dislocation Theory of Chirality-Controlled Nanotube Growth.* Proceedings of the National Academy of Sciences, 2009. **106**(8): p. 2506-2509.

213. Wagner, R.S., *Defects in Silicon Crystals Grown by the VLS Technique.* Journal of Applied Physics, 1967. **38**(4): p. 1554-1560.

214. Wagner, R.S. and C.J. Doherty, *Controlled Vapor-Liquid-Solid Growth of Silicon Crystals.* Journal of the Electrochemical Society, 1966. **113**(12): p. 1300-1305.

215. Campos, L.C., M. Tonezzer, A.S. Ferlauto, V. Grillo, R. Magalhes-Paniago, S. Oliveria, L.O. Ladeira, and R.G. Lacerda, *Vapor-Solid-Solid Growth Mechanism Driven by Epitaxial Match between Solid AuZn Alloy Catalyst Particles and ZnO Nanowires at Low Temperatures.* Advanced Materials, 2008. **20**: p. 1499-1504.

216. Wang, H. and G.S. Fischman, *Role of liquid droplet surface diffusion in the vapor-liquid-solid whisker growth mechanism.* Journal of Applied Physics, 1994. **76**(3): p. 1557-1562.

CHAPTER 2

EXPERIMENTAL METHODS

For this research, samples of nanostructures of various materials were grown using catalyzed techniques and then characterized using X-ray diffraction (XRD), as well as scanning electron microscopy (SEM) and transmission electron microscopy (TEM). The purpose of this chapter is to detail the furnace setup and synthesis parameters used to grow the nanostructures, and to discuss the characterization techniques used to investigate the nanostructures.

2.1 Synthesis Techniques

Nanostructures that were to be characterized only after the completion of growth were synthesized in a horizontal tube furnace, as discussed in section 2.1.1 below. Samples of Au-catalyzed ZnO, Sn-catalyzed ZnO and Au-catalyzed iron oxide nanostructures were grown in the horizontal tube furnace. Nanostructures to be characterized *in-situ*, during growth, were synthesized in furnaces attached to an X-ray diffractometer, as discussed in section 2.1.2 below. Samples of Au-catalyzed Si and self-catalyzed ZnO nanostructures were grown in the X-ray diffractometer furnace.

2.1.1 Synthesis in a Horizontal Tube Furnace

2.1.1.1 Tube Furnace Setup

Nanostructure synthesis in a horizontal tube furnace enables multiple temperature zones: a higher temperature zone for the vaporization of the source material powder, and

a lower temperature zone for the growth of the nanostructures. The samples were synthesized in a Thermolyne 79300 horizontal tube furnace, fit with an alumina tube with a diameter of 44 mm and a length of 76 cm, as seen in Figure 2.1. End caps can be placed on each end of the alumina tube. One end cap, on the downstream end of the tube, has a connection to the vacuum system. The low internal pressure, generated by an Edwards vacuum pump, holds the end caps tightly against the alumina tube. The other end cap, on the upstream end of the tube, has a connection to the gas system, to allow the introduction of various gases during growth.

Each end cap is water-cooled, both to protect the materials in the end cap, as well as to generate a temperature gradient along the length of the alumina tube. The alumina tube will have the highest temperature in the center, with the temperature decreasing as the distance from the center increases. The temperature profile within the furnace was characterized using a thermocouple. The temperature of the source materials is controlled by the furnace controller. The temperature of the substrates is controlled by controlling the distance of the substrates from the center of the furnace.

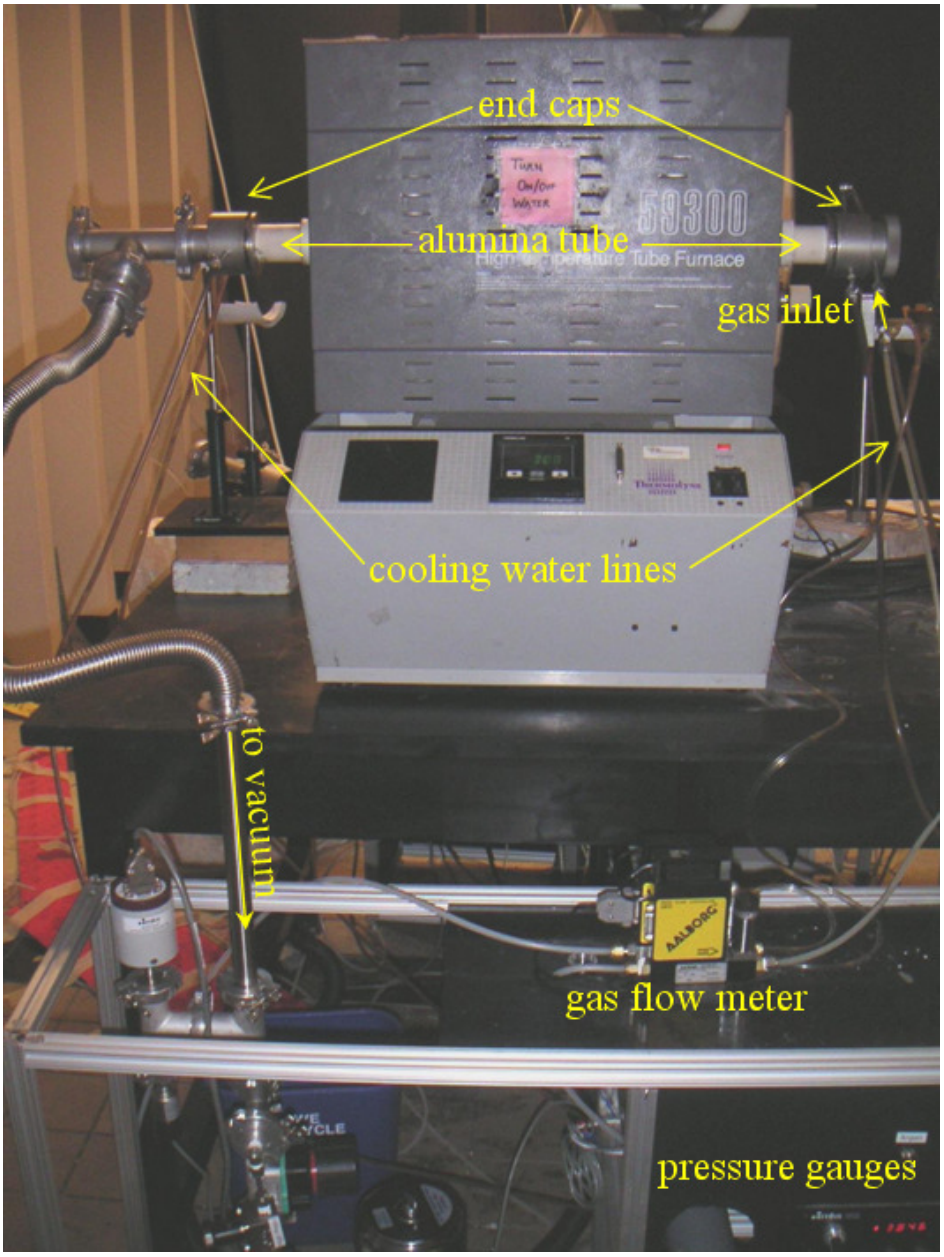

Figure 2.1 Horizontal tube furnace setup for nanostructures synthesis.

Generally, the source material to be vaporized is placed on an alumina boat in the center of the alumina tube. The substrates are placed on a second alumina boat on the downstream end of the alumina tube. The substrates are coated with a thin metal layer, usually gold, either by sputtering or by thermal evaporation. Upon heating to temperatures above approximately 300ºC, the polycrystalline deposit separates into gold nanoparticles, with diameters around 20 to 30 nm. The furnace is heated up to the growth temperature, and the source material begins to vaporize. An inert carrier gas is introduced, and the gas flow carries the vaporized source material to the substrates, where the nanostructures grow.

2.1.1.2 Setup for Pulsed Laser Deposition (PLD)–Assisted Growth

For the samples of iron oxide nanostructures, vaporization of the source was aided using laser heating, as described in reference [1]. The laser used is a Lambda Physik Compex series excimer 102 laser (20 Hz, 30 kV, ~300 mJ). An optical window in the upstream end cap allows entry of the beam, as seen in Figure 2.2. Energy is added by the laser impinging on the source material target, which ablates the target. The laser spot size is approximately 1 mm by 5 mm. The substrates are placed directly below and in front of the target, where the ablated species fall.

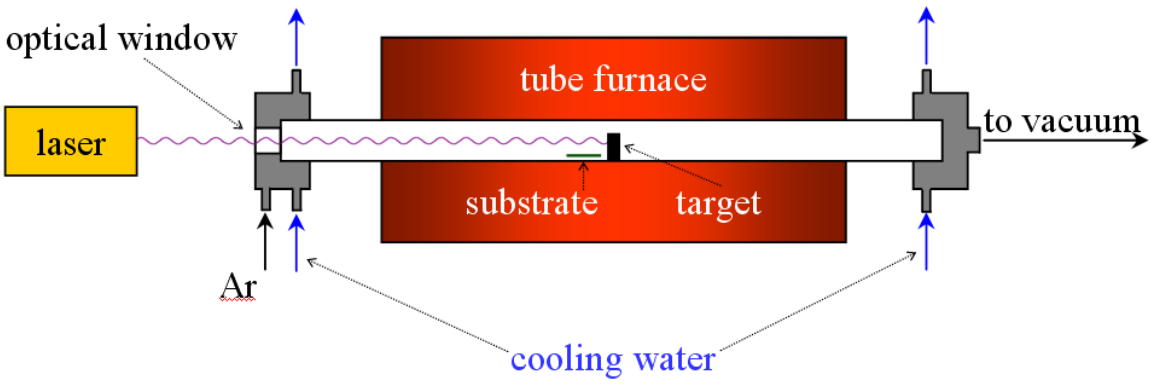

Figure 2.2 Schematic of tube furnace setup with laser for PLD-assisted growth of Fe_xO_y nanostructures.

2.1.2 Synthesis in an X-Ray Diffractometer Furnace

Samples to be characterized *in-situ* during synthesis were grown in one of two furnaces, an oven-type furnace or a strip furnace, attached to an X-ray diffractometer. This section describes the synthesis setup and parameters. Section 2.2.2.4 below will describe the experimental setup for XRD data collection.

2.1.2.1 Oven-Type Furnace

The oven-type furnace, an Anton-Paar HTK1200, can be attached to a Panalytical X'Pert PRO Multi-Purpose Diffractometer (MPD), as seen in Figure 2.3. The sample sits on an alumina pedestal, loaded from the bottom of the furnace. Kanthal APM (22% Cr, 5.8% Al, bal. Fe) heating elements surround the sample, giving a relatively uniform temperature profile throughout the furnace. The furnace temperature is measured by a type S (Pt-10%RhPt) thermocouple embedded in the alumina pedestal. The maximum temperature of the furnace is around 1000ºC. Aluminum-coated Kapton windows allow for entry and exit of the X-ray beams. The sample height is adjusted by raising or lowering the entire furnace with a motorized control.

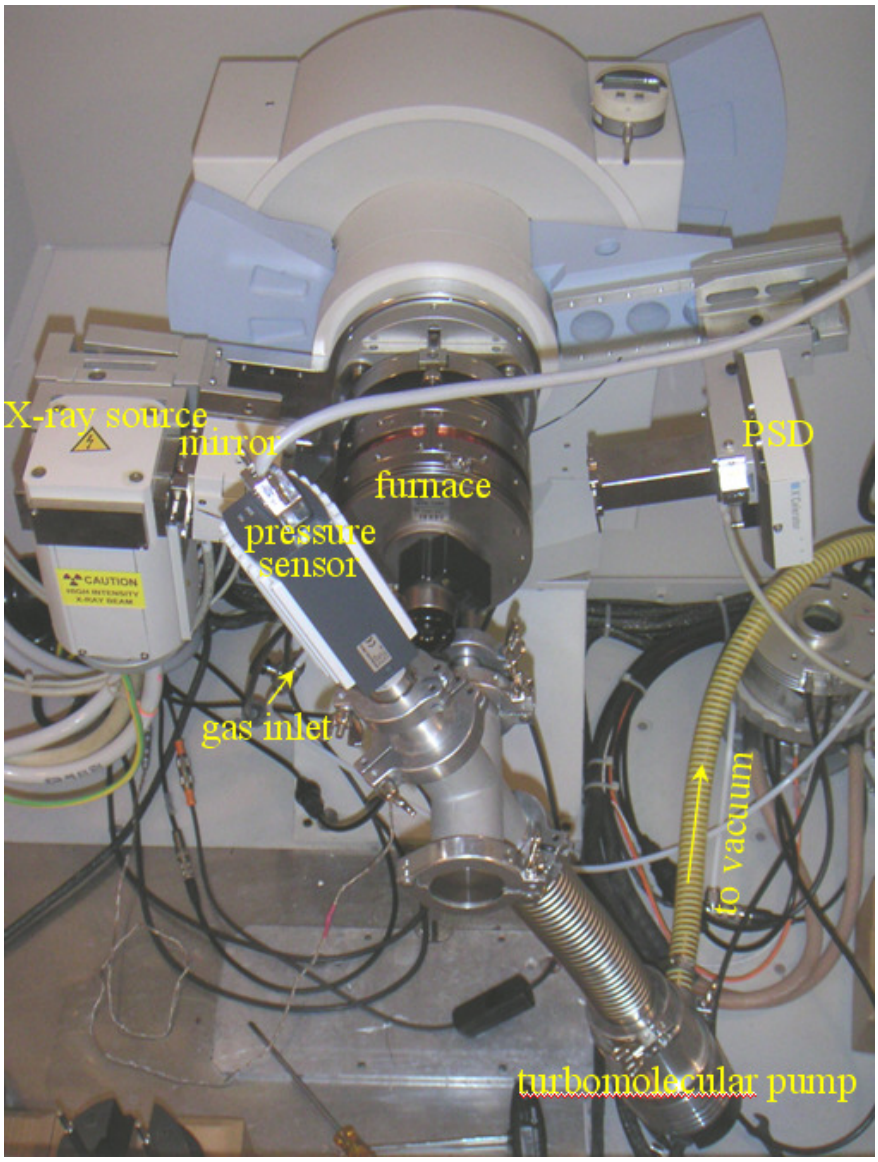

Figure 2.3 HTK1200 furnace setup on MPD for high-temperature X-ray diffraction.

2.1.2.2 Strip Furnace

The strip furnace, an Anton-Paar HTK 2000, can also be attached to the MPD. The temperature is controlled by resistively heating a strip. Two of the more common strip materials are platinum and tungsten. The temperature is measured by a thermocouple (type S Pt-10%RhPt for the Pt strip, W3Re/W25Re for the W strip) attached to the bottom side of the heating strip. The sample sits directly on the top of the strip. With the platinum strip, the furnace can be heated to a maximum temperature of 1450°C in vacuum, air, or other atmospheres. However, platinum strips cannot generally be used for silicon-containing samples, as the silicon reacts with the platinum to form Pt_3Si, which causes the strip to melt at 830°C [2]. Tungsten strips are more resistant to silicon. In addition, tungsten strips can be heated to higher temperatures than platinum strips, up to 2300°C. However, due to the danger of oxidation, tungsten strips can only be used under high vacuum (less than 10^{-4} mbar) or reducing atmospheres. Kapton windows allow for entry and exit of the X-ray beams. The sample height is adjusted by raising or lowering the entire furnace.

2.1.2.3 Comparison Between Oven-Type and Strip Furnaces

The strip furnace can be heated to higher temperatures than the oven-type furnace. However, the strip furnace also experiences large temperature gradients, depending on the distance of the sample from the strip. Because of this, the temperature of the sample can vary significantly from the displayed temperature, depending on the quality of the thermal contact between the strip and sample. The oven-type furnace has a relatively uniform temperature throughout the furnace chamber. In addition, the oven-type furnace can be used with a wider variety of atmospheres than the strip furnace, due to concerns

about reactions with the strip material. For these reasons, the oven-type furnace was preferentially employed for this research, with the strip furnace being reserved for higher-temperature experiments above the range of the oven-type furnace.

2.1.2.4 Temperature Validation

Regardless of the type of furnace used, the sample temperature must be validated to compensate for variations between the temperatures of the thermocouple and sample. Because the variations can depend on the sample loading and furnace atmosphere, the temperature must be validated under the same conditions as the experiment. There are two main approaches to temperature validation, using either the known thermal expansion or phase transitions of standard materials.

When using a thermal expansion standard, XRD patterns are collected at a range of temperatures on a material, such as MgO or Al_2O_3, and the thermal expansion behavior determined. Comparison with the known thermal expansion of the material allows the temperature to be validated over a wide range on a single sample. However, the lattice parameter must be determined very accurately for this method, which was not possible for our experimental setup due to sample surface displacement error, as discussed in section 2.2.2 below.

Therefore, the temperatures of our furnaces were validated using phase transition standards. In this method, XRD patterns are collected at a range of temperatures around a known crystallographic phase transition for the standard. This method only allows for validating one temperature per standard, generally, but the data analysis is simpler than with thermal expansion standards, since accurate lattice parameters are not required, only verification of the presence or absence of certain peaks.

For validating our furnaces, the phase transition standards used are shown in Table 2.1 below. Standards were chosen to cover the range of operating temperatures of the furnace. For the oven-type furnace in still air at atmospheric pressure, the displayed temperature is fairly consistently 19° lower than the actual temperature, as seen in Figure 2.4 below. For the oven-type furnace at 1 mbar pressure with N_2 flow, the difference between the actual and displayed temperatures is not constant, but instead decreases with increasing temperature, crossing into negative values at high temperatures, as see in Figure 2.5 below. In this work, all temperatures will be reported in actual values.

Table 2.1 Phase transition standard materials used for temperature validation of X-ray furnace.

Standard	Phase Transition	Transition Temp.
KNO_3	α (ortho.) → β (trig.)	129°C
$KClO_4$	ortho. ↔ cub.	300°C
Zn	melting	420°C
K_2SO_4	ortho. ↔ hex.	583°C
K_2CrO_4	ortho. ↔ hex.	665°C
$BaCO_3$	ortho. ↔ trig.	810°C

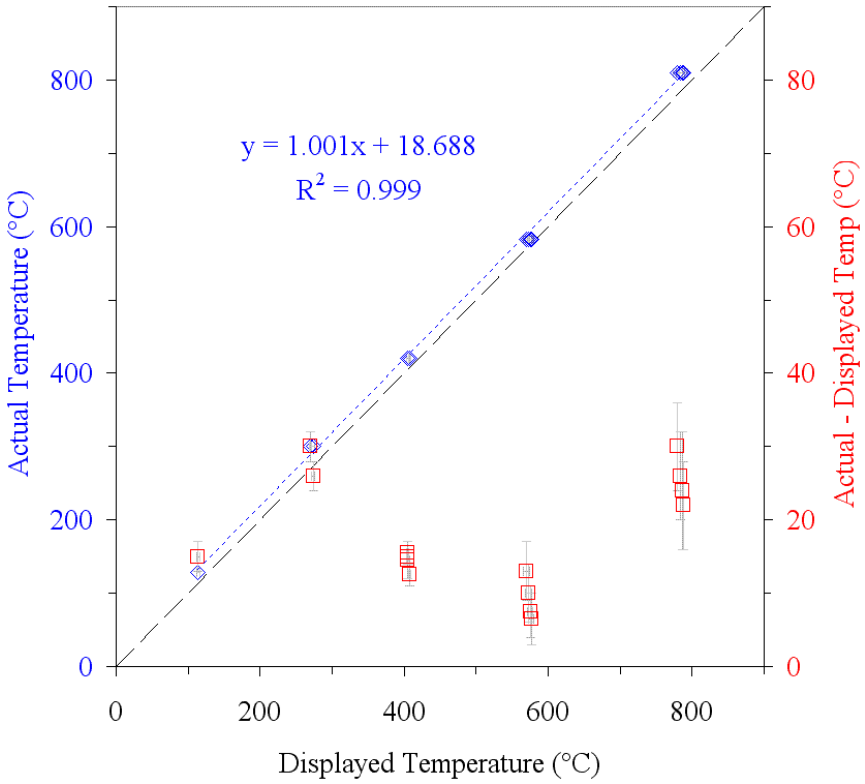

Figure 2.4 Temperature validation curve of the HTK-1200 oven-type furnace in still air. The blue diamonds indicate the actual temperature of the furnace on the left axis. The red squares indicate the difference between the actual and displayed temperatures on the right axis. The black dashed line indicates where the actual and displayed temperatures are equal.

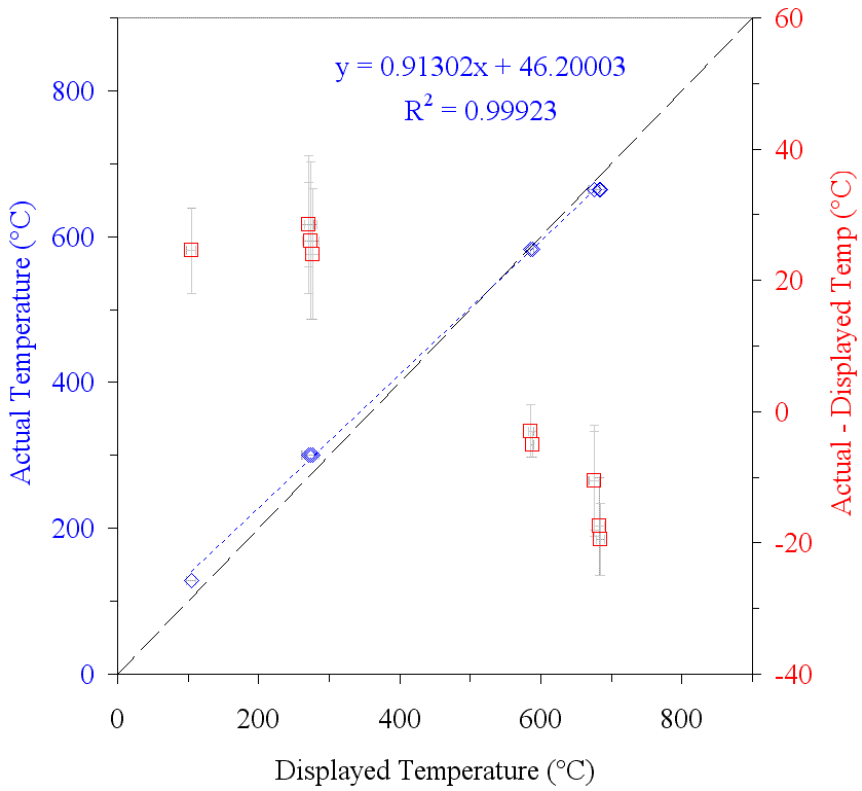

Figure 2.5 Temperature validation curve for HTK1200 furnace at 1 mbar under N2 flow. The blue diamonds indicate the actual temperature of the furnace on the left axis. The red squares indicate the difference between the actual and displayed temperatures on the right axis. The black dashed line indicates where the actual and displayed temperatures are equal.

2.1.2.5 Atmosphere Control

Both furnaces may be connected to a vacuum system, consisting of a Leybold Trivac B rotary vane vacuum pump, and a Leybold Turbovac turbomolecular pump. The minimum attainable pressure is around 1×10^{-5} mbar. Inlets into both furnaces allow the flow various gases. For inert atmospheres, either nitrogen, helium or argon gases are flowed. For reducing atmospheres, a mixture of helium with 3.85% hydrogen is flowed. As this is below the lower flammability limit of hydrogen (4%, Airgas material safety data sheet (MSDS) #001026), no extraordinary safety precautions are needed. For the growth of silicon nanostructures, a mixture of nitrogen with 1% silane (SiH_4) is flowed. Again, this is below the lower explosive limit of silane (1.4%, Airgas MSDS #001073); consequently no extraordinary safety precautions are needed.

2.1.3 Nanostructure Synthesis Parameters

2.1.3.1 Gold-Catalyzed Zinc Oxide Nanostructures

The Au-catalyzed ZnO nanostructures were grown in the horizontal tube furnace. The source material was ZnO powder. The ZnO was mixed, in equal amounts by weight, with graphite, in order to aid the vaporization of the ZnO. The substrate, *c*-plane sapphire, was coated with first AlN, then $Al_{0.5}Ga_{0.5}N$. The thicknesses of the two coating layers were around 500 and 200 nm, respectively. The AlN and $Al_{0.5}Ga_{0.5}N$ layers help to bridge the lattice mismatch between the *c*-planes of the Al_2O_3 substrate and the ZnO nanorods. For the catalyst, gold was plasma sputtered onto the substrates to a thickness of seven to eight nm.

Prior to growth, the tube furnace was vacuumed to a pressure around 0.02 mbar with a vacuum pump. During growth, argon was introduced as an inert carrier gas. The

argon flow was supplemented with 2% oxygen, for a total flow rate of 50 standard cubic centimeters per minute (sccm) at a growth pressure of 30 mbar. The source materials were heated to 950ºC at a rate of 50º per minute. The substrates were in a temperature region around 850ºC. The furnace was held at temperature for 30 minutes, and then cooled under argon flow.

2.1.3.2 Tin-Catalyzed Zinc Oxide Nanostructures

For the growth of Sn-catalyzed ZnO nanostructures, a slightly different procedure was necessary. Tin readily oxidizes to form tin dioxide, which would be detrimental to its function as a catalyst. Therefore, when a tin catalyst was desired, SnO_2 and graphite were mixed with the ZnO source material powder [3, 4] in a molar ratio of 2:1:1 ($ZnO:SnO_2:C$). When heated, the graphite reduces the SnO_2 to metallic tin, and the vapor species, including both source and catalyst, are carried to the substrate. Some formation of tin nanoparticles and growth of nanostructures may occur in the gas flow during transit to the substrate.

Prior to growth, the tube furnace was vacuumed to pressures around 0.4mbar with a vacuum pump. During growth, argon was flowed through the furnace as an inert carrier gas at a flow rate of 20 sccm with a growth pressure of 200 mbar. The mixed source and catalyst materials were heated to 1150°C at a rate of 20°/min. The nanostructures were collected on substrates of polycrystalline corundum (Al_2O_3) or *c*-plane single crystals of Al_2O_3 or ZnO. The substrates were placed in a temperature region around 350 to 400°C and around 550 to 600°C. The furnace was held at temperature for five to sixty minutes, and then cooled under Ar flow.

2.1.3.3 Gold-Catalyzed Iron Oxide Nanostructures

For the growth of Au-catalyzed iron oxide nanostructures, a laser was used to aid the vaporization of the source material, as discussed in more detail in section 2.1.1.2 above. The source material was magnetite (Fe_3O_4) powder, which was pressed into a solid rod, with a diameter of 9.5 mm, to serve as a target for the laser. The substrates, generally polycrystalline or single-crystal Al_2O_3 (*a*- or *c*-plane oriented), were coated with two nanometers of gold.

Prior to growth, the tube furnace was vacuumed to pressures around 0.02 mbar with a vacuum pump. During growth, argon was flowed through the furnace as an inert carrier gas, at a flow rate of 50 sccm with a growth pressure of around 10 mbar. The source material rod was heated to around 800 to 900°C at a rate of 20°/min. The substrates were placed immediately in front of the source material rod. The furnace was held at temperature for 60 minutes, while the target was ablated by the laser, and then cooled under vacuum.

2.1.3.4 Gold-Catalyzed Silicon Nanostructures

Since the Au-catalyzed Si nanostructures were grown in the HTK1200 oven-type X-ray furnace, a somewhat different procedure was used. In this case, the source, rather than being a vaporized powder, was silane (SiH_4) gas. The substrates, generally oxidized Si (100) single-crystal substrates, were sputtered with Au to thicknesses around 5 to 10 nm.

Prior to growth, the X-ray furnace was vacuumed to pressures around 1 to 10×10^{-3} mbar with the vacuum and turbo-molecular pumps. The chamber was then purged with N_2 for several hours to further reduce the oxygen partial pressure. The

furnace was heated up to the growth temperature, generally 685°C, at 25°/min, and then held for around one hour. After the high temperature hold, silane was introduced into the furnace, increasing the flow rate until the pressure reached the desired growth pressure, generally 3 mbar. The silane was flowed for the desired growth time, generally 30 minutes to one hour, after which the furnace was cooled under high vacuum (around 10^{-3} mbar).

2.2 Characterization Techniques

The samples were characterized using primarily electron microscopy, including both SEM and TEM, and X-ray diffraction. XRD data were collected both *in-situ*, i.e. during growth, and after growth.

2.2.1 Electron Microscopy

Nanostructure morphologies were initially characterized using two SEMs, a LEO 1530 and a LEO 1550. Both SEMs have thermally-assisted field emission guns, and imaging was conducted with the accelerating voltages generally being 10 kV. By using a lower accelerating voltage, the samples did not require coating with carbon or gold to prevent excessive charging from the electron beam, even for samples on insulating substrates. Both SEMs are equipped with annular in-lens detectors for improved resolution (1 nm at 20 kV), and Oxford Instruments INCA Dry Cool energy dispersive X-ray spectroscopy (EDS) systems with Si(Li) detectors for chemical analysis.

Nanostructures were further characterized using three different TEMs. The first is a JEOL 100CX II TEM, with a tungsten filament. Data was collected at an accelerating voltage of 100 kV. Electron diffraction patterns were collected with this TEM using camera lengths of 55 and 83 cm. The JEOL 100CX II TEM has a maximum

magnification of 320kX. The second is a Hitachi HF-2000 TEM, with a field emission gun. Data were collected at an accelerating voltage of 200 kV. This TEM is equipped with a ThermoScientific NORAN System Six EDS system with a Si drift detector for chemical analysis. The Hitachi HF-2000 TEM has a maximum magnification of 1500kX. High-resolution TEM (HRTEM) data were collected on a JEOL4000EX TEM at an accelerating voltage of 400 kV. This TEM has a maximum resolution of 0.18 nm.

Nanostructures to be analyzed were deposited on copper TEM grids with either holey-or solid-carbon films. The grids were loaded by lightly touching or brushing the surface of the substrate. If this could not result in sufficient transfer of nanostructures to the grid, the substrate was scrapped with a razor blade to loosen the nanostructures first.

2.2.2 X-Ray Diffraction

X-ray diffraction was the primary tool used for characterization of the crystal structure of the nanostructures. Techniques used include phase identification, lattice parameter determination, crystallite size and microstrain determination, texture analysis and rocking curve analysis.

2.2.2.1 Phase Identification and Lattice Parameter Determination

In phase identification, the most basic of XRD analyses, observed angles of the diffraction peaks are linked to the expected distances between adjacent parallel lattice planes in a database of known crystal structures through Bragg's law, as below.

$$\lambda = 2d_{hkl} \sin\theta_{hkl} \tag{1.1}$$

λ is the X-ray wavelength, d_{hkl} is the lattice plane spacing, and θ_{hkl} is the angle between the diffracting planes and the X-ray beams. From the observed diffraction angles, the

corresponding *d*-spacings may be calculated and compared to those from databases of known materials. This technique may also be used to monitor phase transitions as they occur when using an *in-situ* XRD setup, as in section 2.1.2 above. For example, melting can be clearly observed, as the diffraction peaks disappear along with the long-range order.

X-ray diffraction may also be used to determine the lattice parameter of a material with a high degree of accuracy and precision, on the order of 0.001 to 0.0001 Å. When measuring the lattice parameter, there are five main sources of possible error in the peak positions, which must be controlled, namely sample surface displacement, axial divergence, 2θ-zero, flat specimen and transparency errors [5, 6]. Sample surface displacement error can occur when the sample surface is not at the correct height, which is at the diffractometer axis and tangent to the focusing circle. This error was eliminated by the use of parallel beam geometry. When the incoming X-rays are parallel in the radial direction, errors in the sample height do not change the peak position, only the intensity. Another source of error is low angle peak asymmetry, which occurs when the X-rays diverge in the axial direction. The asymmetrical shape of the peak can obscure the correct peak position. This error was reduced by using Soller slits to reduce the axial divergence. A 2θ-zero error occurs when the angles of the diffractometer arms are incorrectly set, leading to a uniform position error across the entire 2θ range. This error was ameliorated by aligning the direct beam to 0º 2θ before XRD data collection. As a final check on all possible sources of error, the peaks from the substrate were used as an internal standard to correct the peak positions of the sample.

When dealing with thin depositions on single crystal substrates, as in the present work, the X-ray diffraction signal from the substrate can easily overshadow the XRD signal from the nanostructures. Two variations of the standard θ/2θ scan can ameliorate this problem. The first variation is an offset scan. In an offset scan, the sample is tilted in ω by a few degrees from the standard symmetric position. The substrate peaks, being from a single crystal, will be narrower than the peaks from the nanostructures. By tilting the sample, the offset scan can mostly miss the substrate peaks, while still hitting the sides of the peaks from the nanostructure. The second variation is a grazing incidence X-ray diffraction (GIXRD) scan. In a GIXRD scan, the angle between the incident beam and the sample, ω, is held fixed at a low value, typically 1-2°, while the detector is scanned through 2θ, as in a standard θ/2θ scan [7]. Because of the low incidence angle, the X-ray beam footprint will spread out over a larger area, and at the same time, the beam will penetrate less deeply into the sample. In this way, the signal from the surface is increased relative to the signal from the substrate. One side effect of the GIXRD beam geometry is that the scan will take a curved path through reciprocal space, missing most, if not all, peaks from single crystal substrates and highly crystallographically aligned phases, while crossing the diffraction rings from randomly oriented phases.

2.2.2.2 Crystallite Size and Microstrain Determination

In addition to phase and lattice parameter information gained from the position of the diffraction peaks, information about the crystallite size and microstrain can be gained from the width of the diffraction peaks. The crystallite size, as determined by XRD, corresponds to the average size of coherently diffracting domains, i.e. single crystal regions uninterrupted by grain boundaries, free surfaces, or other symmetry breaking

elements. The crystallite size may be smaller than the particle size determined by electron microscopy. However, for nanoparticles, it is reasonable to assume that each nanoparticle is a single crystallite.

Diffraction peaks broaden with decreasing crystallite size due to an interference effect. When X-rays impinge on a crystal at an angle slightly off the Bragg condition, the intensity scattered from the first plane is canceled by the intensity scattered from another plane some distance further down into the crystal. However, if the crystallite size is less than the distance of the canceling plane, the off-Bragg X-rays will not be completely cancelled, and therefore, the diffraction peak will broaden [6].

Microstrain refers to inhomogeneous variations in the lattice spacings. For example, around an edge dislocation, some areas will have the atoms packed more tightly, leading to smaller lattice spacings, while other areas will have the atoms spread further out, leading to larger lattice spacings. This variation in lattice spacing leads to a continuous variation in peak position. When diffracted X-rays from the entire crystal are summed, the diffraction peak will be broadened [6].

2.2.2.2.1 Scherrer Method

The simplest treatment of line broadening is the Scherrer method. This approach ignores the contribution from microstrain, and assumes that all line broadening is due to the crystallite size. First, the instrumental broadening is determined by collecting a diffraction pattern on a broadening standard, generally LaB_6 (National Institute of Standards and Technology (NIST) standard reference material (SRM) 660a). The line broadening is quantified by measuring the full width of the peak at half of the maximum

height (the full-width at half-max or FWHM). The instrumental broadening is then subtracted from the experimentally observed peak widths using the following equation,

$$B_{sample}{}^{n} = B_{obs}{}^{n} - B_{inst}{}^{n} \tag{0.1}$$

where B_{sample} is the broadening due to the sample, B_{obs} is the experimentally observed peak width, B_{inst} is the instrumental broadening, and n is an exponent that depends on the peak shape. For pure Lorentzian, also known as Cauchy, peaks, n is equal to 1, while for pure Gaussian peaks, n is equal to 2 [6]. Real peaks are neither pure Gaussian nor pure Lorentzian, but may be considered as a combination of the two. For this research, a value of 1.3 was used for n.

Once the broadening due to the sample has been determined, the crystallite size can be calculated according to an equation developed by Paul Scherrer in 1918 [8], as below.

$$t = \frac{K\lambda}{B_{sample}\cos\theta} \tag{0.2}$$

In this equation, t is the crystallite size, K is a shape factor, λ is the X-ray wavelength, B is the peak broadening and θ is the Bragg angle. The shape factor, K, depends on the shape of the crystallite, and is typically around 0.9 to 1 [6]. A value of 0.9 was used for this research. For typical lattice spacings, this technique is only feasible for crystallite sizes less than approximately 100 nm; larger crystallites result in broadening insufficient to be measured. Indeed, this restriction is true for all measurements of crystallite size by XRD.

2.2.2.2.2 Williamson-Hall Method

The Williamson-Hall method of line profile analysis includes the two separate effects of size and microstrain peak broadening. The broadening due to both effects is summed as in the equations below. The size broadening term is the same as the Scherrer equation above. The microstrain broadening term is a function of the tangent of θ, which can be separated into a sine and cosine, as follows.

$$\begin{aligned} B_{sample} &= B_{size} + B_{strain} \\ B_{sample} &= \frac{K\lambda}{t\cos\theta} - 2\varepsilon\tan\theta \\ B_{sample} &= \frac{K\lambda}{t\cos\theta} - \frac{2\varepsilon\sin\theta}{\cos\theta} \\ B_{sample}\cos\theta &= \frac{K\lambda}{t} - 2\varepsilon\sin\theta \end{aligned} \tag{0.3}$$

In these equations, ε is the microstrain, and the other terms are as defined for equation (0.2) above. Because the crystallite size broadening is inversely proportional to the cosine of θ, and the microstrain broadening is inversely proportional to the tangent of θ, the size and strain contributions to the peak broadening can be separated by plotting B•cos θ versus sin θ. As can be seen from equation (0.3) above, the plot should be linear, with the *y*-intercept determined by the crystallite size and the slope determined by the microstrain [6]. It is important to have enough peaks to allow a good linear fit.

The Williamson-Hall method generally assumes an isotropic crystallite shape and microstrain. However, this method may be extended to anisotropic materials by constructing separate Williamson-Hall plots for each family of lattice planes [9]. For example, by plotting the peak widths for the {111}, {222} and {333} peaks only, the

crystallite size and microstrain perpendicular to those planes may be determined. Again, this requires sufficient peaks in each family to allow a good linear fit.

2.2.2.2.3 Warren-Averbach Method

Both the Scherrer equation and the Williamson-Hall method assume an empirical peak shape function, generally Gaussian, Lorentzian or some combination of the two. This assumption may be avoided by using Fourier techniques, as in the Warren-Averbach method of line profile analysis [10]. Diffraction peak profiles are a convolution of contributions from the instrumental, size and strain broadening. The difficulty of working with convolutions generally requires the approximation of the peak shape using an empirical function. By working in Fourier space, however, the convolutions are transformed into simple multiplication, and so no such approximations are required. Additionally, the Warren-Averbach method can yield both an area- and volume-weighted average crystallite size, allowing the crystallite size distribution to be determined, assuming a log-normal form [11].

2.2.2.3 Rocking Curves and Orientation Analysis

Rocking curves and texture analysis are both used to investigate the alignment of crystal structures. In the XRD methods described in sections 2.2.2.1 and 2.2.2.2 above, data is collected while scanning through reciprocal space, which is represented, through Bragg's law, by the diffraction angles. However, in the rocking curve and texture methods, the position in reciprocal space is held fixed, and data is collected while scanning through real space.

Rocking curves are commonly used to investigate the mosaicity of epitaxially-grown thin films. To collect the data, the X-ray source and detector are held fixed at a

given diffraction angle corresponding to a peak from the phase of interest. Then, the intensity is recorded as the sample is tilted, or rocked (hence the name), through a few degrees ω (where ω is the angle between the incident beam and the sample surface). The width of the resultant peak is a measure of the degree of misalignment. For a perfect single crystal, the peak will be no wider than its Darwin width convoluted with the inherent instrumental breadth. For a randomly oriented sample, the intensity will not change as the sample is rocked. For this research, rocking curves were used to probe the degree of misalignment for vertically-aligned nanostructures.

Texture analysis is commonly used to probe changes in crystal alignment due to the mechanical deformation of metals. This analysis determines the location of poles (i.e. normals) to a specified set of lattice planes with respect to the sample orientation. Similar to rocking curves, the X-ray source and detector are held fixed at a given diffraction angle corresponding to the lattice planes of interest. Then, the intensity is recorded as the sample is rotated in plane (ϕ) and tilted along an axis co-planar with the incident and diffracted X-ray beams (ψ). The sample is generally rotated in ϕ a full 360º, and tilted in ψ close to 90º, in order to sample a hemisphere of possible sample orientations.

The recorded intensity is plotted in a stereographic projection, called a pole figure. Peaks in the pole figure indicate crystallites oriented with the poles of the specified planes in the direction given by the rotation (ϕ) and tilt (ψ) angles. Intensity values in a pole figure are shown in "times random" units, where the observed intensity is normalized by the expected intensity if there were no preferred orientation.

Multiple pole figures collected on a sample from different reflections of the same phase can be combined to calculate an orientation distribution function (ODF), which shows the full crystal orientation of the phase. ODFs combine the information in several pole figures to represent the directions of the [001] poles of a particular phase in the sample with respect to the sample geometry. The directions are represented using three Euler angles (ϕ_1, Φ and ϕ_2 in the Bunge notation), as seen in Figure 2.6. The angle ϕ_1 corresponds to a rotation about the normal to the sample surface. The angle Φ corresponds to a tilt of the [001] pole away from the sample normal. The angle ϕ_2 corresponds to a rotation about the tilted [001] pole. By examining the distribution of intensity in three-dimensional ϕ_1-Φ-ϕ_2 space, the distribution of crystal orientations can be determined. Once the ODF is determined, inverse pole figures can be calculated, which show the distribution of a certain sample direction in crystal space.

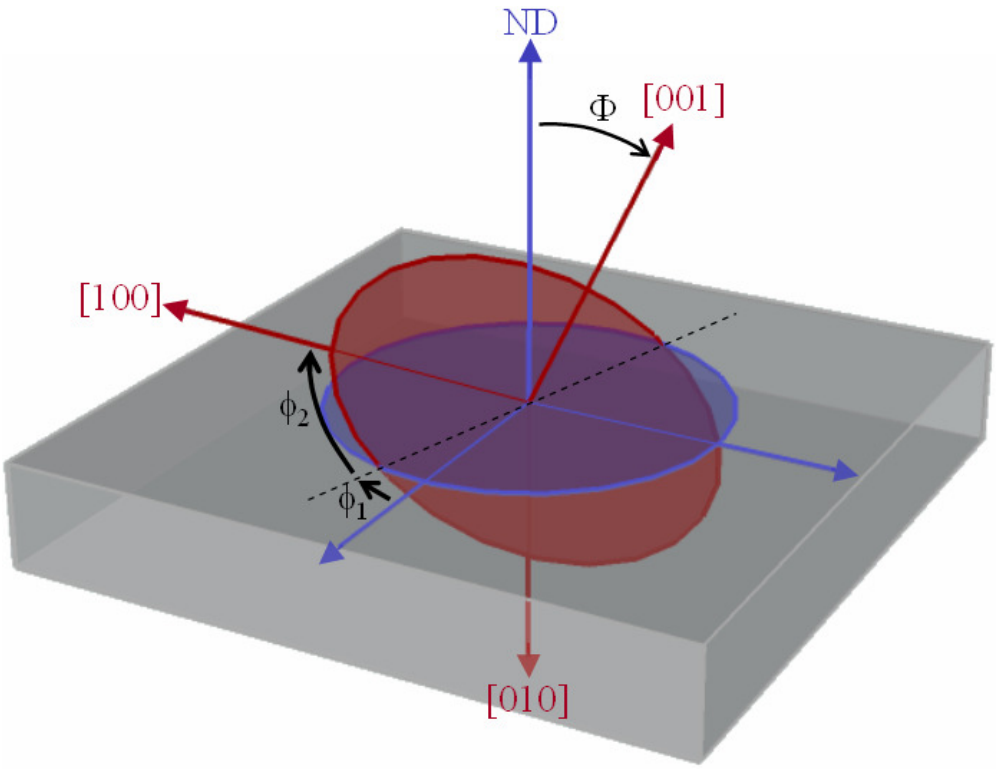

Figure 2.6 The three Euler angles in Bunge notation (ϕ_1, Φ, and ϕ_2) for relating crystal axes (in red) and sample axes (in blue), where ND is the sample normal direction. After Cullity and Stock [6].

2.2.2.4 Diffractometers Setups

XRD data for this research were collected on three different X-ray diffractometers. All three instruments were run with a Cu X-ray source and a tube power of 45 kV and 40 mA.

2.2.2.4.1 For Phase Identification

General θ/2θ scans for phase identification were collected on a Panalytical X'Pert PRO Alpha-1 Diffractometer (α-1), which is a vertical θ-2θ diffractometer with parafocusing optics. On the incident side, a Johansson monochromator removes $K_{\alpha 2}$ and

K_β wavelengths in order to provide only Cu $K_{\alpha 1}$ (λ = 1.540562 Å) radiation. A beam mask (5 to 20 mm) and fixed divergence slit (1/32° to 1º) define the beam, and an anti-scatter slit (twice the size of the divergence slit) reduces stray X-rays. On the receiving side, an anti-scatter slit (generally 5 mm wide) and a beam tube block stray X-rays from entering the detector. The detector is a solid-state linear position-sensitive detector (PSD), which allows a scan to be collected in a fraction of the time required with a traditional point detector.

2.2.2.4.2 For Size/Strain, Lattice Parameter and Rocking Curves

For crystallite size and microstrain determination, lattice parameter measurement and rocking curves, data were collected with parallel beam optics on a Panalytical X'Pert PRO Materials Research Diffractometer (MRD), which is a horizontal θ-2θ diffractometer. On the incident side, a Göbel mirror (equatorial divergence <0.05°) parallelizes the beam in the radial direction (i.e. within the plane of the diffractometer circle). The beam cross-section given by the mirror is a line, the width of which is determined by a divergence slit, and the length by a mask, both of which are placed in front of the mirror.

On the receiving side, a 0.09º parallel plate collimator further conditions the beam in the radial direction before it enters a proportional point detector. Incident and receiving Soller slits (0.04 rad) condition the beam in the axial direction. When using parallel beam geometry, variations in the sample height do not shift the peak (i.e. sample surface displacement error is eliminated). This is beneficial, particularly for lattice parameter determination, which relies on accurately and precisely determining the peak positions. When collecting data from iron-containing samples, a graphite flat crystal

monochromator was added directly in front of the detector. Fe fluoresces under Cu radiation, which can lead to very high background counts, unless the resulting radiation is blocked by a diffracted beam monochromator.

2.2.2.4.3 For Texture Analysis

Texture data were also collected on the MRD with parallel beam optics. This diffractometer is fit with an Eulerian cradle, which allows the sample to be moved with six degrees of freedom: three translations (x, y and z) and three rotations (ω, ϕ and ψ), as seen in Figure 2.7. For texture analysis, the parallel beam is generated using a polycapillary lens (divergence around 0.3°), with a Ni filter to reduce Kβ radiation. The benefit of a polycapillary lens is that it gives an equiaxial beam cross-section, the width and height of which are determined by crossed adjustable slits. The size of the beam is chosen according to the sample size. With an equiaxial cross-section, the beam footprint will not change as a sample is rotated through ψ, as it is in texture analysis. On the receiving side, a 0.09º parallel plate collimator conditions the beam and blocks stray radiation from entering the proportional point detector. Again, a diffracted beam monochromator was added for scans of iron-containing samples.

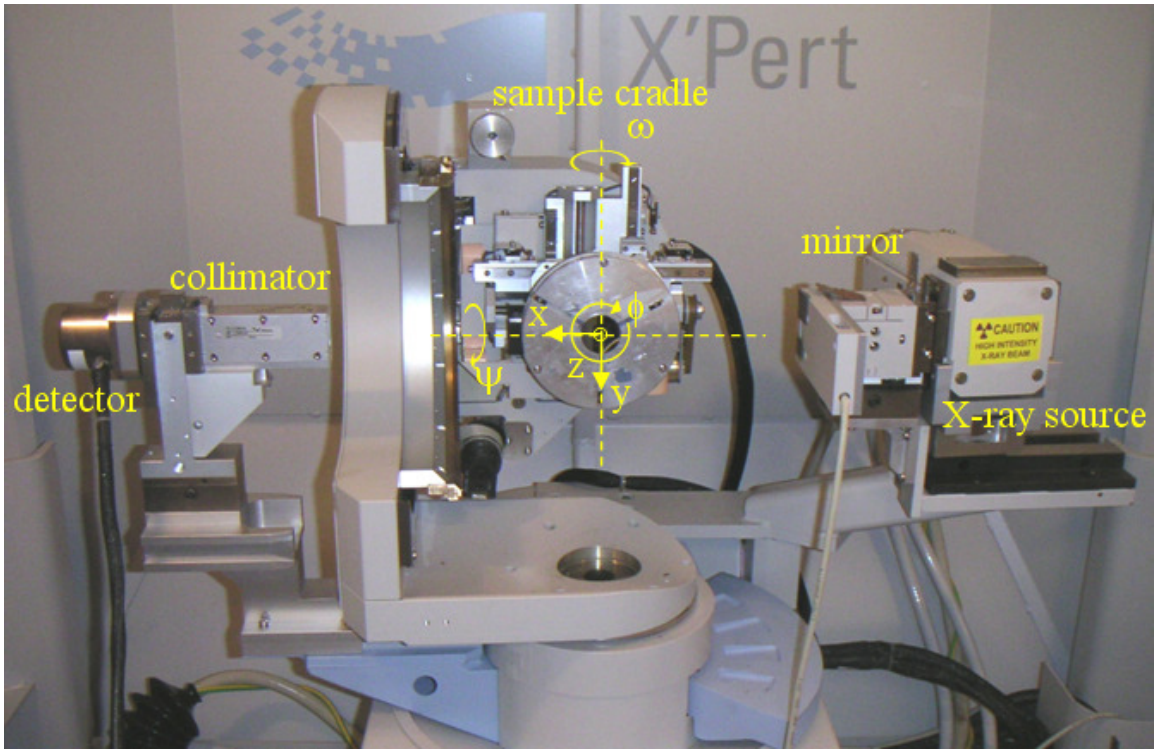

Figure 2.7 MRD setup for high-resolution XRD with cradle translations (*x*, *y*, and z) and rotations (ω, ϕ and ψ) indicated.

2.2.2.4.4 For In-Situ Analysis

In-situ and high temperature analyses were conducted on a Panalytical X'Pert PRO Multi-Purpose Diffractometer (MPD), which is a vertical θ-θ diffractometer, fit with the Anton-Paar HTK 1200 or HTK 2000 furnaces, as discussed in section 2.1.2 above. Diffraction data were collected on the MPD, with a modified parallel beam geometry. On the incident side, a Göbel mirror parallelizes the beam in the radial direction (i.e. within the plane of the diffractometer circle), while a mask and divergence slit define the beam size. On the receiving side, an anti-scatter slit (generally 5 mm wide) and a beam tube block stray X-rays from entering the linear position-sensitive detector. The combination of a parallel beam with the position-sensitive detector allows for maximum intensity with minimum scan times. However, this combination also removes the

insensitivity to sample height generally found with parallel beam geometry. Therefore, lattice parameter determination will be subject to sample surface displacement error, particularly since the sample height can change during a batch due to thermal expansion of the furnace.

2.2.2.4.5 Data Analysis

XRD data were analyzed using several computer programs. Jade (Materials Data, Incorporated) was used for phase identification, Scherrer size and Williamson-Hall analyses, peak fitting for lattice parameter determination, and Pawley (whole pattern) fitting, as well as plotting three-dimensional scan overlays. Pawley whole pattern fitting simultaneously fits the peaks from all phases present, in order to determine the lattice parameters and phase fractions of each phase. It differs from Rietveld refinement in that the integrated intensities are refined, and crystal structure data for each phase is not required, though cell parameters can be refined. Panalytical High Score was used for phase identification. Panalytical Texture was used for pole figure plotting and ODF calculation. Panalytical Line Profile Analysis (LPA) was used for Warren-Averbach analysis.

2.3 References

1. Morber, J.R., Y. Ding, M.S. Haluska, Y. Li, J.P. Liu, Z.L. Wang, and R.L. Snyder, *PLD-Assisted VLS Growth of Aligned Ferrite Nanorods, Nanowires, and Nanobelts-Synthesis, and Properties.* Journal of Physical Chemistry B, 2006. **110**(43): p. 21672-21679.

2. *HTK 2000 High-Temperature Chamber Instruction Manual*. 2003, Anton Paar GmbH: Graz, Austria. p. 66.

3. Ding, Y., P.X. Gao, and Z.L. Wang, *Catalyst-Nanostructure Interfacial Lattice Mismatch in Determining the Shape of VLS Grown Nanowires and Nanobelts: A Case of Sn/ZnO.* Journal of the American Chemical Society, 2004. **126**: p. 2066-72.

4. Gao, P.X., Y. Ding, and I.L. Wang, *Crystallographic orientation-aligned ZnO nanorods grown by a tin catalyst.* Nano Letters, 2003. **3**(9): p. 1315-1320.

5. Warren, B.E., *X-Ray Diffraction*. 1990, New York: Dover Publications, Inc. p. 381.

6. Cullity, B.D. and S.R. Stock, *Elements of X-Ray Diffraction*. 3rd ed. 2001: Prentice Hall. p. 664.

7. Als-Nielsen, J. and D. McMorrow, *Elements of Modern X-Ray Physics*. 2001, New York: Wiley. p. 318.

8. Patterson, A.L., *The Scherrer Formula for X-Ray Particle Size Determination.* Physical Review, 1939. **56**: p. 978-982.

9. Louër, D., J.P. Auffrédic, J.I. Langford, D. Ciosmak, and J.C. Niepce, *A Precise Determination of the Shape, Size and Distribution of Size of Crystallites in Zinc Oxide by X-ray Line-Broadening Analysis.* Journal of Applied Crystallography, 1983. **16**: p. 183-191.

10. Warren, B.E. and B.L. Averbach, *The Separation of Cold-Work Distortion and Particle Size Broadening in X-Ray Patterns.* Journal of Applied Physics, 1952. **23**(4): p. 497.

11. Krill, C.E. and R. Birringer, *Estimating grain-size distributions in nanocrystalline materials from X-ray diffraction profile analysis.* Philosophical Magazine a-Physics of Condensed Matter Structure Defects and Mechanical Properties, 1998. **77**(3): p. 621-640.

CHAPTER 3

METAL OXIDE NANOSTRUCTURES

3.1 Introduction

This investigation into the catalyzed growth of 1D nanostructures began with metal oxide nanostructures. Many examples of metal oxide nanowires, nanobelts and other 1D nanostructures can be found in the literature. Nanostructures have been grown from 2+ cations (including ZnO [1-26], CdO [27-29] and MgO [30-38]), 3+ cations (including In_2O_3 [39-41], Bi_2O_3 [42] and Ga_2O_3 [39, 43-46]) and 4+ cations (SnO_2 [39, 47-50] and SiO_2 [51]), as well as mixed valency cations (Fe_xO_y [52]).

These metal oxide 1D nanostructures have demonstrated promise for applications in a variety of areas [53]. For example, SnO_2 nanowires and nanobelts have been shown to be effective pH [54], gas [55, 56] and humidity [57] sensors. Iron oxide nanowires may be used for medical diagnosis and treatment [58]. MgO nanorods have been used as pinning agents to improve the properties of superconductors [59, 60]. ZnO 1D nanostructures have been the most extensively studied of all metal oxide nanostructures. The piezoelectric property of ZnO lends itself to interesting applications, such as nanogenerators [61-66] and force sensors [67, 68], while the semiconducting property of ZnO allows its use in areas such as dye-sensitized solar cells [69, 70], ultraviolet (UV) detectors [71-73], nanolasers [74, 75] and light emitting diodes (LEDs) [76-78].

This research on metal oxide nanostructures focused on Au-catalyzed ZnO nanorods. The synthesis and morphology of the nanorods will be presented, along with XRD investigations into the crystallographic orientations of the phases present and a

lattice parameter analysis of the gold catalyst particles. In addition to the Au-catalyzed ZnO nanorods, investigations of Sn-catalyzed ZnO nanostructures and Au-catalyzed Fe_xO_y nanostructures are presented. For the Sn-catalyzed ZnO nanostructures, the synthesis and morphology of the nanostructures will be presented, along with XRD investigations into the crystallite size, microstrain and lattice parameter of the tin catalyst particles. For the Au-catalyzed Fe_xO_y nanostructures, the synthesis and morphology of the nanostructures will be presented, along with XRD investigations into the crystallographic orientations of the phases present and into the crystallite size, microstrain and lattice parameter of the gold catalyst particles. The implications of the findings for each type of nanostructure grown towards the growth model of the catalyzed growth of nanostructures will also be discussed.

3.2 Au-Catalyzed Zinc Oxide Nanostructures

3.2.1 Synthesis and Morphology

The Au-catalyzed ZnO nanostructures were grown in the horizontal tube furnace. The source material was ZnO powder mixed with graphite. The substrate, *c*-plane sapphire, was coated with first AlN, then $Al_{0.5}Ga_{0.5}N$ to bridge the lattice mismatch between the *c*-planes of the Al_2O_3 substrate and the ZnO nanorods. For the catalyst, gold was sputtered onto the substrates. During growth, Ar flow supplemented with 2% oxygen was introduced into the tube furnace. The source materials were heated to 950ºC, and the substrates to around 850ºC. The furnace was held at temperature for 30 minutes, and then cooled under Ar flow. (For synthesis details, see section 2.1.3.1.)

The samples were imaged with scanning electron microscopy as shown in Figure 3.1. The nanorods are straight, with a columnar shape. The average length is 284±72

nm, and the cross section is circular, with an average diameter of 35±11 nm, as determined from SEM images. The catalyst diameters are the same as those of the nanowires, with an average diameter of 33±12 nm. There is a somewhat large variation in the size of the nanostructures, as evidenced by the standard deviation values above. The nanorods are aligned vertically.

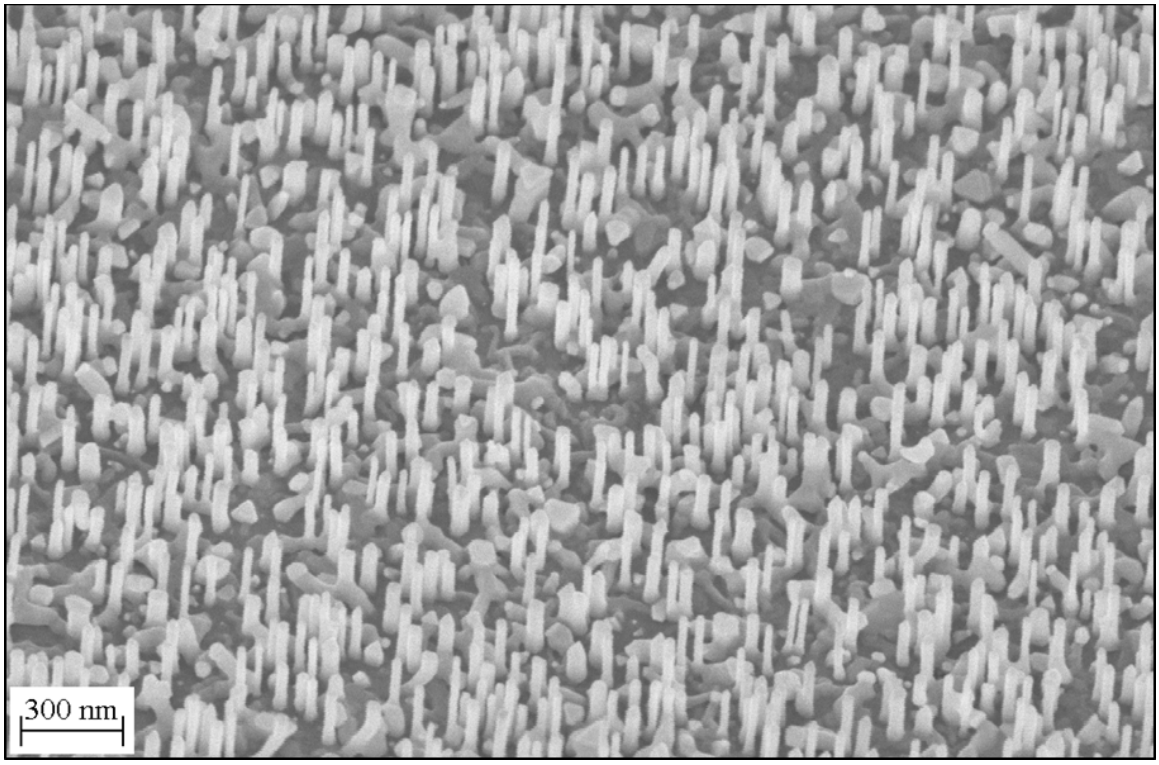

Figure 3.1 SEM image of aligned Au-catalyzed ZnO nanorods.

3.2.2 Crystallographic Orientation Analysis

3.2.2.1 θ/2θ XRD Patterns

The vertical alignment of the ZnO nanorods suggests that there may be an epitaxial crystallographic orientation alignment between the nanorods and substrate. This is substantiated by the initial θ/2θ XRD scan. Diffracted X-rays always make an angle

with the diffraction planes equal to that between the incident beam and diffracted planes. For a standard θ/2θ scan, all diffraction will occur from crystallographic planes parallel to the sample surface. Therefore, in θ/2θ diffraction patterns from a sample of vertically aligned nanostructures, the presence or absence of diffraction peaks can give information about the crystallographic orientation of each phase, as well as the growth direction of the nanostructures.

A θ/2θ X-ray diffraction pattern from the sample of vertically-aligned, Au-catalyzed ZnO nanorods is shown in Figure 3.2. This scan was collected with a 1˚ offset in the value of ω (angle between the incident beam and the sample surface) in order to minimize the signal from the Al_2O_3 substrate. Only the following peaks are observed: Au {111} and {222}, ZnO {0002} and {0004}, $Al_{0.5}Ga_{0.5}N$ {0002} and {0004}, and AlN {0002} and {0004}. In XRD patterns with no ω offset, the Al_2O_3 {000 ℓ} peaks are also visible. These results indicate that the following families of planes from each phase are parallel to the sample surface: Al_2O_3 {000ℓ}, AlN {000ℓ}, $Al_{0.5}Ga_{0.5}N$ {000ℓ}, ZnO {000ℓ} and Au {*hhh*}. In addition, these results, combined with the observed vertical alignment of the nanorods, show the nanorod growth direction to be [0001], perpendicular to the basal plane of the hexagonal unit cell. No evidence was found in the XRD scans for the presence of Au-Zn intermetallics, as reported in [79], or any other phases besides those reported above.

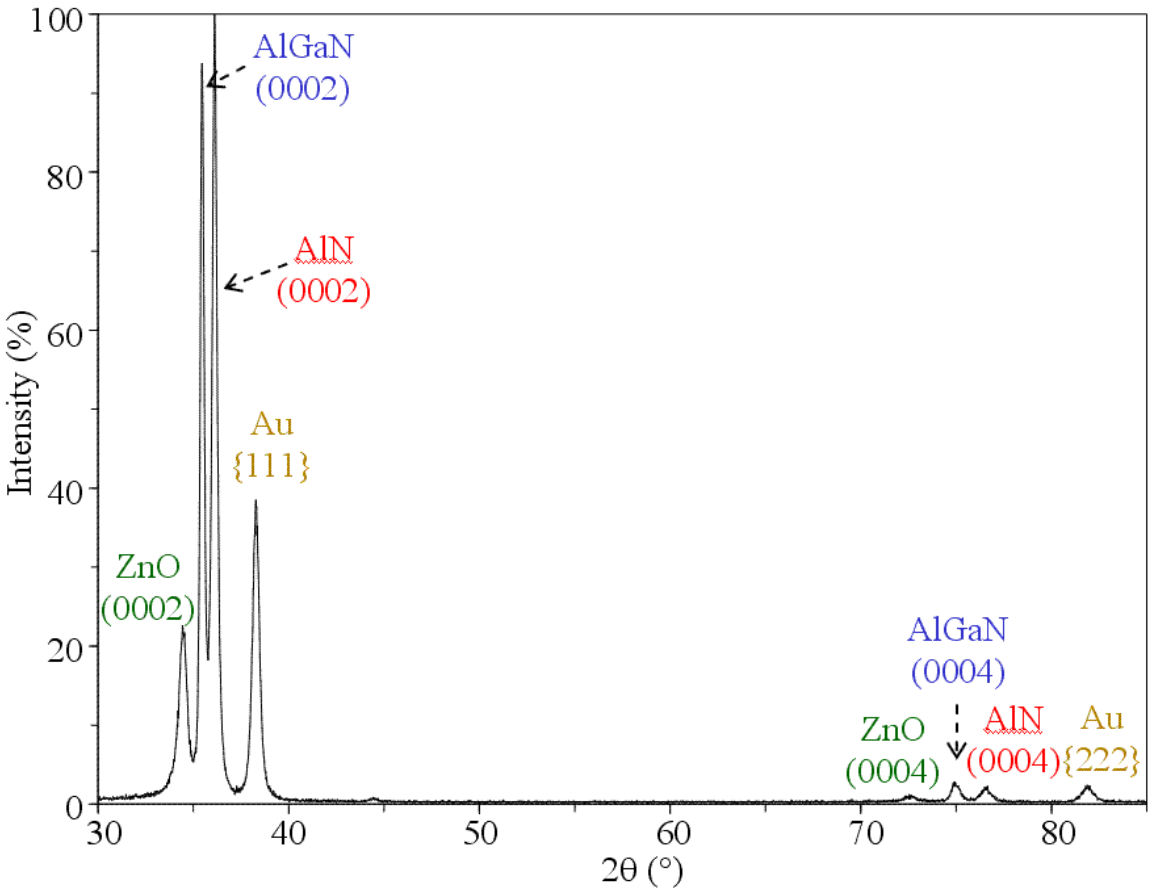

Figure 3.2 Offset θ/2θ XRD scan of vertically-aligned Au-catalyzed ZnO nanorods grown on an $Al_{0.5}Ga_{0.5}N$ / AlN / Al_2O_3 (*c*-plane) substrate.

3.2.2.2 Rocking Curves

In order to further investigate the crystallographic alignment and to determine the degree of misalignment, rocking curves were collected on each phase, as seen in Figure 3.3. The scans are plotted in terms of Δω (the difference between ω and θ), and the intensities are normalized, in order to aid comparisons between the different phases. The FWHMs of the rocking curve peaks are presented in Table 3.1. Since the Al_2O_3 phase is a single crystal, the width of its rocking curve peak is indicative of the inherent instrumental broadening only. Generally, each successive layer has a higher degree of misalignment, indicated by wider rocking curve peaks. (The exception is the $Al_{0.5}Ga_{0.5}N$

and AlN layers, which have very similar peak widths, with the AlN being slightly wider.) The misalignment of each layer builds on that of the layer beneath it. However, all of the rocking curve peak widths are low, below 2˚. This small degree of misalignment indicates that the nanostructures grow epitaxially and very well aligned.

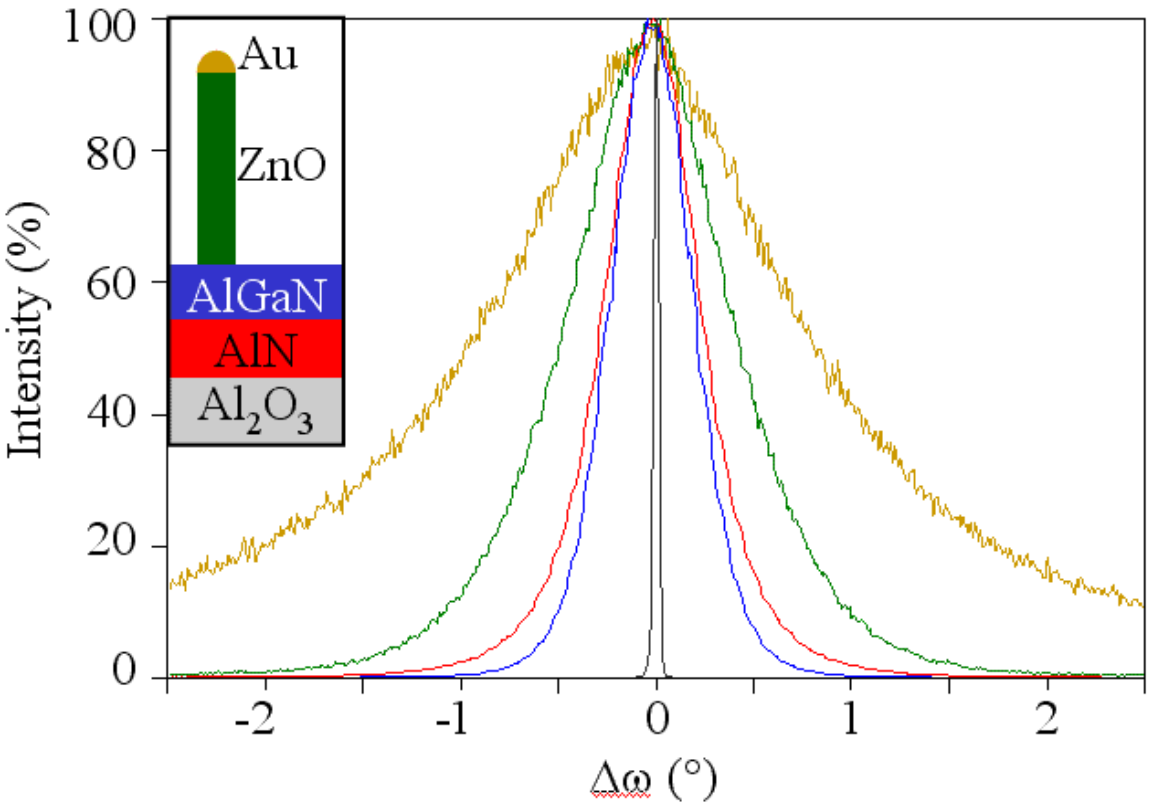

Figure 3.3 Rocking curves collected from vertically-aligned Au-catalyzed ZnO nanorods grown on an $Al_{0.5}Ga_{0.5}N$ / AlN / Al_2O_3 (*c*-plane) substrate. The inset shows a schematic of a nanorod on the substrate.

Table 3.1 FWHMs of rocking curve peaks of each phase from sample of vertically-aligned, Au-catalyzed ZnO nanorods.

Phase	Peak	FWHM
Au	(111)	1.788° ± 0.038°
ZnO	(0002)	0.940° ± 0.052°
$Al_{0.5}Ga_{0.5}N$	(0002)	0.461° ± 0.022°
AlN	(0002)	0.540° ± 0.024°
Al_2O_3	(0006)	0.026° ± 0.001°

3.2.2.3 Texture Data Collection

For a more detailed and in-depth crystallographic orientation analysis, texture data were collected on the sample of vertically-aligned, Au-catalyzed ZnO nanorods. As discussed in section 2.2.2.3 above, texture data is collected by fixing the tube and detector to a particular diffraction angle and recording the intensity as the sample is rotated through 360° φ and tilted through 85-90° ψ. For the sample of vertically-aligned, Au-catalyzed ZnO nanorods, texture data were collected on the following reflections: {111}, {200}, {220} and {311} for the Au catalyst particles; $\{10\bar{1}0\}$, $\{10\bar{1}2\}$, $\{10\bar{1}3\}$ and $\{11\bar{2}0\}$ for the ZnO nanorods; $\{10\bar{1}0\}$, $\{10\bar{1}2\}$ and $\{10\bar{1}3\}$ for the $Al_{0.5}Ga_{0.5}N$ layer; and $\{10\bar{1}0\}$, (0002), $\{10\bar{1}1\}$ and $\{10\bar{1}2\}$ for the AlN layer. The step sizes of the scans were 5° in φ and in ψ, with a count time of 8 s.

For sample alignment, the Al_2O_3 single crystal substrate was used. Scans of ω and ψ around the {0006} peak ensured that the sample was mounted flat. Scans of *x* and *y* around the same peak centered the sample around the X-ray beam. Finally, an abbreviated pole figure from the Al_2O_3 $\{02\bar{2}4\}$ reflection was collected before each run in order to align the sample rotation, φ. (The 2θ zero point and sample height, *z*, were aligned using the standard direct-beam approach.) For data analysis, the texture data were plotted in pole figures, with a Wulff net grid. All the pole figures are in Appendix APPENDIX A for reference.

3.2.2.4 Orientation Distribution Function Calculation and Results

For each phase, the texture data from all the pole figures for that phase were used to calculate an orientation distribution function (ODF). ODFs show the locations of the

[001] poles in terms of three Euler angles, φ_1, Φ and φ_2 in the Bunge notation, where φ_1 corresponds to a rotation about the normal to the sample surface, Φ corresponds to a tilt of the [001] pole away from the sample normal, and φ_2 corresponds to a rotation about the tilted [001] pole, as shown in Figure 2.6. For this analysis, the following settings were used: Because there are many phases in this sample, overlap between peaks of different phases is a significant problem, particularly for the single-crystal substrate. The substrate peaks are so intense that even the tails, far from the peak center, have sufficient intensity to leave strong overlapped peaks in the pole figures of other phases. This problem was mitigated by choosing for the ODF calculation pole figures with minimum overlap with substrate peaks. However, overlap with substrate peaks could not be completely avoided, leading to increased noise in the ODFs. The ODFs were normalized, and a calculated defocusing correction applied.

The ODF for the AlN phase, shown in Figure 3.4, was calculated from the $\{10\bar{1}0\}$, (0002), $\{10\bar{1}1\}$ and $\{10\bar{1}2\}$ pole figures. Multiple slices at constant Φ are shown through the three-dimensional φ_1-Φ-φ_2 space. Only the $\Phi = 0^\circ$ and $\Phi = 5^\circ$ planes have significant intensity, indicating that the {0001} poles are tilted no more than 5° from the sample normal. Therefore, the AlN is {0001} oriented, i.e. with the {0001} plane parallel to the sample surface, as expected. The spread of intensity into the $\Phi = 5^\circ$ plane could indicate a small degree of misalignment.

The ODF for the $Al_{0.5}Ga_{0.5}N$ phase, shown in Figure 3.5, was calculated from the $\{10\bar{1}0\}$, $\{10\bar{1}2\}$ and $\{10\bar{1}3\}$ pole figures. Again, only the $\Phi = 0^\circ$ and $\Phi = 5^\circ$ planes have significant intensity, indicating that the {0001} poles are parallel to the sample normal. Therefore, the AlGaN is (0001) oriented, as expected.

The ODF for the ZnO phase, shown in Figure 3.6, was calculated from the $\{10\bar{1}0\}$, $\{10\bar{1}2\}$, $\{10\bar{1}3\}$ and $\{11\bar{2}0\}$ pole figures. Similarly to the above phases, only the $\Phi = 0^{\circ}$ and $\Phi = 5^{\circ}$ planes have significant intensity, indicating that the {0001} poles are tilted no more than 5º from the sample normal. Therefore, the ZnO is {0001} oriented, as expected. The overall intensity is lower, as compared to the AlN and $Al_{0.5}Ga_{0.5}N$ layers, due to the lower amount of the ZnO nanorods.

The ODF for the gold, shown in Figure 3.7, was calculated from the {111}, {200}, {220} and {311} pole figures. Only the $\Phi = 55^{\circ}$ plane has significant intensity, indicating that the {001} poles are tilted 55˚ from the sample normal. The calculated angle between the {001} and {111} planes in cubic crystal structures, like Au, is 54.74˚. Therefore, the Au is {111} oriented, as expected. Again, the intensity is low, comparable to that for the ZnO phase. The orientation relationships, including parallel planes and directions, are summarized in Table 3.2.

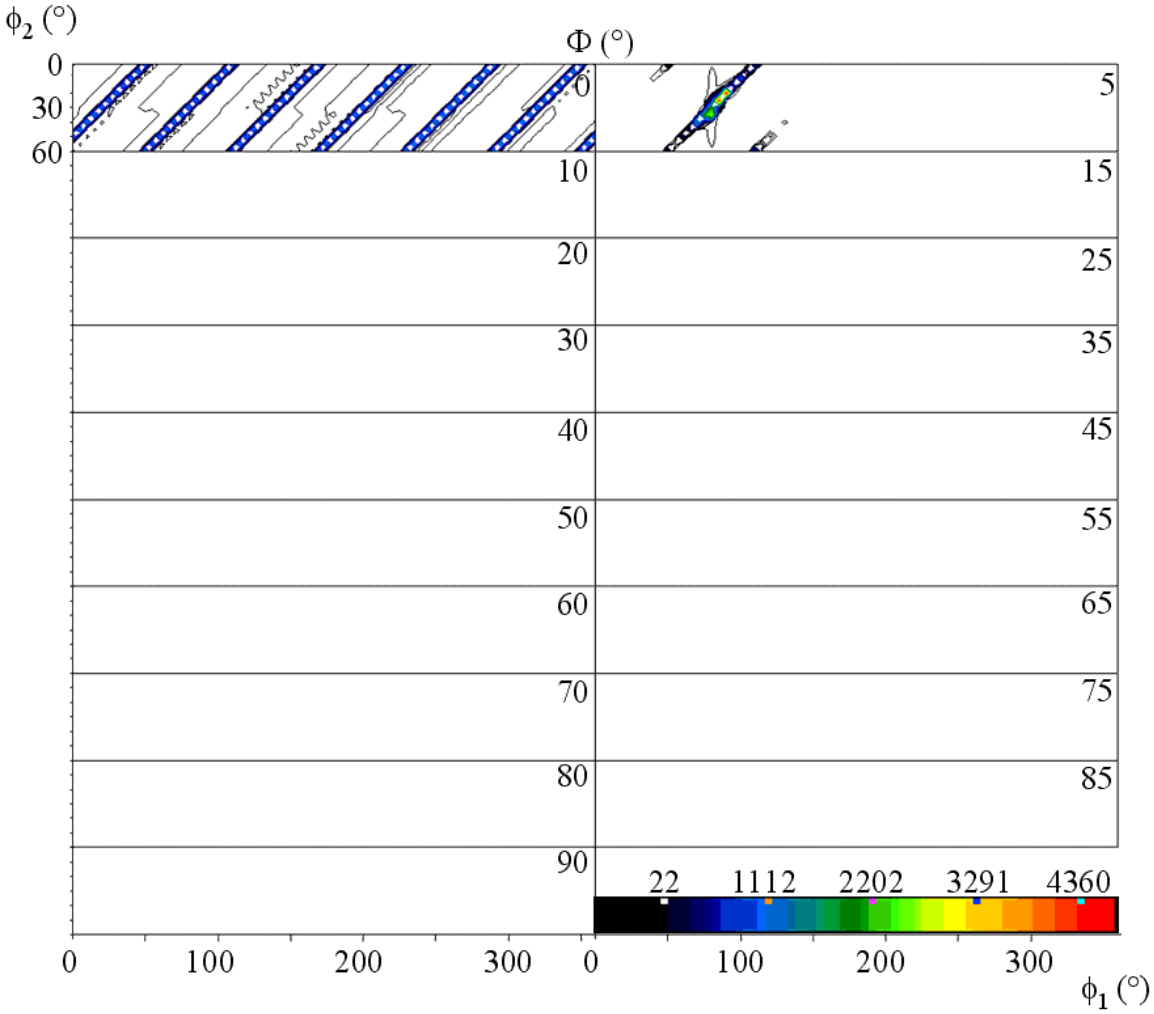

Figure 3.4 ODF calculated from four pole figures collected on the AlN substrate layer in a sample of Au-catalyzed ZnO nanorods.

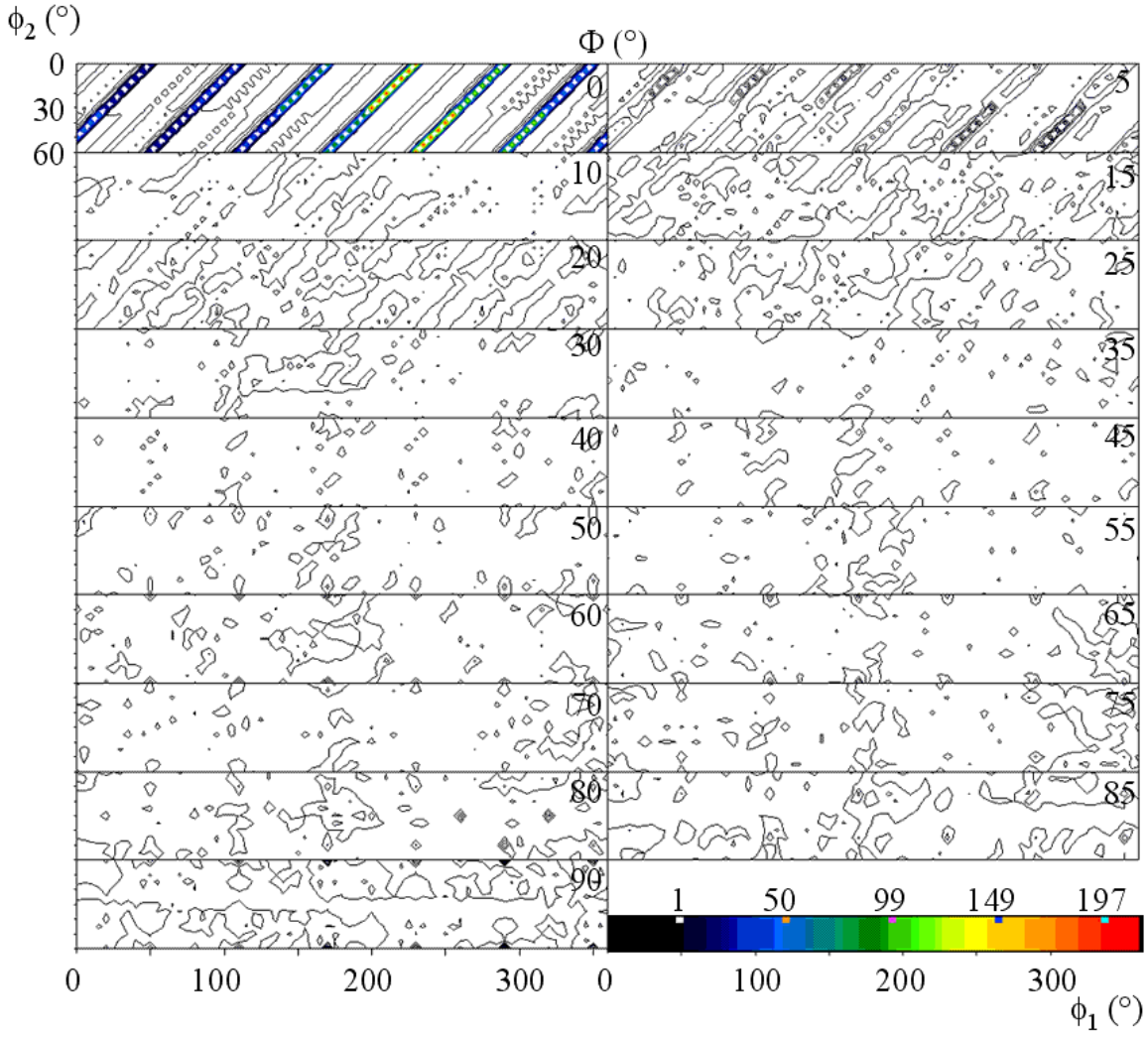

Figure 3.5 ODF calculated from three pole figures collected on the $Al_{0.5}Ga_{0.5}N$ substrate layer in a sample of Au-catalyzed ZnO nanorods.

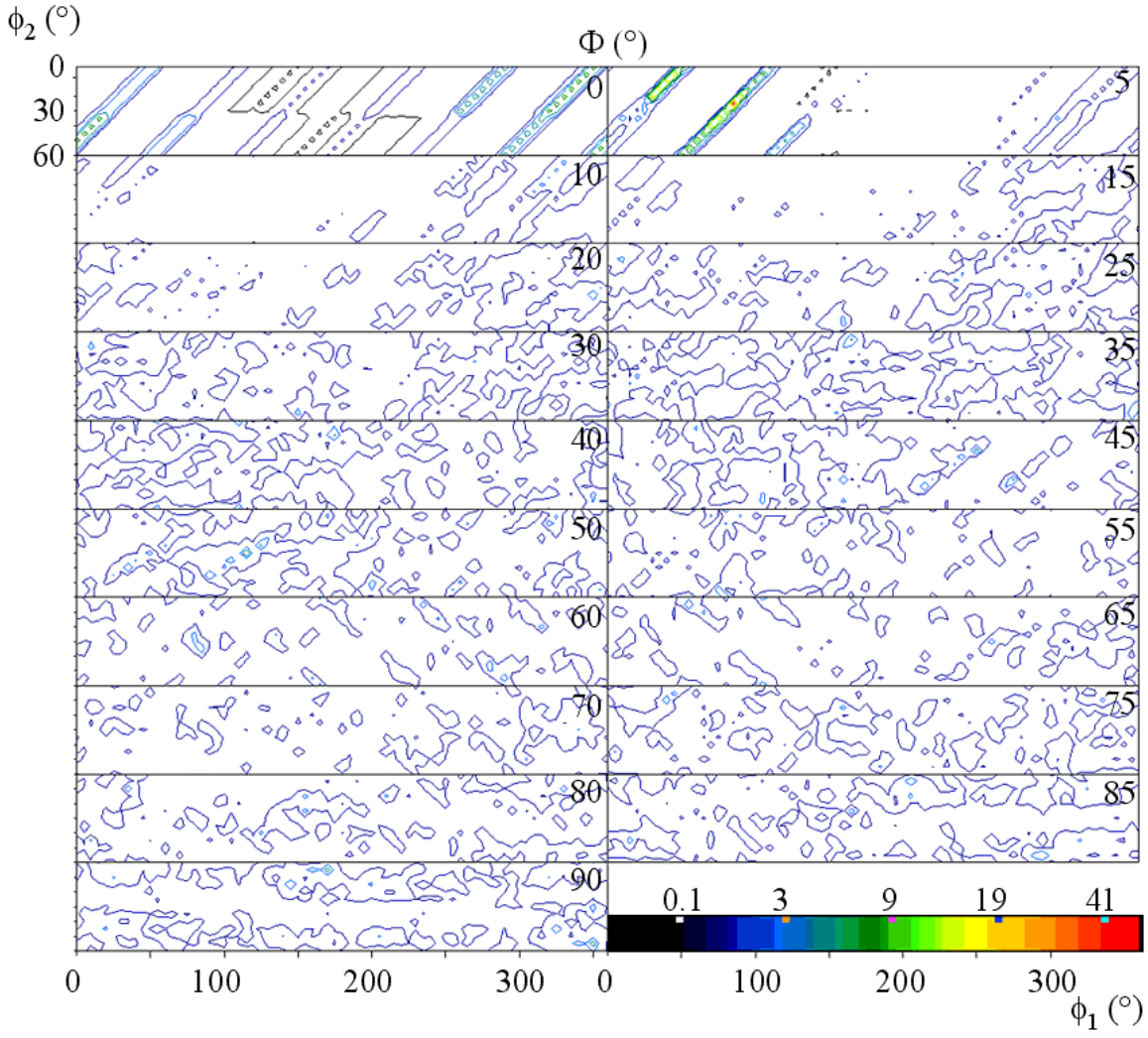

Figure 3.6 ODF calculated from four pole figures collected on the ZnO nanorods in a sample of Au-catalyzed ZnO nanorods.

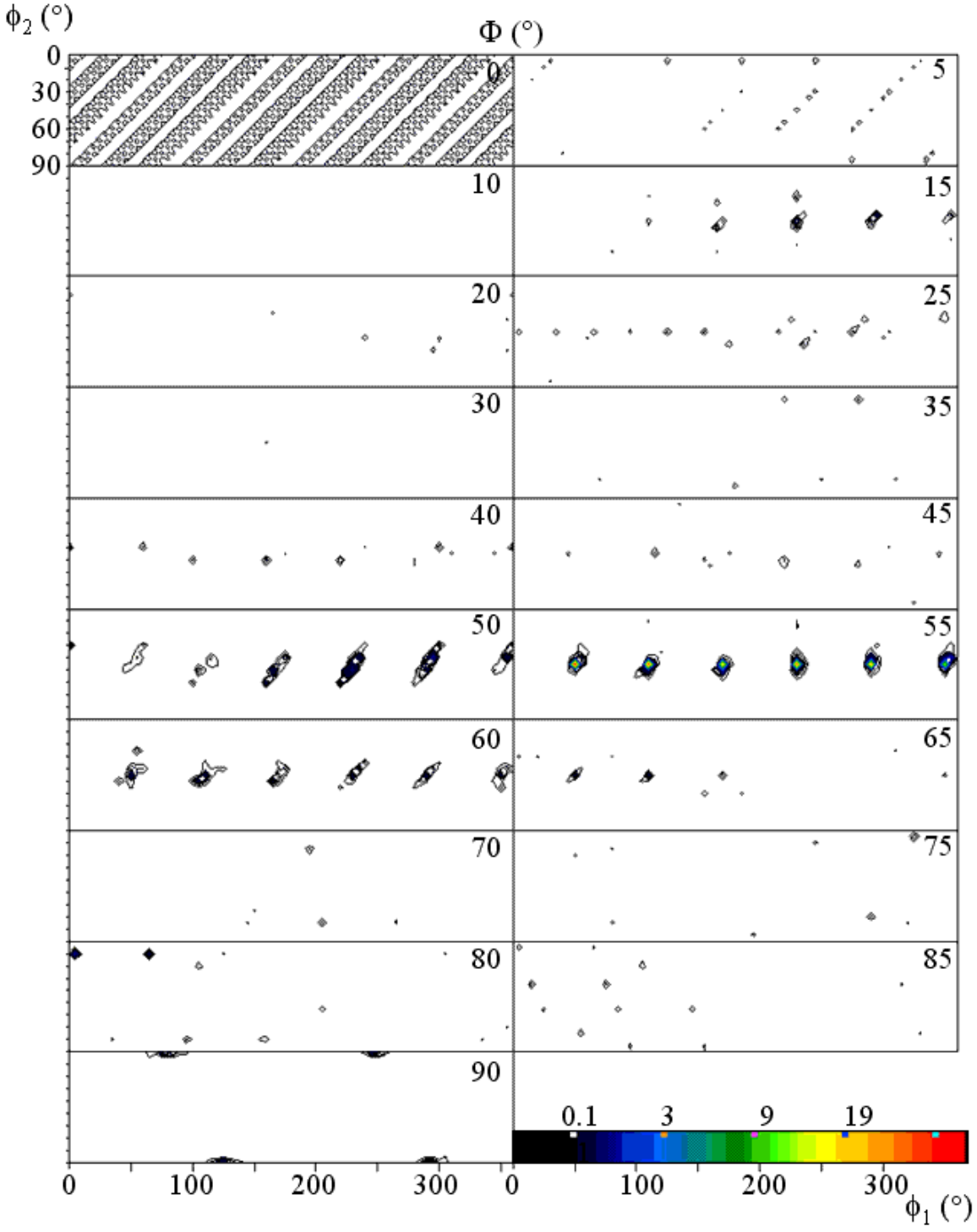

Figure 3.7 ODF calculated from four pole figures collected on the Au catalyst particles in a sample of Au-catalyzed ZnO nanorods.

Table 3.2 Orientation relationships between the Au, ZnO, $Al_{0.5}Ga_{0.5}N$, AlN and Al2O3 phases as determined from texture analysis.

Phase	Parallel Plane	Parallel Direction
Au	{111}	$\langle \bar{1}10 \rangle$
ZnO	{0001}	$\langle \bar{1}2\bar{1}0 \rangle$
$Al_{0.5}Ga_{0.5}N$	{0001}	$\langle \bar{1}2\bar{1}0 \rangle$
AlN	{0001}	$\langle \bar{1}2\bar{1}0 \rangle$
Al_2O_3	{0001}	$\langle 10\bar{1}0 \rangle$

3.2.2.5 Discussion of Crystallographic Orientations

AlN, $Al_{0.5}Ga_{0.5}N$ and ZnO all have the same wurtzite crystal structure with 6-fold symmetry in the basal plane. Al_2O_3 is rhombohedral, also with 6-fold symmetry in the basal plane. Therefore, it is expected that AlN, AlGaN and ZnO will take the same *c*-plane crystallographic orientation as the Al_2O_3 substrate. Since gold has the face-centered cubic (FCC) structure, the Au {111} plane has 3-fold hexagonal-like symmetry, so a Au {*hhh*} orientation is also predicted. The θ/2θ XRD scans confirm these predicted crystallographic orientations for each phase. Additionally, the rocking curves show that the degree of misalignment is small. The texture data and ODFs give additional information about the crystallographic orientation, including the parallel directions within the parallel planes.

An unexpected result from the texture analysis was the discovery of two orientations for the Au phase. In the Au ODF (Figure 3.7), six discrete points of intensity are observed in the $\Phi = 55^\circ$ slice, at $\varphi_2 = 45^\circ$ and $\varphi_1 = 60^\circ \cdot n - 10^\circ$, where n is an integer from 1 to 6. This indicates that the Au catalyst particles have six crystallographic orientations with in-plane rotations of 60º. However, the Au {111} plane has only three-fold symmetry, and therefore one unique crystallographic orientation can only explain

three of the rotations. The additional three rotations must be due to the existence of a second unique crystallographic orientation related to the first by a 60º rotation about the sample normal. The presence of these two gold orientations, both with 3-fold symmetry, follows from the hexagonal symmetry of the substrate.

The hexagonal symmetries of the AlN {0001}, $Al_{0.5}Ga_{0.5}N$ {0001} and ZnO {0001} interfaces match the pseudo-hexagonal symmetry of the Al_2O_3 {0001} plane, with $\langle 10\bar{1}0 \rangle_{Al2O3}$ parallel to $\langle \bar{1}2\bar{1}0 \rangle_{AlN}$ parallel to $\langle \bar{1}2\bar{1}0 \rangle_{AlGaN}$ parallel to $\langle \bar{1}2\bar{1}0 \rangle_{ZnO}$. These lattice mismatches are generally small, with the Al_2O_3/AlN lattice mismatch being around 15%, and the mismatch of the other interfaces being around 2%. The pseudo-hexagonal symmetry of the Au {111} plane also matches that of the ZnO {0001} plane, with $\langle \bar{1}2\bar{1}0 \rangle_{ZnO}$ parallel to $\langle \bar{1}10 \rangle_{Au}$. The lattice mismatch at this interface is 13%, which is relatively low.

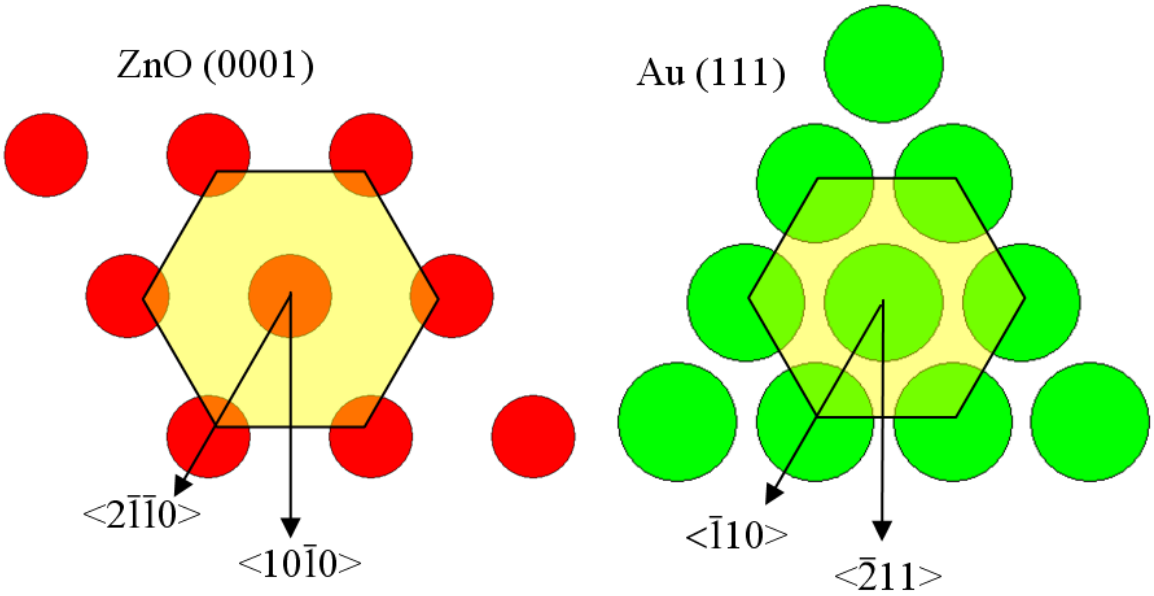

Figure 3.8 Schematic showing crystallographic orientations of the ZnO and Au phases in a sample of Au-catalyzed ZnO nanorods.

3.2.3 Gold Lattice Parameter Analysis

3.2.3.1 Lattice Parameter Determination

The lattice parameter of a material, which can be determined accurately and precisely with X-ray diffraction, can give much useful information about the state of the material, such as composition. For this study, the information available from the gold lattice parameter was of particular interest. The lattice parameter of the gold in the ZnO nanorod sample was averaged from fourteen XRD scans of the Au {111} and {222} peaks, and determined to be 4.073±0.001 Å, slightly smaller than the bulk value of 4.0786 Å (PDF #4-784).

One possible concern is that if there is any gold sitting on the substrate that did not catalyze the growth of nanorods, it could be affecting the diffraction signal from the gold catalyst particles at the tips of the nanorods. However, a few intensity calculations indicate that this should not be a problem. From the intensity equation [80], the volume ratio of the ZnO and Au phases can be calculated from the integrated intensities, as fitted with Jade, of the ZnO {000ℓ} and Au {*hhh*} θ/2θ diffraction peaks, taking into account the Lorentz-polarization, multiplicity and temperature factors. For this sample, the volume ratio of ZnO to Au is estimated to be around 220 ± 40 to 1. From the catalyst particle and nanorod sizes as determined by SEM (see section 3.2.1 above), and assuming that the catalyst particles are hemispherical and the nanorods are cylindrical in shape, the expected volume ratio of ZnO to Au if all the gold is located at the tips of nanowires can be calculated to be 29 to 1, less than that measured from the sample. The presence of additional gold on the substrate surface would only reduce this ratio further. Therefore, it

is unlikely that any extraneous gold is present in the sample to affect the signal from the gold catalyst particles on the ZnO nanorods.

3.2.3.2 Contraction Due to Nanoparticle Size

The observed decrease in gold lattice parameter, as compared to the reference value, is expected due to the known lattice contraction occurring in nanoparticles. Qi and Wang [81] developed a model to quantify the change in lattice parameter, *a*, for metal nanoparticles as a function of the particle diameter (*D*) and shape (represented by the shape factor α), shear modulus (*G*) and surface energy (γ), as in the equation below, where a_0 is the bulk lattice parameter and a_n is the nanoparticle lattice parameter.

$$\frac{a_n - a_0}{a_0} = -\frac{1}{1 + D \cdot \left(\frac{G\sqrt{\alpha}}{\gamma} \right)}$$

For 33 nm hemispherical gold particles, the change in lattice parameter is –0.1433%, leading to an expected lattice parameter of 4.0731 Å, which is consistent with the experimentally measured gold lattice parameter of 4.073 ± 0.001 Å. Therefore, no additional effects on the lattice parameter, for example a shift due to alloying with zinc, are needed to explain its value, as will be discussed in more detail in section 3.2.3.4 below.

3.2.3.3 Control Sample

In order to verify that nanoparticle size contraction fully explains the observed lattice parameter, a control sample was prepared and analyzed using SEM and XRD, including grazing incidence (GIXRD) and θ/2θ scans with an ω offset to minimize the signal from the substrate. Five nanometers of gold were thermally evaporated onto a

GaN layer on a *c*-plane oriented, single-crystal Al_2O_3 substrate. After the gold deposition, the sample was heated at 600ºC and then 850ºC for 30 and 60 min, respectively.

Before annealing, a small number of gold nanoparticles were observed on the sample surface, and XRD patterns show evidence of polycrystalline Au, though the weak Au signal prevents detailed analysis. After annealing, the sample is densely covered with Au nanoparticles with an average diameter of 32 ± 12 nm, as seen in Figure 3.9. An XRD pattern (with a 2º ω offset to reduce the Al_2O_3 substrate signal) indicates that the gold is primarily {111}-oriented. The gold lattice parameter was averaged from five offset and five GIXRD scans, and was determined to 4.073 ± 0.002 Å, which is the same as that measured from the ZnO nanorod sample. This verifies that nanoparticle size contraction fully explains the observed lattice parameter of the nanorod sample.

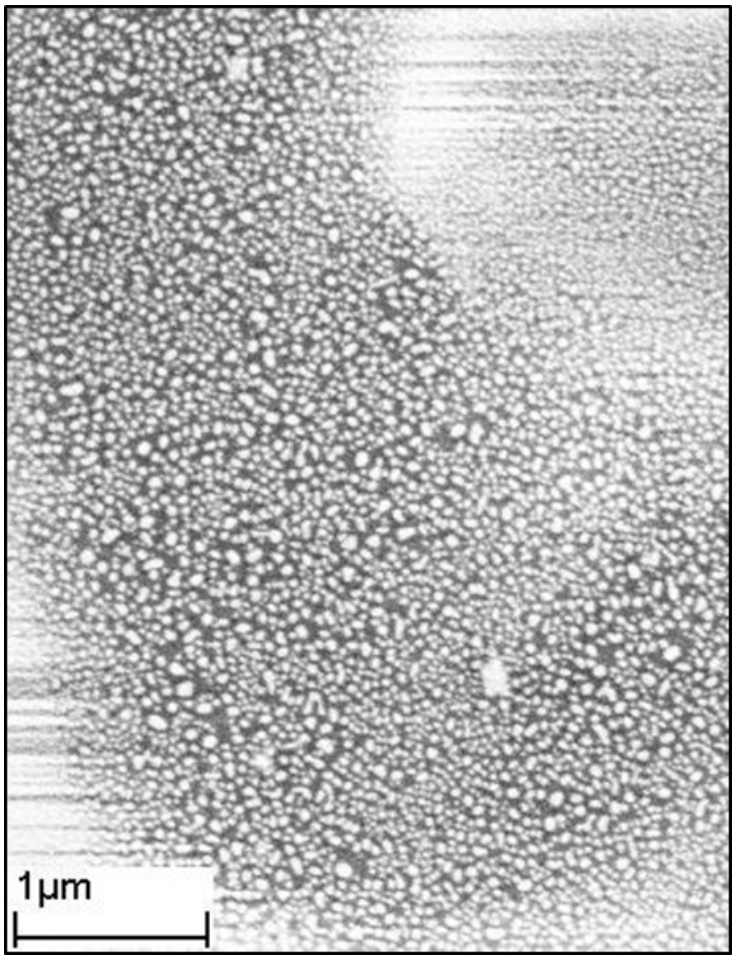

Figure 3.9 SEM image of control sample of gold nanoparticles on single-crystal Al_2O_3 substrate.

3.2.3.4 Discussion of Gold Lattice Parameter

The fact that the gold lattice parameters measured from both the nanorod sample and the control sample, which was not exposed to ZnO, are equal (4.073 Å) establishes that there is no zinc in the catalyst particles. Solid solutions of solute atoms in a solvent lattice will have altered lattice parameters, for both interstitial and substitutional solid solutions. When interstitial atoms are alloyed into a crystal structure, the unit cell, and therefore lattice parameter, must expand in order to accommodate the extra atom. When substitutional atoms are alloyed into a crystal structure, the difference in radii between

the solute atom and the solvent atom it replaced causes the atoms around the substitutional site to become more closely or loosely packed. With a sufficient concentration of solute atoms, a measurable change in the average lattice parameter, either an increase or a decrease depending on the relative atom size, can be observed [80].

The relationship between the concentration of the solute atom and the lattice parameter is often quantized using Vegard's law. First proposed by Vegard in 1921 [82] for ionic salt alloys, Vegard's law states that the lattice parameter of a solid solution will be linearly proportional to the composition. Since its original formulation, Vegard's law has been applied to many types of solid solutions, including mixed III-V semiconductors, such as $Al_xGa_{1-x}N$ [80, 83], and metallic solutions. In the case of metallic solid solutions, real alloys generally exhibit some deviation from the ideal linear behavior predicted by Vegard's law [80]. However, it remains a useful tool for relating composition to lattice parameter.

A Vegard's law relationship for Au-Zn alloys cannot be established directly from the end members, since gold and zinc have different crystal structures (FCC and hexagonal close packed (HCP), respectively). However, a Vegard's law plot can be constructed for the Au-rich region using Au-Zn substitutional intermetallics with FCC superstructures [84], as seen in Figure 3.10. Adding a correction factor for the nanoparticle size contraction (according to Qi and Wang [81] as discussed in section 3.2.3.2 above) shifts the line slightly to lower lattice parameters. From this plot, even the minimum gold lattice parameter (i.e. 3σ less than the average value) corresponds to a

maximum Zn content of 1.3at%. Therefore, the Au catalyst particles contain little to no Zn.

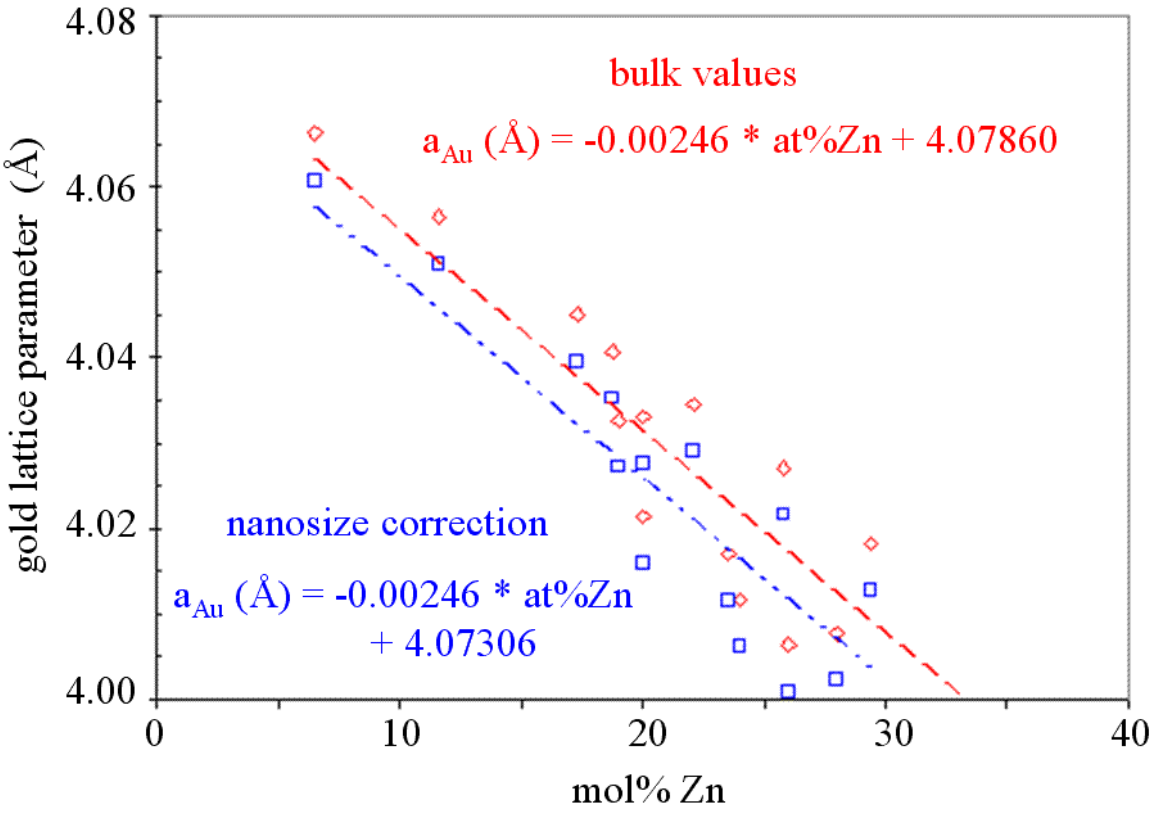

Figure 3.10 Vegard's law plot for Au-rich Au-Zn alloys constructed from Au-Zn substitutional intermetallics with FCC superstructures [84].

3.2.4 Implications for Growth Models

3.2.4.1 Catalyst State

The finding that the Zn is not diffusing into the gold catalyst particles has significant implications for the proposed growth model. The standard VLS synthesis mechanism depends on diffusion of the source material into the catalyst particle in order to cause eutectic melting of the catalyst particle when synthesis is conducted below the melting point of the pure material, as is typical. As can be seen from the Au-Zn phase

diagram [85] seen in Figure 3.11, the Au-Zn interaction is complex, with many intermetallic phases In the gold-rich region, there is extensive solid solubility of Zn in FCC gold, up to around 33at% at the Au-rich eutectic temperature of 684ºC. At room temperature, the maximum solid solubility is still around 7%. Since the growth temperature of the Au-catalyzed ZnO nanorods was well below the melting temperature of pure gold (850ºC as compared to 1063ºC), alloying of Zn into the gold catalyst particles would be necessary for the catalyst particles to be molten. However, the maximum Zn content (i.e. 3σ greater than the average value) according to the Vegard's law relationship above is 1.3at%. According to the phase diagram, the melting temperature of Au with1.3at%Zn is ~1015ºC, which is still much higher than the growth temperature.

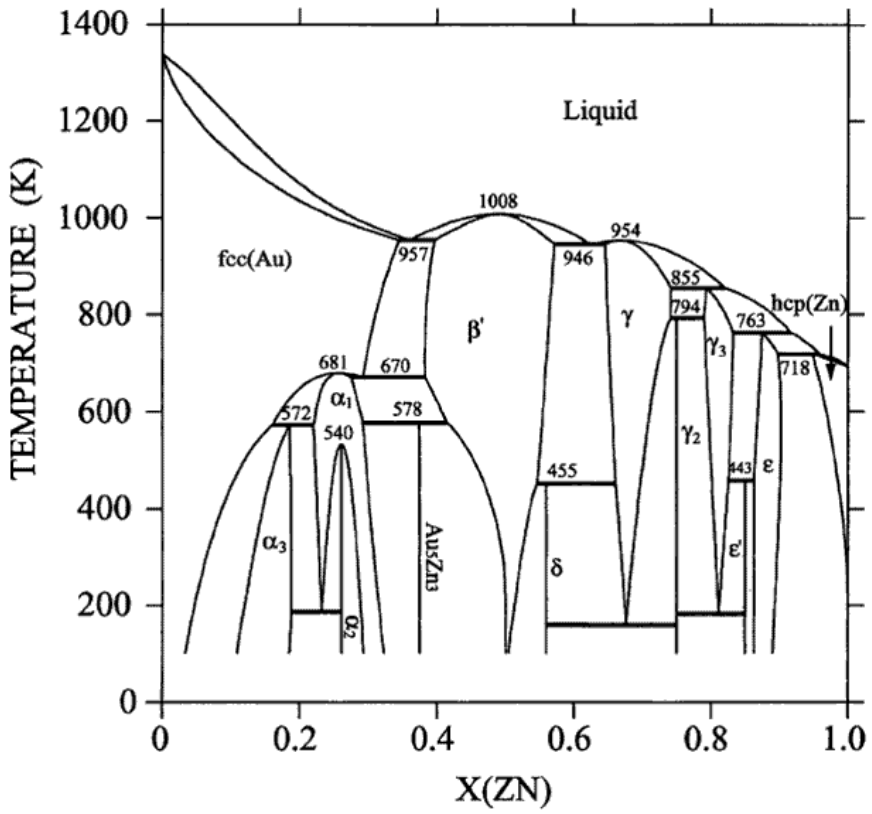

Figure 3.11 Au-Zn phase diagram, reprinted with permission from [85].

Another factor to be considered is melting point depression due to nanoparticle size. Buffat and Borel first reported in 1976 [86] that the melting temperature of gold nanoparticles decreases with decreasing particle size, as seen in Figure 3.12. This effect has been confirmed in other nanostructures as well [87-91], and has been modeled [92]. The depression of the melting temperature of nanostructures is due to the presence of broken bonds on the surface, and the high surface-to-volume ratio of nanostructures. However, this size effect on the melting temperature is only significant for nanoparticles less than approximately 10 nm in diameter, and is therefore insufficient to cause melting at the synthesis temperature for the Au-catalyzed ZnO nanorods, where the gold nanoparticles are larger than 30 nm in diameter. According to the model of Buffat and Borel, 33 nm gold nanoparticles should melt at 1031ºC, well above the ZnO nanorod synthesis temperature of approximately 850ºC.

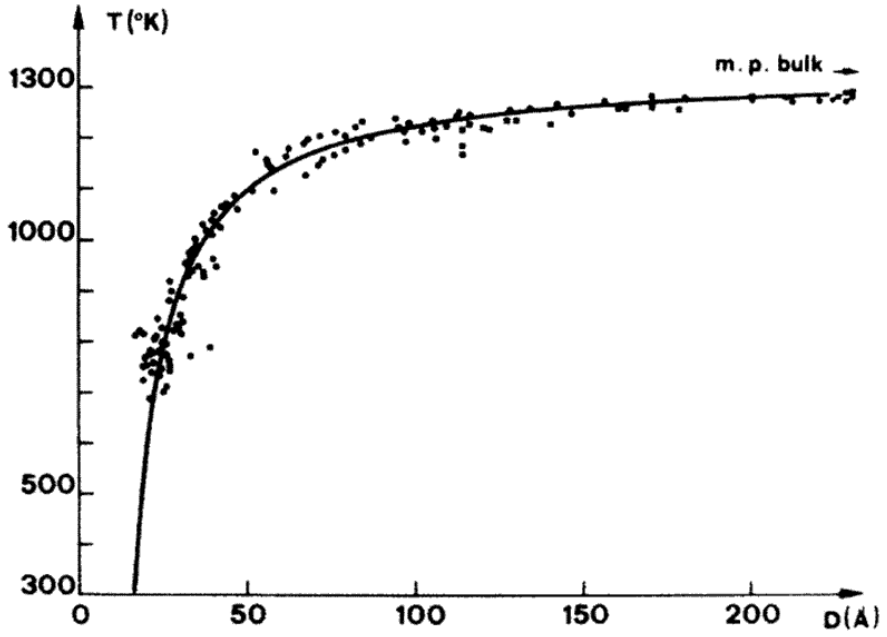

Figure 3.12 Melting temperature of gold nanoparticles as a function of diameter. Reprinted with permission from [86], ©1976 by the American Physical Society.

3.2.4.1.1 Verification by In-Situ X-Ray Diffraction

In order to verify the melting point of the gold catalyst particles, *in-situ* XRD data were collected at elevated temperatures on the Au-catalyzed ZnO nanorods. Offset θ/2θ scans of the Au {111} reflection were collected from 518 to 1018ºC, in 100º increments, seen in Figure 3.13. Scans were not collected at any temperatures above 1018ºC due to technical limitations of the furnace (HTK-1200 oven-type). Data were collected with parafocusing geometry and a position sensitive detector. The radiation was Mo K_α (λ=0.710730 Å).

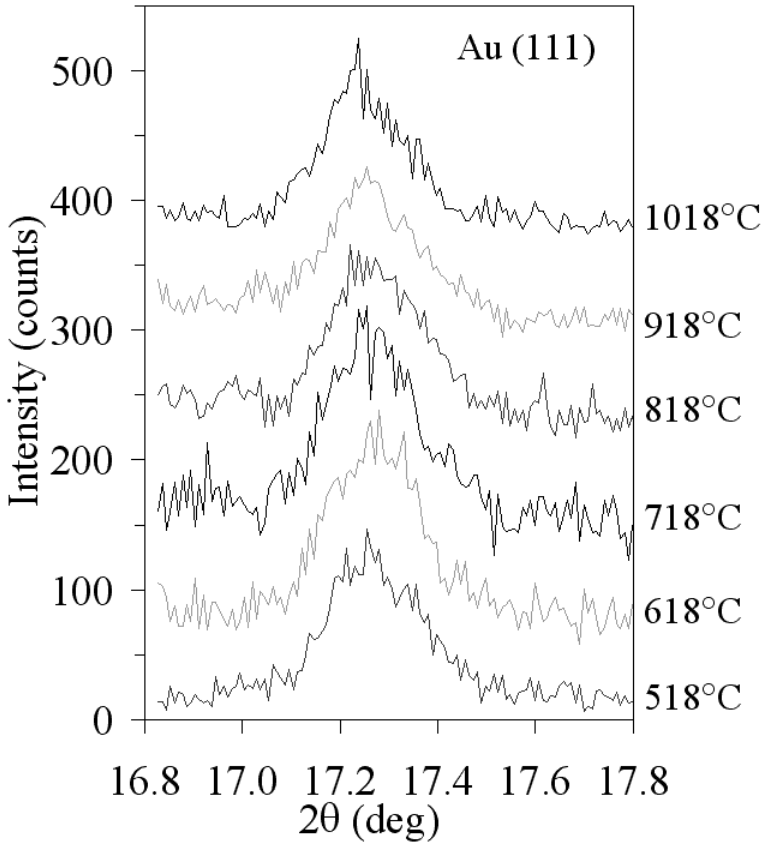

Figure 3.13 *In-situ* XRD data of Au-catalyzed ZnO nanorods collected from 518 to 1018ºC, showing the Au {111} peak.

The Au {111} reflection is clearly present in all scans, including that at 1018ºC, indicating that the gold nanoparticles did not melt up to 1018ºC. These results confirm the absence of Zn in the gold, as only ~1at% Zn in the Au would cause melting at 1018ºC, according to the phase diagram as seen in Figure 3.11. Since the synthesis temperature was around 850ºC, it is likely that the gold catalyst particles remain solid during synthesis, indicating that growth is by the VSS synthesis mechanism, not the VLS synthesis mechanism.

3.2.4.2 Diffusion Path

The absence of Zn in the gold catalyst particle also indicates that growth cannot be proceeding by a supersaturation–nucleation process, as previously considered. The likely explanation for the observed results relates to the bonding types of the catalyst particle and the source. A mass spectroscopy study of thermally evaporated ZnO [93] has shown that the ZnO dissociates into ionic species. Following the general chemical principle of "like dissolves like", ionic Zn^{2+} species would be unlikely to dissolve into and alloy with metallic Au. Therefore, bulk diffusion through the catalyst particle is not favorable.

A more likely diffusion path for the Zn to get to the growing nanowire is around the surface of the gold catalyst particle. Wang and Fischman [94] and later Cheyssac et al. [95] have proposed surface diffusion as a significant part of the VLS mechanism, supported by the fact that liquid surface diffusion rates are significantly higher than liquid bulk diffusion rates and the high surface-to-volume ratio of nanostructures.

The same holds true for solid surface and bulk diffusion rates; the surface diffusion coefficient of solid gold is several orders of magnitude greater than the bulk

diffusion coefficient [96]. In addition, the gold nanoparticles can have a disordered, quasi-liquid layer (QLL) on the surface due to surface reconstruction [97, 98]. In other metals, such layers have been found to have unusually high self-diffusion coefficients at temperatures approaching the melting point, similar to or even exceeding the bulk liquid diffusivity [99]. Such quasi-liquid layers will also have a large Langmuir sticking coefficient, aiding the adsorption of growth species in the vapor onto the catalyst particle surface, relative to adsorption on the substrate, which promotes the formation of 1D nanostructures.

3.3 Sn-Catalyzed Zinc Oxide Nanostructures

3.3.1 Synthesis and Morphology

The Sn-catalyzed ZnO nanostructures were grown in the horizontal tube furnace. The source material was ZnO powder. Samples were grown on *c*-plane sapphire and *c*-plane ZnO substrates. For the catalyst, SnO_2 and graphite were mixed with the ZnO source material. When heated, the graphite reduces the SnO_2 to metallic tin, and the vapor species, including both source and catalyst, are carried to the substrate. During growth, the source materials were heated to 1150ºC, and the substrates to temperatures around 350-600ºC. (For synthesis details, see section 2.1.3.2 above.)

The samples were imaged with scanning electron microscopy as shown in Figure 3.14. The morphology is similar for both types of substrates, but several types of morphology are observed on each sample. A common morphology is 1D nanostructures with widths of 46 ± 18 . Previous TEM analysis of these Sn-catalyzed ZnO nanostructures has shown them to include nanowires, with a [0001] growth direction and nanobelts, with rectangular cross-sections and growth directions of $[01\bar{1}0]$ and $[2\bar{1}\bar{1}0]$

[23]. The nanostructures are straight with catalyst particles at the tip. The average diameter of the catalyst particles is 140 ± 33 nm, much greater than the width of the nanostructures.

Hierarchical structures are often found, with branches growing perpendicularly from a central nanostructure. The nanostructures do not generally grow aligned, even though the substrates are single crystalline. As the catalyst is vaporized with the source material, the nanostructures may begin to grow during vapor transport, before they reach the substrate, and therefore, no crystallographic orientation with the substrate is taken. This is particularly apparent for the hierarchical structures, which appear to be sitting on top of the substrate with minimal interaction. The branches themselves are also likely due to the vaporization of the catalyst, which may precipitate on the surface of already grown nanowires and subsequently catalyze the growth of branches.

Under the hierarchical nanostructures, covering the substrate are microrods, with diameters of 2.6 ± 0.6 μm. The hexagonal symmetry of ZnO is apparent in the sample on a *c*-plane ZnO substrate, and indicates that these microrods are *c*-plane oriented. ZnO will take a crystallographic orientation to match the *c*-plane orientation of the substrate. Shorter nanostructures are also observed growing epitaxially from the microrods. Besides the small nanobelts and the large microrods nanorods are observed, with diameters of 392 ± 24 Å. No catalyst particles are present at the tips of the nanorods. Finally, large spherical particles, likely composed of tin, are commonly observed sitting on the substrate. The diameter of the large particles is generally around 10 μm.

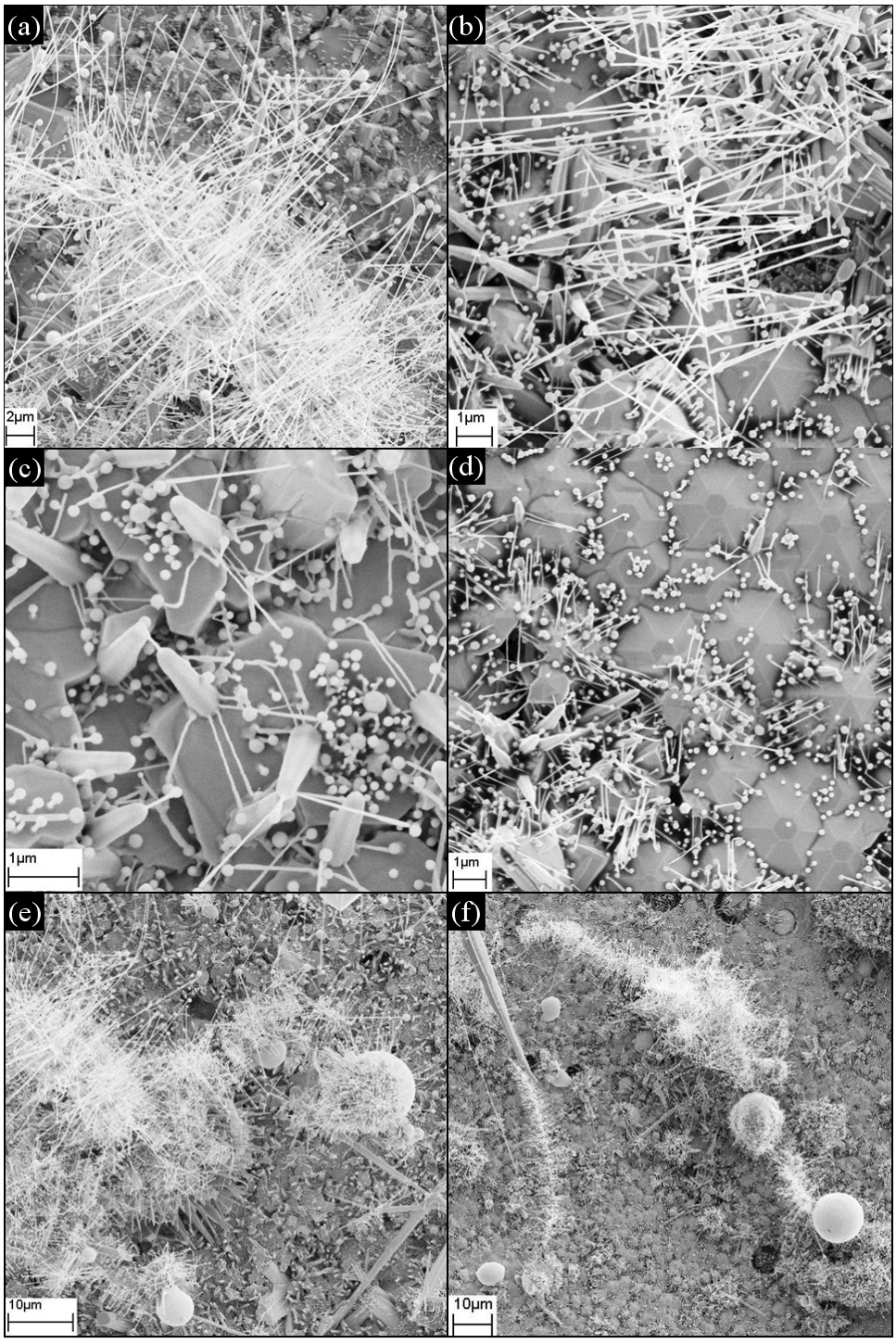

Figure 3.14 SEM images of Sn-catalyzed ZnO nanowires and other structures, including (a) and (b) hierarchial nanostructures, (c) and (d) micro and nanorods, and (d) and (e) low magnification images showing large tin particles.

3.3.2 Crystallite Size and Microstrain Analysis

The crystallite size and microstrain in the tin and ZnO phases for the sample synthesized on *c*-plane sapphire were investigated, using the Williamson-Hall analysis method. Scans collected on LaB_6 powder (SRM 660a) were used to determine the instrumental contribution to peak broadening. A typical Williamson-Hall plot for the tin phase is shown in Figure 3.15a. The data are somewhat scattered. The *y*-intercept is near zero, indicating the absence of any significant peak broadening due to crystallite size. The absence of any crystallite size broadening suggests that the XRD signal from the Sn phase is being dominated by the large tin particles. Additionally, the slope of the tin Williamson-Hall plot is positive, indicating peak broadening due to a tensile microstrain. The results from three scans were combined to give an average microstrain of $0.0240 \pm 0.0085\%$.

A typical Williamson-Hall plot for the ZnO phase is shown in Figure 3.15b. Qualitatively, it is similar to that observed for the tin phase, though the scatter in the data is less. There is no evidence of peak broadening due to crystallite size. The absence of size broadening is likely due to the presence of the ZnO microrods. The slope of the Williamson-Hall plot is positive, indicating tensile microstrain. The results from five scans were combined to give an average microstrain of $0.058 \pm 0.018\%$.

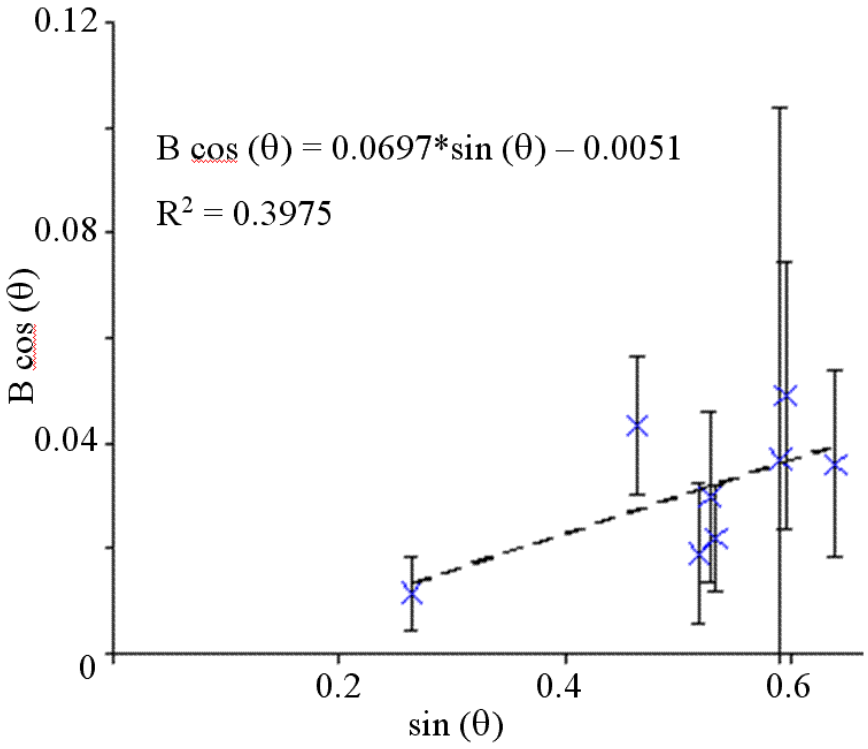

(a)

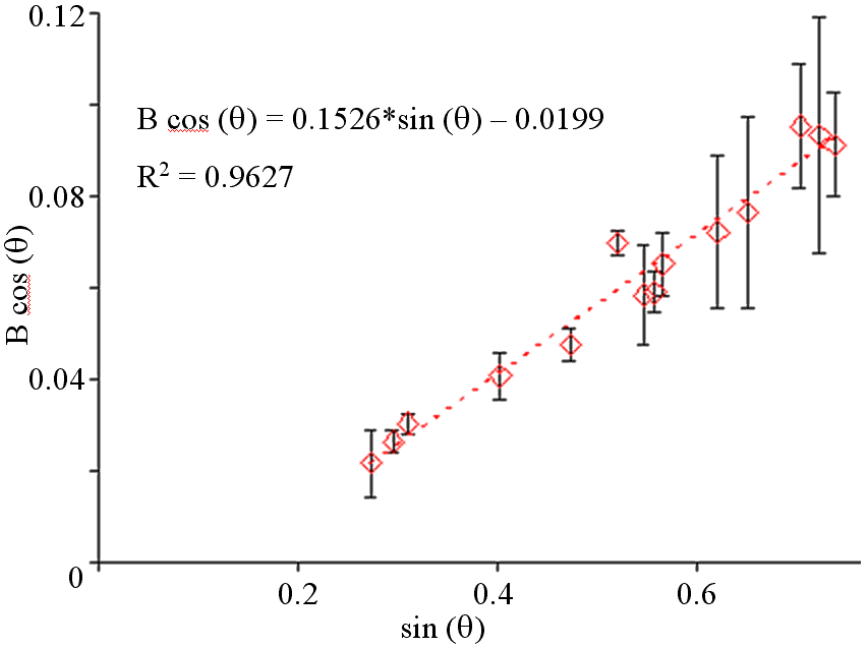

(b)

Figure 3.15 Williamson-Hall plots for the (a) Sn and (b) ZnO phases in a sample of Sn-catalyed ZnO nanowires.

3.3.3 Lattice Parameter Analysis

The tin lattice parameter was determined by X-ray diffraction. For the sample on a *c*-plane sapphire substrate, the Al_2O_3 {00ℓ} peaks from the substrate obscured the tin peaks. Therefore, an XRD scan was collected with an ω-offset to reduce the intensity of the substrate peaks. Also, since the tin particles are not crystallographically aligned with the substrate, as is apparent in the SEM images in Figure 3.14, analysis by grazing incidence is possible, and therefore, three GIXRD scans collected. All four scans were analyzed with Pawley whole pattern fitting, and the average tin lattice parameters determined to be 5.8319 ± 0.0005 Å for the *a*-axis and 3.1830 ± 0.0009 Å for the *c*-axis. The measured lattice parameters are not statistically significantly (i.e. greater than 3σ) different than those for pure tin (5.8308 Å and 3.1810 Å, PDF #4-4-7747), indicating that there is no significant amount of Zn in the tin. Lattice parameters measured from the sample on a *c*-plane ZnO substrate (5.8329 ± 0.0010 Å and 3.1818 ± 0.0010 Å for the *a* and *c*-axes, respectively) are also within 3σ of the bulk value, confirming the absence of Zn in the tin.

A Vegard's law relationship for Sn-Zn alloys cannot be established directly from the end members, since tin and zinc have different crystal structures (tetragonal and hexagonal close packed (HCP), respectively). However, a Vegard's law plot can be constructed for the Sn-rich region using literature reports of Sn-Zn alloys [100], as seen in Figure 3.16. The data has been plotted in terms of unit cell volume, to incorporate both axes. It can be observed that alloying of Zn into Sn should cause a significant decrease of the tin unit cell volume. The absence of a decrease in the tin unit cell volume

suggests that there is no Zn in the Sn after growth, though the presence of a small amount of Zn in the tin cannot be ruled out, as will be discussed further in section 3.3.4 below.

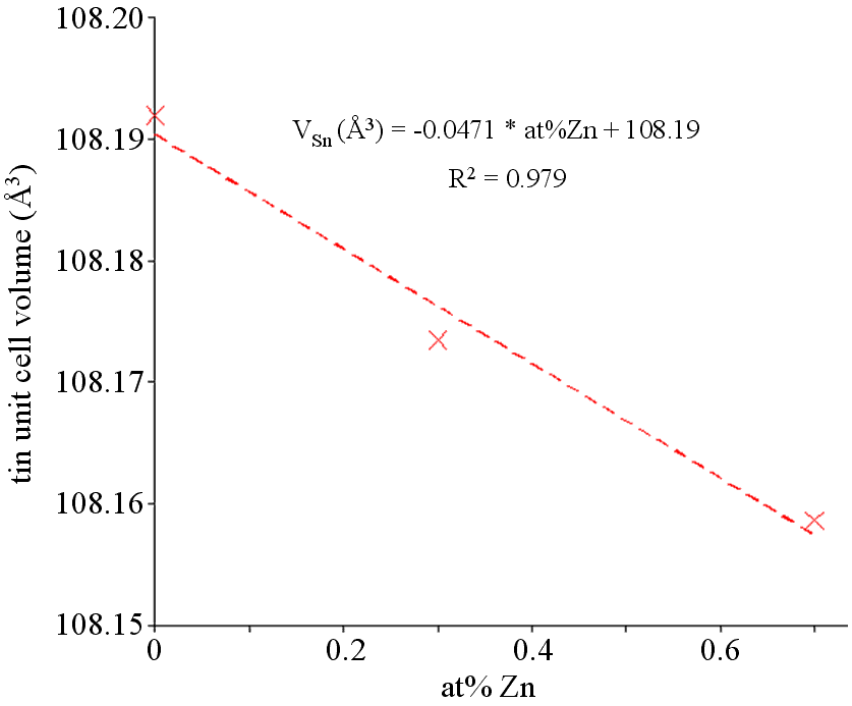

Figure 3.16 Vegard's law relationship for Sn-rich Sn-Zn alloys, constructed using data from [100].

One unknown factor is the effect of the large micron-sized tin particles in the sample. Due to their size, these large particles may be less likely than the catalyst nanoparticles to absorb Zn through their entire volume. If the X-ray signal is dominated by diffraction from the large particles, as is suggested by the lack of crystallite size broadening and nanoparticle lattice contraction, the XRD results may not apply to the catalyst nanoparticles.

3.3.4 Implications for Growth Model

Keeping the previous discussion in mind, the implications these XRD results for the growth model may be considered. An inspection of the Sn-Zn phase diagram, as in

Figure 3.17 [101], reveals that the growth temperatures of 350-600ºC are well above not only the Sn-Zn eutectic (~200ºC) but also the pure Sn melting temperature (232ºC). Therefore, the tin catalyst particles must be liquid during growth, regardless of the presence or absence of Zn in the tin. From the phase diagram, it may also be observed that the maximum solid solubility of Zn in Sn is quite low, around 0.6 at% Zn. If Zn was dissolved in the molten tin during growth, the excess Zn above the solid solubility limit should precipitate out of the tin upon cooling and solidification. This would leave behind no more than 0.6 at% Zn, which would lead to a tin unit cell volume of 108.16 $Å^3$, according to the Vegard's law relationship discussed in section 3.3.3 above. This value is not statistically significantly different than the tin unit cell volume measured from the nanobelt sample (108.3 ± 0.1º $Å^3$ for the sample on a *c*-plane sapphire substrate). Therefore, no conclusions may be drawn concerning the presence or absence of Zn in the tin catalyst particles during growth. However, the finding that 1D nanostructures of ZnO may be grown from both liquid (tin) and solid (gold, as discussed in section 3.2 above) catalysts indicates that a particular catalyst state is not necessary for growth and that the catalyzed growth of 1D nanostructures is more flexible than originally imagined.

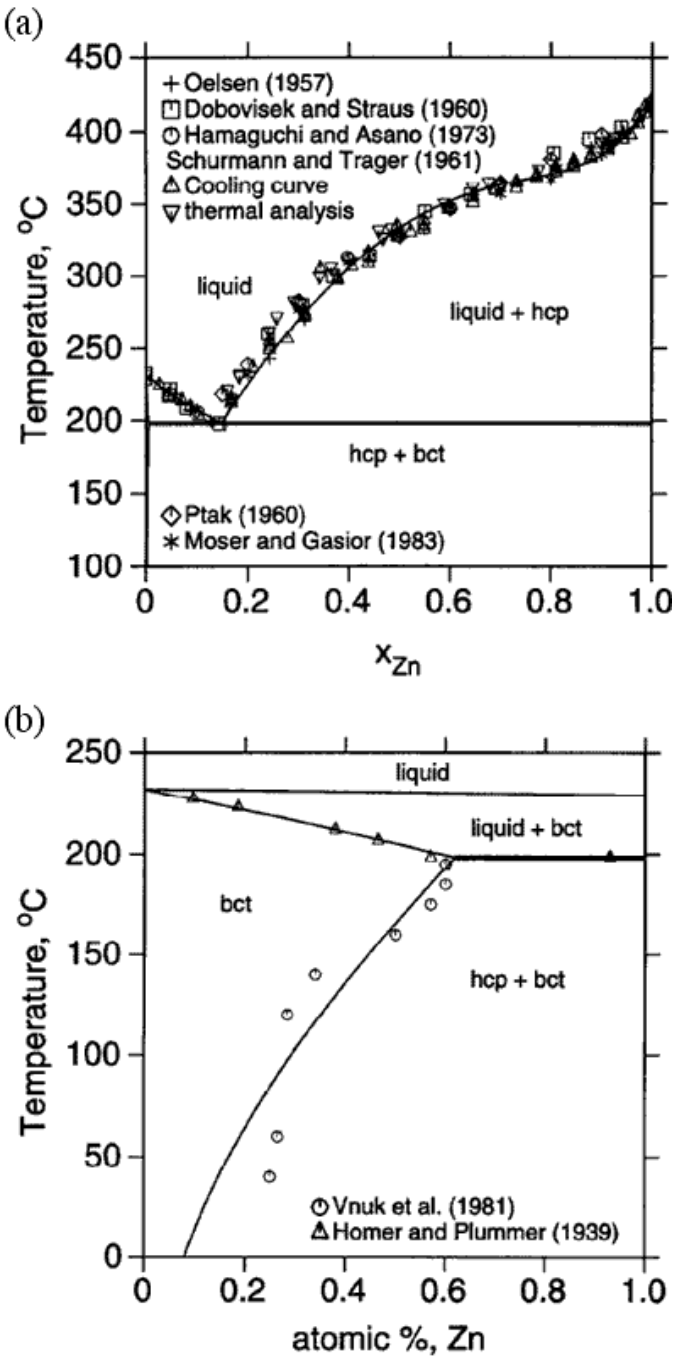

Figure 3.17 Sn-Zn phase diagram, showing (a) the whole range and (b) a detail of the Sn-rich region. Reprinted from [101] with permission from Elsevier.

3.4 Au-Catalyzed Iron Oxide Nanostructures

3.4.1 Synthesis and Morphology

The Au-catalyzed Fe_xO_y nanostructures were grown in the horizontal tube furnace with the laser system to aid vaporization of the source material. The source material was magnetite (Fe_3O_4) powder pressed into a solid target rod. Samples were grown on three types of Al_2O_3 substrates: polycrystalline, single-crystalline *a*-plane oriented or single-crystalline *c*-plane oriented). For the catalyst, a gold film was deposited on the substrates. Data will be presented from all three types of substrate, with analysis focusing on the single-crystal *c*-plane substrate.

The target and substrates were placed in the center of the tube furnace, with the substrates lying just in front of the target. The tube furnace was heated to around 800 to 900ºC and held at temperature for 60 minutes while the target was irradiated with the laser, and then the furnace was cooled under vacuum. (For synthesis details, see section 2.1.3.3.)

The samples were imaged with scanning electron microscopy. For the samples grown on *c*-plane sapphire, the nanorods are vertically aligned, with an average diameter of 99 ± 22 nm and an average length of 1.1 ± 0.5 μm, as seen in Figure 3.18. The diameter of the catalyst nanoparticles at the tips is the same as that of the nanorods. For the samples grown on *a*-plane sapphire, the nanorods grow in-plane, i.e. parallel to the sample surface, and at right angles to each other, as seen in

Figure 3.19. The nanorods have an average diameter of 118 ± 39 nm and an average length of 1.4 ± 0.5 μm. For the samples grown on corundum substrates (i.e. polycrystalline Al_2O_3), the nanorods are not aligned in one direction, due to the randomness of the substrate orientation, as seen in Figure 3.20. The nanorods have an average diameter of 38 ± 11 nm and lengths around 1 μm, while the diameter of the catalyst nanoparticles at the tips is the approximately the same as that of the nanorods.

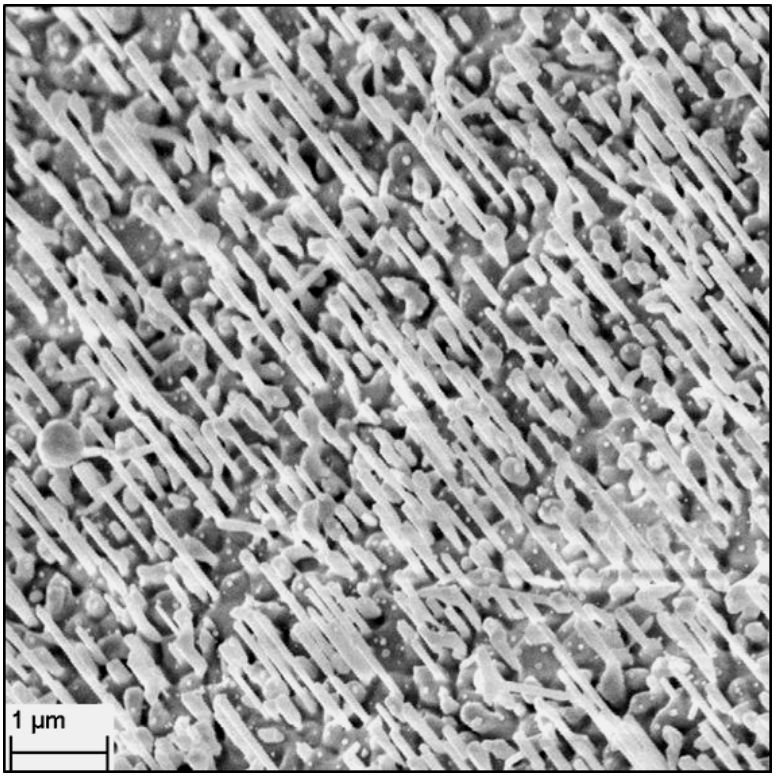

Figure 3.18 SEM images of samples of Au-catalyzed Fe_xO_y nanorods grown on a *c*-plane sapphire substrate.

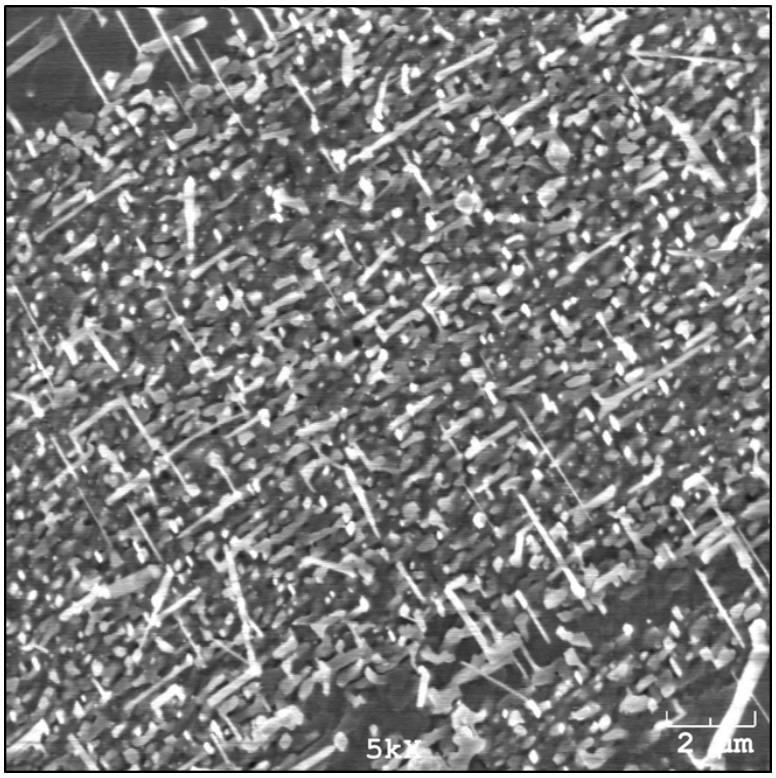

Figure 3.19 SEM images of samples of Au-catalyzed Fe_xO_y nanorods grown on an *a*-plane sapphire substrate.

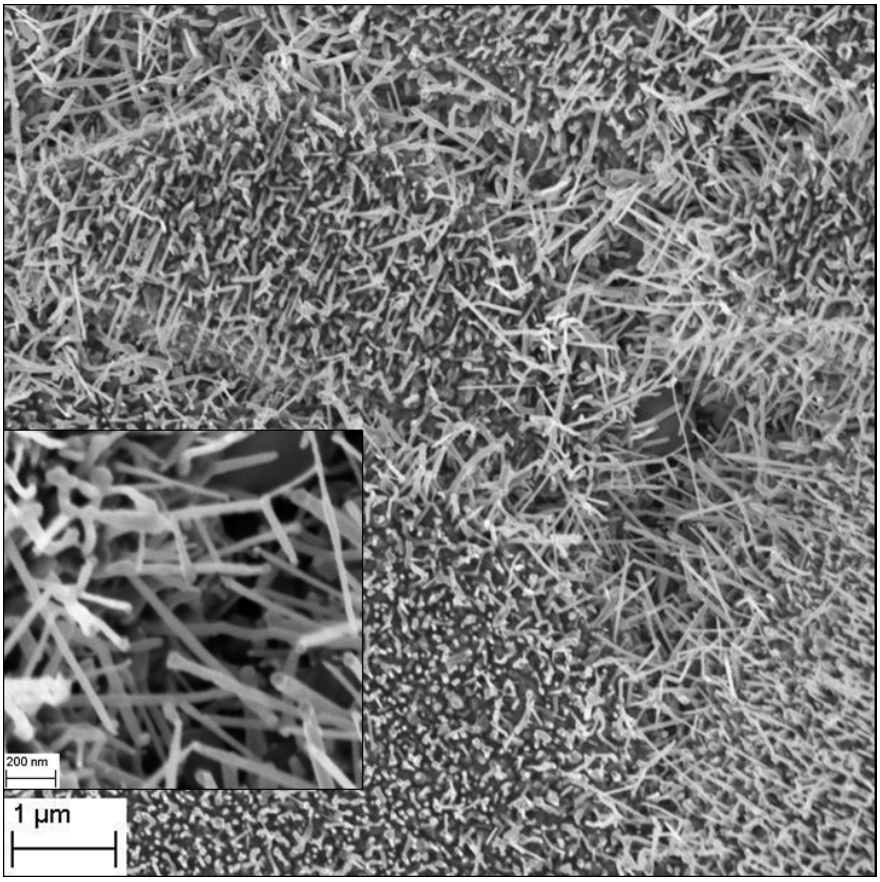

Figure 3.20 SEM images of samples of Au-catalyzed Fe_xO_y nanorods grown on a polycrystalline corundum substrate.

3.4.2 Crystallographic Orientation Analysis

3.4.2.1 With *c*-Plane Sapphire Substrate

3.4.2.1.1 θ/2θ XRD Patterns

For the samples grown on *c*-plane sapphire, the crystallographic orientations were first investigated with θ/2θ XRD scans, as seen in Figure 3.21. In addition to the substrate {000ℓ} peaks, hematite (Fe_2O_3) peaks are observed. For the hematite phase, only the {0006} and {0,0,0,12} peaks are present. Additionally, in longer scans traces of

the magnetite (Fe_3O_4) {111}, {222}, {333} and {444} peaks are present. No evidence was found of ε-Fe_2O_3 nanobelts, which have been previously observed [52, 102]. Finally, gold {111} and {222} peaks are observed. These results indicate that the following families of planes from each phase are parallel to the sample surface: Al_2O_3 {000ℓ}, Fe_2O_3 {000ℓ}, Fe_3O_4 {*hhh*} and Au {*hhh*}.

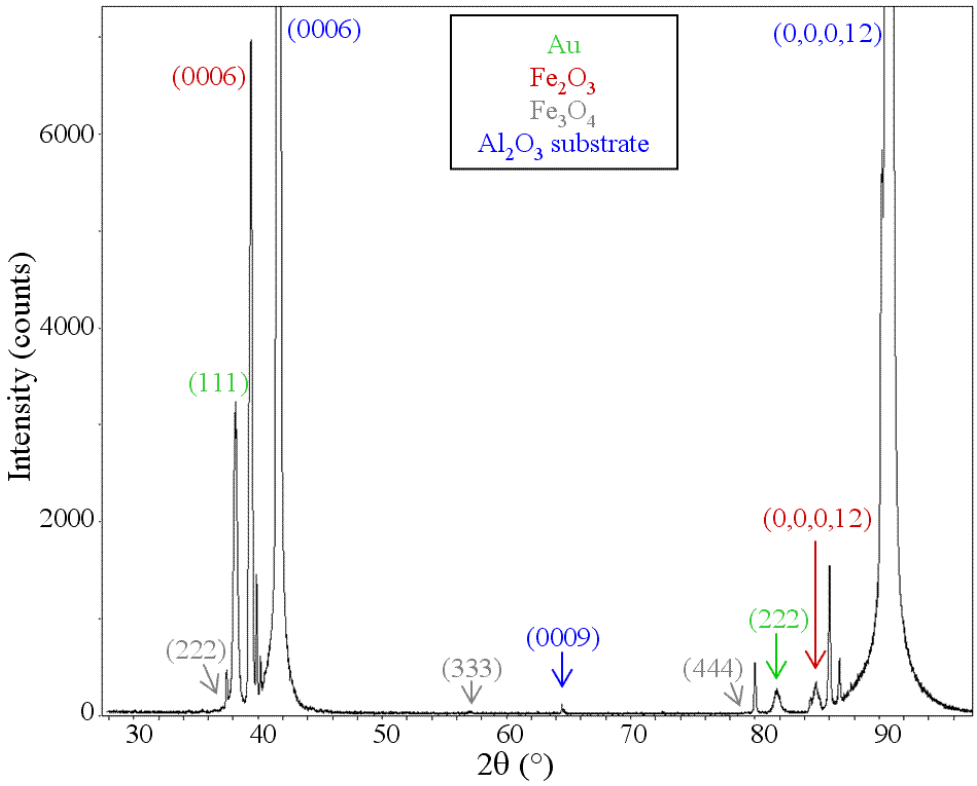

Figure 3.21 θ/2θ XRD scan of Au-catalyzed Fe_xO_y nanowires synthesized on a *c*-plane sapphire substrate.

In addition, the XRD results, combined with the observed vertical alignment of the nanorods, indicated that the nanorod growth direction is [0001] for hematite and [111] for magnetite. Previous TEM analysis [52] of a similar sample grown on an alumina substrate also showed the growth direction of the magnetite nanowires to be [111].

However, the growth direction of the hematite nanowires was found to be [11$\bar{2}$0] in the previous TEM analysis. The presence of single crystal sapphire substrates in the current samples may have affected the growth direction of the hematite nanowire, particularly considering the close lattice match between Al_2O_3 and Fe_2O_3 (4.7602 and 12.9933 Å for Al_2O_3 (PDF #4-4-2852), and 5.0342 and 13.7483 Å for Fe_2O_3 (PDF #4-3-2900), for the *a* and *c* axes respectively).

3.4.2.1.2 Texture Analysis

Texture data were collected from the gold, hematite and magnetite phases for the samples grown on *c*-plane sapphire substrates, following the methods discussed for Au-catalyzed ZnO nanorods in section 3.2.2.3 above. All the pole figures are in Appendix APPENDIX B for reference. One pole figure for each phase will be shown here to illustrate the measured crystallographic orientations.

For the gold phase, pole figures were collected on the {111} and {200} peaks. The Au {111} pole figure is shown in Figure 3.22. The central peak confirms the {111} orientation observed in the θ/2θ scan. The peak is slightly off-center, likely due to a slight sample misalignment. Six peaks are observed at a ψ-tilt angle of 75° and evenly spaced every 60º in φ. These six peaks indicate the presence of two crystallographic {111} orientations, rotated about the sample normal by 60º from each other. Each orientation explains three of the observed peaks by the {111}-equivalent planes ($\bar{1}$11), (1$\bar{1}$1) and (11$\bar{1}$). The expected angle between {111} planes is 71°, which is consistent with the ψ-tilt angles measured. The other, {200} pole figure collected on the gold phase confirms these orientation relationships found from the {111} pole figure.

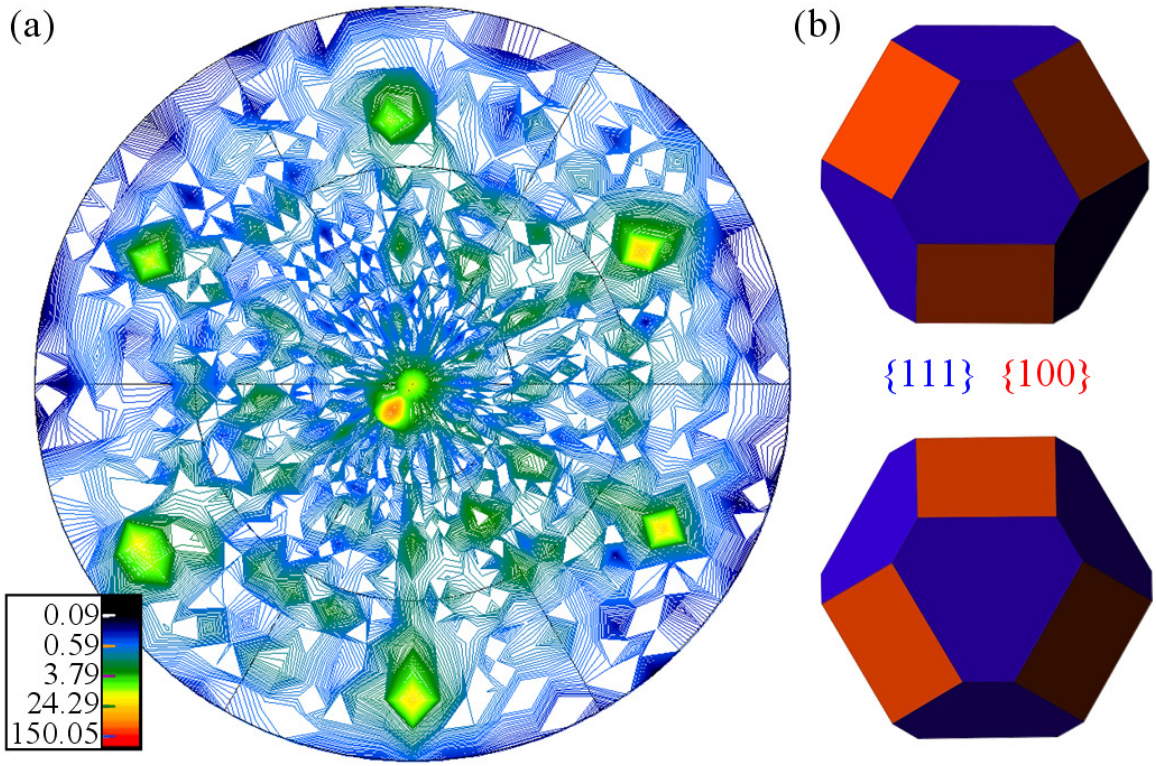

Figure 3.22 Crystallographic orientation of the gold catalyst particles on a sample of Au-catalyzed Fe_xO_y nanowires grown on a *c*-plane sapphire substrate, showing (a) the Au {111} pole figure and (b) the two gold orientations, related by a 60° rotation. The blue {111} planes correspond to the intensity peaks in the pole figure.

For the hematite phase, pole figures were collected on the $\{10\bar{1}4\}$, $\{02\bar{2}4\}$ and $\{11\bar{2}3\}$ peaks. Hematite has the same crystal structure and similar lattice parameters (a_{Fe2O3} = 5.0342 Å and a_{Al2O3} = 4.7602 Å, c_{Fe2O3} = 13.7483 Å and c_{Al2O3} = 12.9933 Å; PDF #4-3-2900 and #4-4-2852, respectively) to the sapphire substrate, which allows the substrate peaks to obscure some peaks from the hematite phase, namely those that would match the crystallographic orientation of the substrate. However, peaks from other crystallographic orientation may be distinguished, as seen in the Fe_2O_3 $\{02\bar{2}4\}$ pole figure shown in Figure 3.23. Six peaks are observed at a ψ-tilt angle of 60-65° and

evenly spaced every 60º in φ. The three strong peaks at φ-rotation angles of 0º, 120º and 240º are from the *c*-plane sapphire substrate and likely obscured hematite peaks with a matching {0001} crystallographic orientation. The expected angle between the {0001} and $\{02\bar{2}4\}$ planes is 58°, which is consistent with the ψ-tilt angles measured. The three weak peaks at φ-rotation angles of 60º, 180º and 300º indicate a second hematite {0001} crystallographic orientation rotated from the first by 60º about the sample normal. The other pole figures collected on the hematite phase confirm these orientation relationships found from the $\{02\bar{2}4\}$ pole figure.

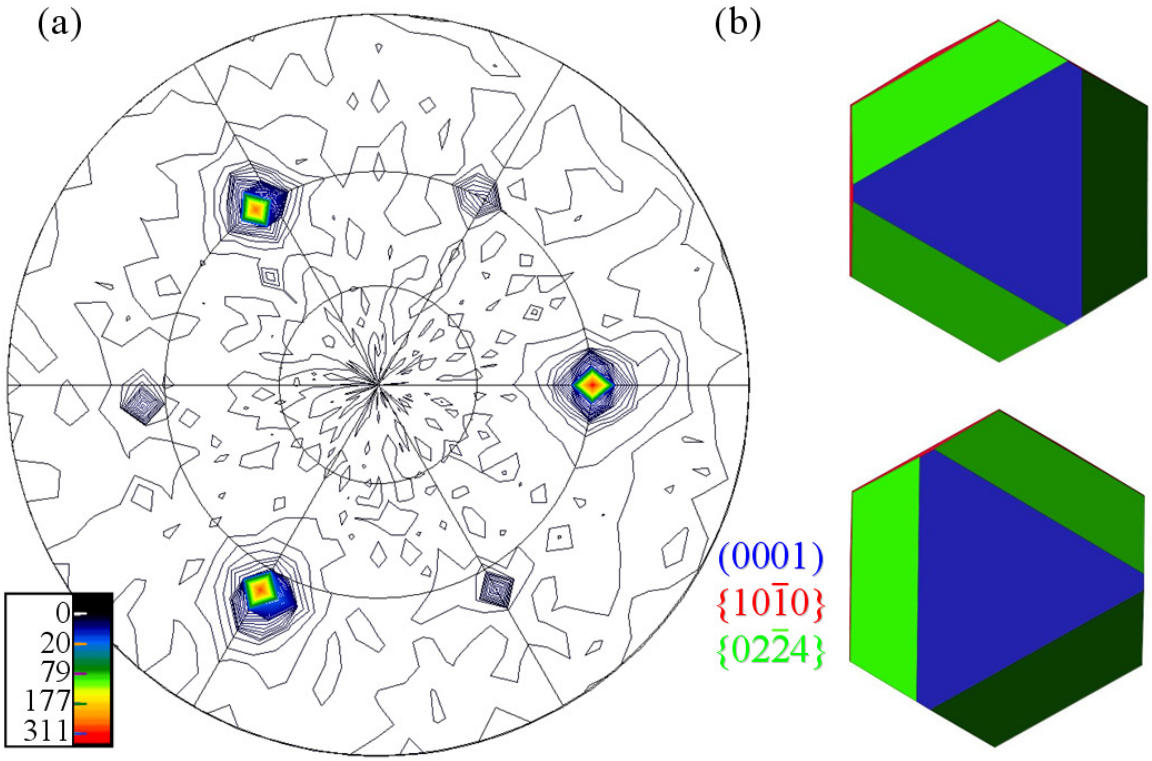

Figure 3.23 Crystallographic orientation of the hematite phase on a sample of Au-catalyzed Fe_xO_y nanowires grown on a *c*-plane sapphire substrate, showing (a) the Fe_2O_3 $\{02\bar{2}4\}$ pole figure and (b) the two hematite orientations, related by a 60° rotation. The green $\{02\bar{2}4\}$ planes correspond to the intensity peaks in the pole figure.

For the magnetite phase, pole figures were collected on the {111}, {220} and {311} peaks. The Fe_3O_4 {311} pole figure is shown in Figure 3.24. The three strong peaks at a ψ-tilt angle of 45° are overlap from the Al_2O_3 {$10\bar{1}4$} reflection of the substrate. The expected angle between Al_2O_3 {0001} and {$10\bar{1}4$} planes is 38°, which is consistent with angles measured from the pole figure. Six peaks are observed at a ψ-tilt angle of 60-65° and evenly spaced every 60º in φ. This confirms the {111} orientation of the magnetite phase, as observed in the θ/2θ scans. These six peaks correspond to the ($\bar{1}13$), ($\bar{1}31$), ($13\bar{1}$), ($31\bar{1}$), ($3\bar{1}1$) and ($1\bar{1}3$) planes, which have an expected angle of 59° with the (111) plane, consistent with the angle measured from the pole figure. Six additional peaks are observed at a ψ-tilt angle of 35° and evenly spaced every 60º in φ. These six peaks indicate the presence of two crystallographic {111} orientations, rotated about the sample normal by 60º from each other. Each orientation explains three of the observed peaks by the {311}-equivalent planes (311), (131) and (113). The expected angle between these planes and the (111) plane is 29°, which is consistent with the angles measured from the pole figure. Some indication of the ($\bar{1}\bar{1}3$), ($\bar{1}3\bar{1}$) and ($3\bar{1}\bar{1}$) peaks are also observed in the pole figure. However, the ψ-tilt angle is too high (at an expected angle of 80°) to allow them to be clearly distinguished. The other pole figures collected on the magnetite phase confirm these orientation relationships found from the {311} pole figure. The orientation relationships measured for all three phases, including parallel planes and direction, are summarized in Table 3.3.

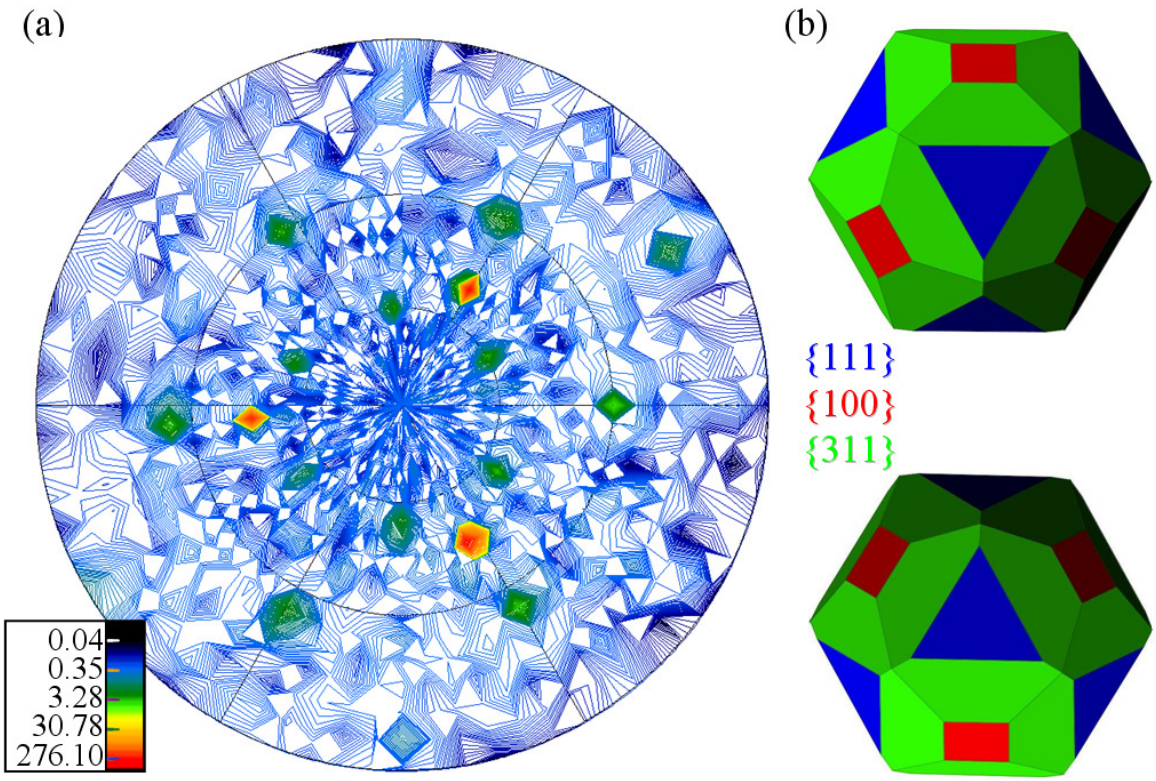

Figure 3.24 Crystallographic orientation of the magnetite phase on a sample of Au-catalyzed Fe_xO_y nanowires grown on a *c*-plane sapphire substrate, showing (a) the Fe_3O_4 {311} pole figure and (b) the two magnetite orientations, related by a 60° rotation. The green {311} planes correspond to the intensity peaks in the pole figure, with the exception of the three strongest peaks, which are overlap from the substrate.

Table 3.3 Crystallographic orientations between the Au, Fe_2O_3, Fe_3O_4 and Al_2O_3 phases for Au-catalyzed Fe_xO_y nanostructures on *c*-plane sapphire.

Phase	Parallel Plane	Parallel Directions	
Au	{111}	$\langle \bar{2}11 \rangle$	$\langle 11\bar{2} \rangle$
Fe_2O_3	{0001}	$\langle 11\bar{2}0 \rangle$	$\langle 2\bar{1}\,\bar{1}0 \rangle$
Fe_3O_4	{111}	$\langle \bar{2}11 \rangle$	$\langle 11\bar{2} \rangle$
Al_2O_3	{0001}	$\langle 2\bar{1}\,\bar{1}0 \rangle$	$\langle 2\bar{1}\,\bar{1}0 \rangle$

3.4.2.1.3 Discussion of Crystallographic Orientations

Al_2O_3 and Fe_2O_3 have the same rhombohedral crystal structure with 6-fold symmetry in the basal plane. Therefore, it is expected that the hematite will take the same $\{000\ell\}$ crystallographic orientation as the sapphire substrate. Since gold and magnetite have face-centered cubic (FCC) symmetry, the {111} planes of both phases have three-fold hexagonal-like symmetry. Therefore, gold and magnetite are expected to take $\{hhh\}$ orientations. The θ/2θ XRD scans confirm these predicted crystallographic orientations for each phase.

The texture analysis gives additional information about the crystallographic orientation, including the parallel directions within the parallel planes. The presence of two crystallographic orientations rotated about the sample normal by 60º from each other for the gold, hematite and magnetite phases results from the six-fold symmetry of the substrate. The hexagonal or hexagonal-like symmetries of the interfacial planes for each phase in these samples match, as illustrated in Figure 3.25. The lattice mismatches between all phases of this sample are low, below 10%, as shown in Table 3.4.

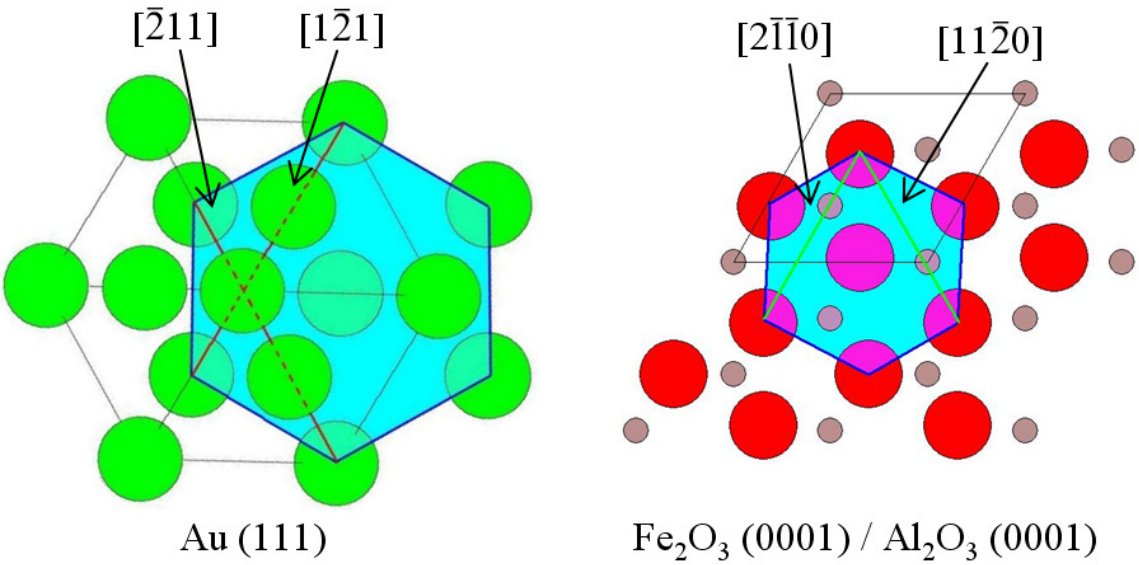

Figure 3.25 Schematics showing crystallographic orientations of the Au, Fe_2O_3 and Al_2O_3 phases in a sample of Au-catalyzed Fe_xO_y nanowires on a *c*-plane sapphire substrate.

Table 3.4 Calculated lattice mismatches between Au, Fe_2O_3, Fe_3O_4 and Al_2O_3 with crystallographic orientations as outlined in Table 3.3 above, for Au-catalyzed Fe_xO_y nanostructures on *c*-plane sapphire.

Phase 1	Phase 2	Lattice Mismatch
Au	Fe_2O_3	0.5188%
Au	Fe_3O_4	2.736%
Au	Al_2O_3	-4.830%
Fe_2O_3	Fe_3O_4	2.217%
Fe_2O_3	Al_2O_3	-5.348%
Fe_3O_4	Al_2O_3	-7.563%

3.4.2.2 With *a*-Plane Sapphire Substrate

For the sample grown on *a*-plane sapphire, the crystallographic orientations were investigated with θ/2θ XRD scans, as seen in Figure 3.26. Offset scans were collected in order to reduce the signal from the substrate {*hh*·0} peaks, which overlap other peaks of the sample. Two phases are observed: hematite (Fe_2O_3) and gold. For the hematite

phase, only the $\langle 11\bar{2}0 \rangle$ and $\langle 22\bar{4}0 \rangle$ peaks are present, and for the gold phase, only the {111} and {222} peaks. These results indicate that the following families of planes from each phase are parallel to the sample surface: Al_2O_3 {*hh*·0}, Fe_2O_3 {*hh*·0} and Au {*hhh*}. No evidence was found of the magnetite or ε-Fe_2O_3 phases. Usable texture data were not able to be collected due to the small size of the sample.

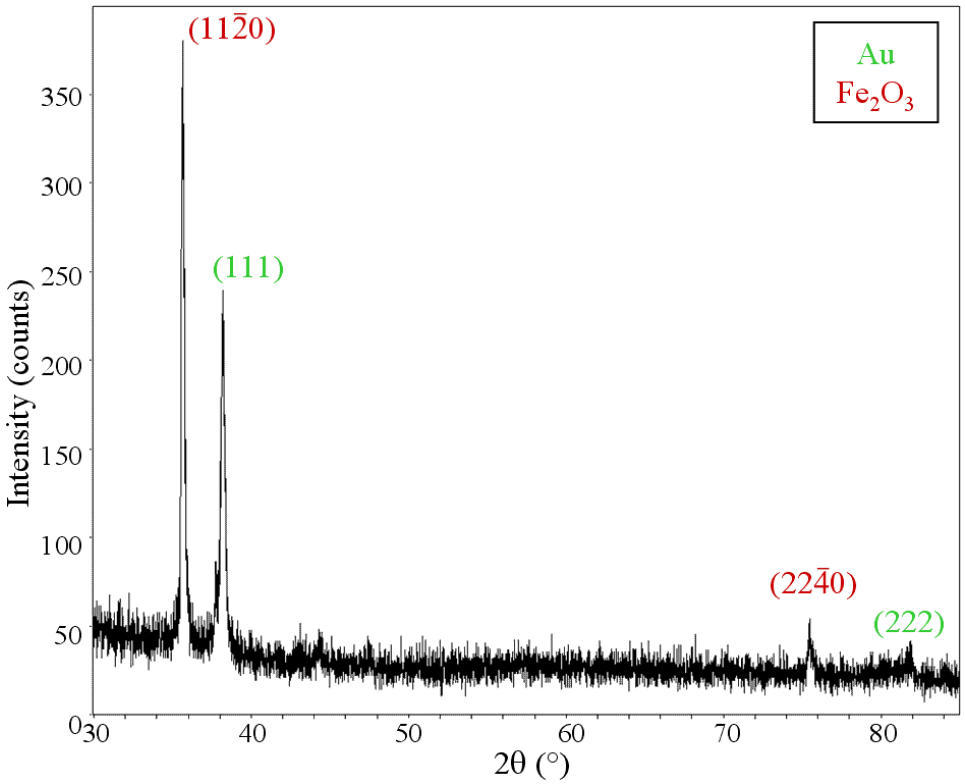

Figure 3.26 Offset XRD scan of Au-catalyzed Fe_xO_y nanowires grown on an *a*-plane sapphire substrate.

Hematite and alumina have the same structure with the same space group ($R\bar{3}c$) and similar lattice parameters. Therefore, it is understandable that they have the same orientation with the {11$\bar{2}$0} planes parallel to the sample surface. The lattice mismatch between these planes is also small, less than 6%. The gold phase takes the same

crystallographic orientation on both the *a*-plane and *c*-plane sapphire substrates, suggesting that the orientation of gold may be governed more by the surface energy of the nanoparticles, than by lattice match with the substrate.

3.4.3 Crystallite Size and Microstrain Analysis

The average crystallite size and microstrain were determined for the gold particles catalyzing Fe_xO_y nanostructures on *c*-plane sapphire with the Warren-Averbach method, as discussed in 2.2.2.2.3. The size and strain were calculated from the Au {111} and {222} peaks, with LaB_6 peaks correcting for instrumental broadening. The average crystallite size was determined to be 25.5 ± 0.2 nm, and the root-mean-square microstrain to be 0.161 ± 0.004%. For the sample on *a*-plane sapphire, the gold peaks were partially obscured by substrate peaks, preventing Warren-Averbach analysis. However the average crystallite size was calculated using the Scherrer equation to be 52 ± 5 nm. These results confirm that the gold is nanocrystalline.

3.4.4 Gold Lattice Parameter Analysis

3.4.4.1 Lattice Parameter Determination

The gold lattice parameter was determined by X-ray diffraction. Data were collected on three samples, two on *c*-plane oriented substrates and one on an *a*-plane oriented sapphire substrate. Four to ten θ/2θ and/or ω-offset scans of Au {*hhh*} peaks were collected on each sample, and the results averaged. The lattice parameters for each sample are not statistically significantly different (i.e. within 3σ) from each other. The average lattice parameter is 4.0787 ± 0.0016 Å, which is equal to the bulk value of 4.0786 Å (PDF #4-784). A control sample was synthesized by heating at gold-coated *c*-

plane sapphire substrate under the same conditions as those used for the nanowire synthesis, omitting only the laser-ablated source. The lattice parameter of the control sample was determined to be 4.0763 ± 0.0015 Å, which is statistically the same as both the bulk value and the results from the nanowire samples.

3.4.4.2 Discussion of Gold Lattice Parameter

As discussed in section 3.2.3.4 above, the diffusion of a solute, such as Fe, into a solvent, such as the gold catalyst particles, will change the lattice parameter. A Vegard's law relationship for Au-Fe alloys cannot be established directly from the end members, since gold and iron have different crystal structures (FCC and BCC, respectively). However, a Vegard's law plot can be constructed for the Au-rich region using literature reports of Au-Fe alloys, as seen in Figure 3.27. The Vegard's law plot was constructed using lattice parameters from the control sample along with two literature reports. The $Au_{0.5}Fe_{0.5}$ phase, which was generated using alternate monatomic multilayer deposition, has the $L1_0$ structure, which is similar to FCC, with alternating Au and Fe layers and a slight tetrahedral distortion [103]. The lattice parameters were averaged to obtain an equivalent FCC lattice parameter. The $Au_{0.7}Fe_{0.3}$ and $Au_{0.8}Fe_{0.2}$ phases, which were synthesized by spin-quenching from the melt, are simple FCC alloys [104].

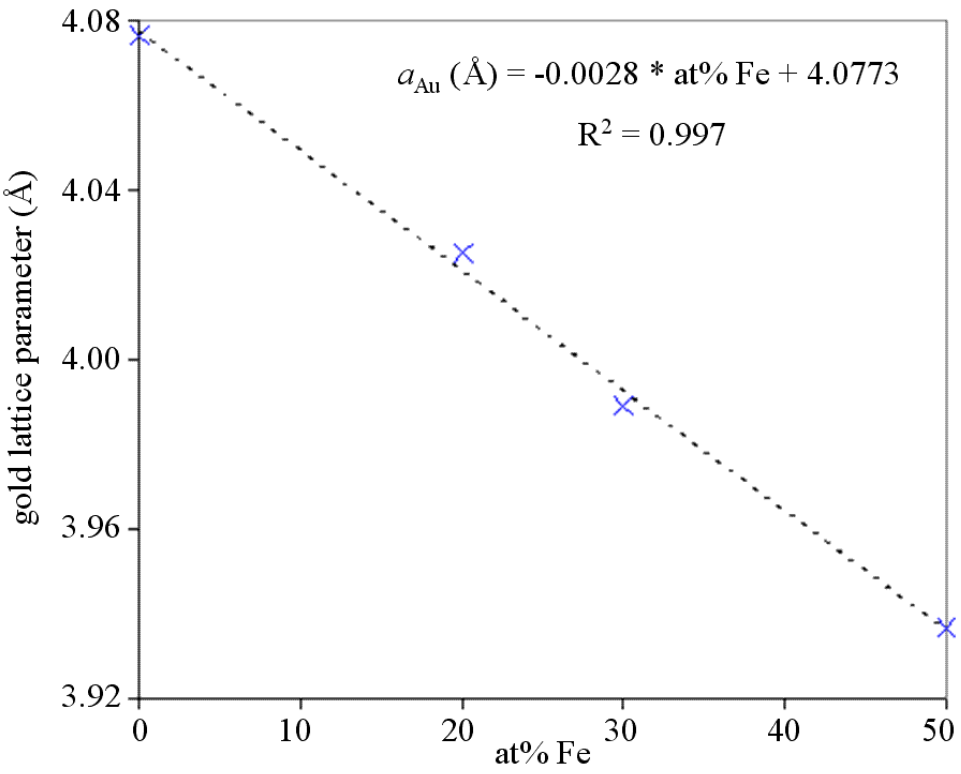

Figure 3.27 Vegard's law relationship for Au-Fe alloys, constructed using data from [103] and [104].

It can be observed that alloying of Fe into Au should cause a significant decrease of the gold lattice parameter. The absence of a decrease in the gold lattice parameter suggests that there is no Fe in the gold after growth. The expected contraction is significant at as little as 1.2at% Fe, where the lattice parameter is 4.0739 Å (c.f. the experimentally measure lattice parameter of 4.0787 ± 0.0016 Å).

3.4.5 Implications for Growth Model

3.4.5.1 Catalyst Particle State

The above results have significant implications for the proposed growth model, similar to the results from Au-catalyzed ZnO nanorods discussed in section 3.2.4 above.

As can be seen from the Au-Fe phase diagram [105] seen in Figure 3.28, the eutectic temperature (1036°C) is not much less than the melting temperature of pure gold. The growth temperature of the Au-catalyzed Fe_xO_y nanorods (800-900°) was well below even the Au-Fe eutectic temperature. Additionally, melting point depression due to nanoparticle size is insufficient to cause melting for the size of nanoparticles in these samples (~100 nm) at the growth temperature, as may be seen in Figure 3.12. Therefore, the catalyst particles must be solid during growth, regardless of whether or not Fe is diffusing into the gold catalyst particles.

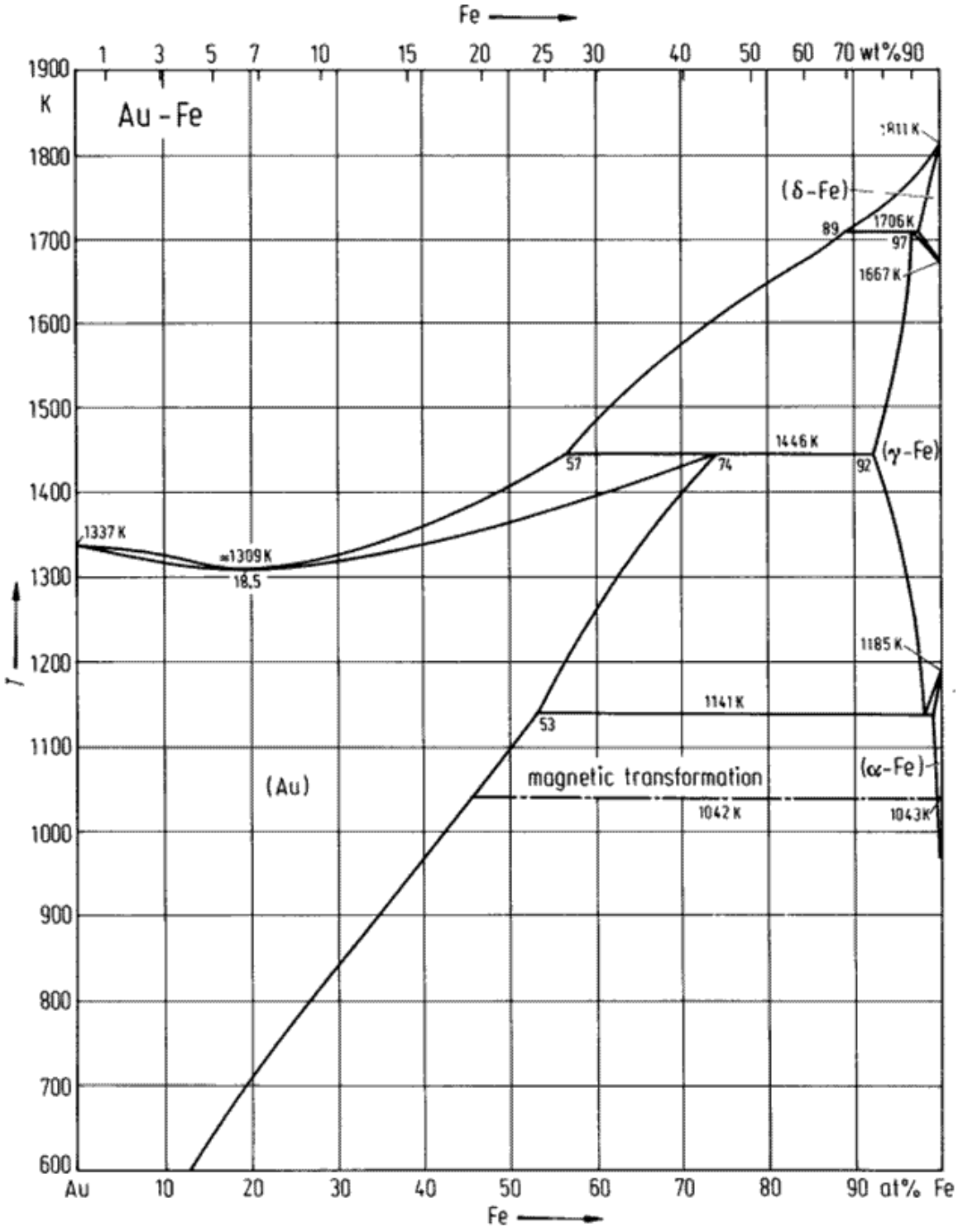

Figure 3.28 Au-Fe phase diagram [105]. With kind permission of Springer Science+Business Media.

3.4.5.2 Diffusion Path

The absence of Fe in the gold catalyst particles has significant implications concerning the diffusion path of the Fe to the growth front. Looking again at the phase diagram in Figure 3.28, there is significant solid solubility of Fe in Au at the growth temperature, around 45 to 50 at%. If Fe were dissolved in the gold to the point of supersaturation during growth, as in the conventional understanding of the VLS mechanism, a significant amount of Fe should be left in the gold after growth. However, no evidence of Fe in the gold was found after growth, suggesting that no Fe was in the gold during growth. If no Fe is present in the gold, the Fe must not be diffusing through the bulk of the catalyst particle, and is more likely to be diffusing around the surface, which is indeed a faster diffusion pathway, as discussed in section 3.2.4.2 above.

3.5 References

1. Borchers, C., S. Müller, D. Stichtenoth, D. Schwen, and C. Ronning, *Catalyst-Nanostructrue Interaction in the Growth of 1-D ZnO Nanostructures.* Journal of Physical Chemistry B, 2006. **110**: p. 1656-1660.

2. Chen, Y.X., M. Lewis, and W.L. Zhou, *ZnO nanostructure fabricated through a double-tube vapor-phase transport synthesis.* Journal of Crystal Growth, 2005. **282**: p. 85-93.

3. Fan, H.J., B. Fuhrmann, R. Scholz, F. Syrowatka, A. Dadgar, A. Krost, and M. Zacharias, *Well-ordered ZnO nanowire arrays on GaN substrate fabricated via nanosphere lithography.* Journal of Crystal Growth, 2006. **287**(1): p. 34-38.

4. Hejazi, S.R. and H.R. Hosseini, *A Diffusion-Controlled Kinetic Model for Growth of Au-Catalyzed ZnO Nanorods: Theory and Experiment.* Journal of Crystal Growth, 2007. **309**: p. 70-75.

5. Li, Y.J., M. Feneberg, A. Reiser, M. Schirra, R. Enchelmaier, A. Ladenburger, A. Langlois, R. Sauer, K. Thonke, J. Cai, and H. Rauscher, *Au-catalyzed growth processes and luminescence properties of ZnO nanopillars on Si.* Journal of Applied Physics, 2006. **99**(5): p. 054307.

6. Philipose, U., S.V. Nair, S. Trudel, C.F.d. Souza, S. Aouba, R.H. Hill, and H.E. Ruda, *High-temperature ferromagnetism in Mn-doped ZnO nanowires.* Applied Physics Letters, 2006. **88**: p. 263101.

7. Tseng, Y.-K., I.-N. Lin, K.-S. Liu, T.-S. Lin, and I.-C. Chen, *Low-temperature growth of ZnO nanowires.* Journal of Materials Research, 2003. **18**(3): p. 714-718.

8. Wang, X.D., C.J. Summers, and Z.L. Wang, *Large-scale hexagonal-patterned growth of aligned ZnO nanorods for nano-optoelectronics and nanosensor arrays.* Nano Letters, 2004. **4**(3): p. 423-426.

9. Wang, X.D., J.H. Song, P. Li, J.H. Ryou, R.D. Dupuis, C.J. Summers, and Z.L. Wang, *Growth of uniformly aligned ZnO nanowire heterojunction arrays on GaN, AIN, and Al0.5Ga0.5N substrates.* Journal of the American Chemical Society, 2005. **127**(21): p. 7920-7923.

10. Wang, X.D., J.H. Song, C.J. Summers, J.H. Ryou, P. Li, R.D. Dupuis, and Z.L. Wang, *Density-controlled growth of aligned ZnO nanowires sharing a common contact: A simple, low-cost, and mask-free technique for large-scale applications.* Journal of Physical Chemistry B, 2006. **110**(15): p. 7720-7724.

11. Yang, P., H. Yan, S. Mao, R. Russo, J. Johnson, R. Saykally, N. Morris, J. Pham, R. He, and H.-J. Choi, *Controlled Growth of ZnO Nanowires and Their Optical Properties.* Advanced Functional Materials, 2002. **12**(5): p. 323-331.

12. He, J.H., J.H. Hsu, C.W. Wang, H.N. Lin, L.J. Chen, and Z.L. Wang, *Pattern and feature designed growth of ZnO nanowire arrays for vertical devices.* Journal of Physical Chemistry B, 2006. **110**(1): p. 50-53.

13. Hejazi, S.R., H.R.M. Hosseini, and M.S. Ghamsari, *The Role of Reactants and Droplet Interfaces on Nucleation and Growth of ZnO Nanorods Synthesized by Vapor-Liquid-Solid (VLS) Mechanism.* Journal of Alloys and Compounds, 2008. **455**: p. 353-357.

14. Mai, W., P. Gao, C. Lao, Z.L. Wang, A.K. Sood, D.L. Polla, and M.B. Soprano, *Vertically Aligned ZnO Nanowire Arrays on GaN and SiC Substrates.* Chemical Physics Letters, 2008. **460**: p. 253-256.

15. Huang, M.H., Y. Wu, H. Feick, N. Tran, E. Weber, and P. Yang, *Catalytic Growth of Zinc Oxide Nanowires by Vapor Transport.* Advanced Materials, 2001. **13**(2): p. 113-116.

16. Zhu, Z., T.-L. Chen, Y. Gu, J. Warren, and R.M. Osgood, Jr., *Zinc Oxide Nanowires Grown by Vapor-Phase Transport Using Selected Metal Catalysts: A Comparative Study.* Chemistry of Materials, 2005. **17**: p. 4227-4234.

17. Kong, X., X. Sun, X. Li, and Y. Li, *Catalytic growth of ZnO nanotubes.* Materials Chemistry and Physics, 2003. **82**: p. 997-1001.

18. Kirkham, M., X. Wang, Z.L. Wang, and R.L. Snyder, *Solid Au nanoparticles as a catalyst for growing aligned ZnO nanowires: a new understanding of the VLS process.* Nanotechnology, 2007. **18**: p. 365304.

19. Iwanga, H., N. Shibata, M. Hirose, and K. Suzuki, *Growth Mechanism of ZnO Ribbon Crystals from ZnS.* Journal of Crystal Growth, 1976. **35**: p. 159-164.

20. Gao, P.X., Y. Ding, and I.L. Wang, *Crystallographic orientation-aligned ZnO nanorods grown by a tin catalyst.* Nano Letters, 2003. **3**(9): p. 1315-1320.

21. Gao, P.X. and Z.L. Wang, *Substrate atomic-termination-induced anisotropic growth of ZnO nanowires/nanorods by the VLS process.* Journal of Physical Chemistry B, 2004. **108**(23): p. 7534-7537.

22. Yang, R.S. and Z.L. Wang, *Growth of Self-Assembled ZnO Nanowire Arrays.* Philosophical Magazine, 2006. **87**(14-15): p. 2097-2104.

23. Ding, Y., P.X. Gao, and Z.L. Wang, *Catalyst-Nanostructure Interfacial Lattice Mismatch in Determining the Shape of VLS Grown Nanowires and Nanobelts: A*

Case of Sn/ZnO. Journal of the American Chemical Society, 2004. **126**: p. 2066-2072.

24. Zhuang, H., D. Wang, J. Shen, C. Xue, X. Zhang, and H. Liu, *Fabrication and Characterization of Novel Bicrystalline ZnO Nanowires.* Journal of Materials Research, 2009. **24**(8): p. 2536-2540.

25. Wang, Y.W., L.D. Zhang, G.Z. Wang, X.S. Peng, Z.Q. Chu, and C.H. Liang, *Catalytic growth of semiconducting zinc oxide nanowires and their photoluminescence properties.* Journal of Crystal Growth, 2002. **234**: p. 171-175.

26. Wang, X., Q. Li, Z. Liu, J. Zhang, Z. Liu, and R. Wang, *Low-temperature growth and properties of ZnO nanowires.* Applied Physics Letters, 2004. **84**(24): p. 4941-4943.

27. Liu, X., C. Li, S. Han, J. Han, and C. Zhou, *Synthesis and electronic transport studies of CdO nanoneedles.* Applied Physics Letters, 2003. **82**(12): p. 1950-1952.

28. Kuo, T.-J. and M.H. Huang, *Gold-Catalyzed Low-Temperature Growth of Cadmium Oxide Nanowires by Vapor Transport.* Journal of Physical Chemistry B, 2006. **110**: p. 13717-13721.

29. Koparanova, N., Z. Zlatev, D. Genchev, and G. Popovich, *Cadmium oxide whisker crystals grown by the vapour-liquid-solid mechanism using various elements as growth initiators.* Journal of Materials Science, 1994. **29**: p. 103-109.

30. Kalyanikutty, K.P., F.L. Deepak, C. Edem, A. Govindaraj, and C.N.R. Rao, *Carbon-Assisted Synthesis of Nanowires and Related Nanostructures of MgO.* Materials Research Bulletin, 2005. **40**: p. 831-839.

31. Kar, S. and S. Chaudhuri, *Synthesis and Characterization of One-Dimensional MgO Nanostructures.* Journal of Nanoscience and Nanotechnology, 2006. **6**: p. 1447-1452.

32. Yanagida, T., K. Nagashima, H. Tanaka, and T. Kawai, *Mechanism of critical catalyst size effect on MgO nanowire growth by pulsed laser deposition.* Journal of Applied Physics, 2008. **104**: p. 016101.

33. Kim, G., R.L. Martens, G.B. Thompson, B.C. Kim, and A. Gupta, *Selective Area Synthesis of Magnesium Oxide Nanowires.* Journal of Applied Physics, 2007. **102**: p. 104906.

34. Han, S., C. Li, Z. Liu, B. Lei, D. Zhang, W. Jin, X. Liu, T. Tang, and C. Zhou, *Transition Metal Oxide Core-Shell Nanowires: Generic Synthesis and Transport Studies.* Nano Letters, 2004. **4**(7): p. 1241-1246.

35. Nagashima, K., T. Yanagida, H. Tanaka, and T. Kawai, *Control of Magnesium Oxide Nanowire Morphologies by Ambient Temperature.* Applied Physics Letters, 2007. **90**: p. 233103.

36. Yanagida, T., K. Nagashima, H. Tanaka, and T. Kawai, *Mechanism of catalyst diffusion on magnesium oxide nanowire growth.* Applied Physics Letters, 2007. **91**: p. 061502.

37. Zhan, J., Y. Bando, J. Hu, and D. Goldberg, *Bulk Synthesis of Single-Crystalline Magnesium Oxide Nanotubes.* Inorganic Chemistry, 2004. **43**: p. 2462-2464.

38. Kim, H.W., S.H. Shim, and J.W. Lee, *Sn-catalyzed growth of MgO nanowires.* Journal of Nanoscience and Nanotechnology, 2007. **7**(12): p. 4434-4438.

39. Johnson, M.C., S. Aloni, D.E. McCready, and E.D. Bourret-Courchesne, *Controlled Vapor-Liquid-Solid Growth of Indium, Gallium, and Tin Oxide Nanowires via Chemical Vapor Transport.* Crystal Growth & Design, 2006. **6**(8): p. 1936-1941.

40. Li, C., D. Zhang, S. Han, X. Liu, T. Tang, and C. Zhou, *Diameter-Controlled Growth of Single-Crystalline In_2O_3 Nanowires and Their Electronic Properties.* Advanced Materials, 2003. **15**(2): p. 143-146.

41. Zhang, J., X. Qing, F. Jiang, and Z. Dai, *A route to Ag-catalyzed growth of the semiconducting In_2O_3 nanowires.* Chemical Physics Letters, 2003. **371**(3): p. 311-316.

42. Park, S., H. Kim, C. Lee, D.H. Lee, and S.S. Hong, *Synthesis of Very Straight Bismuth Oxide Nanowires by Using Thermal Evaporation of Bismuth Powders.* Journal of the Korean Physical Society, 2008. **53**(4): p. 1965-1970.

43. Choi, Y.J., S.Y. Moon, J.H. Park, J.G. Park, and S. Nahm, *Synthesis of gallium oxide nanostructures and their structural properties.* Journal of the Korean Physical Society, 2006. **49**(3): p. 1152-1155.

44. Chang, K.-W. and J.-J. Wu, *Catalytic growth and characterization of Ga_2O_3 nanowires.* Applied Physics A, 2003. **76**: p. 629-631.

45. Chang, K.W. and J.J. Wu, *One-dimensional β-Ga_2O_3 nanostructures on sapphire (0001): Low-temperature epitaxial nanowires and high-temperature nanorod bundles.* Journal of Materials Research, 2005. **20**(12): p. 3397-3403.

46. Zhang, J., F. Jiang, Y. Yang, and J. Li, *Catalyst-Assisted Vapor-Liquid-Solid Growth of Single-Crystal Ga_2O_3 Nanobelts.* Journal of Physical Chemistry B, 2005. **109**: p. 13143-13147.

47. Nguyen, P., H.T. Ng, and M. Meyyappan, *Catalyst Metal Selection for Synthesis of Inorganic Nanowires.* Advanced Materials, 2005. **17**: p. 1773-1777.

48. Nguyen, P., H.T. Ng, J. Kong, A.M. Cassell, R. Quinn, J. Li, J. Han, M. McNeil, and M. Meyyappan, *Epitaxial Directional Growth of Indium-Doped Tin Oxide Nanowire Arrays.* Nano Letters, 2003. **3**(7): p. 925-928.

49. Liu, Z., D. Zhang, S. Han, C. Li, T. Tang, W. Jin, X. Liu, B. Lei, and C. Zhou, *Laser Ablation Synthesis and Electron Transport Studies of Tin Oxide Nanowires.* Advanced Materials, 2003. **15**(20): p. 1754-1757.

50. He, J.H., T.H. Wu, C.L. Hsin, K.M. Li, L.J. Chen, Y.L. Chueh, L.J. Chou, and Z.L. Wang, *Beaklike SnO_2 Nanorods with Strong Photoluminescent and Field-Emission Properties.* Small, 2006. **2**(1): p. 116-120.

51. Yu, D.P., Q.L. Hang, Y. Ding, H.Z. Zhang, Z.G. Bai, J.J. Wang, Y.H. Zou, W. Qian, G.C. Xiong, and S.Q. Feng, *Amorphous silica nanowires: Intensive blue light emitters.* Applied Physics Letters, 1998. **73**(21): p. 3076-3078.

52. Morber, J.R., Y. Ding, M.S. Haluska, Y. Li, J.P. Liu, Z.L. Wang, and R.L. Snyder, *PLD-Assisted VLS Growth of Aligned Ferrite Nanorods, Nanowires, and Nanobelts-Synthesis, and Properties.* Journal of Physical Chemistry B, 2006. **110**(43): p. 21672-21679.

53. Shen, G., P.-C. Chen, K. Ryu, and C. Zhou, *Devices and Chemical Sensing Applications of Metal Oxide Nanowires.* Journal of Materials Chemistry, 2009. **19**: p. 828-839.

54. Cheng, Y., P. Xiong, C.S. Yun, G.F. Strouse, J.P. Zheng, R.S. Yang, and Z.L. Wang, *Mechanism and Optimization of pH Sensing Using SnO_2 Nanobelt Field Effect Transistors.* Nano Letters, 2008. **8**(12): p. 4179-4184.

55. Fields, L.L., J.P. Zheng, Y. Cheng, and P. Xiong, *Room-Temperature Low-Power Hydrogen Sensor Based on a Single Tin Dioxide Nanobelt.* Applied Physics Letters, 2006. **88**: p. 263102.

56. Sysoev, V.V., B.K. Button, K. Wepsiec, S. Dmitriev, and A. Kolmakov, *Toward the Nanoscopic "Electronic Nose": Hydrogran vs Carbon Monoxide Discrimination with an Array of Individual Metal Oxide Nano- and Mesowire Sensors.* Nano Letters, 2006. **6**(8): p. 1584-1588.

57. Kuang, Q., C. Lao, Z.L. Wang, Z. Xie, and L. Zheng, *High-Sensitivity Humidity Sensor Based on Single SnO_2 Nanowire.* Journal of the American Chemical Society, 2007. **129**: p. 6070-6071.

58. Park, J.-H., G. von Maltzahn, L. Zhang, M.P. Schwartz, E. Ruoslahti, S.N. Bhatia, and M.J. Sailor, *Magnetic Iron Oxide Nanoworms for Tumor Targeting and Imaging.* Advanced Materials, 2008. **20**: p. 1630-1635.

59. Yang, P. and C.M. Lieber, *Nanorod-Superconductor Composities: A Pathway to Materials with High Critical Current Densities.* Science, 1996. **273**: p. 1836-1840.

60. Yang, P. and C.M. Lieber, *Nanostructured high-temperature superconductors: Creation of strong-pinning columnar defects in nanorod/superconductor composites.* Journal of Materials Research, 1997. **12**: p. 2981-2996.

61. Wang, Z.L. and J.H. Song, *Piezoelectric nanogenerators based on zinc oxide nanowire arrays.* Science, 2006. **312**(5771): p. 242-246.

62. Gao, P.X., J. Song, J. Liu, and Z.L. Wang, *Nanowire Piezoelectric Nanogenerators on Plastic Substrates as Flexible Power Sources for Nanodevices.* Advanced Materials, 2006. **19**(1): p. 67-72.

63. Qin, Y., X. Wang, and Z.L. Wang, *Microfibre-nanowire hybrid structure for energy scavenging.* Nature, 2008. **451**: p. 809-813.

64. Wang, X., J. Song, J. Liu, and Z.L. Wang, *Direct-Current Nanogenerator Driven by Ultrasonic Waves.* Science, 2007. **316**: p. 102-105.

65. Wang, X., J. Liu, J. Song, and Z.L. Wang, *Integrated Nanogenerators in Bio-Fluid.* Nano Letters, 2007. **7**(8): p. 2475-2479.

66. Yang, R., Y. Qin, C. Li, G. Zhu, and Z.L. Wang, *Converting Biomechanical Energy into Electricity by a Muscle-Movement-Driven Nanogenerator.* Nano Letters, 2009. **9**(3): p. 1201-1205.

67. Wang, X., J. Zhou, J. Song, J. Liu, N. Xu, and Z.L. Wang, *Piezoelectric-Field Effect Transistor and Nano-Force-Sensor Based on a Single ZnO Nanowire.* Nano Letters, 2006. **6**(12): p. 2768-2772.

68. Zhou, J., C.S. Lao, P. Gao, W. Mai, W.L. Hughes, S.Z. Deng, N.S. Xu, and Z.L. Wang, *Nanowire as pico-gram balance at workplace atmosphere.* Solid State Communiations, 2006. **139**: p. 222-226.

69. Galoppini, E., J. Rochford, H. Chen, G. Saraf, Y. Lu, A. Hagfeldt, and G. Boschloo, *Fast Electron Transport in Metal Organic Vapor Deposition Grown Dye-Sensitized ZnO Nanorod Solar Cells.* Journal of Physical Chemistry B Letters, 2006. **110**: p. 16159-16161.

70. Xu, C., X. Wang, and Z.L. Wang, *Nanowire Structure Hybrid Cell for Concurrently Scavenging Solar and Mechanical Energies.* Journal of the American Chemical Society, 2009. **131**(16): p. 5866-5872.

71. He, J.H., S.T. Ho, T.B. Wu, L.J. Chen, and Z.L. Wang, *Electrical and photoelectrical performances of nano-photodiode based on ZnO nanowires.* Chemical Physics Letters, 2006. **435**: p. 119-122.

72. Hsu, C.L., S.J. Chang, Y.R. Lin, P.C. Li, T.S. Lin, S.Y. Tsai, T.H. Lu, and I.C. Chen, *Ultraviolet Photodetectors with Low Temperature Synthesized Vertical ZnO Nanowires.* Chemical Physics Letters, 2005. **416**(1-3): p. 75-78.

73. Lao, C., M.-C. Park, Q. Kuang, Y. Deng, A.K. Sood, D.L. Polla, and Z.L. Wang, *Giant Enhancement in UV Response of ZnO Nanobelts by Polymer Surface-Functionalization.* Journal of the American Chemical Society, 2007. **129**: p. 12096-12097.

74. Huang, M.H., S. Mao, H. Feick, H.Q. Yan, Y.Y. Wu, H. Kind, E. Weber, R. Russo, and P.D. Yang, *Room-Temperature Ultraviolet Nanowire Nanolasers.* Science, 2001. **292**(5523): p. 1897-1899.

75. Yang, H.Y., S.P. Lau, S.F. Yu, A.P. Abiyasa, M. Tanemura, T. Okita, and H. Hatano, *High-Temperature Random Lasing in ZnO Nanoneedles.* Applied Physics Letters, 2006. **89**: p. 011103.

76. Bao, J., M.A. Zimmler, F. Capasso, X. Wang, and Z.F. Ren, *Broadband ZnO Single-Nanowire Light-Emitting Diode.* Nano Letters, 2006. **6**(8): p. 1719-1722.

77. Sun, J.C., J.Z. Zhao, H.W. Liang, J.M. Bian, L.Z. Hu, H.Q. Zhang, X.P. Liang, W.F. Liu, and G.T. Du, *Realization of Ultraviolet Electroluminescence from ZnO Homojunction with n-ZnO/p-ZnO:As/GaAS Structure.* Applied Physics Letters, 2007. **90**: p. 121128.

78. Zhang, X.-M., M.-Y. Lu, Y. Zhang, L.-J. Chem, and Z.L. Wang, *Fabrication of a High-Brightness Blue Light Emission Diode Fabricated Using ZnO Nanowires Array Grown on p-GaN Thin Film.* Advanced Materials, 2008. **21**: p. 1-4.

79. Campos, L.C., M. Tonezzer, A.S. Ferlauto, V. Grillo, R. Magalhes-Paniago, S. Oliveria, L.O. Ladeira, and R.G. Lacerda, *Vapor-Solid-Solid Growth Mechanism Driven by Epitaxial Match between Solid AuZn Alloy Catalyst Particles and ZnO Nanowires at Low Temperatures.* Advanced Materials, 2008. **20**: p. 1499-1504.

80. Cullity, B.D. and S.R. Stock, *Elements of X-Ray Diffraction*. 3rd ed. 2001, New Jersey: Prentice Hall. p. 664.

81. Qi, W.H. and M.P. Wang, *Size and Shape Dependent Lattice Parameters of Metallic Nanoparticles.* Journal of Nanoparticle Research, 2005. **7**(1): p. 51-57.

82. Vegard, L., *Die Konstitution der Mischkristalle und die Raumfüllung der Atome.* Zeitschrift für Physik, 1921. **5**: p. 17-26.

83. Fewster, P.F., *X-ray Scattering from Semiconductors*. 2nd ed. 2003, London: Imperial College Press. p. 299.

84. Iwasaki, H., *Study on the Ordered Phases with Long Period in the Gold-Zinc Alloy System II. Structure Analysis of $Au_3Zn[R_1]$, $Au_3Zn[R_2]$ and $Au_{3+}Zn$.* Journal of the Physical Society of Japan, 1962. **17**(10): p. 1620-33.

85. Liu, H.S., K. Ishida, Z.P. Jin, and Y. Du, *Thermodynamic assessment of the Au-Zn binary system.* Intermetallics, 2003. **11**(10): p. 987-994.

86. Buffat, P. and J.P. Borel, *Size Effect on the Melting Temperature of Gold Particles.* Physical Review A, 1976. **13**(6): p. 2287-2298.

87. Depero, L.E., E. Bontempi, L. Sangaletti, and S. Pagliara, *Melting of nanostructured Sn probed by in-situ x-ray diffraction.* Journal of Chemical Physics, 2003. **118**(3): p. 1400-1403.

88. Guisbiers, G. and S. Pereira, *Theoretical investigation of size and shape effects on the melting temperature of ZnO nanostructures.* Nanotechnology, 2007. **18**: p. 435710.

89. Jiang, H., K.-s. Moon, H. Dong, F. Hua, and C.P. Wong, *Size-dependent melting properties of tin nanoparticles.* Chemical Physics Letters, 2006. **429**: p. 492-496.

90. Lai, S.L., J.Y. Guo, V. Petrova, G. Ramanath, and L.H. Allen, *Size-Dependent Melting Properties of Small Tin Particles: Nanocalorimetric Measurements.* Physical Review Letters, 1996. **77**(1): p. 99-102.

91. Kofman, R., P. Cheyssac, Y. Lereah, and A. Stella, *Melting of clusters approaching 0D.* European Physical Journal D, 1999. **9**: p. 441-444.

92. Qi, W.H., *Size Effect on Melting Temperature of Nanosolids.* Physica B, 2005. **368**: p. 46-50.

93. Makarow, A.V., S.G. Zbezhneva, V.V. Kovalenko, and M.N. Rumyantseva, *Mass Spectrometric Study of Nanocrystalline ZnO Vaporization.* Inorganic Materials, 2003. **39**(6): p. 594-598.

94. Wang, H. and G.S. Fischman, *Role of liquid droplet surface diffusion in the vapor-liquid-solid whisker growth mechanism.* Journal of Applied Physics, 1994. **76**(3): p. 1557-1562.

95. Cheyssac, P., M. Sacilotti, and G. Patriarche, *Vapor-liquid-solid mechanisms: Challenges for nanosized quantum cluster/dot/wire materials.* Journal of Applied Physics, 2006. **100**: p. 044315.

96. Beszeda, I., I.A. Szabó, and E.G. Gontier-Moya, *Morphological evolution of thin gold films studied by Auger electron spectroscopy in beading conditions.* Applied Physics A, 2004. **78**: p. 1079-1084.

97. Ajayan, P.M. and T.J. Marks, *Experimental Evidence for Quasimelting in Small Particles.* Physical Review Letters, 1989. **63**(3): p. 279-282.

98. Krakow, W., M. Jóse-Yacamán, and J.L. Aragón, *Observation of quasimelting at the atomic level in Au nanoclusters.* Physical Review B, 1994. **49**(15): p. 591-596.

99. Frenken, J.W.M., J.P. Toennies, and C. Wöll, *Self-Diffusion at a Melting Surface Observed by He Scattering.* Physical Review Letters, 1988. **60**(17): p. 1727-1730.

100. Lee, J.A. and G.V. Raynor, *The Lattice Spacings of Binary Tin-Rich Alloys.* Proceedings of the Physical Society B, 1954. **67**: p. 737-747.

101. Lee, B.-J., *Thermodynamic Assessments of the Sn-Zn and In-Zn Binary Systems.* Calphad, 1996. **20**(4): p. 471-480.

102. Ding, Y., J.R. Morber, R.L. Snyder, and Z.L. Wang, *Nanowire structural evolution from Fe_3O_4 to epsilon-Fe_2O_3.* Advanced Functional Materials, 2007. **17**(7): p. 1172-1178.

103. Mitani, S., K. Takanashi, H. Nakajima, K. Sato, R. Schreiber, P. Grnberg, and H. Fujimori, *Structural and magnetic properties of Fe/noble metal monatomic multilayers equivalent to $L1_0$ ordered alloys.* Journal of Magnetism and Magnetic Materials, 1996. **156**: p. 7-10.

104. Bosco, E., S. Enzo, and M. Baricco, *X-ray analysis of microstructure in Au-Fe melt spun alloys.* Journal of Magnetism and Magnetic Materials, 2003. **262**: p. 136-141.

105. Predel, B., *Au-Fe (Gold-Iron)*, in *Landolt-Börnstein - Group IV Physical Chemistry*, O. Madelung, Editor. 1991, Springer-Verlag. p. 1-5.

CHAPTER 4

ELEMENTAL NANOSTRUCTURES

4.1 Introduction

The category of elemental 1D nanostructures encompasses some of the most well studied types of nanostructures. For example, carbon nanotubes (CNTs) have been extensively studied since they were first described in 1991 [1] by Iijima, using arc-discharge. CNTs are also often grown from the decomposition of a carbon-containing gas, such as methane (CH_4), over a metal catalyst, typically nickel or iron, in a manner similar to the VLS and VSS mechanisms [2-11]. Also, single-component metal nanowires have been grown, typically using a template method, where the metal is deposited in a mesoporous material [12, 13].

This research focuses on the growth of silicon nanowires. Silicon nanowires have been studied since the early 1990s [14-16], when synthesis was typically by a top-down approach involving reactive ion etching. Bottom-up approaches to Si nanowire growth were also developed, generally involving the decomposition and/or deposition of a Si-containing source material on the surface of a metal catalyst. Early research on silicon whiskers (i.e. high aspect ratio crystals in the micron range) often used silicon tetrachloride ($SiCl_4$) as the source material [17-23]. In 1997, Westwater et al. [24] found that silicon nanowire synthesis could be better controlled, and thinner nanowires could be obtained, when using silane (SiH_4) as the silicon source, which has since become the standard method for synthesizing silicon nanowires [25-38]. A similar technique decomposes germane (GeH4) on catalysts to synthesize germanium nanowires [39-44].

Additionally, silicon nanowires have been synthesized without catalysts using an oxide-assisted growth (OAG) mechanism [45-51].

Though most initial research focused on silicon nanowire synthesis, progress has been made on potential applications of silicon nanowires. Silicon nanowires have been used for electrical sensing in bio-systems [52], including neurons [53] and hearts [54]. Silicon nanowires perform better than traditional materials in anodes for lithium ion batteries, having a higher charge capacity [55-58]. Silicon nanowires have also found application in solar cells, both as absorber and as an anti-reflective coating [59-62]. Basic logic and memory elements including silicon nanowires have been demonstrated [63, 64], presaging applications in nano-electronics.

This research focused on gold-catalyzed silicon nanowires. First the synthesis parameters and methods will be presented, along with electron microscopy analysis of the nanowire morphologies. Results from several control samples will be included. Next, X-ray characterization results of the silicon nanowires will be presented, including *in-situ* XRD, size/strain analysis and lattice parameter analysis. Finally, this chapter will discuss the implications of these findings towards the growth model of the catalyzed growth of nanostructures.

4.2 Growth of Nanostructures

4.2.1 Synthesis Parameters

Gold-catalyzed silicon nanowires were grown in an X-ray furnace in order that *in-situ* X-ray diffraction data could be collected during growth, as detailed in section 2.1.3.4 above. The nanowires were grown in the HTK1200 oven-type furnace. The substrates, oxidized single-crystal Si (100) sputtered with five to ten nanometers of gold,

where placed in the center of the furnace. Base pressures prior to heating were around 10^{-3} to 10^{-2} mbar. Oxygen contamination was found to be a significant factor in nanowire growth, and therefore the residual oxygen was further reduced by purging the chamber with N_2 and by holding the furnace at the growth temperature for one hour prior to starting growth. The growth temperature ranged from 503 to 777°C, with 685°C being the most common. The source gas, a mixture of 1% silane (SiH_4) in nitrogen was flowed for anywhere from ten minutes to one hour, with 30 min being the most common. The growth pressure was 1 to 10 mbar, with 3 mbar being the most common. Finally, the furnace was cooled under vacuum.

4.2.2 Electron Microscopy Analysis

4.2.2.1 Morphology

The samples were imaged with scanning electron microscopy as shown in Figure 4.1. The density of nanowire growth is high, with the nanowires forming a tangled layer. Measuring the nanowire lengths is difficult, due to the tangled nature of the growth. However, the lengths appear to be on the order of several microns or greater. The nanowires have diameters of 21 ± 7 nm. The aspect ratio of the nanowires is on the order of 100. The total thickness of the nanowire layer is on the order of 10 μm, as seen in Figure 4.2.

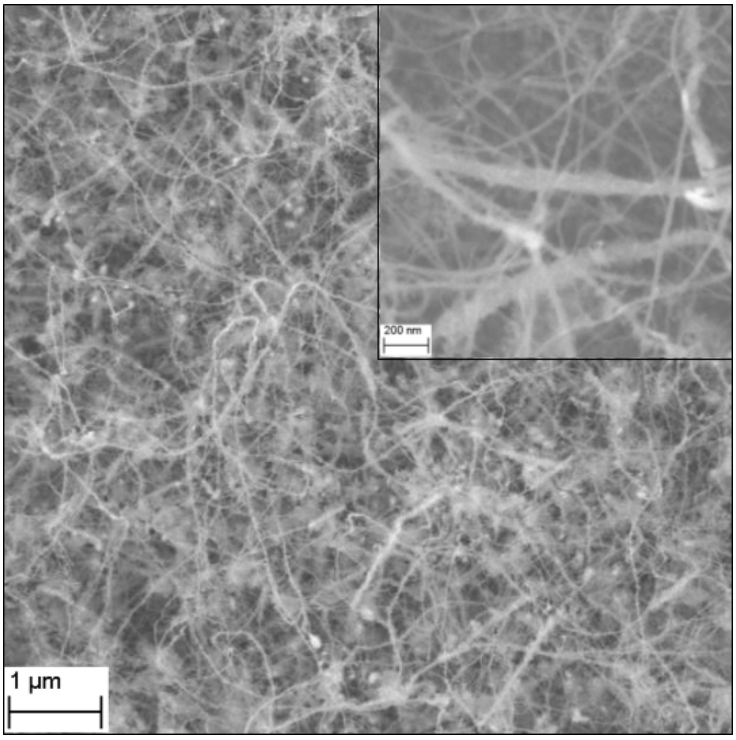

Figure 4.1 SEM images of the typical tangled nanowire growth morphology. The inset is at a higher magnification.

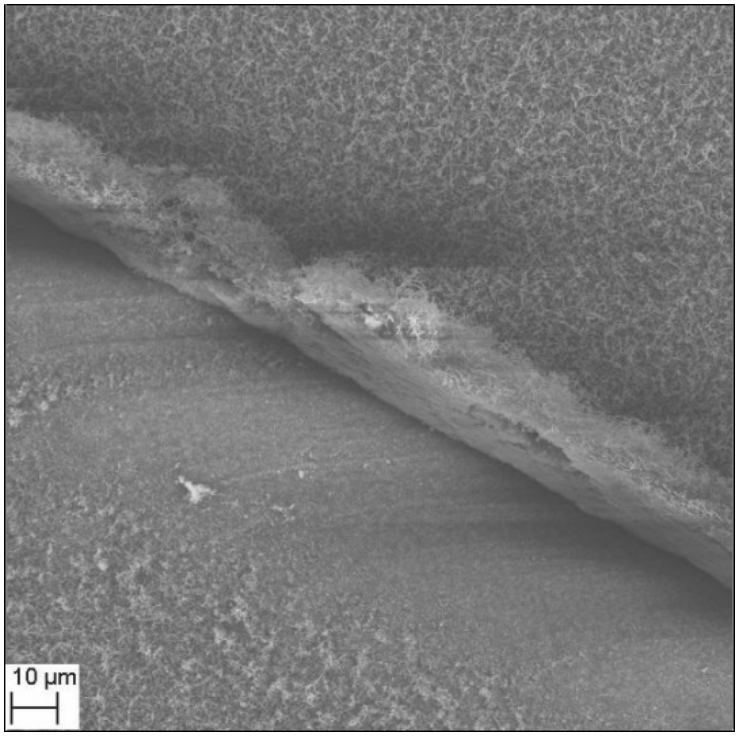

Figure 4.2 SEM image showing the thickness of the nanowire layer to be around 10µm.

In some samples, thicker nanowires were observed, with diameters on the order of 100 nm, as seen in Figure 4.3. While the thinner nanowires generally have smooth sides, these thicker nanowires have rough surfaces, which may be due to partial oxidation of thinner nanowires by residual oxygen in the furnace, as these rough nanowires were more often observed when the base oxygen partial pressure was higher. Indeed, TEM imaging reveals a thin, smooth nanowire at the core of some of the thick, rough nanowires, as seen in Figure 4.3a. However, in many cases smooth and rough nanowires were observed in the same area of the same sample, as seen in Figure 4.1.

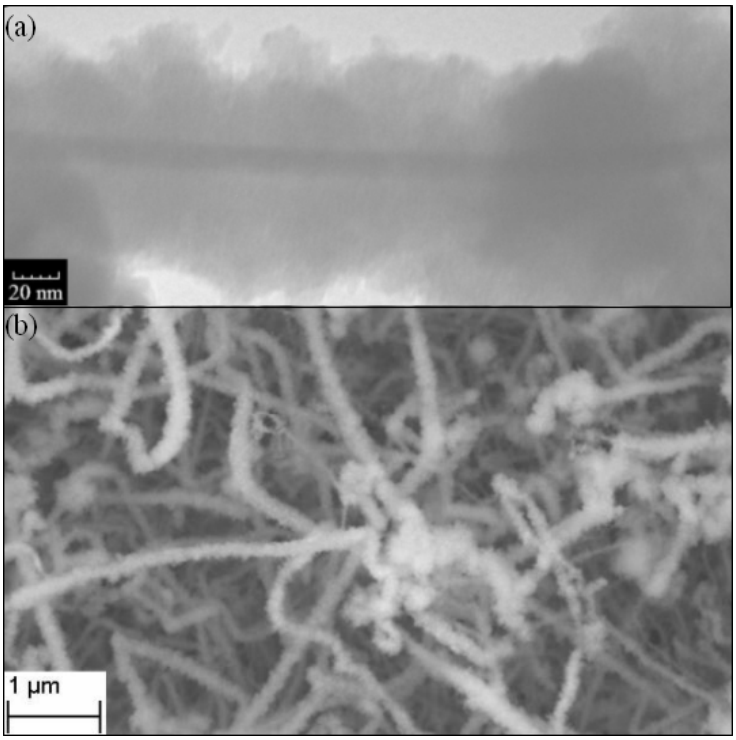

Figure 4.3 (a) TEM and (b) SEM images of thick, rough nanowires, showing thin core.

Closer examination with TEM reveals catalyst particles at the tips of the nanowires, as seen in Figure 4.4. The catalyst particles are roughly hemispherical in shape, with diameters around 20 nm. The catalyst particles and nanowires are covered

with a layer, around 2 nm thick, which is likely amorphous silica. EDS spectra confirm the presence of Au in the catalyst particles, and its absence in the nanowires, as seen in Figure 4.5. The Cu and C peaks are from the TEM grid and film. The O peak may come jointly from impurities in the C grid and from amorphous silica.

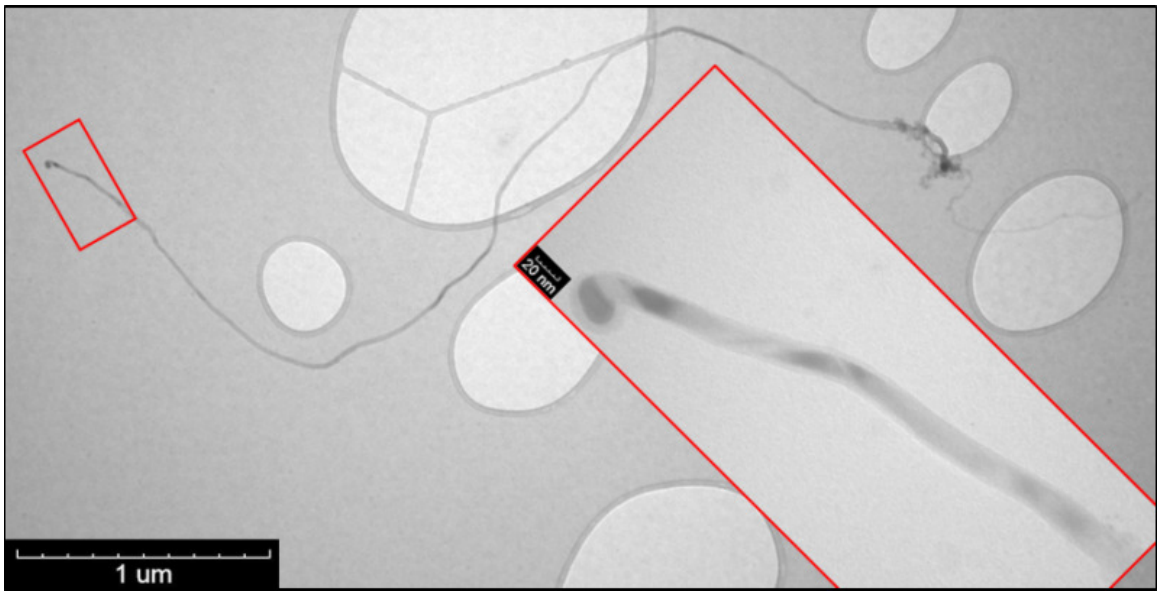

Figure 4.4 TEM images of nanowire. Inset from area in red box, showing catalyst particle and covering layer.

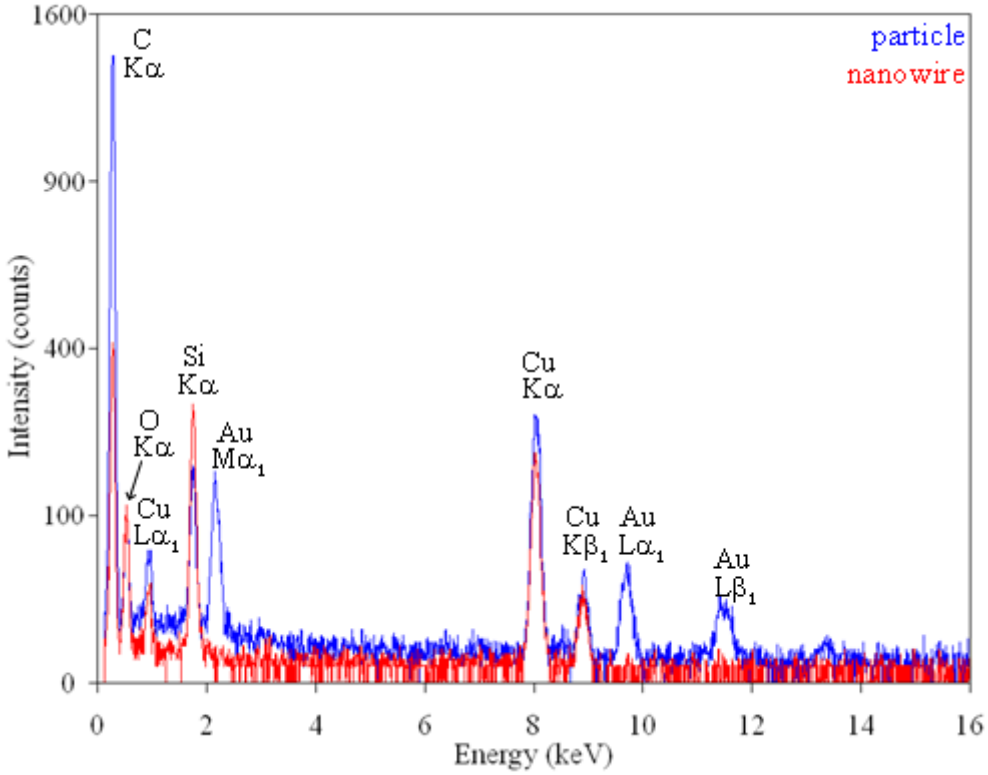

Figure 4.5 EDS spectra collected in TEM from catalyst particle (in blue) and nanowire (in red).

The nanowires are thinnest at the tips, around 15 nm, and thickest at the base, around 25 nm, suggesting two possibilities. One possibility is that a small, but non-negligible, amount of lateral growth occurs on the sides of the nanowires by a vapor-solid (VS) process. The presence of lateral growth will lead the base, which has had a longer time to grow than the tip, to being thicker [29, 39, 66]. The other possibility is that the catalyst particles have decreased in diameter with time, due to diffusion of the catalyst away from the tip. As the diameter of the nanowire is determined by the diameter of the catalyst particle, the decreasing catalyst particle size leads to tapered nanowires [30, 36, 37, 67]. The bases of the nanowires have rough surfaces, as do some isolated sections around 100 nm in length in the middle of the nanowire. These sections may have been in

greater contact with the oxidized substrate, causing the nanowire in those sections to become more oxidized than other sections.

4.2.2.2 Growth Direction and Twinning

The nanowires were further characterized with high-resolution transmission electron microscopy (HRTEM). The nanowires are crystalline, with a growth direction of (111), as seen in Figure 4.6a. The average lattice spacing is around 3.5 Å, as determined by a fast Fourier transformation (FFT) of a broad line scan perpendicular to the lattice planes. This value is consistent with the calculated (111) lattice spacing of 3.1355 Å, when considering the difficultly in calibrating HRTEM distances. Some areas were not fully crystalline, as seen in Figure 4.6b, likely due to partial oxidation of the silicon nanowires to amorphous silica. Also visible is an amorphous coating on the nanowires with a thickness around 2 to 3 nm, as previously observed.

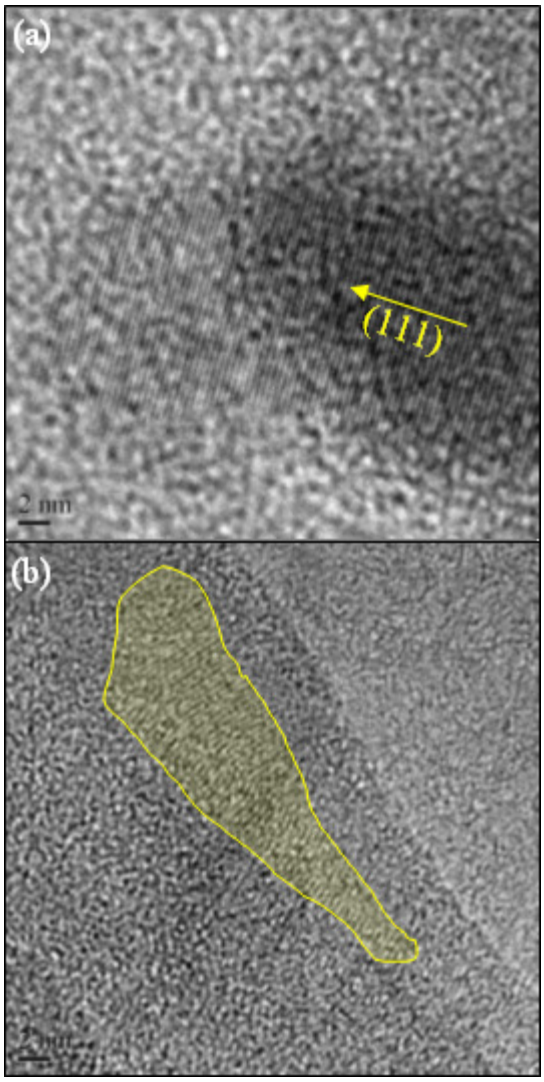

Figure 4.6 HRTEM images of silicon nanowire, showing (a) (111) growth direction and (b) partially crystalline nanowire, with the crystalline areas outlined in yellow.

HRTEM images collected from some curved areas of the nanowires show crystal defects, as seen in Figure 4.7, namely twins and stacking faults. The twin planes are parallel to each other and make an angle of approximately 70º with the (111) crystal planes. This indicates that the twin planes are {111}, as the calculated angle between equivalent {111} planes is 70.5º. The observed crystal defects may be what allows the nanowires to remain crystalline while they are strongly curved. Indeed, (111) deformation twins have been reported in materials with the diamond cubic crystal structure [68]. Also, (111) twin planes have been reported in silicon nanocrystals formed by ion implantation [69].

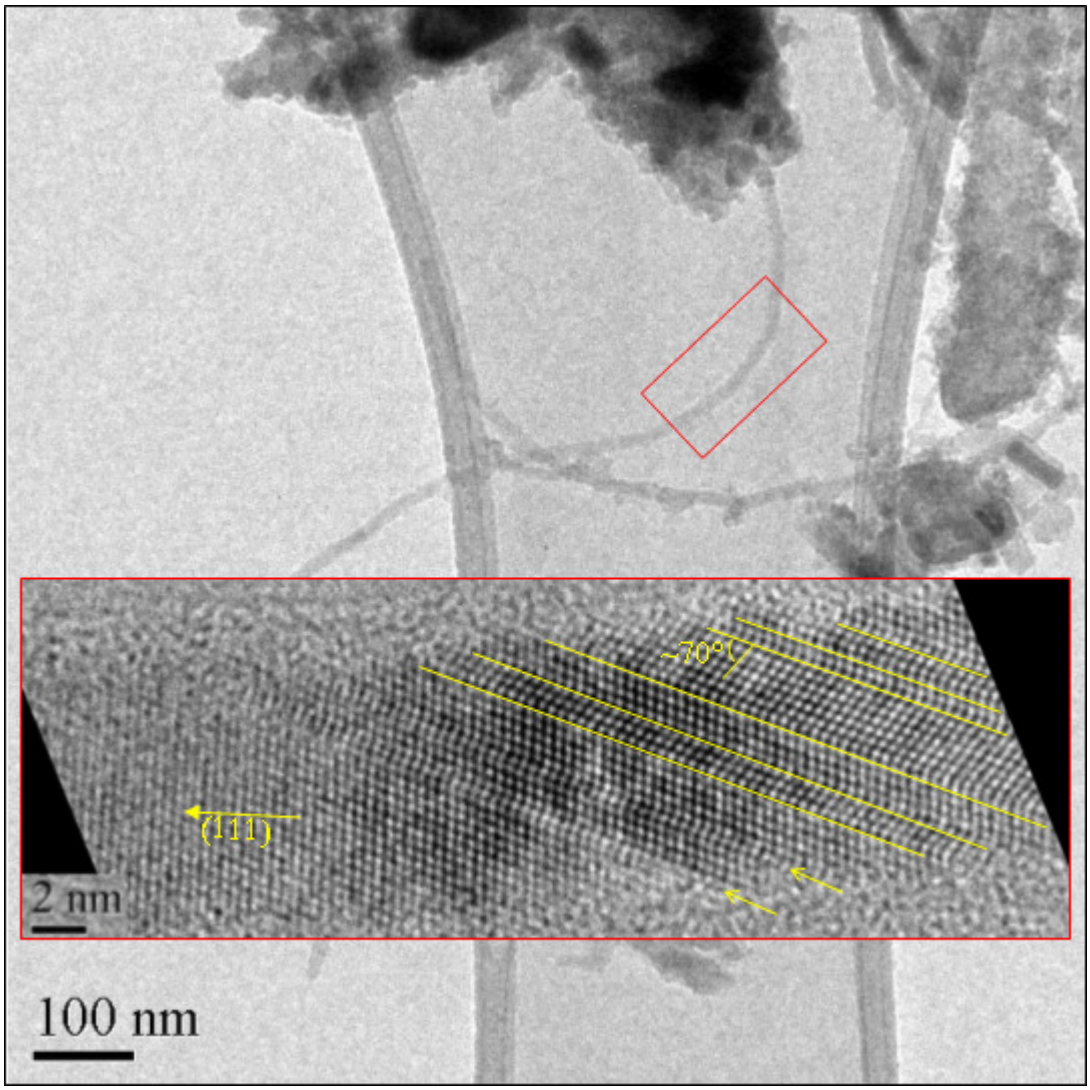

Figure 4.7 HRTEM image of bent section of nanowire, showing twin planes (yellow lines) and stacking faults (marked with arrows). The inset image is from the area marked with a red box.

4.2.3 Control Samples

In order to further investigate the synthesis process, several control samples were synthesized, keeping the same synthesis conditions, but changing one key factor in each control. For one sample, no gold was deposited on the substrate. Without the gold, no nanowires grew, as seen in Figure 4.8a, though some rough deposition, presumably silicon, was observed on the substrate. Other substrates with gold deposited in only some areas grew nanowires only in the areas with gold. The lack of nanowires indicates that the gold is necessary to catalyze the growth of nanowires.

For another control sample, the substrates were coated with gold, but the N_2/silane mixture source gas was replaced with pure N_2 gas. Again, no nanowires grew, as seen in Figure 4.8b, indicating that the silane is necessary for growth, and suggesting that the silicon substrate does not contribute to the process. The gold formed nanoparticles with diameters of 76 ± 41 nm. The gold lattice parameter was determined to be 4.0785 ± 0.0006 Å, which is within 1σ of the bulk value (4.0786 Å, PDF#4-1-2616). There is no evidence of lattice contraction due to the particle size. The gold lattice parameter of the control sample will be used for comparison to the gold lattice parameter from silicon nanowire samples in section 4.3.2 below.

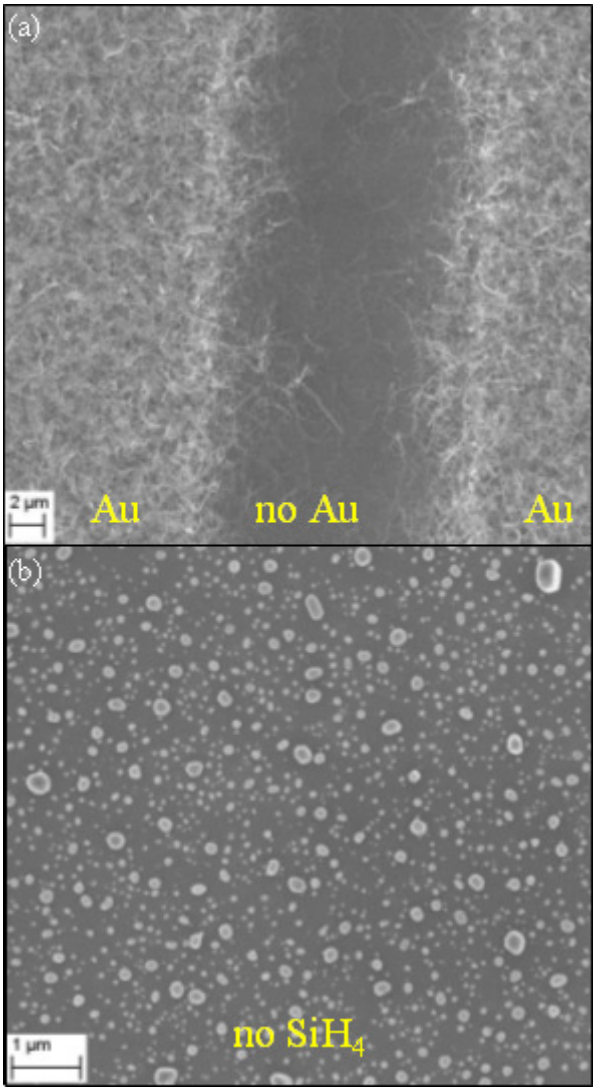

Figure 4.8 SEM images of control samples with (a) areas with no gold and (b) no silane.

To further investigate the substrate effect, two samples were synthesized on different substrates, an MgO (100) single crystal, glass and a Si (100) substrate that had been etched with a dilute HF solution in order to remove the surface oxide. All the control substrates were sputtered with gold in the same way as the standard substrates. Nanowires grew on all three types of substrates, as can be seen in Figure 4.9, confirming that a particular crystallographic orientation and lattice match with the substrate is not necessary for growth.

The nanowire morphology observed on the HF-etched Si (100) substrate was fundamentally the same as that observed on non-etched Si (100) substrates. However, some differences were observed on the MgO and glass substrates. On the MgO substrates, the nanowires were curlier and had a wide distribution of diameters, around 30 to 200 nm. On the glass substrate, the nanowires were similar to those on standard substrates, but were only found in a few scattered areas. These results indicate that the substrate does have an effect on the morphology, as evidenced by the sample grown on an MgO substrate in particular. Chemical interaction between MgO and either gold or silane is unlikely at these conditions. The observed difference in morphology may be due to lattice mismatch between the substrate and gold nanoparticle.

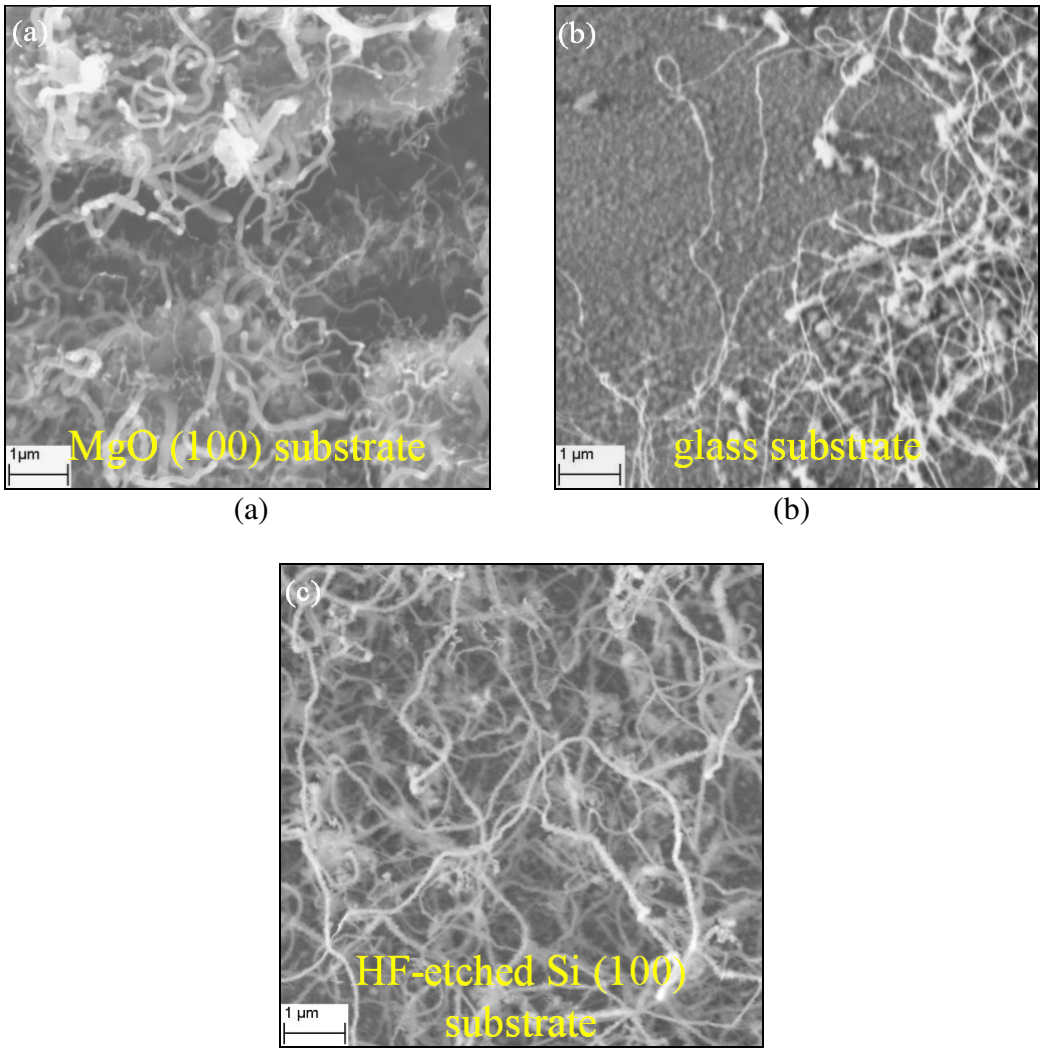

Figure 4.9 SEM images of nanowires synthesized on three different substrates: (a) MgO (100), (b) glass and (c) HF-etched Si (100).

4.3 X-Ray Analysis

4.3.1 *In-Situ* X-Ray Diffraction

In-situ XRD data were collected during the growth of the silicon nanowires. An incident-side Göbel mirror generated a parallel beam. The diffracted beam was detected by a linear position sensitive detector, for faster scans. This optic combination was found to give the highest intensity. However, this combination left the XRD data vulnerable to sample surface displacement error. This error is particularly egregious in *in-situ* X-ray diffraction, because thermal expansion of the furnace and sample can cause significant height changes. Therefore, accurate lattice parameter results could not be determined from the *in-situ* data. However, useful phase transition data could still be determined.

4.3.1.1 Gold Catalyst Particle State

The *in-situ* XRD data for a typical sample are shown in Figure 4.10. In the initial heating stage, the gold (111) peak increases in intensity and narrows. This is indicative of the as-sputtered gold increasing in crystallinity as it is annealed, and forming (111)-oriented nanoparticles. During the one-hour hold at the growth temperature before the introduction of silane, there is little change in the X-ray scans. Once the silane flow starts, the gold peaks immediately and quickly begin to disappear, indicating that the gold nanoparticles are losing their crystal structure. The gold peaks reappear after cooling to room temperature, as they resolidify from the molten state. After growth, the gold signal is that of a randomly oriented polycrystalline material. As the gold is now at the tips of the nanowires, it no longer preserves an epitaxial relationship with the substrate. For samples where nanowires did not grow, the gold did not melt, almost without exception.

Out of 27 samples synthesized, only one did not follow the standard relationship between gold melting and nanowire growth.

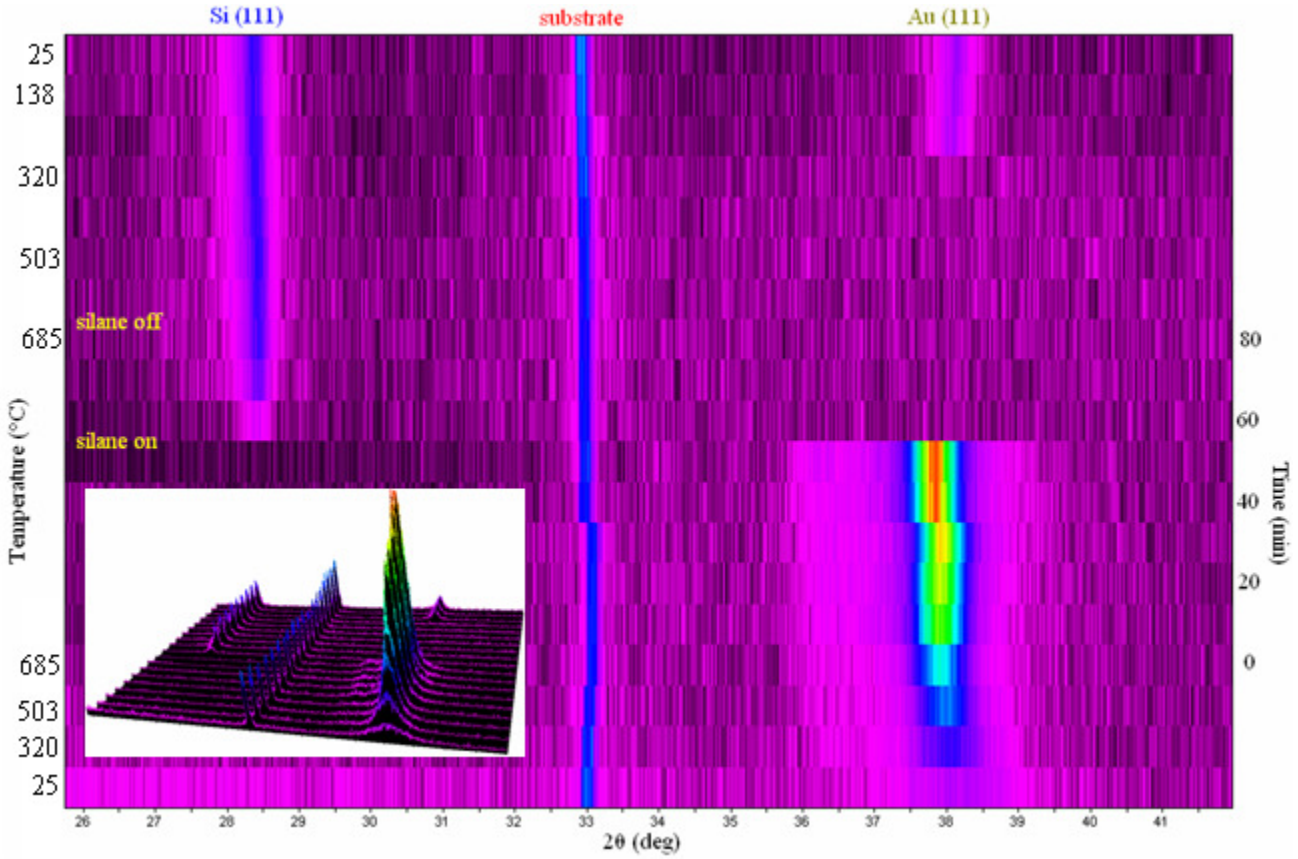

Figure 4.10 *In-situ* XRD data from the growth of Au-catalyzed Si nanowires. Each horizontal line is one XRD scan, with the intensity represented by the color. The first scan is at the bottom, and time progresses upward. The inset shows the same data in a 3D view.

4.3.1.2 Oxygen Effect

For some samples, the gold peaks decreased in intensity after the silane addition, but did not completely disappear, indicating that the gold did not melt completely. The degree to which the gold melted is shown as a function of the base oxygen partial pressure in Figure 4.11. The degree of melting is quantified by normalizing the percentage reduction in the gold (111) peak area, as fitted by Jade, with the length of time of silane exposure. The base oxygen partial pressure is estimated based on the total base pressure and amount of N_2 purging, if any. Outside a few outliers, the degree of gold melting increases as the residual oxygen decreases. Oxygen will react with silane to form SiO_2 and H_2. Residual oxygen in the furnace may react with the silane, leaving less silane to interact with the gold catalyst particles.

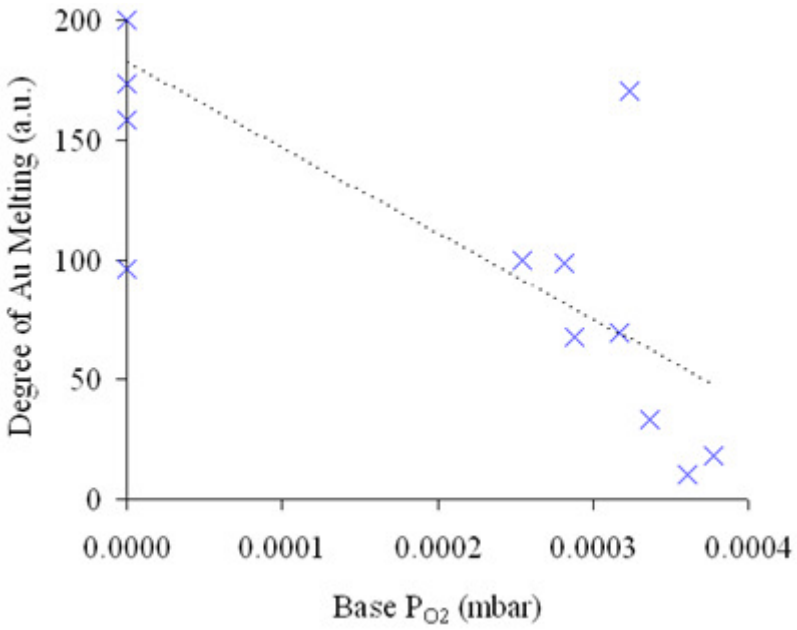

Figure 4.11 Degree of Au melting as a function of base oxygen partial pressure. The degree of Au melting is calculated from difference between the integrated intensities of the Au (111) peaks before and after the introduction of silane, normalized for the total time of silane exposure.

4.3.1.3 Gold Recrystallization Temperature

For several samples, *in-situ* XRD data were also collected during cooling after growth, in order to investigate the gold recrystallization temperature. As seen in Figure 4.12, the gold peaks do not reappear until the scan at 284ºC. This is significantly below the gold eutectic temperature of ~364ºC [70]. The eutectic temperature may be lowered for the Au nanoparticles due to the Gibbs-Thompson effect, as has been previously reported during the growth of Ge nanowires [44]. The Gibbs-Thompson effect relates the radius of curvature of a particle, and consequently the diameter, to the vapor pressure and further to other properties, including the melting temperature.

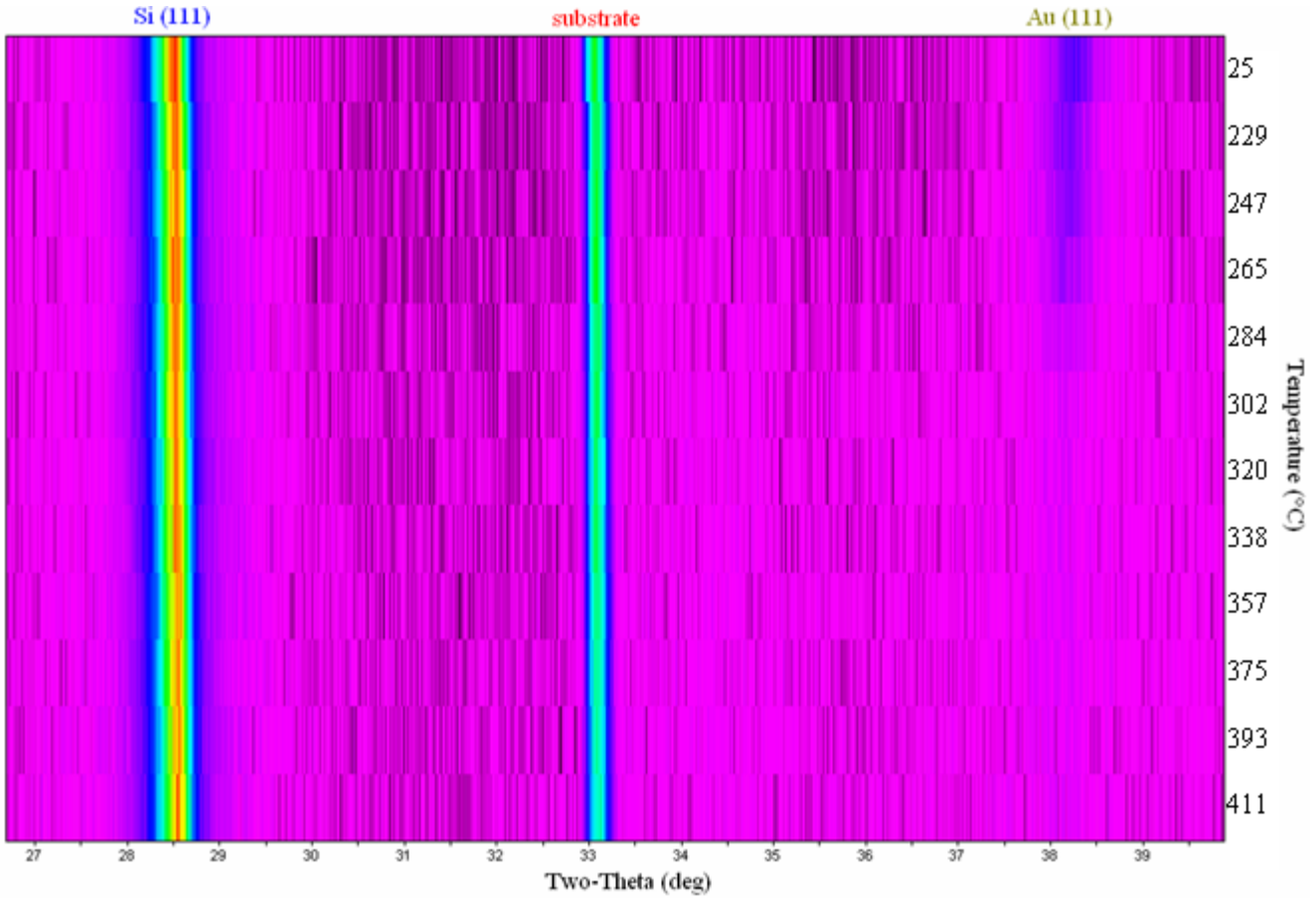

Figure 4.12 *In-situ* XRD data collected during cooling from growth temperature, showing gold recrystallization.

4.3.2 Post-Growth X-Ray Diffraction

After synthesis in the X-ray furnace, the silicon nanowire samples were further characterized using X-ray diffraction. The XRD data were collected on the MRD optimized for accurate lattice parameter determination, being outfitted with the Göbel mirror, 0.09º parallel plate collimator and 0.04 rad Soller slits. Since the nanowires are not aligned, as can be clearly seen in Figure 4.1 above, the grazing incidence technique could be employed to increase the signal from the nanowires. Additionally, as the substrate is single crystal, it will not appear in GIXRD scans, allowing the signal from the nanowires to be clearly distinguished. Signals from both the gold catalyst particles and silicon nanowires are present, as seen in Figure 4.13. No other phases, including any silica phases, are observed.

Since many peaks from each phase may be observed, Pawley whole pattern fitting may be applied to the scans. For this sample, the patterns were fitted using a second-order polynomial background curve and a pseudo-Voight peak shape function. 2θ zero and sample surface displacement errors were not refined, as they were aligned before measurement and eliminated through the use of parallel beam optics, respectively. At least three GIXRD scans were collected from each of three samples, and the results averaged.

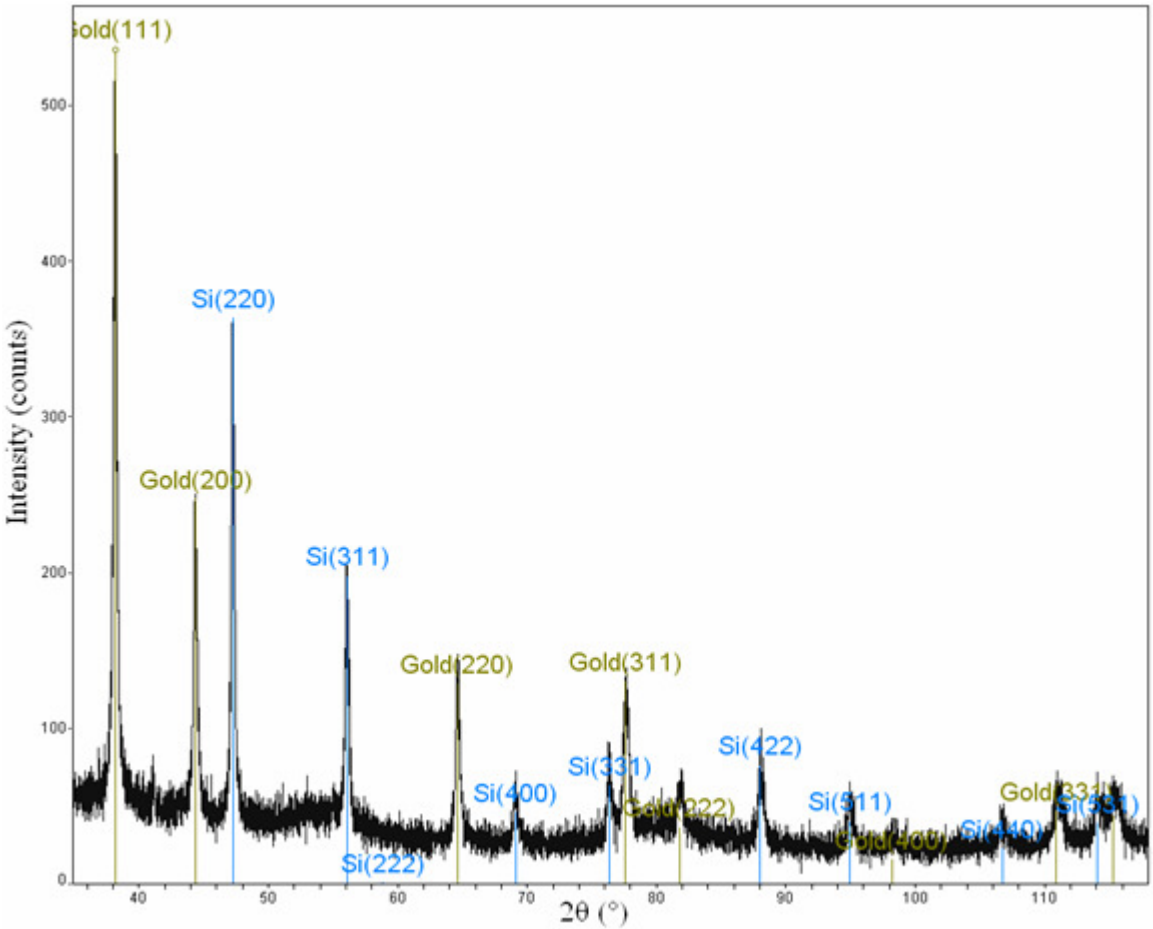

Figure 4.13 GIXRD scan of Au-catalyzed Si nanowires.

For the gold phase, the lattice parameter averaged over the three samples was determined to be 4.0731 ± 0.0025 Å. This value is statistically the same (i.e. within 3σ) as that measured from a control sample never exposed to SiH_4 (4.0785 ± 0.0006 Å), as discussed in section 4.2.3 above. However, there were small but significant differences between the three samples. The lattice parameters determined from the first two samples (4.0727 ± 0.0006 Å and 4.0711 ± 0.0002 Å) are statistically the same, but they are smaller than the lattice parameters determined from the third sample (4.0760 ± 0.0003 Å) and from the control sample. The first two samples did have a slightly different synthesis procedure. The chamber was not purged with N_2; consequently the base oxygen partial

pressure was higher, and the gold only partially melted during synthesis. The third sample, which was under the best conditions, has a lattice parameter within 3σ of the control value. It is unclear why these differences in the synthesis would have resulted in differences in the gold lattice parameter. However, the average lattice parameter from all three samples was statistically the same as that of the control sample, which indicates that there is no significant amount of Si dissolved into the Au. This follows from the same Vegard's law principle discussed further in section 4.4.1 below and in section 3.2.3.4 above for Au-catalyzed ZnO nanorods.

4.4 Implications for the Growth Model

4.4.1 Absence of Silicon in Gold Catalyst Particles

The finding that the gold lattice parameter from a sample of silicon nanowires is the same as the gold lattice parameter from a sample that was not exposed to silane and grew no nanowires indicates that no silicon is dissolved in the gold at room temperature after growth. A Vegard's law relationship for Au and silicon cannot be established directly from the end members, since gold and silicon have different crystal structures (FCC and diamond cubic, respectively). Additionally, there is a dearth of crystallographic studies of Au-Si alloys in the literature, from which a Vegard's law plot for the Au-rich region could be constructed. Pure gold and pure silicon phases easily segregate [71]; therefore most studies are of rapidly quenched alloys or thin film depositions. The intermetallics phases studied include hexagonal, orthorhombic and primitive and body-centered cubic structures [72, 73].

There are, however, two reported Au-Si intermetallics with FCC-based supercells, which may be used for a Vegard's law plot construction. The first, around 15mol% Si,

has a cubic unit cell, with lattice parameter of 7.844 Å, composed of eight FCC units, with an FCC equivalent lattice parameter of half the unit cell length (3.922 Å, PDF#26-723 [74]). The second, around 35mol% Si, has a cubic unit cell, with lattice parameter of 19.503 Å, composed of 125 FCC units, with an FCC equivalent lattice parameter of one-fifth the unit cell length (3.9006 Å, PDF#26-724 [74]). A more recent study of the second phase, at a composition of 33mol%Si, places the supercell lattice parameter at 19.6 Å and the FCC equivalent lattice parameter at 3.92 Å [71], using HRTEM.

The Vegard's law plot constructed from these data points, as well as the control sample, is seen in Figure 4.14. The fit is poor, but it can be observed that alloying of Si into Au should cause a significant decrease of the gold lattice parameter. As no significant decrease was seen in the gold lattice parameter from the sample Si nanowires, it may be concluded that there is no Si in the Au after growth.

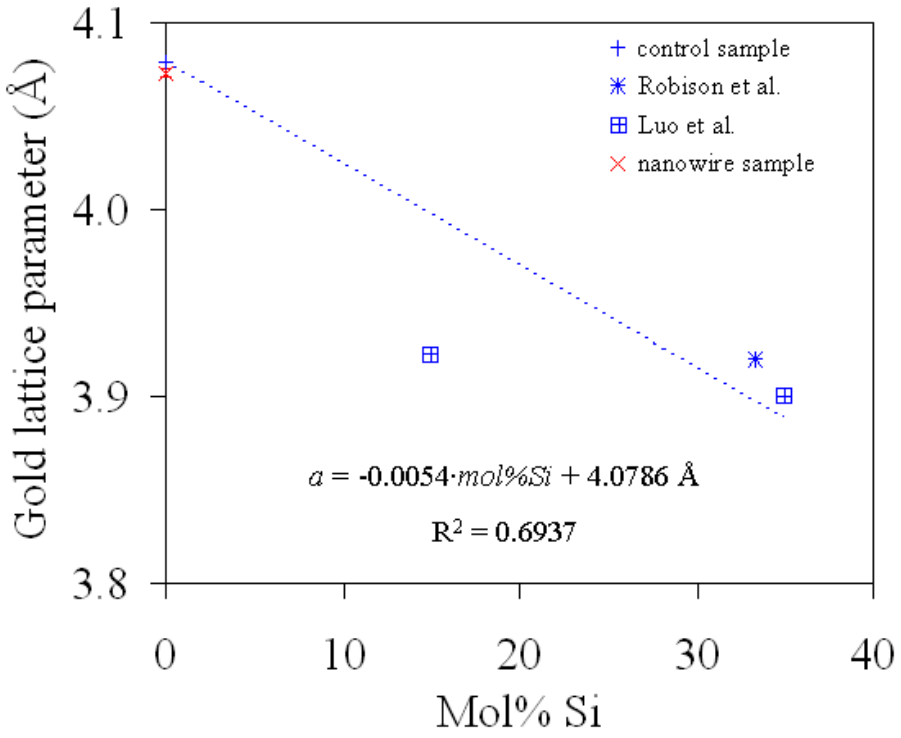

Figure 4.14 Vegard's law plot construction for silicon in gold, based on data from Luo, Klement and Anantharman [74] and Robison, Sharma and Eyring [71].

4.4.2 Catalyst Particle State

The results above on gold-catalyzed silicon nanowires have some interesting implications for the growth model. The *in-situ* XRD data clearly and conclusively show that the gold catalyst particles are molten during nanowire growth. This is in contrast with the results for gold-catalyzed ZnO nanowires, as reported in section 3.2.4.1, where the catalyst particle was determined to be solid during growth. The difference is likely to due to differences in the type of bonding of the source, as will be discussed further in section 5.1.1.

The melting point of pure gold (1063°C) is well above the growth temperature of the nanowires, even when accounting for the Gibbs-Thompson effect on the melting

point of nano-sized particles [75]. Therefore, for the gold to have melted, as it did, another factor must have come into play. Silicon and gold have a eutectic interaction, as seen in the phase diagram in Figure 4.15 [70], with a eutectic temperature well below the growth temperature. Therefore, silicon must have dissolved into the gold catalyst particles during growth, in order to cause eutectic melting. However, as shown above, no silicon is present in the gold at room temperature after growth. Looking again at the phase diagram in Figure 4.15, it may be seen that there is little solid solubility of silicon in gold. This is supported by literature reports, which have found that rapid quenching from a Au-Si melt is necessary to prevent the formation of separate gold and silicon phases upon solidification [76, 77]. Therefore, the silicon likely exsolves out of the gold nanoparticles as they recrystallize on cooling. The small dimensions of the nanoparticles may allow the silicon time to diffuse to the surface, where it forms a thin shell, as seen in Figure 4.4.

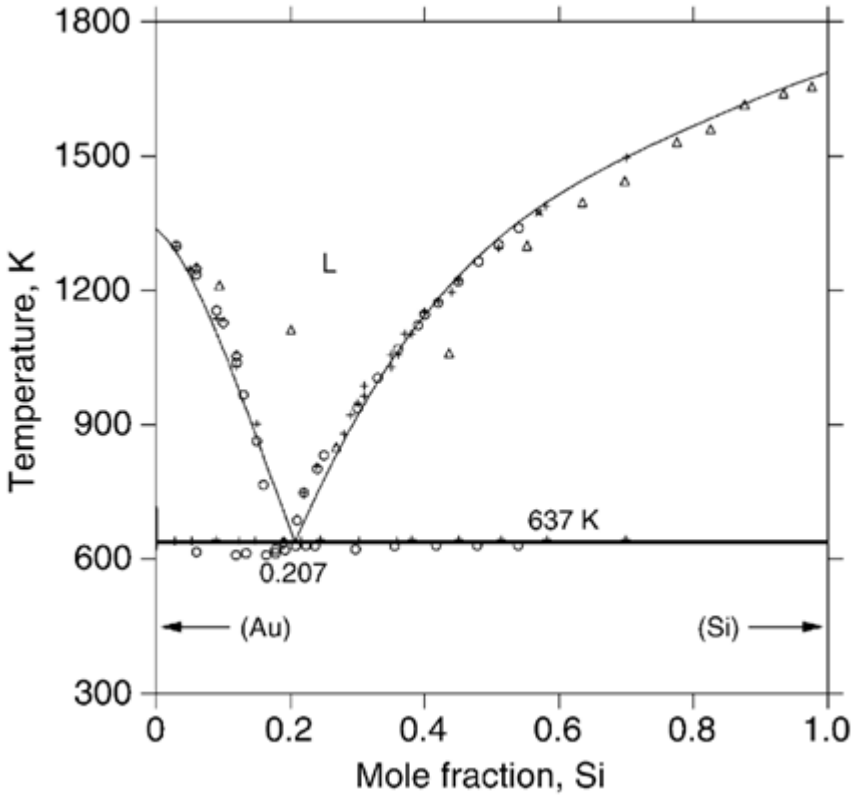

Figure 4.15 Gold-silicon phase diagram. Reprinted from [70] with permission from Elsevier.

4.5 References

1. Iijima, S., *Helical Microtubules of Graphitic Carbon.* Nature, 1991. **354**: p. 56-58.

2. Lin, C.C., I.C. Leu, J.H. Yen, and M.H. Hon, *A possible approach exploring the melting state of catalysts during the low-temperature growth of carbon nanotubes.* Diamond and Related Materials, 2005. **14**(11-12): p. 1901-1905.

3. Homma, Y., Y. Kobayachi, T. Ogino, D. Takagi, R. Ito, Y.J. Jung, and P.M. Ajayan, *Role of Transition Metal Catalysts in Single-Walled Carbon Nanotube Growth in Chemical Vapor Depostion.* Journal of Physical Chemistry B, 2003. **107**: p. 12161.

4. Kukovitsky, E.F., S.G. L'vov, and N.A. Sainov, *VLS-growth of carbon nanotubes from the vapor.* Chemical Physics Letters, 2000. **317**: p. 65-70.

5. Lin, M., J.P.Y. Tan, C. Boothroyd, K.P. Loh, E.S. Tok, and Y.-L. Foo, *Dynamical Observation of Bamboo-like Carbon Nanotube Growth.* Nano Letters, 2007. **7**(8): p. 2234-2238.

6. Harutyunyan, A.R., T. Tokune, and E. Mora, *Liquid as a required catalyst phase for carbon single-walled nanotube growth.* Applied Physics Letters, 2005. **87**: p. 051919.

7. Hofmann, S., G. Csnyi, A.C. Ferrari, M.C. Payne, and J. Robertson, *Surface Diffusion: The Low Activation Energy Path for Nanotube Growth.* Physical Review Letters, 2005. **95**: p. 036101.

8. Hofmann, S., C. Ducati, J. Robertson, and B. Kleinsorge, *Low-temperature growth of carbon nanotubes by plasma-enhanced chemical vapor deposition.* Applied Physics Letters, 2003. **83**(1): p. 135-137.

9. Chen, M., C.-M. Chen, S.-C. Shi, and C.-F. Chen, *Low-Temperature Synthesis Multiwalled Carbon Nanotubes by Microwave Plasma Chemical Vapor Deposition Using CH_4-CO_2 Gas Mixture.* Japanese Journal of Applied Physics, 2003. **42**: p. 614-619.

10. Seidel, R., G.S. Duesberg, E. Unger, A.P. Graham, M. Liebau, and F. Kreupl, *Chemical Vapor Deposition Growth of Single-Walled Carbon Nanotubes at 600ºC and a Simple Growth Model.* Journal of Physical Chemistry B, 2004. **108**: p. 1888-1893.

11. Helveg, S., C. López-Cartes, J. Sehested, P.L. Hansen, B.S. Clausen, J.R. Rostrup-Nielsen, F. Abild-Pedersen, and J.K. Norskov, *Atomic-scale imaging of carbon nanofibre growth.* Nature, 2004. **427**: p. 426-429.

12. Hulteen, J.C. and C.R. Martin, *A General Template-Based Method for the Preparation of Nanomaterials.* Journal of Materials Chemistry, 1997. **7**(7): p. 1075-1787.

13. Huczko, A., *Template-Based Synthesis of Nanomaterials.* Applied Physics A, 2000. **70**: p. 365-376.

14. Liu, H.I., N.I. Maluf, R.F.W. Pease, D.K. Biegelsen, N.M. Johnson, and F.A. Ponce, *Oxidation of Sub-50 nm Si Columns for Light Emission Study.* Journal of Vacuum Science and Technology B, 1992. **10**(6): p. 2846-2850.

15. Liu, H.I., D.K. Biegelsen, N.M. Johnson, F.A. Ponce, and R.F.W. Pease, *Self-Limiting Oxidation of Si Nanowires.* Journal of Vacuum Science and Technology B, 1993. **11**(6): p. 2532-2537.

16. Namatsu, H., Y. Takahashi, M. Nagase, and K. Murase, *Fabrication of Thickness-Controlled Silicon Nanowires and Their Characteristics.* Journal of Vacuum Science and Technology B, 1995. **13**(6): p. 2166-2169.

17. Givargizov, E.I., *Periodic Instability in Whisker Growth.* Journal of Crystal Growth, 1973. **20**: p. 219-226.

18. Givargizov, E.I. and N.N. Sheftal, *Morphology of silicon whiskers grown by the VLS-technique.* Journal of Crystal Growth, 1971. **9**: p. 326-9.

19. Wagner, R.S. and W.C. Ellis, *Vapor-Liquid-Solid Mechanism of Single Crystal Growth.* Applied Physics Letters, 1964. **4**(5): p. 89-90.

20. Weyher, J. and M. Surowiec, *Structure of VLS Silicon-Crystals Grown with Platinum and Gold.* Journal of Crystal Growth, 1978. **43**(2): p. 245-249.

21. Weyher, J., *The Liquid Surface Tension as a Factor Influencing the VLS Growth of Silicon Crystals.* Materials Science and Engineering, 1975. **20**: p. 171-177.

22. Weyher, J., *Some Notes on Growth Kinetics and Morphology of VLS Silicon-Crystals Grown with Platinum and Gold as Liquid-Forming Agents.* Journal of Crystal Growth, 1978. **43**(2): p. 235-244.

23. James, D.W.F. and C. Lewis, *Silicon whisker growth and epitaxy by the vapour-liquid-solid mechanism.* British Journal of Applied Physics, 1965. **16**: p. 1089-1096.

24. Westwater, J., D.P. Gossain, S. Tomiya, and S. Usui, *Growth of silicon nanowires via gold/silane vapor-liquid-solid reaction.* Journal of Vacuum Science and Technology B, 1997. **15**(3): p. 554-557.

25. Nimmatoori, P., Q. Zhang, E.C. Dickey, and J.M. Redwing, *Suppression of the vapor-liquid-solid growth of silicon nanowires by antimony addition.* Nanotechnology, 2009. **20**: p. 025607.

26. Hofmann, S., R. Sharma, C.T. Wirth, F. Cervantes-Sodi, C. Ducati, T. Kasama, R.E. Dunin-Borkowski, J. Drucker, P. Bennett, and J. Robertson, *Ledge-Flow-Controlled Catalyst Interface Dynamics During Si Nanowire Growth.* Nature Materials, 2008. **7**: p. 372-375.

27. Allen, J.E., E.R. Hemesath, D.E. Perea, J.L. Lensch-Falk, Z.Y. Li, F. Yin, M.H. Gass, P. Wang, A.L. Bleloch, R.E. Palmer, and L.J. Lauhon, *High-Resolution Detection of Au Catalyst Atoms in Si Nanowires.* Nature Nanotechnology, 2008. **3**: p. 168-173.

28. Colli, A., A. Fasoli, P. Beecher, P. Servati, S. Pisana, Y. Fu, A.J. Flewitt, W.I. Milne, J. Robertson, C. Ducati, S. De Franceschi, S. Hofmann, and A.C. Ferrari, *Thermal and Chemical Vapor Deposition of Si Nanowires: Shape Control, Dispersion, and Electrical Properties.* Journal of Applied Physics, 2007. **102**: p. 034302.

29. Wang, Y., V. Schmidt, S. Senz, and U. Gösele, *Epitaxial growth of silicon nanowires using an aluminium catalyst.* Nature Nanotechnology, 2006. **1**: p. 186-189.

30. Kodambaka, S., J. Tersoff, M.C. Reuter, and F.M. Ross, *Diameter-independent kinetics in the vapor-liquid-solid growth of Si nanowires.* Physical Review Letters, 2006. **96**(9): p. 096105.

31. Colli, A., S. Hofmann, A. Fasoli, A.C. Ferrari, C. Ducati, R.E. Dunin-Borkowski, and J. Robertson, *Synthesis and Optical Properties of Silicon Nanowires Grown by Different Methods.* Applied Physics A, 2006. **85**: p. 247-253.

32. Xing, Y.-J., D.-P. Yu, Z.-H. Xi, and Z.-Q. Xue, *Investigation of the growth process of Si nanowires using the vapour-liquid-solid mechanism.* Chinese Physics, 2002. **11**(10): p. 1047-1050.

33. Kamins, T.I., R.S. Williams, T. Hesjedal, and J.S. Harris, *Chemically vapor deposited Si nanowires nucleated by self-assembled Ti islands on patterned and unpatterned Si substrates.* Physica E, 2002. **13**: p. 995-998.

34. Kamins, T.I., R.S. Williams, D.P. Basile, T. Hesjedal, and J.S. Harris, *Ti-catalyzed Si nanowires by chemical vapor deposition: Microscopy and growth mechanisms.* Journal of Applied Physics, 2001. **89**(2): p. 1008-1016.

35. Wu, Y., Y. Cui, L. Huynh, C.J. Barrelet, D.C. Bell, and C.M. Lieber, *Controlled Growth and Structures of Molecular-Scale Silicon Nanowires.* Nano Letters, 2004. **4**(3): p. 433-436.

36. Cao, L., B. Garipcan, J.S. Atchison, C. Ni, B. Nabet, and J.E. Spanier, *Instability and Transport of Metal Catalyst in the Growth of Tapered Silicon Nanowires.* Nano Letters, 2006. **6**(9): p. 1852-1857.

37. Hannon, J.B., S. Kodambaka, F.M. Ross, and R.M. Tromp, *The influence of the surface migration of gold on the growth of silicon nanowires.* Nature, 2006. **440**(7080): p. 69-71.

38. Kalache, B., P.R. Cabarrocas, and A.F. Morral, *Observation of incubation times in the nucleation of silicon nanowires obtained by the vapor-liquid-solid method.* Japanese Journal of Applied Physics Part 2-Letters & Express Letters, 2006. **45**(7): p. L190-L193.

39. Bootsma, G.A. and H.J. Gassen, *A Quantitative Study on the Growth of Silicon Whiskers from Silane and Germanium Whiskers from Germane.* Journal of Crystal Growth, 1971. **10**: p. 223-234.

40. Dailey, J.W., J. Taraci, T. Clement, D.J. Smith, J. Drucker, and S.T. Picraux, *Vapor-liquid-solid growth of germanium nanostructures on silicon.* Journal of Applied Physics, 2004. **96**(12): p. 7556-7567.

41. Sutter, E. and P. Sutter, *Phase Diagram of Nanoscale Alloy Particles Used for Vapor-Liquid-Solid Growth of Semiconductor Nanowires.* Nano Letters, 2008. **8**(2): p. 411-414.

42. Greytak, A.B., L.J. Lauhon, M.S. Gudiksen, and C.M. Lieber, *Growth and Transport Properties of Complementary Germanium Nanowire Field-Effect Transistors.* Applied Physics Letters, 2004. **84**(21): p. 4176-4178.

43. Kodambaka, S., J. Tersoff, M.C. Reuter, and F.M. Ross, *Germanium Nanowire Growth Below the Eutectic Temperature.* Science, 2007. **316**: p. 729-732.

44. Adhikari, H., A.F. Marshall, C.E.D. Chidsey, and P.C. McIntyre, *Germanium Nanowire Epitaxy: Shape and Orientation Control.* Nano Letters, 2006. **6**(2): p. 318-323.

45. Pan, Z.W., Z.R. Dai, L. Xu, S.T. Lee, and Z.L. Wang, *Temperature-Controlled Growth of Silicon -Based Nanostructures by Thermal Evaportaion of SiO Powder.* Journal of Physical Chemistry B, 2001. **105**: p. 2507-2514.

46. Wang, N., Y.F. Zhang, Y.H. Tang, C.S. Lee, and S.T. Lee, *SiO_2-enhanced synthesis of Si nanowires by laser ablation.* Applied Physics Letters, 1998. **73**(26): p. 3902-3904.

47. Zhang, Y.F., Y.H. Tang, C. Lam, N. Wang, C.S. Lee, I. Bello, and S.T. Lee, *Bulk-Quantity Si Nanowires Synthesized by SiO Sublimation.* Journal of Crystal Growth, 2000. **212**: p. 115-118.

48. Wang, N., Y.H. Tang, Y.F. Zhang, C.S. Lee, and S.T. Lee, *Nucleation and Growth of Si Nanowires from Silicon Oxide.* Physical Review B, 1998. **58**(24): p. R16024-R16026.

49. Tang, Y.H., Y.F. Zhang, N. Wang, W.S. Shi, C.S. Lee, I. Bello, and S.T. Lee, *Si Nanowires Synthesized from Silicon Monoxide by Laser Ablation.* Journal of Vacuum Science and Technology B, 2001. **19**: p. 317-319.

50. Shi, W.-S., H.-Y. Peng, Y.-F. Zheng, N. Wang, N.-G. Shang, Z.-W. Pan, C.-S. Lee, and S.-T. Lee, *Synthesis of Large Areas of Highly Oriented Very Long Silicon Nanowires.* Advanced Materials, 2000. **12**(18): p. 1343-1345.

51. Zhang, Y.F., Y.H. Tang, N. Wang, C.S. Lee, I. Bello, and S.T. Lee, *One-Dimensional Growth Mechanism of Crystalline Silicon Nanowires.* Journal of Crystal Growth, 1999. **197**: p. 136-140.

52. Roy, S. and Z. Gao, *Nanostructure-Based Electrical Biosensors.* Nano Today, 2009. **4**: p. 318-334.

53. Patolsky, F., B.P. Timko, G. Yu, Y. Fang, A.B. Greytak, G. Zheng, and C.M. Lieber, *Detection, Stimulations, and Inhibition of Neuronal Signals with High-Density Nanowire Transistor Arrays.* Science, 2006. **313**: p. 1100-1104.

54. Timko, B.P., T. Cohen-Karni, G. Yu, Q. Qing, B. Tian, and C.M. Lieber, *Electrical Recording from Hearts with Flexible Nanowire Device Arrays.* Nano Letters, 2009. **9**(2): p. 914-918.

55. Chan, C.K., H. Peng, G. Liu, K. McIlwrath, X.F. Zhang, R.A. Huggins, and Y. Cui, *High-Performance Lithium Battery Anodes Using Silicon Nanowires.* Nature Nanotechnology, 2008. **3**: p. 31-35.

56. Chan, C.K., R. Ruffo, S.S. Hong, R.A. Huggins, and Y. Cui, *Structural and Electrochemical Study of the Reaction of Lithium with Silicon Nanowires.* Journal of Power Sources, 2009. **189**: p. 34-39.

57. Peng, K., J. Jie, W. Zhang, and S.-T. Lee, *Silicon Nanowires for Rechargeable Litium-Ion Battery Anodes.* Applied Physics Letters, 2008. **93**: p. 033105.

58. Ruffo, R., S.S. Hong, C.K. Chan, R.A. Huggins, and Y. Cui, *Impedance Analysis of Silicon Nanowire Lithium Ion Battery Anodes.* Journal of Physical Chemistry C, 2009. **113**: p. 11390-11398.

59. Fang, H., X. Li, S. Song, Y. Xu, and J. Zhu, *Fabrication of Slantingly-Aligned Silicon Nanowire Arrays for Solar Cell Applications.* Nanotechnology, 2008. **19**: p. 255703.

60. Peng, K., X. Wang, and S.-T. Lee, *Silicon Nanowire Array Photoelectrochemical Solar Cells.* Applied Physics Letters, 2008. **92**(16): p. 163103.

61. Stelzner, T., M. Pietsch, G. Andrä, F. Falk, E. Ose, and S. Christiansen, *Silicon Nanowire-Based Solar Cells.* Nanotechnology, 2008. **19**: p. 295203.

62. Tsakalakos, L., J. Balch, J. Fronheiser, B.A. Korevaar, O. Sulima, and J. Rand, *Silicon Nanowire Solar Cells.* Applied Physics Letters, 2007. **91**: p. 233117.

63. Huang, Y., X. Duan, Y. Cui, L.J. Lauhon, K.-H. Kim, and C.M. Lieber, *Logic Gates and Computation from Assembled Nanowire Building Blocks.* Science, 2001. **294**: p. 1313-1317.

64. Duan, X., Y. Huang, and C.M. Lieber, *Nonvolatile Memory and Programmable Logic from Molecule-Gated Nanowires.* Nano Letters, 2002. **2**(5): p. 487-490.

65. Wang, X., Q. Li, Z. Liu, J. Zhang, Z. Liu, and R. Wang, *Low-temperature growth and properties of ZnO nanowires.* Applied Physics Letters, 2004. **84**(24): p. 4941-4943.

66. Nagashima, K., T. Yanagida, K. Oka, H. Tanaka, and T. Kawai, *Mechanism and control of sidewall growth and catalyst diffusion on oxide nanowire vapor-liquid-solid growth.* Applied Physics Letters, 2008. **93**: p. 153103.

67. Kodambaka, S., J.B. Hannon, R.M. Tromp, and F.M. Ross, *Control of Si Nanowire Growth by Oxygen.* Nano Letters, 2006. **6**(6): p. 1292-1296.

68. Churchman, A.T., G.A. Geach, and J. Winton, *Deformation Twinning in Materials of the A4 (Diamond) Crystal Structure.* Proceedings of the Royal Society of London A, 1956. **238**(1213): p. 194-203.

69. Wang, Y.Q., R. Smirani, and G.G. Ross, *Stacking Faults in Si Nanocrystals.* Applied Physics Letters, 2005. **86**: p. 221920.

70. Meng, F.G., H.S. Liu, L.B. Liu, and Z.P. Jin, *Thermodynamic Description of the Au-Si-Sn System.* Journal of Alloys and Compounds, 2007. **431**: p. 292-297.

71. Robison, W., R. Sharma, and L. Eyring, *Observation of Gold-Silicon Alloy Formation in Thin Films by High Resolution Electron Microscopy.* Acta Metallurgica et Materialia, 1991. **39**(2): p. 179-186.

72. Ashtikar, M.S. and G.L. Sharma, *Structural Investigation of Gold Induced Crystallization in Hydrogenated Amorphous Silicon Thin Films.* Japanese Journal of Applied Physics, 1995. **34**(10): p. 5520-5526.

73. Hultman, L., A. Robertson, H.T.G. Hentzell, I. Engström, and P.A. Psaras, *Crystallization of amorphous silicon during thin-film gold reaction.* Journal of Applied Physics, 1987. **62**(9): p. 3647-3655.

74. Luo, H.L., W. Klement, Jr., and T.R. Anantharaman, *Effects of Liquid Quenching on the Constitution and Structure of Silver-Silicon and Gold-Silicon Alloys.* Transactions of the Indian Institute of Metals, 1965. **18**: p. 214-218.

75. Buffat, P. and J.P. Borel, *Size Effect on the Melting Temperature of Gold Particles.* Physical Review A, 1976. **13**(6): p. 2287-2298.

76. Suryanarayana, C. and T.R. Anantharaman, *On the Crystal Structure of a Non-Equilibrium Phase in the Gold-Silicon System.* Materials Science and Engineering, 1974. **13**: p. 73-81.

77. George, D.K., A.A. Johnson, and R.J. Storey, *Preparation of the Metastable Compound Au_3Si by Quenching Liquid Droplets of a Au-25% at.% Si Alloy into Water.* Materials Science and Engineering B, 1998. **55**: p. 221-224.

CHAPTER 5

GROWTH MECHANISM

5.1 Revisiting the Open Questions

Among the unresolved issues surrounding the catalyzed growth of 1D nanostructures are two central open questions, as previously outlined in 1.2.3. First, what is the state of the catalyst particle during growth, liquid or solid? Second, what is the diffusion path of source material to the growth front, bulk diffusion through the catalyst or surface diffusion around it? This purpose of this section is to investigate these two open questions and to apply the results of this research toward addressing them.

5.1.1 Catalyst Particle State

5.1.1.1 The Possibility of Solid Catalyst Particles

In the VLS mechanism, the catalyst particle is liquid during growth. However, some studies in the literature have reported that 1D nanostructures may also be grown by solid catalyst particles, which has been termed the vapor-solid-solid (VSS) mechanism. The term "VSS" was first employed in 1971 by Bootsma and Gassen [1]. The authors demonstrated the growth of Ge whiskers from germane (GeH_4) with Au catalysts at temperatures down to around 50º below the eutectic temperature, though they still attributed growth to the VLS mechanism, arguing that the melting temperature of the catalyst nanoparticles was lowered, due to the Gibbs-Thompson effect. The possibility of a solid catalyst particle was not invoked again until 2001, in a study of Ti-catalyzed Si

nanowires grown from silane at temperatures around 700º below the eutectic temperature (around 1330ºC) [4].

Since then, there have been several more reports of 1D nanostructure growth from solid catalyst particles, in most cases for growth below the eutectic temperature. Solid catalyst particles have been reported for the growth of ZnO nanostructures. Campos et al. [5] grew Au-catalyzed ZnO nanowires at 200-450ºC ($T_{eutectic} \approx 730$ºC). The catalyst particle was identified as γ-AuZn via XRD. Two studies of Sn-catalyzed ZnO nanostructures found evidence for the persistence of some amount of crystallinity in the catalyst particles at temperatures well above even the melting temperature of pure tin. Ding, Gao and Wang [6] found that one single-crystalline tin particle could catalyze the growth of two nanostructures, each with a crystal orientation matching the catalyst particle, and hypothesized the presence of a partially crystalline surface on the catalyst particles. Zhuang et al. [7] grew Sn-catalyzed ZnO bi-crystalline nanostructures with twin boundaries running parallel to the length, and hypothesized that these bi-crystalline nanostructures resulted from nucleation from a catalyst particle with a twin defect.

Solid catalyst particles have also been reported for the growth of Ge nanostructures. Ge nanowires have been grown from Ni catalysts at temperatures below the eutectic using a supercritical fluid, instead of vapor, as the source phase [8, 9]. Ge nanowires have also been grown from Au catalysts at temperatures below the eutectic [10, 11]. Kodambaka, Tersoff, Reuter and Ross [11] investigated the nanowire growth *in-situ* in a TEM. They found that nanowires could grow from solid and liquid catalysts at the same temperature, depending on the source material pressure and thermal history. Other systems for which solid catalyst particles have been reported include Ni,Co-

catalyzed W nanowires [12] and Au-catalyzed GaAs nanowires [13]. Studies of Au-catalyzed InAs and InP nanowires have even reported that growth could only occur with solid catalyst particles [14, 15]. No nanowire growth was observed above the eutectic temperature.

5.1.1.2 Implications of the Experimental Results

This research investigated the catalyst particle state for four material systems: Au- and Sn-catalyzed ZnO nanostructures, Au-catalyzed Fe_xO_y nanowires and Au-catalyzed Si nanowires. Gold catalyst particles were directly observed, via *in-situ* XRD, to be liquid during the growth of silicon nanowires from silane. Tin catalyst particles were also determined to be liquid for the growth of samples of ZnO nanostructures, as the growth temperatures were well above even the bulk melting temperature of pure tin. However, gold catalyst particles were determined to be solid for the growth of samples of Fe_xO_y nanostructures, as the growth temperatures were well below the Au-Fe eutectic temperature. Additionally, the gold catalyst particles were determined to be solid for the growth of samples of ZnO nanostructures. Although the growth temperatures were above the Au-Zn eutectic temperature, no Zn was present in the gold to cause eutectic melting.

These results indicate that 1D nanostructures, even of the same material (e.g. ZnO), can be grown from either liquid or solid catalyst particles. The catalyst particle state depends on two factors: the growth temperature and the presence of source material species dissolved in the catalyst particle. If the growth temperature is well above the bulk melting temperature of the catalyst, or well below the eutectic temperature, the catalyst will be liquid or solid, respectively. Of more interest, is growth at temperatures above the eutectic temperature, but below the bulk melting temperature. In these cases, the catalyst

particle state depends on whether or not the source material diffuses into the catalyst particle, which relates to the relationship between the types of bonding in the catalyst and source material, as will be discussed further in section 5.1.3 below.

The possibility of growth from either liquid or solid catalysts indicates that the catalyzed growth of 1D nanostructures is more flexible than originally imagined in the VLS mechanism. Catalyst materials do not necessarily have to be chosen so as to allow a liquid catalyst at the growth temperature, as has been postulated in the past. Growth from a solid catalyst particle also opens up the possibility of low temperature growth on flexible substrates.

5.1.2 Diffusion Path

5.1.2.1 The Possibility of Surface Diffusion

In the conventional understanding of the VLS mechanism, diffusion of the source material to the growth front occurs through the catalyst particle (bulk). However, a few studies have pointed to the possibility of surface diffusion around the catalyst particle [16, 17]. The possibility of surface diffusion of the growth species around the catalyst nanoparticle instead of through it, though it has not been extensively studied, is reasonable. The high surface-to-volume ratio in the nano-size regime causes surface related effects to gain prominence, and surface diffusion coefficients are generally several orders of magnitude larger than bulk diffusion coefficients, due to broken and dangling bonds on the surface. Therefore, it is reasonable that the catalyzed growth of 1D nanostructures could proceed by surface diffusion of the growth species around the catalyst.

Bootsma and Gassen in 1971 first raised the possibility of surface diffusion [1]. Experimental evidence for surface diffusion was found in a study of the growth of Ni, Co and Fe catalyzed carbon nanofibers [18, 19]. The authors measured a low activation energy, comparable to that for the diffusion of carbon on Ni and Co surfaces and much smaller than for the diffusion of carbon through bulk Ni and Co. Also, a study of Au-catalyzed InAs/GaAs heterostructures found a sharp interface between InAs and GaAs when the source material was switched during growth from trimethyl indium to triethyl gallium [20]. If growth proceeds by bulk supersaturation, a region of mixed composition should have been observed.

In addition, metal nanoparticles can have a quasi-liquid layer (QLL) on the surface [21, 22]. The dangling, broken bonds on the surface and the high surface curvature of nanoparticles weakens the surface bonds and causes the surface atoms to adopt a disordered arrangement in order to reduce the surface energy, with a liquid-like structure [23]. The QLL is thicker for smaller diameters (higher curvature) and at higher temperatures [24]. QLLs have been found to have unusually high diffusion coefficients, to the point of approaching, or even exceeding, the bulk liquid diffusion coefficient at temperatures approaching the melting point [25]. The presence of such a liquid-like layer on the surface of the catalyst particles would further favor surface diffusion of the growth species to the growth front.

5.1.2.2 Diffusion Rate Approximations

An order-of-magnitude comparison of the diffusion rates through the bulk and surface of a catalyst particle was made, taking a similar approach to Wang and

Fischmann [16]. Fick's first law of diffusion relates the flux, J, to the diffusion coefficient, D, and the concentration gradient, (dC/dx).

$$J = -D\left(\frac{dC}{dx}\right)$$

The concentration gradient may be approximated by the change in concentration (ΔC) divided by the distance traveled (Δx). In order to calculate the diffusion distance, the catalyst particle geometry may be approximated as a cylinder of height h and diameter d, as shown in Figure 5.1. Additionally, it is assumed that diffusion along the catalyst/nanostructure interface may be treated as surface diffusion.

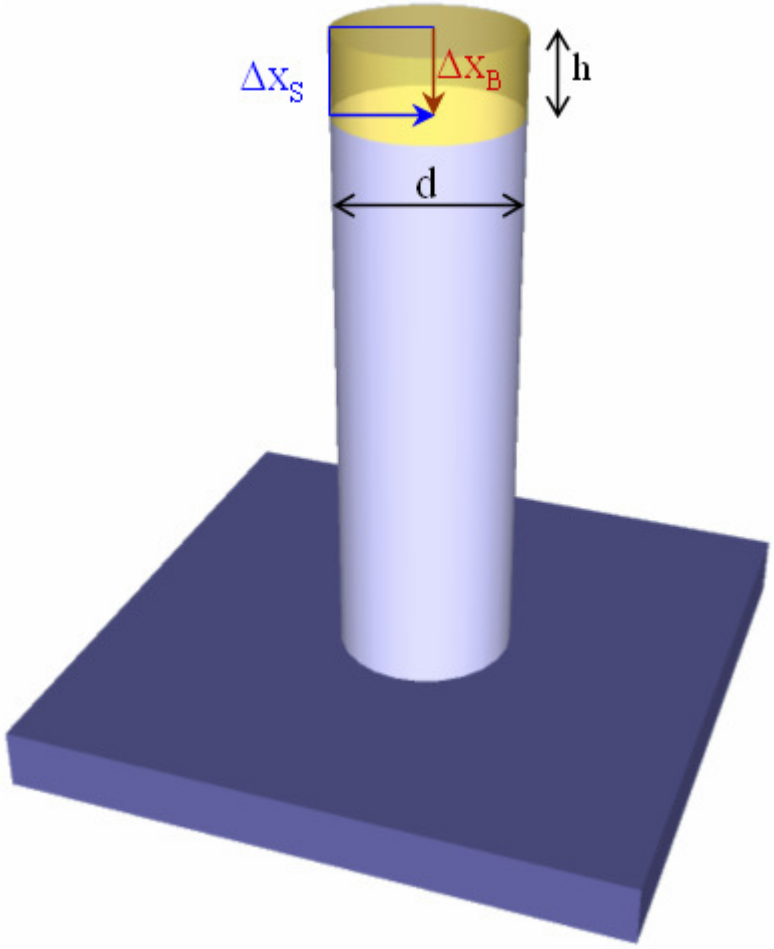

Figure 5.1 Schematic of nanowire geometry for diffusion rate approximations, in which the catalyst particle of diameter d and height h is

shown in yellow, and the nanowire in light blue, showing the surface (Δx_S) and bulk (Δx_B) diffusion paths.

If we take a growth species impinging on the center of the top of the catalyst particle and diffusing to the center of the catalyst/nanowire interface, then the distances traveled for bulk (Δx_B) and surface (Δx_S) diffusion, and therefore the concentration gradients, may be stated as follows,

$$\Delta x_B = h$$
$$\left(\frac{dC}{dx}\right)_B \approx \left(\frac{\Delta C}{\Delta x}\right)_B = \frac{\Delta C_B}{h}$$

$$\Delta x_S = h + d$$
$$\left(\frac{dC}{dx}\right)_S \approx \left(\frac{\Delta C}{\Delta x}\right)_S = \frac{\Delta C_S}{h + d}$$

where the subscripts *B* and *S* indicate quantities for bulk and surface diffusion, respectively. Both diffusion paths have the same starting and ending points, and so the change in concentration, ΔC, for both paths will be equal. Therefore the bulk and surface fluxes will be as follows.

$$J_B = -D_B\left(\frac{dC}{dx}\right)_B = -D_B\left(\frac{\Delta C}{h}\right)$$
$$J_S = -D_S\left(\frac{dC}{dx}\right)_S = -D_S\left(\frac{\Delta C}{h + d}\right)$$

As the flux is simply the amount crossing a unit area per unit time, the diffusion rate is the flux times the area. The diffusion area for the bulk and surface paths are, respectively, a circle with diameter *d* and a ring with diameter *d* and thickness *t*. From the fluxes and diffusion areas, the ratio of the bulk and surface diffusion rates (R_B *and* R_S, respectively) may be determined.

$$\frac{R_S}{R_B} = \frac{J_S A_S}{J_B A_B} \approx \frac{-D_S\left(\frac{\Delta C}{h+d}\right)(\pi d \cdot t)}{-D_B\left(\frac{\Delta C}{h}\right)\left(\frac{\pi d^2}{4}\right)} = \left(\frac{D_S}{D_B}\right)\left(\frac{4t \cdot h}{d(h+d)}\right)$$

The second term in the above equation is a geometric factor depending on the catalyst particle size and surface thickness. For surface thicknesses of 1-2 atomic layers, and particle diameters and heights around 10-50 nm, the geometric factor is on the order of 10^{-2}. The surface and bulk self-diffusion coefficients of gold at 800ºC are on the order of 10^{-11} and 5×10^{-14} m^2/s, respectively [26], which gives a surface-to-bulk diffusion rate ratio on the order of 1:1 to 20:1. Diffusion coefficients for the heterogeneous diffusion of growth species may give an even larger ratio. From these approximations, it is evident that surface diffusion should play a significant role in mass transport of growth species to the growth front.

5.1.2.3 Implications of the Experimental Results

This research determined the diffusion path for three material systems: Au-catalyzed ZnO nanostructures, Au-catalyzed Fe_xO_y nanowires and Au-catalyzed Si nanowires. Results for Sn-catalyzed ZnO nanostructures were inconclusive. For the Au-catalyzed Si nanowires, the diffusion path was determined to be through the bulk of the catalyst, as the dissolution of Si into the Au is necessary for the observed eutectic melting. However, for the Au-catalyzed ZnO and Au-catalyzed Fe_xO_y nanowires, the diffusion path was determined to be along the surface of the catalyst, as the gold lattice parameters indicated that no Zn or Fe was dissolved in the gold.

These results indicate that during the growth of 1D nanostructures, the source material may diffuse either through the bulk of the catalyst particle or around the surface.

The source material diffusion path relates to the relationship between the types of bonding in the catalyst and source material, as will be discussed further in section 5.1.3 below. In this way, the catalyst particle state and diffusion path are connected, and the same relationships that favor solid catalyst particles also favor a surface diffusion path.

5.1.3 Effect of Relative Bonding Types

Both the question of the catalyst particle state (at temperatures between the eutectic and bulk melting temperatures) and the source material diffusion path fundamentally come down to whether or not the source material will diffuse into the catalyst particle. From this research, it was found that in the cases of Au-catalyzed ZnO and Fe_xO_y nanostructures, the growth species did not diffuse into the catalyst particle, resulting in solid catalyst particles during growth and a surface diffusion path of the source material. In the case of Au-catalyzed Si nanostructures, it was found that the growth species did diffuse into the catalyst particle, resulting in liquid catalyst particles during growth and a largely bulk diffusion path of the source material. By comparing the results, it may be observed that in both of the two cases where the growth species did not diffuse into the catalyst particle, the source material was ionic, and in the case where the growth species did diffuse into the catalyst particle, the source material was non-ionic. This difference in bonding type of the source material may explain the difference in the results. As in the general chemical principle of "like dissolves like", chemical species will more likely dissolve in a solvent of the same bonding type. Since the catalyst particle in all cases was metallic, the ionic growth species (for ZnO and Fe_xO_y) would be unlikely to dissolve into the catalyst particle. However, the non-ionic growth species (for

Si) would be more likely to dissolve into the catalyst particle, allowing a bulk diffusion path and causing eutectic melting of the catalyst particle.

A review of the literature offers some support of the importance of bonding type on growth. Of the studies that have reported, via EDS spectra collected in a TEM, the presence of growth species in the catalyst particle, most were grown with non-ionic source materials [27-36]. The only exception [37] was for a study that grew Au-catalyzed indium tin oxide (ITO) nanowires from a mixture of ITO and graphite. In this case, it is possible that the graphite reduced the ionic source material to metallic growth species, which could then dissolve into the metallic catalyst particle.

5.2 Catalyzed Growth Mechanism

From the above discussions, new insights may be gathered concerning the catalyzed growth of 1D nanostructures, which may be broadly divided into three stages: interaction of the source material and the catalyst particle, nucleation of the nanostructure and further growth, as seen in Figure 5.2

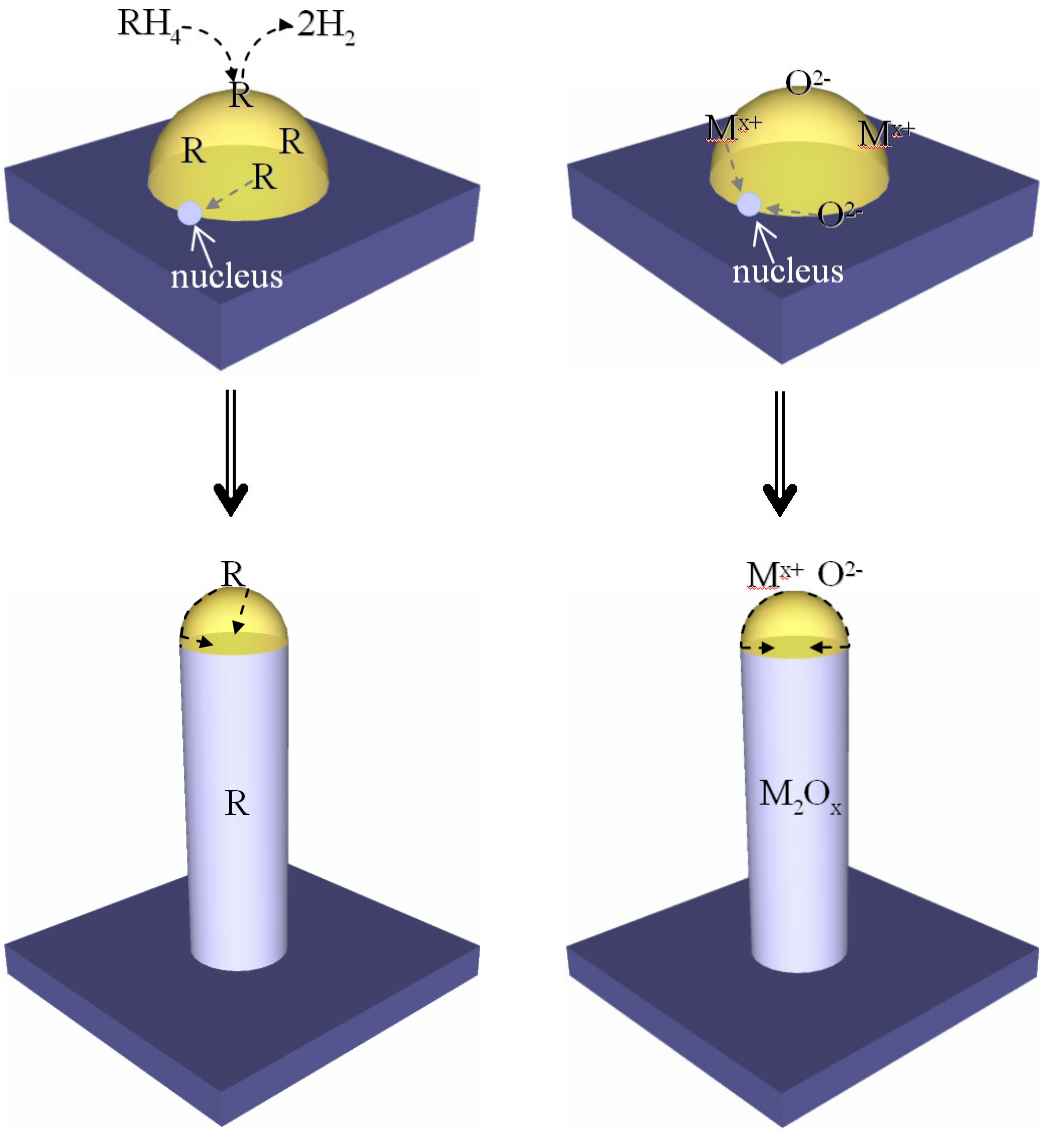

non-ionic source material ionic source material

Figure 5.2 Schematics of nucleation and growth of nanowires using metal catalyst particles from non-ionic and ionic source materials.

The catalyst nanoparticle may be in the liquid or solid state. The catalyst particle state depends on two factors. The first factor is the growth temperature, relative to the melting and eutectic temperatures of the catalyst. The second factor, for growth temperatures between the melting and eutectic temperatures, is the interaction of the growth species with the catalyst particle. When the growth species have incompatible bonding types (such as ionic and metallic), then the growth species will not diffuse into the catalyst particle, and therefore eutectic melting will not occur. Likewise, when the bonding types are compatible, then the growth species may diffuse into the catalyst particle. The growth of nanostructures from solid catalyst particles demonstrates that a liquid catalyst is not necessary.

The growth of nanostructures without bulk diffusion of the growth species into the catalyst particle indicates that growth can occur by a mechanism other than bulk supersaturation and nucleation. Instead, the surface of the catalyst particle may serve as a collection site for the growth species. The quasi-liquid layer on the surface may be an ideal attachment site.

Additionally, the catalyst particle surface can provide an interface for heterogeneous nucleation. Growth species will diffuse on the catalyst surface until a cluster forms, in what can be thought of as a surface supersaturation and nucleation mechanism. When the catalyst particle is sitting on a substrate, the nucleation will preferentially occur at the vapor-catalyst-substrate interface, in order to reduce the interfacial and boundary energy [38]. However, a substrate interface is not necessary for growth, as shown by the Sn-catalyzed ZnO nanostructures.

Once nucleated, reduction of the surface energy will favor continued growth at the catalyst-nanostructure interface, rather than nucleation of new nanostructures. Growth at the existing catalyst-nanostructure interface requires the least additional surface, and therefore surface energy, generation. Surface diffusion will play a significant, if not dominate, role in delivery of growth species to the growth front, even in situations with compatible bonding, in which the growth species can diffuse into the bulk of the catalyst particle. Nanostructure growth occurs in consistent, low index directions, regardless of the substrate orientation, as seen for Au-catalyzed Fe_xO_y nanostructures grown on *c*- and *a*-plane sapphire substrates, and is likely governed by kinetics. However, alignment of the nanostructures strongly depends on the orientation of the substrate, again as seen for Au-catalyzed Fe_xO_y nanostructures grown on *c*- and *a*-plane sapphire substrates.

5.3 References

1. Bootsma, G.A. and H.J. Gassen, *A Quantitative Study on the Growth of Silicon Whiskers from Silane and Germanium Whiskers from Germane.* Journal of Crystal Growth, 1971. **10**: p. 223-234.

2. Westwater, J., D.P. Gossain, S. Tomiya, and S. Usui, *Growth of silicon nanowires via gold/silane vapor-liquid-solid reaction.* Journal of Vacuum Science and Technology B, 1997. **15**(3): p. 554-557.

3. Hiruma, K., M. Yazawa, T. Katsuyama, K. Ogawa, K. Haraguchi, M. Koguchi, and H. Kakibayashi, *Growth and optical properties of nanometer-scale GaAs and InAs whiskers.* Applied Physics Reviews, 1995. **77**(2): p. 447-462.

4. Kamins, T.I., R.S. Williams, D.P. Basile, T. Hesjedal, and J.S. Harris, *Ti-catalyzed Si nanowires by chemical vapor deposition: Microscopy and growth mechanisms.* Journal of Applied Physics, 2001. **89**(2): p. 1008-1016.

5. Campos, L.C., M. Tonezzer, A.S. Ferlauto, V. Grillo, R. Magalhes-Paniago, S. Oliveria, L.O. Ladeira, and R.G. Lacerda, *Vapor-Solid-Solid Growth Mechanism Driven by Epitaxial Match between Solid AuZn Alloy Catalyst Particles and ZnO Nanowires at Low Temperatures.* Advanced Materials, 2008. **20**: p. 1499-1504.

6. Ding, Y., P.X. Gao, and Z.L. Wang, *Catalyst-Nanostructure Interfacial Lattice Mismatch in Determining the Shape of VLS Grown Nanowires and Nanobelts: A Case of Sn/ZnO.* Journal of the American Chemical Society, 2004. **126**: p. 2066-2072.

7. Zhuang, H., D. Wang, J. Shen, C. Xue, X. Zhang, and H. Liu, *Fabrication and Characterization of Novel Bicrystalline ZnO Nanowires.* Journal of Materials Research, 2009. **24**(8): p. 2536-2540.

8. Tuan, H.-Y., D.C. Lee, T. Hanrath, and B.A. Korgel, *Catalytic Solid-Phase Seeding of Silicon Nanowires by Nickel Nanocrystals in Organic Solvents.* Nano Letters, 2005. **5**(4): p. 681-684.

9. Tuan, H.-Y., D.C. Lee, T. Hanrath, and B.A. Korgel, *Germanium Nanowire Synthesis: An Example of Solid-Phase Seeded Growth with Nickel Nanocrystals.* Chemistry of Materials, 2005. **17**: p. 5705-5711.

10. Adhikari, H., A.F. Marshall, C.E.D. Chidsey, and P.C. McIntyre, *Germanium Nanowire Epitaxy: Shape and Orientation Control.* Nano Letters, 2006. **6**(2): p. 318-323.

11. Kodambaka, S., J. Tersoff, M.C. Reuter, and F.M. Ross, *Germanium Nanowire Growth Below the Eutectic Temperature.* Science, 2007. **316**: p. 729-732.

12. Wang, S.L., Y.H. He, J. Zou, Y. Wang, H. Huang, B.Y. Huang, C.T. Liu, and P.K. Liaw, *Catalytic growth of metallic tungsten whiskers based on the vapor-solid-solid mechanism.* Nanotechnology, 2008. **19**: p. 345604.

13. Persson, A.I., M.W. Larsson, S. Stenström, B.J. Ohlsson, L. Samuelson, and L.R. Wallenberg, *Solid-phase diffusion mechanism for GaAs nanowire growth.* Nature Materials, 2004. **3**: p. 677-681.

14. Dick, K.A., K. Deppert, T. Mårtensson, B. Mandl, L. Samuelson, and W. Seifert, *Failure of the Vapor-Liquid-Solid Mechanism in Au-Assisted MOVPE Growth of InAs Nanowires.* Nano Letters, 2005. **5**(4): p. 761-4.

15. Johansson, J., B.A. Wacaser, K.A. Dick, and W. Seifert, *Growth related aspects of epitaxial nanowires.* Nanotechnology, 2006. **17**: p. S355-S361.

16. Wang, H. and G.S. Fischman, *Role of liquid droplet surface diffusion in the vapor-liquid-solid whisker growth mechanism.* Journal of Applied Physics, 1994. **76**(3): p. 1557-1562.

17. Cheyssac, P., M. Sacilotti, and G. Patriarche, *Vapor-liquid-solid mechanisms: Challenges for nanosized quantum cluster/dot/wire materials.* Journal of Applied Physics, 2006. **100**: p. 044315.

18. Hofmann, S., G. Csnyi, A.C. Ferrari, M.C. Payne, and J. Robertson, *Surface Diffusion: The Low Activation Energy Path for Nanotube Growth.* Physical Review Letters, 2005. **95**: p. 036101.

19. Hofmann, S., C. Ducati, J. Robertson, and B. Kleinsorge, *Low-temperature growth of carbon nanotubes by plasma-enhanced chemical vapor deposition.* Applied Physics Letters, 2003. **83**(1): p. 135-137.

20. Ohlsson, B.J., M.T. Björk, A.I. Persson, C. Thelander, L.R. Wallenberg, M.H. Magnusson, K. Deppert, and L. Samuelson, *Growth and characterization of GaAs and InAs nano-whiskers and InAs/GaAs heterostructures.* Physica E, 2002. **13**: p. 1126-1130.

21. Krakow, W., M. Jóse-Yacamán, and J.L. Aragón, *Observation of quasimelting at the atomic level in Au nanoclusters.* Physical Review B, 1994. **49**(15): p. 591-596.

22. Ajayan, P.M. and T.J. Marks, *Experimental Evidence for Quasimelting in Small Particles.* Physical Review Letters, 1989. **63**(3): p. 279-282.

23. Wang, Z.L., J.M. Petroski, T.C. Green, and M.A. El-Sayed, *Shape Transformation and Surface Melting of Cubic and Tetrahedral Platinum Nanocrystals.* Journal of Physical Chemistry B, 1998. **102**(32): p. 6145-6151.

24. Lereah, Y., R. Kofman, J.M. Penisson, G. Deutscher, P. Cheyssac, T.B. David, and A. Bourret, *Time-resolved electron microscopy studies of the structure of*

nanoparticles and their melting. Philosophical Magazine B, 2001. **81**(11): p. 1801-1819.

25. Frenken, J.W.M., J.P. Toennies, and C. Wöll, *Self-Diffusion at a Melting Surface Observed by He Scattering.* Physical Review Letters, 1988. **60**(17): p. 1727-1730.

26. Beszeda, I., I.A. Szabó, and E.G. Gontier-Moya, *Morphological evolution of thin gold films studied by Auger electron spectroscopy in beading conditions.* Applied Physics A, 2004. **78**: p. 1079-1084.

27. Wu, Y. and P. Yang, *Germanium Nanowire Growth via Simple Vapor Transport.* Chemistry of Materials, 2000. **12**: p. 605-607.

28. Wu, Y. and P. Yang, *Direct Observation of Vapor-Liquid-Solid Nanowire Growth.* Journal of the American Chemical Society, 2001. **123**: p. 3165-3166.

29. Park, H.D., A.-C. Gaillot, S.M. Prokes, and R.C. Cammarata, *Observation of size dependent liquid depression in the growth of InAs nanowires.* Journal of Crystal Growth, 2006. **296**: p. 159-164.

30. Chen, C.-C., C.-C. Yeh, C.-H. Chen, M.-Y. Yu, H.-L. Liu, J.-J. Wu, K.-H. Chen, L.-C. Chen, J.-Y. Peng, and Y.-F. Chen, *Catalytic Growth and Characterization of Gallium Nitride Nanowires.* Journal of the American Chemical Society, 2001. **123**(12): p. 2791-2798.

31. Wang, Y., L. Zhang, C. Liang, G. Wang, and X. Peng, *Catalystic growth and photoluminescence properties of semiconductor single-crystal ZnS nanowires.* Chemical Physics Letters, 2002. **357**: p. 314-318.

32. Wang, Y., G. Meng, L. Zhang, C. Liang, and J. Zhang, *Catalytic Growth of Large-Scale Single-Crystal CdS Nanowires by Physical Evaporation and Their Photoluminescence.* Chemistry of Materials, 2002. **14**: p. 1773-1777.

33. Meng, Q., C. Jiang, and S.X. Mao, *Temperature-dependent growth of zinc-blende-structured ZnTe nanostructures.* Journal of Crystal Growth, 2008. **310**: p. 4481-4486.

34. Peng, H., S. Meister, C.K. Chan, X.F. Zhang, and Y. Cui, *Morphology Control of Layer-Structured Gallium Selenide Nanowires.* Nano Letters, 2007. **7**(1): p. 199-203.

35. Chang, K.-W. and J.-J. Wu, *Catalytic growth and characterization of Ga_2O_3 nanowires.* Applied Physics A, 2003. **76**: p. 629-631.

36. Park, S., H. Kim, C. Lee, D.H. Lee, and S.S. Hong, *Synthesis of Very Straight Bismuth Oxide Nanowires by Using Thermal Evaporation of Bismuth Powders.* Journal of the Korean Physical Society, 2008. **53**(4): p. 1965-1970.

37. Nguyen, P., H.T. Ng, J. Kong, A.M. Cassell, R. Quinn, J. Li, J. Han, M. McNeil, and M. Meyyappan, *Epitaxial Directional Growth of Indium-Doped Tin Oxide Nanowire Arrays.* Nano Letters, 2003. **3**(7): p. 925-928.

38. Wacaser, B.A., K.A. Dick, J. Johansson, M.T. Borgström, K. Deppert, and L. Samuelson, *Preferential Interface Nucleation: An Expansion of the VLS Growth Mechanism for Nanowires.* Advanced Materials, 2009. **21**: p. 153-165.

CHAPTER 6

SUMMARY AND FUTURE WORK

6.1 Summary

The catalyzed growth of 1D nanostructures was investigated by characterizing samples grown in four material systems: Au-catalyzed ZnO nanostructures, Sn-catalyzed ZnO nanostructures, Au-catalyzed Fe_xO_y nanostructures and Au-catalyzed Si nanostructures. Of primary interest was the behavior of the catalyst during growth, especially the catalyst particle state and the diffusion path of growth species to the growth front. The types of information collected include crystallographic orientation, catalyst lattice parameter, and high temperature X-ray diffraction. The purpose of this section is to summarize the main experimental results.

6.1.1 Au-Catalyzed ZnO Nanostructures

Vertically aligned, Au-catalyzed ZnO nanorods were grown on *c*-plane AlGaN in a tube furnace from the vaporization of a ZnO source. The crystallographic orientation and interfacial relationships were investigated with texture analysis. It was found that in the interfaces, the various phases took orientations with hexagonal or pseudo-hexagonal symmetry, generally with low lattice mismatches. Analysis of the gold lattice parameter showed, through a Vegard's law relationship, that no Zn was present in the gold, indicating that the growth species diffusion path was around the surface of the catalyst particle, rather than through the bulk. This result also suggested that the gold catalyst particles were in the solid state during growth, which was supported by high temperature

XRD data showing that the gold catalyst particles did not melt on reheating, even up to temperatures above the growth temperature.

6.1.2 Sn-Catalyzed ZnO Nanostructures

Sn-catalyzed ZnO nanostructures were grown in a tube furnace from the vaporization of a mixed SnO_2 catalyst and ZnO source. Analysis of the tin lattice parameter initially suggested, through a Vegard's law relationship, that no Zn was present in the tin. However, the range of error in the lattice parameter correlated with compositions greater than the maximum solid solubility of Zn in Sn. Therefore, no conclusions could be drawn concerning the presence of Zn in the tin. Regardless, the catalyst particles were likely liquid during growth as the growth temperature was much greater than the bulk melting temperature of pure tin.

6.1.3 Au-Catalyzed Fe_xO_y Nanostructures

Vertically and in-plane aligned, Au-catalyzed Fe_xO_y nanorods were grown on *c*- and *a*-plane sapphire substrates, respectively, in a tube furnace from the laser ablation of a Fe_3O_4 source. The crystallographic orientation and interfacial relationships were investigated with texture analysis. It was found that in the interfaces, the various phases took orientations with hexagonal or pseudo-hexagonal symmetry, generally with low lattice mismatches, for the sample grown on a *c*-plane substrate. For the sample grown on an *a*-plane substrate, the orientation of the Fe_2O_3 nanostructures matched that of the substrate, while the Au nanoparticles took a {111} orientation, as for the *c*-plane substrate. Analysis of the gold lattice parameter showed, through a Vegard's law relationship, that no Fe was present in the gold, indicating that the growth species diffusion path was around the surface of the catalyst particle, rather than through the

bulk. Regardless, the catalyst particles were likely solid during growth as the growth temperature was much lower than the Au-Fe eutectic temperature.

6.1.4 Au-Catalyzed Si Nanostructures

Au-catalyzed Si nanowires were grown in a diffractometer furnace from the decomposition of a SiH_4 source. *In-situ* XRD data collected during nanowire growth showed that the gold catalyst particle melted upon the addition of silane to the furnace chamber, staying molten during growth. These results indicated that the Si growth species was diffusing into the Au catalyst particle. Analysis of the gold lattice parameter after growth showed, through a Vegard's law relationship, that no Si was present in the gold at that time. The Si likely precipitates out of the gold when it solidifies upon cooling, which was supported by the observation, via TEM, of an amorphous layer around the catalyst particles.

6.1.5 Conclusions

From the results summarized above, new insights into the catalyzed growth of 1D nanostructures could be drawn. Nanostructure growth does not require a liquid catalyst, as 1D nanostructures were grown from both liquid (Au-catalyzed Si and Sn-catalyzed ZnO nanostructures)and solid (Au-catalyzed ZnO and Fe_xO_y nanostructures) catalyst particles. Nucleation can occur by a surface supersaturation process, and does not require bulk supersaturation, as evidenced by the lack of growth species in the catalyst particles for Au-catalyzed ZnO and Fe_xO_y nanostructures. In addition, surface diffusion should be a significant component of the mass transport of growth species to the growth front, even in cases where the growth species will diffuse into the bulk of the catalyst particle. Finally, the types of bonding in the source material and catalyst particle significantly

affect the behavior of the catalyst during growth. Similar bonding types allow the diffusion of the growth species into the bulk of the catalyst particle, while dissimilar bonding types prevent such diffusion, restricting the growth species to surface diffusion around the catalyst particle.

These findings have important implications toward the synthesis of 1D nanostructures for technologically important applications. A better understanding of the synthesis mechanism allows better control. For example, knowledge of the importance of the source material and catalyst bonding type allows the informed choice of appropriate source materials and catalysts. The ability to grow 1D nanostructures with solid catalysts opens up the possibility of low temperature growth on polymer substrates, for flexible devices. These finding can aid the utilization of 1D nanostructures for 2nd generation, active nanotechnology applications, in chemical sensing, optical, photovoltaic, energy generation and other areas.

6.2 Future Work

This research suggests several areas of further inquiry. The ability to monitor the growth of Si nanowires *in-situ* during growth using X-ray diffraction allows an investigation of the kinetics of the reaction. By monitoring the size of the Si peaks as a function of time, the growth of the silicon nanowires may be tracked, and reaction rate information obtained. Indeed, preliminary work in this area has shown the feasibility of this approach, as seen in Figure 6.1. Comparison of the results at 700 and 800ºC indicates that while growth at 800ºC is initially quicker, it is overtaken by the growth at 700ºC after approximately 10-15 minutes. Further investigation at other temperatures may elucidate the reason for this effect, as well as allow calculation of the activation

energy, which can give information about the rate limiting step for growth. Additionally, *in-situ* XRD allows an investigation of the catalyst particle lattice parameter during growth. Monitoring the lattice parameter during growth would give information about the diffusion of growth species among other information.

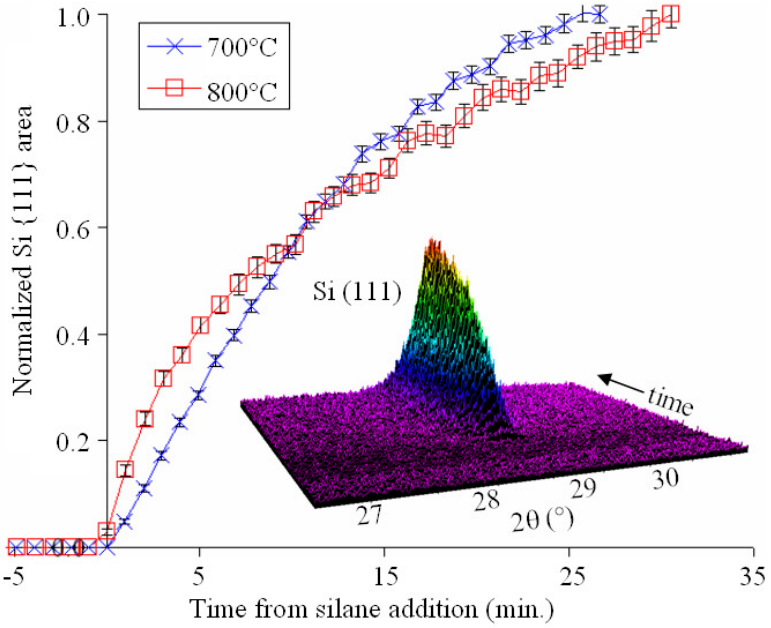

Figure 6.1 Kinetic analysis of the growth of Au-catalyzed Si nanowires at 700 and 800°C. The inset shows the *in-situ* XRD data collected at 700ºC.

Another potential direction of further research would be to chase the low temperature growth of 1D nanostructures. Reduction of the growth temperatures below around 400ºC would allow growth on thermally resistant polymers, such as polyimide. Applying the results of the current research may allow design of a process and materials selection than can achieve growth below around 400ºC. Other possibly fruitful areas of research include investigation of the growth of nanostructures of III-V semiconductors, which are used for electronics applications, and the catalyzed 1D nanostructure growth by metal-organic chemical vapor deposition (MOCVD). The complication of introducing

the growth species in the form a metal-organic complex may affect the growth mechanism.

APPENDIX A
Pole Figures for Vertically-Aligned, Au-Catalyzed ZnO Nanorods

Texture data were collected on a sample of Au-catalyzed, vertically-aligned ZnO nanorods, as outlined in section 3.2.2.3. Texture data were collected on the following reflections: {111}, {200}, {220} and {311} for the Au catalyst particles; $\{10\bar{1}0\}$, $\{10\bar{1}2\}$, $\{10\bar{1}3\}$ and $\{11\bar{2}0\}$ for the ZnO nanorods; $\{10\bar{1}0\}$, $\{10\bar{1}2\}$ and $\{10\bar{1}3\}$ for the $Al_{0.5}Ga_{0.5}N$ layer; and $\{10\bar{1}0\}$, (0002), $\{10\bar{1}1\}$ and $\{10\bar{1}2\}$ for the AlN layer. These pole figures are presented below.

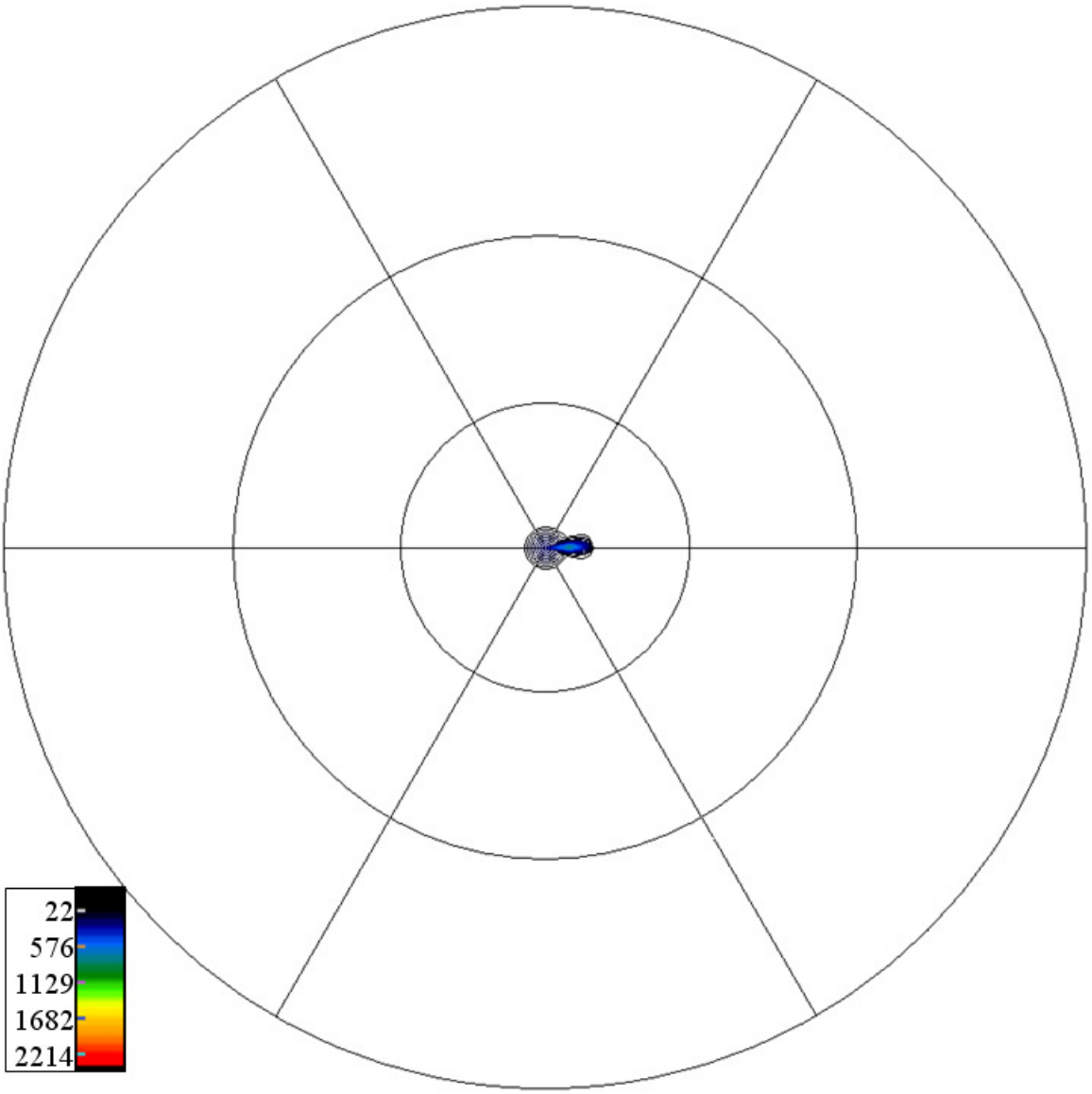

Figure A.1 (0002) pole figure for the AlN layer.

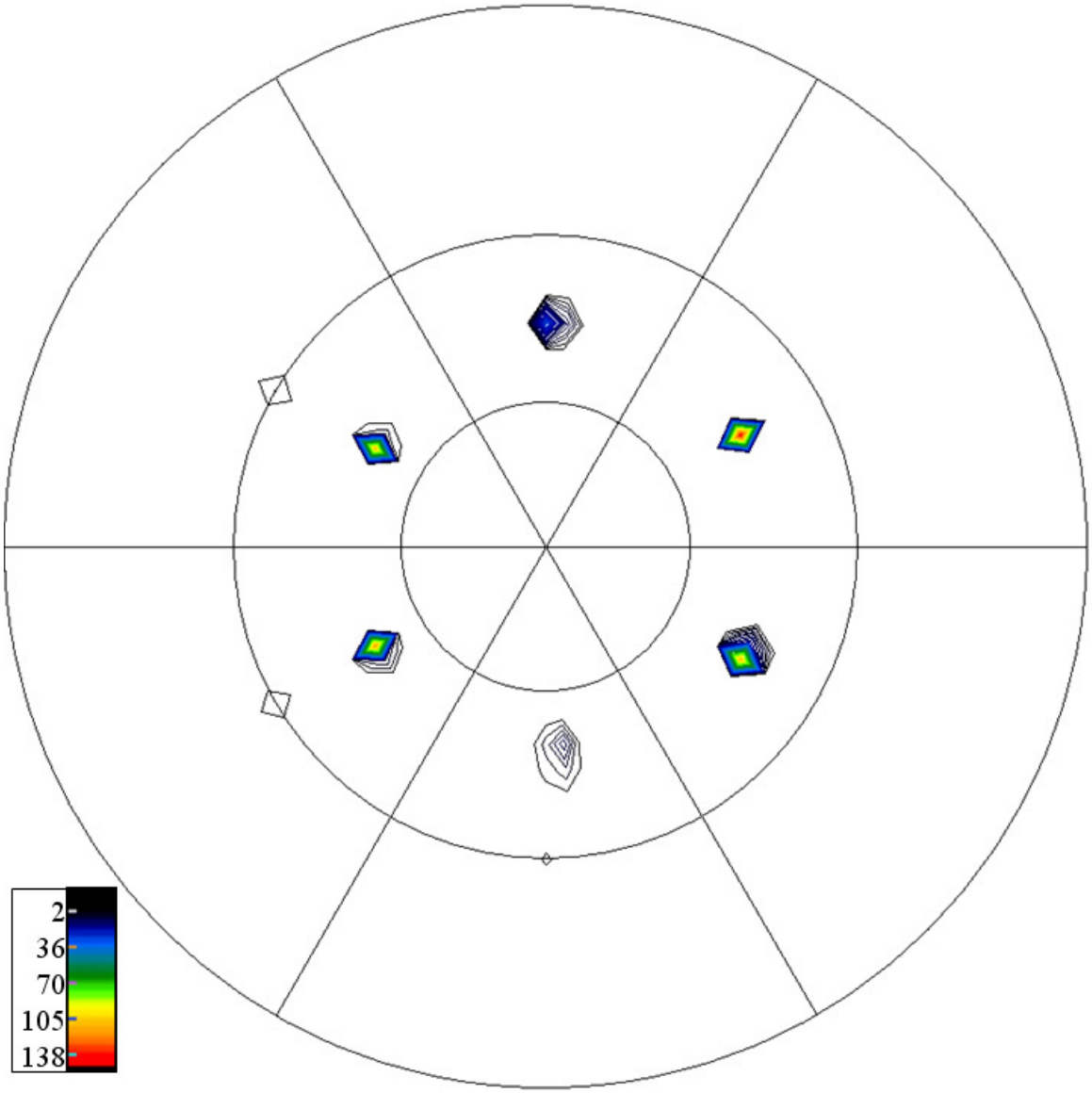

Figure A.2 $(10\bar{1}2)$ pole figure for the AlN layer.

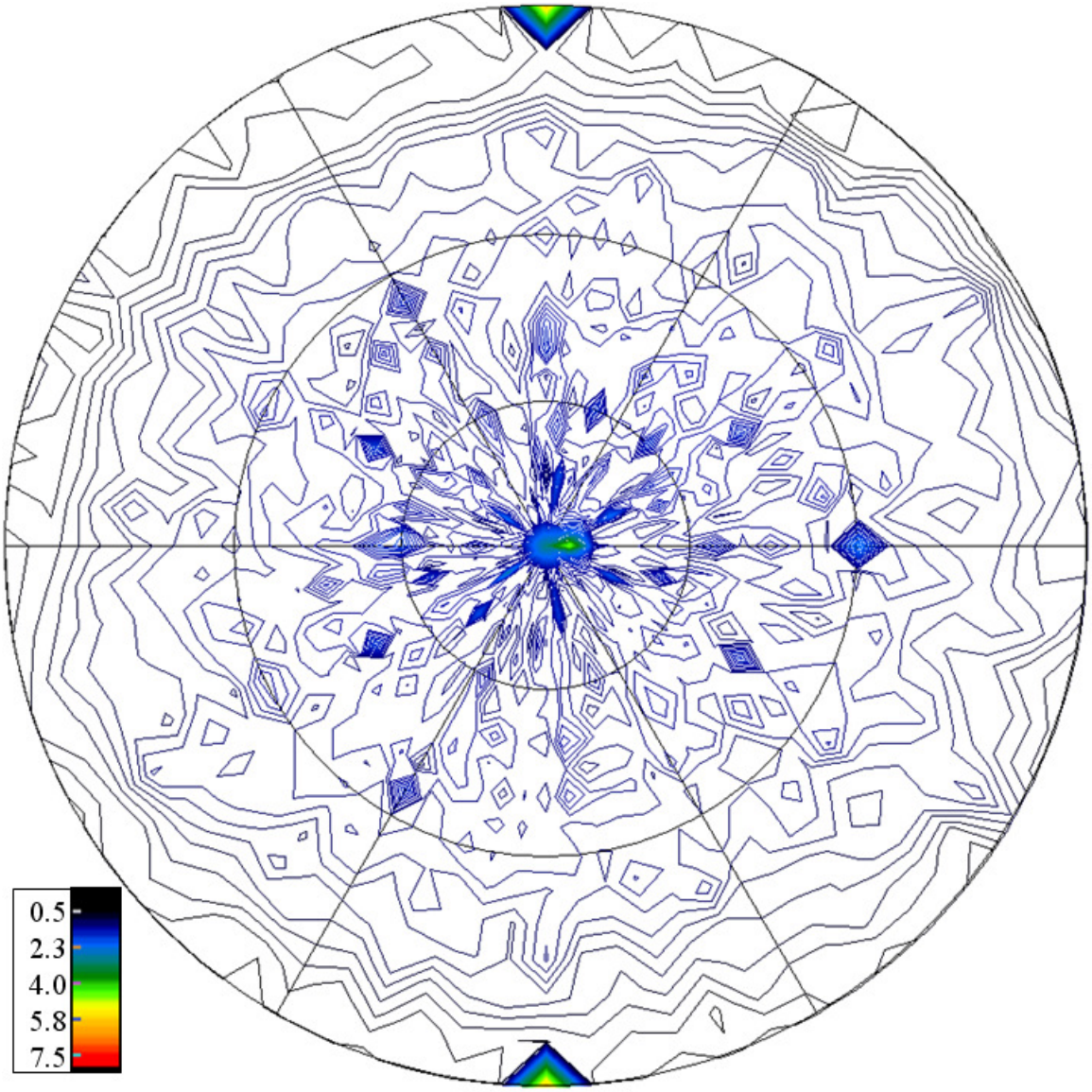

Figure A.3 $(10\bar{1}0)$ pole figure for the AlN layer.

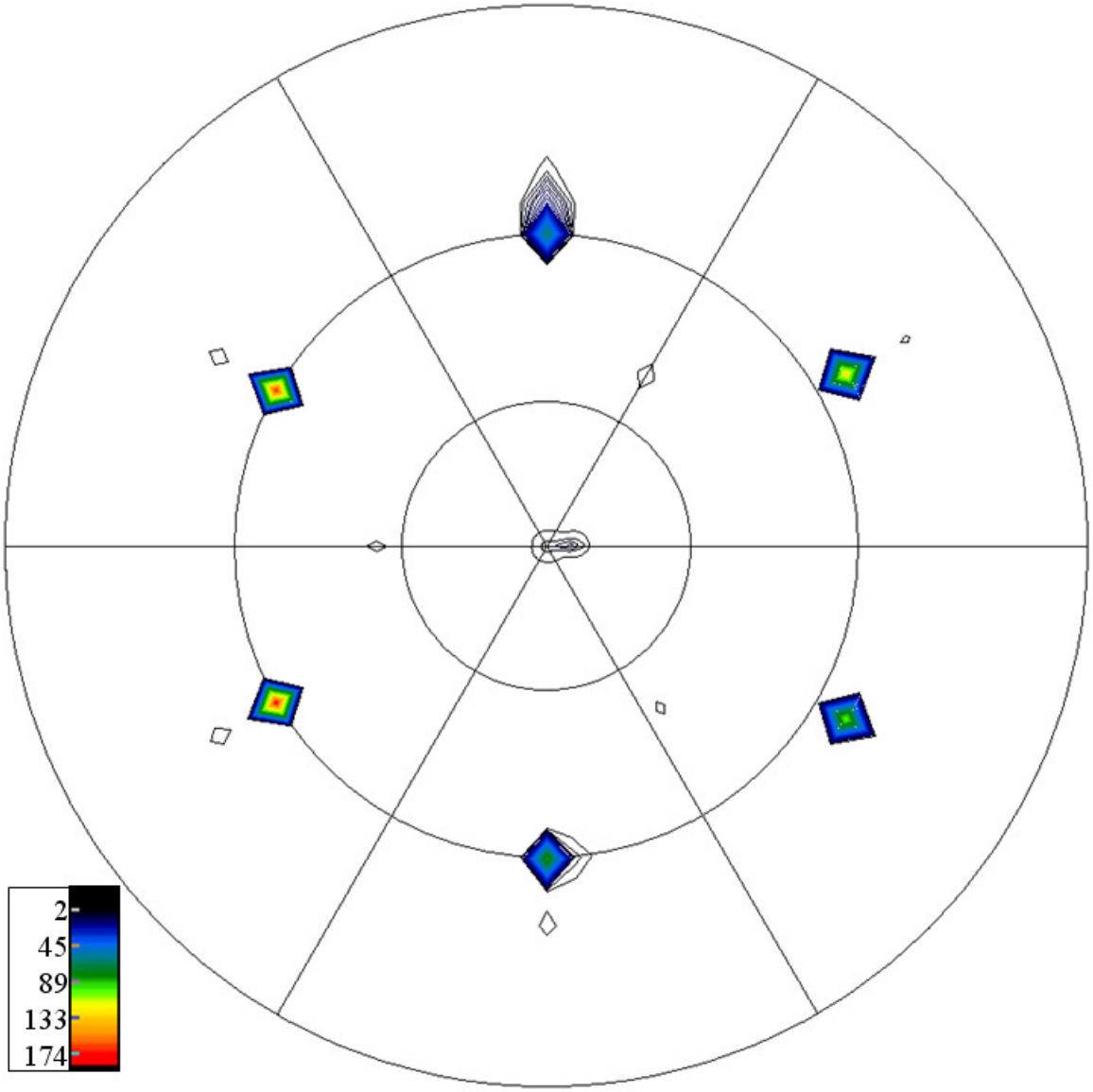

Figure A.4 $(10\bar{1}1)$ pole figure for the AlN layer.

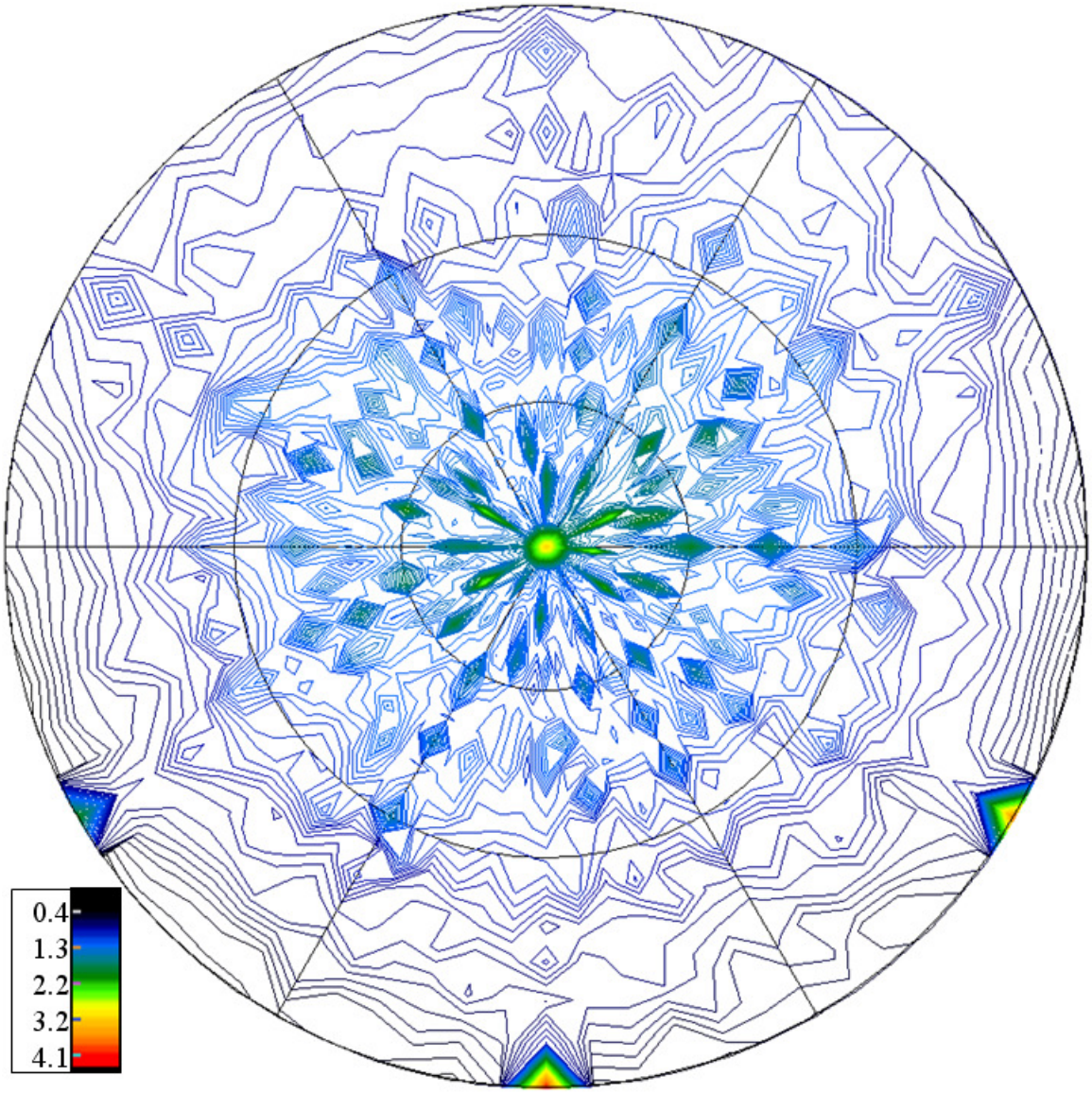

Figure A.5 $(10\bar{1}0)$ pole figure for AlGaN layer.

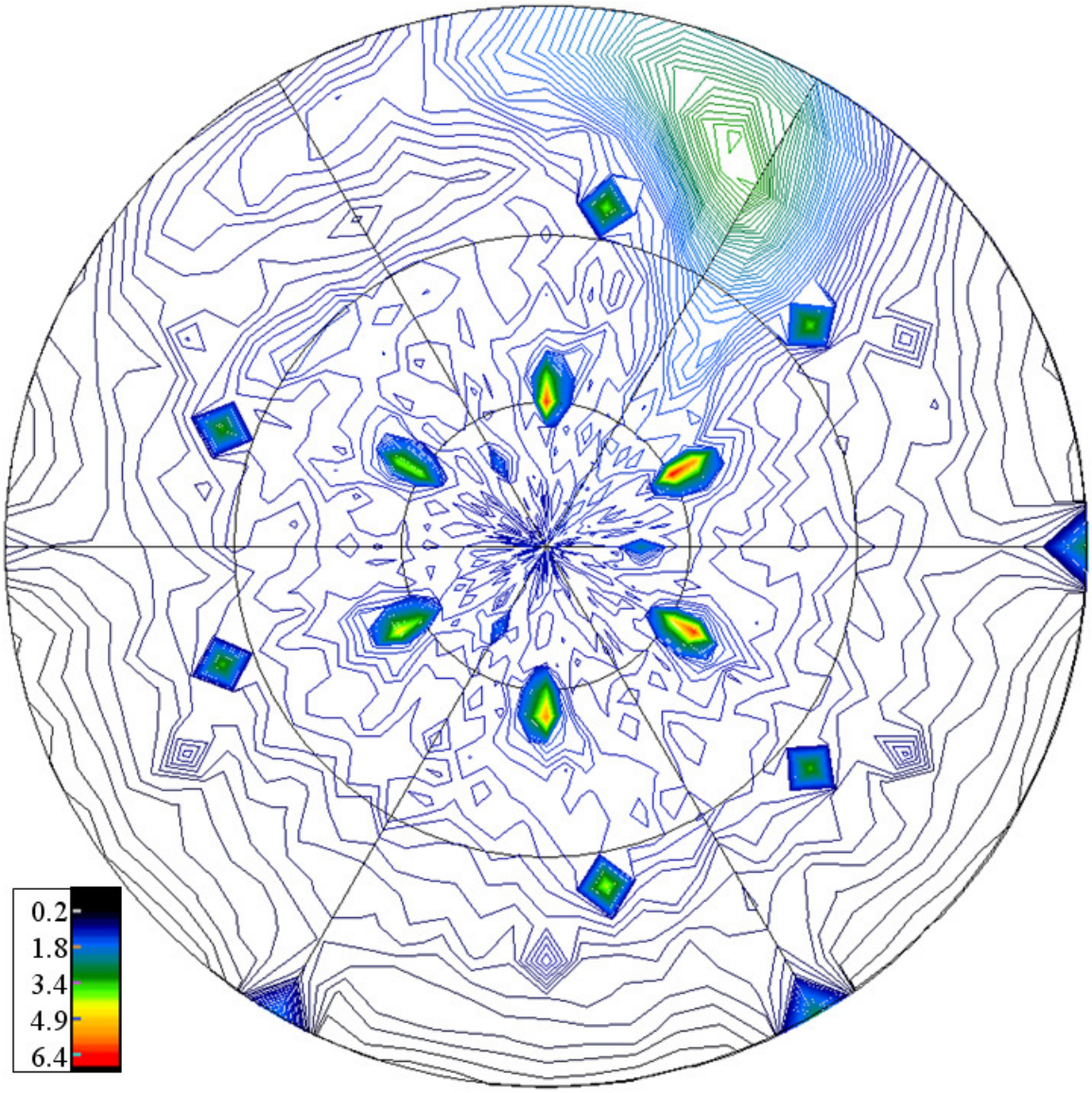

Figure A.6 $(10\bar{1}3)$ pole figure for the AlGaN layer.

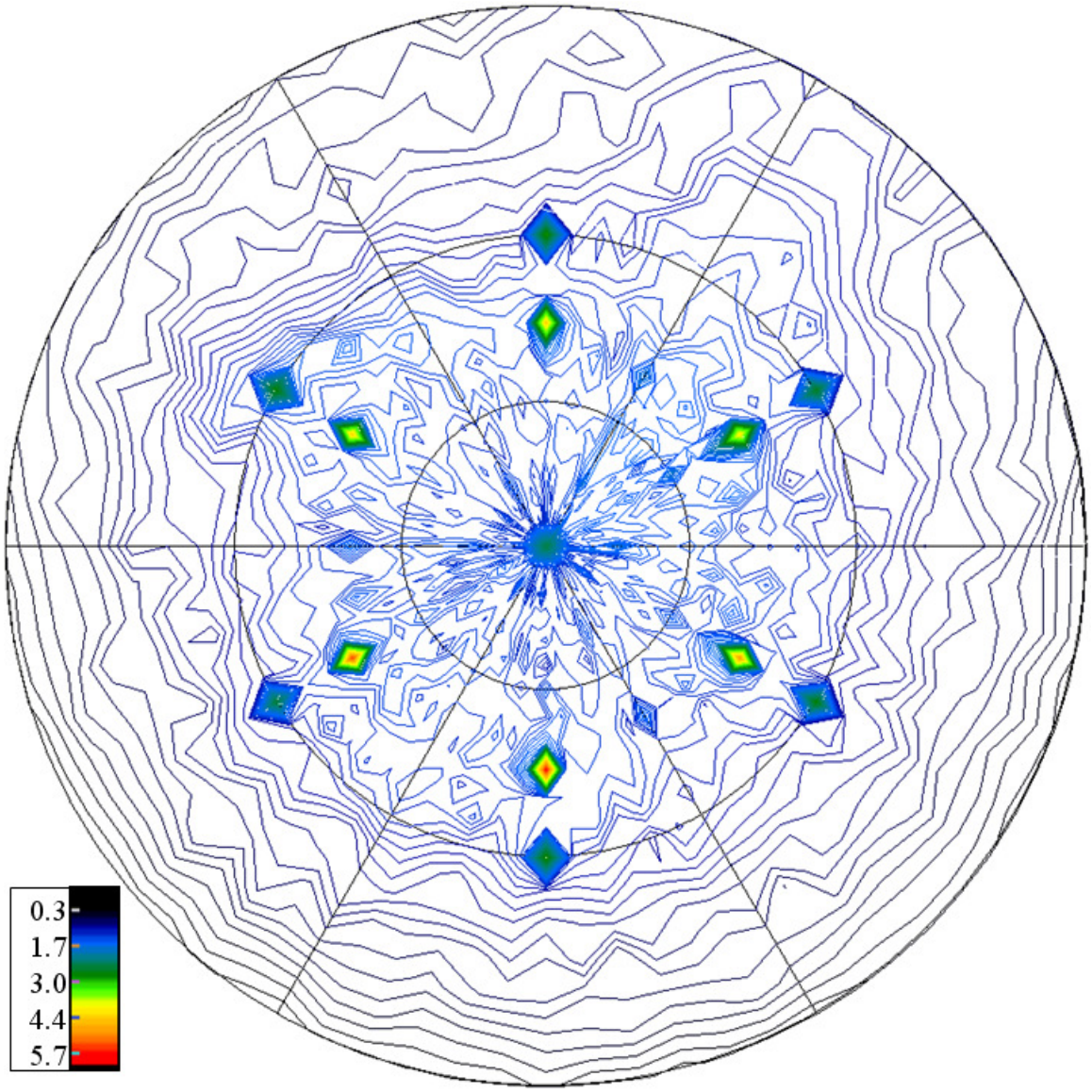

Figure A.7 $(10\bar{1}2)$ pole figure for the AlGaN layer.

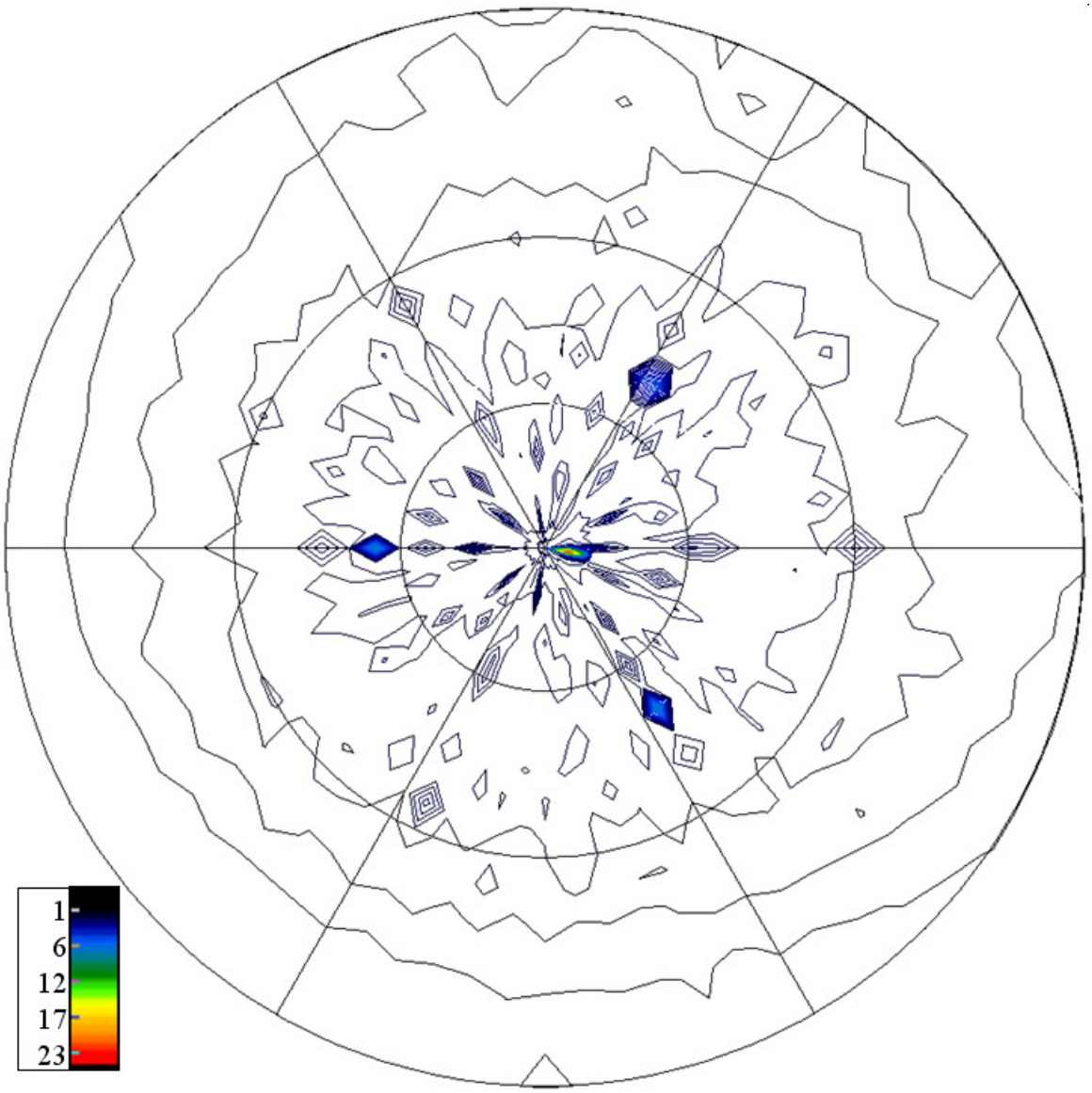

Figure A.8 $(10\bar{1}0)$ pole figure for the ZnO nanorods.

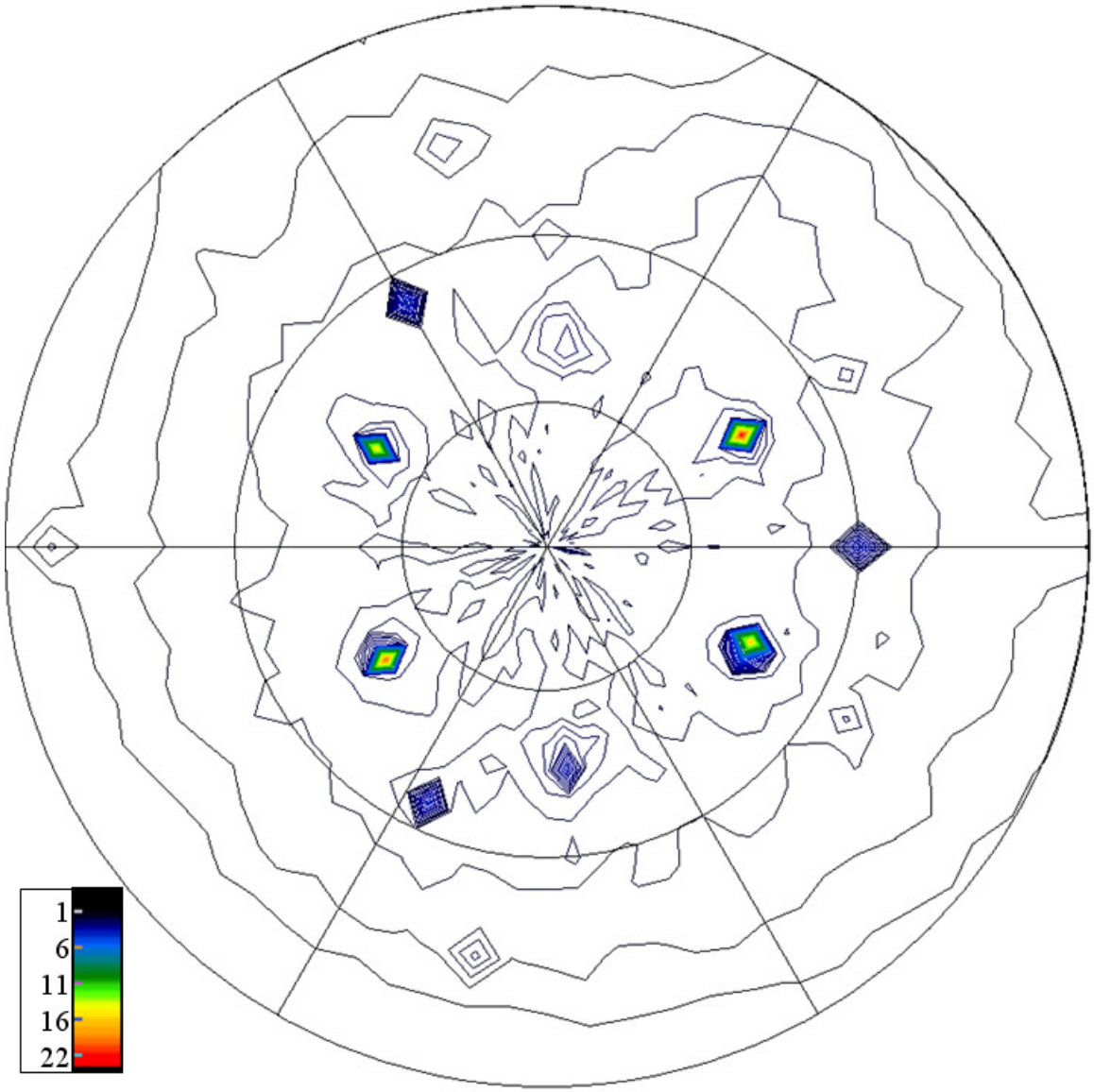

Figure A.9 $(11\bar{2}0)$ pole figure for ZnO nanorods.

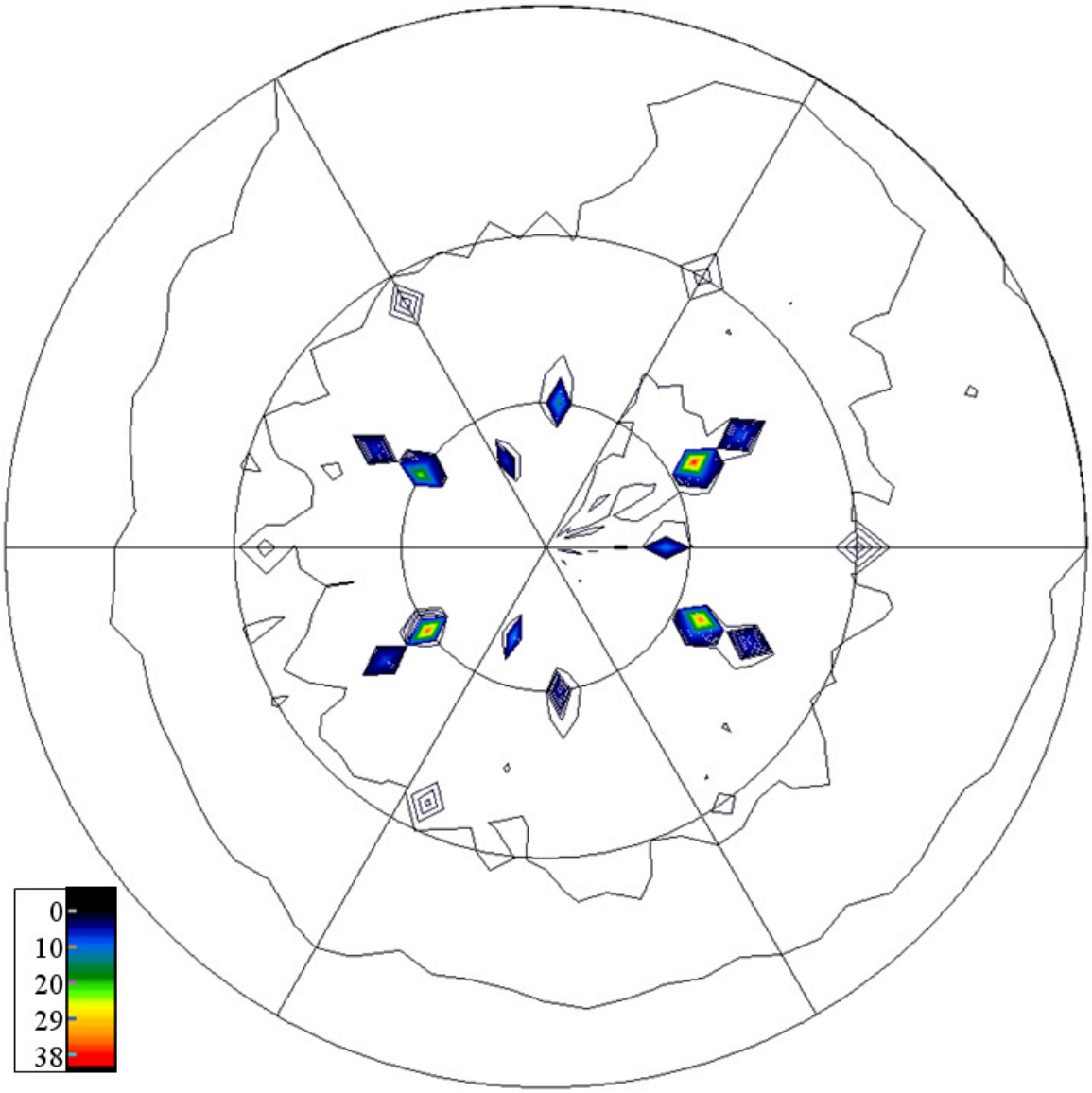

Figure A.10 $(10\bar{1}3)$ pole figure for the ZnO nanorods.

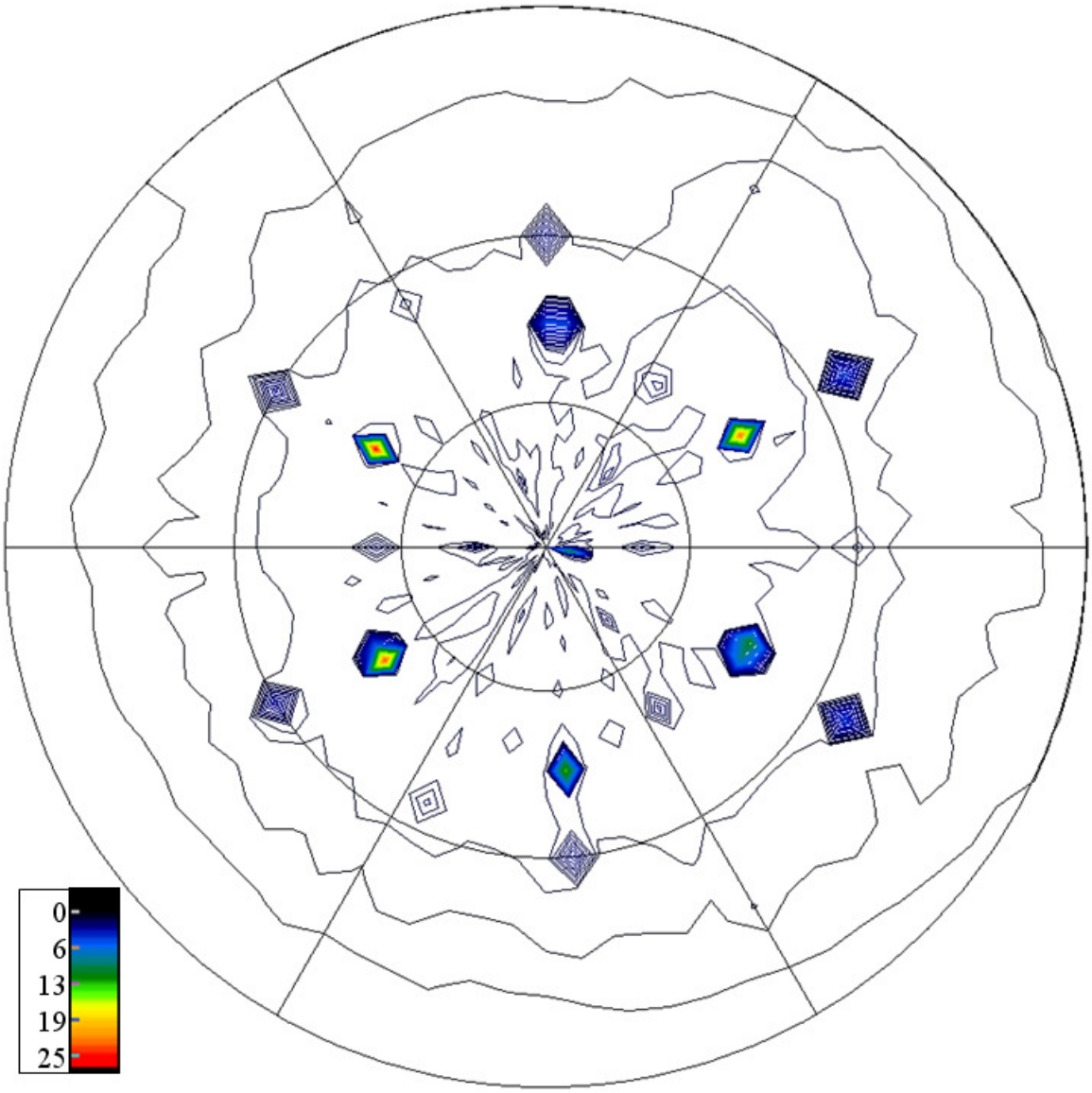

Figure A.11 $(10\bar{1}2)$ pole figure for the ZnO nanorods.

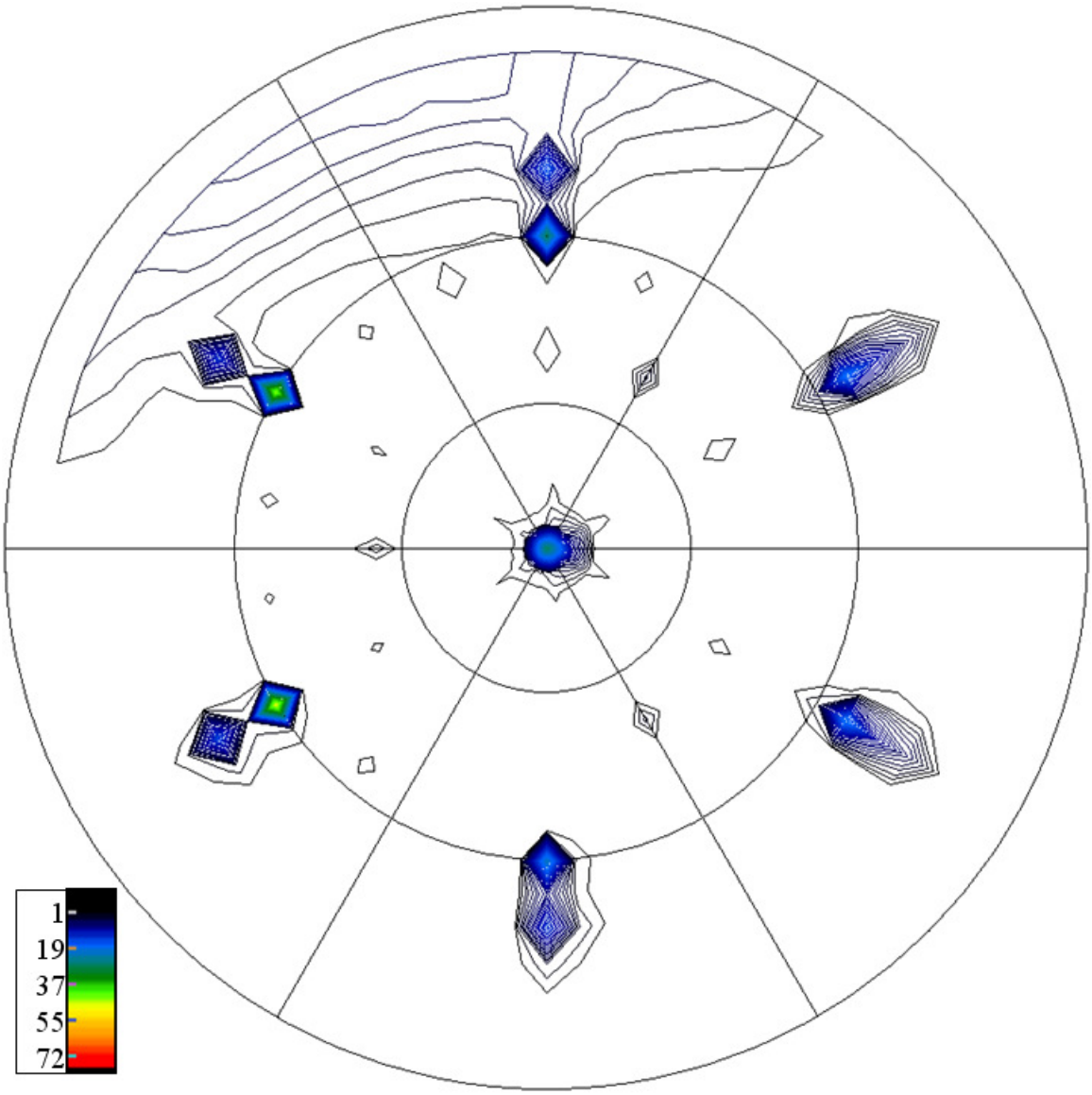

Figure A.12 (111) pole figure for the Au catalyst particles.

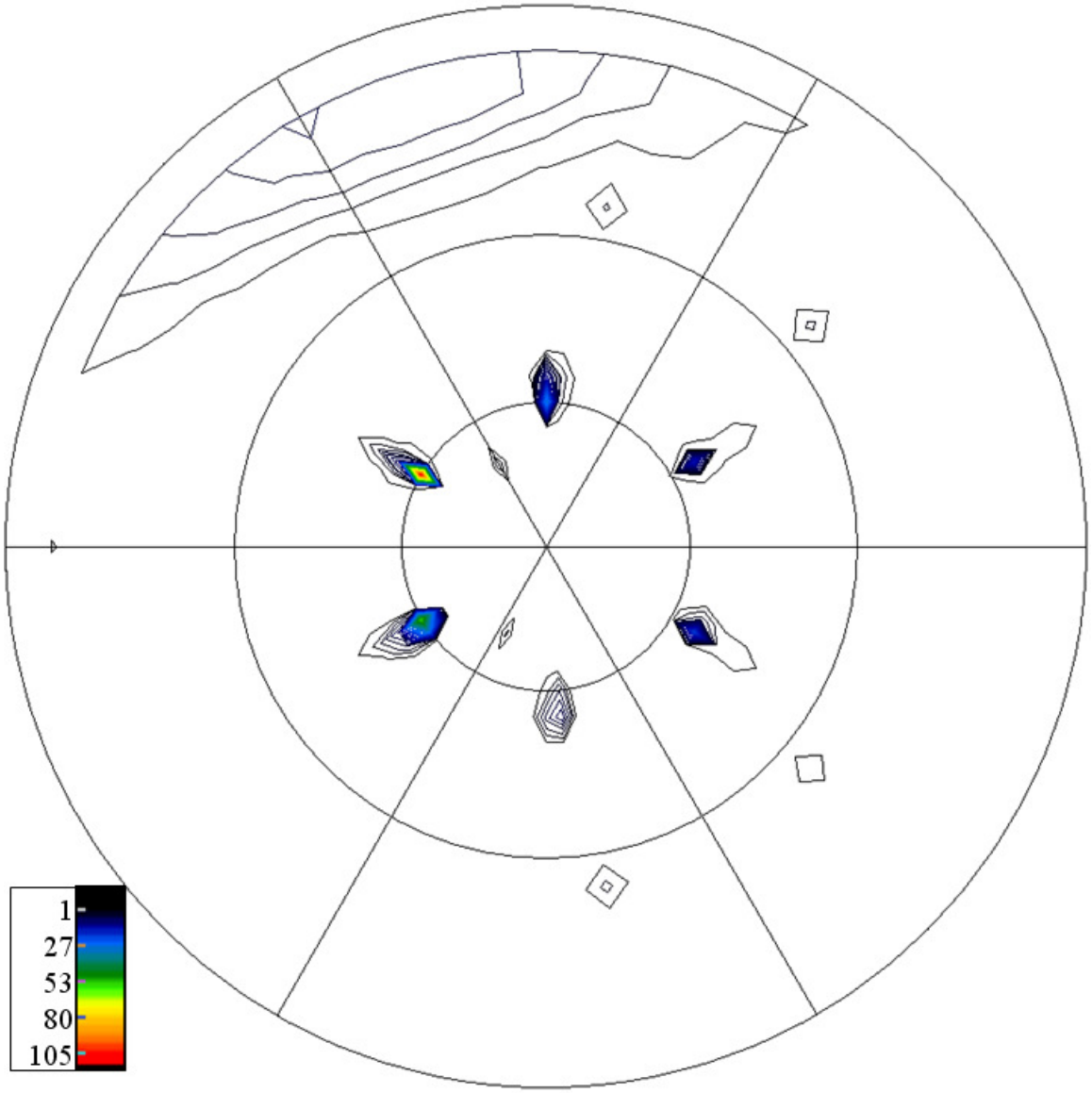

Figure A.13 (220) pole figure for the Au catalyst particles.

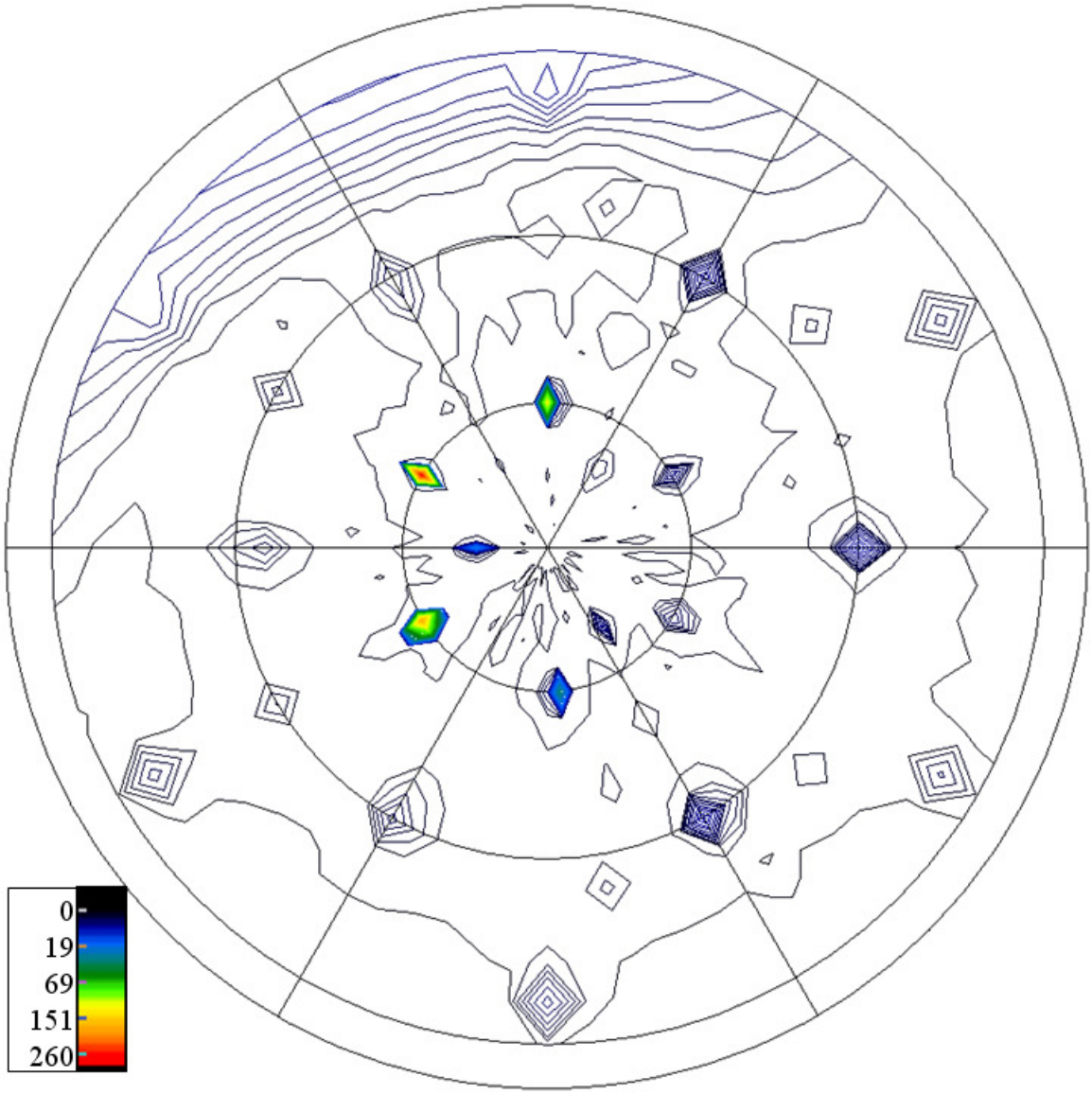

Figure A.14 (311) pole figure for the Au catalyst particles.

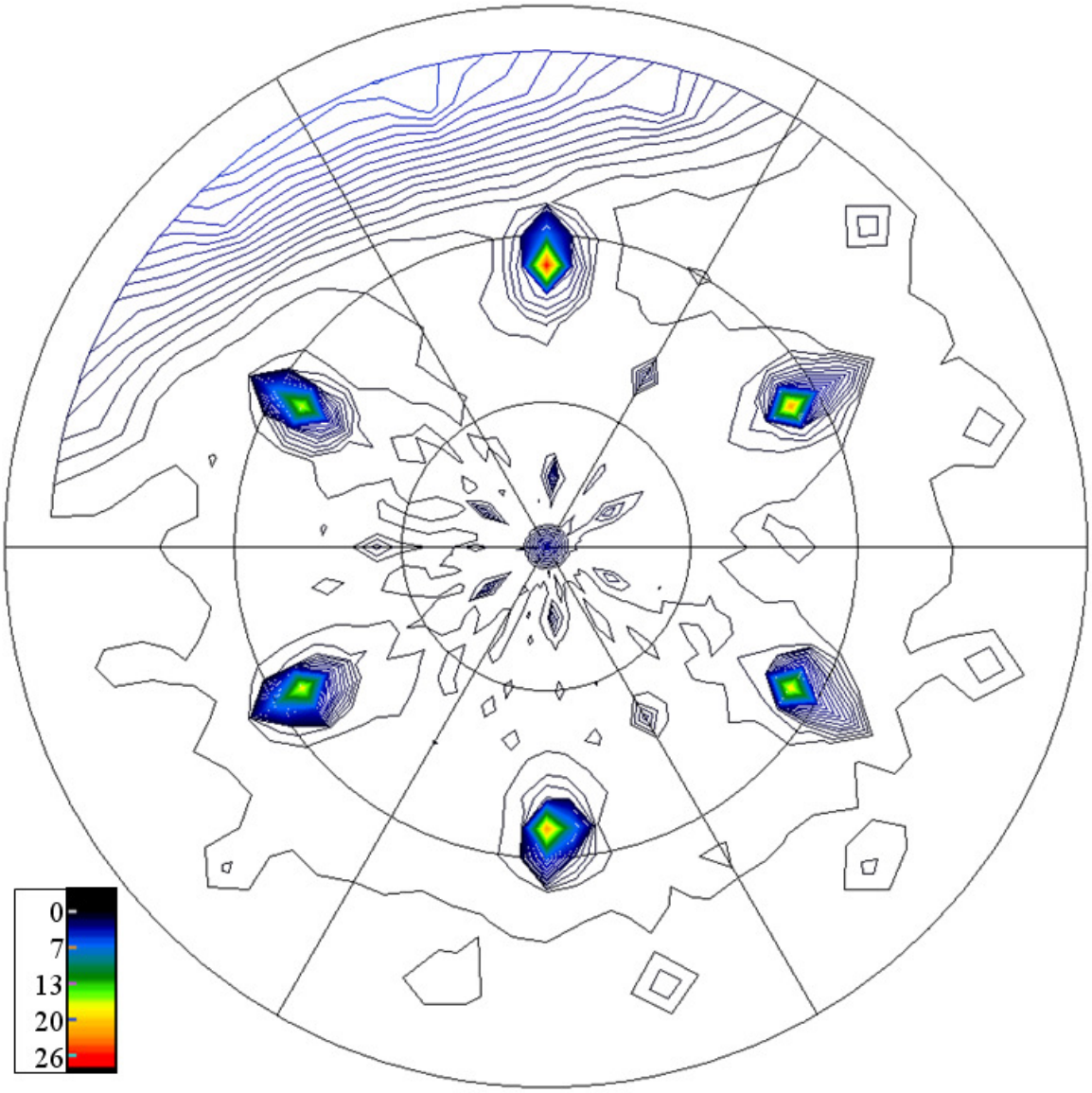

Figure A.15 (200) pole figure for the Au catalyst particles.

APPENDIX B
Pole Figures for Vertically-Aligned, Au-Catalyzed Fe_xO_y Nanowires

Texture data were collected on a sample of Au-catalyzed, vertically-aligned Fe_xO_y nanowires, as outlined in section 3.4.2.1.2. Texture data were collected on the following reflections: {111} and {200} for the Au catalyst particles; $\{10\bar{1}4\}$, $\{11\bar{2}3\}$ and $\{02\bar{2}4\}$ for the hematite (Fe_2O_3) phase; and {111}, {220} and {311} for the magnetite (Fe_3O_4) phase. The Au {111}, Fe_2O_3 $\{02\bar{2}4\}$ and Fe_3O_4 {311} pole figures are presented in section 3.4.2.1.2. The other pole figures are presented below.

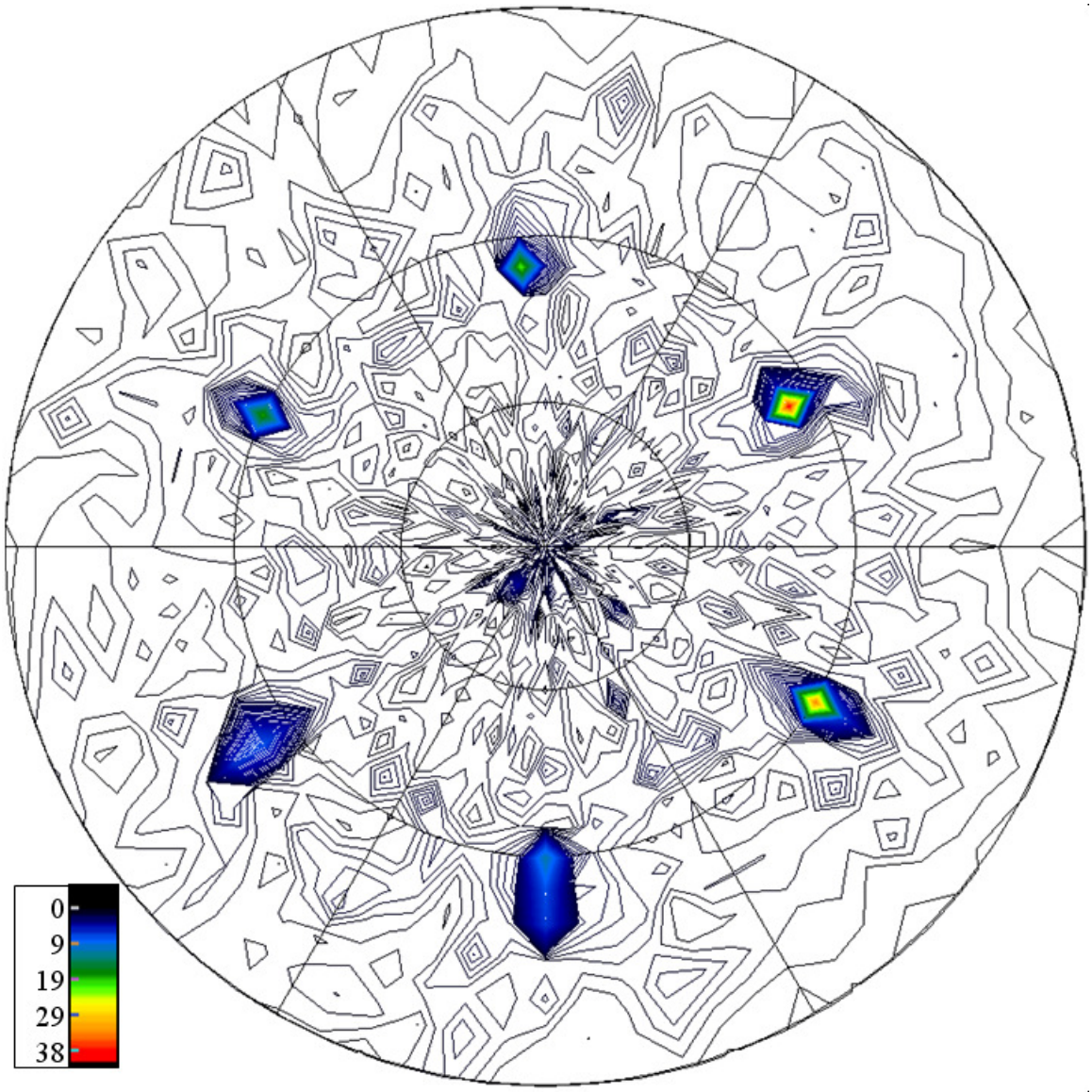

Figure B.1 (200) pole figure for the Au catalyst particles.

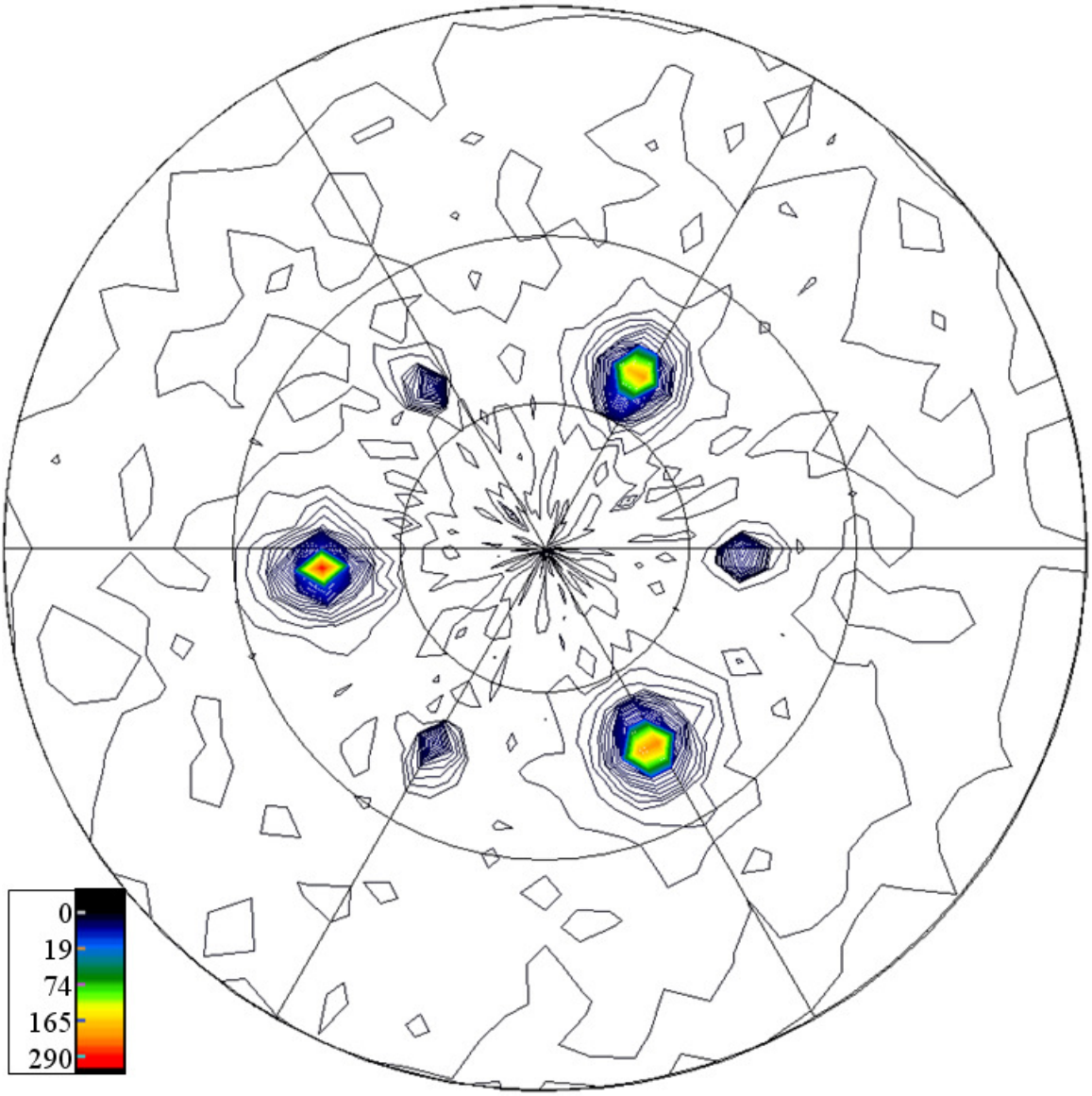

Figure B.2 $(10\bar{1}4)$ pole figure for the Fe_2O_3 phase.

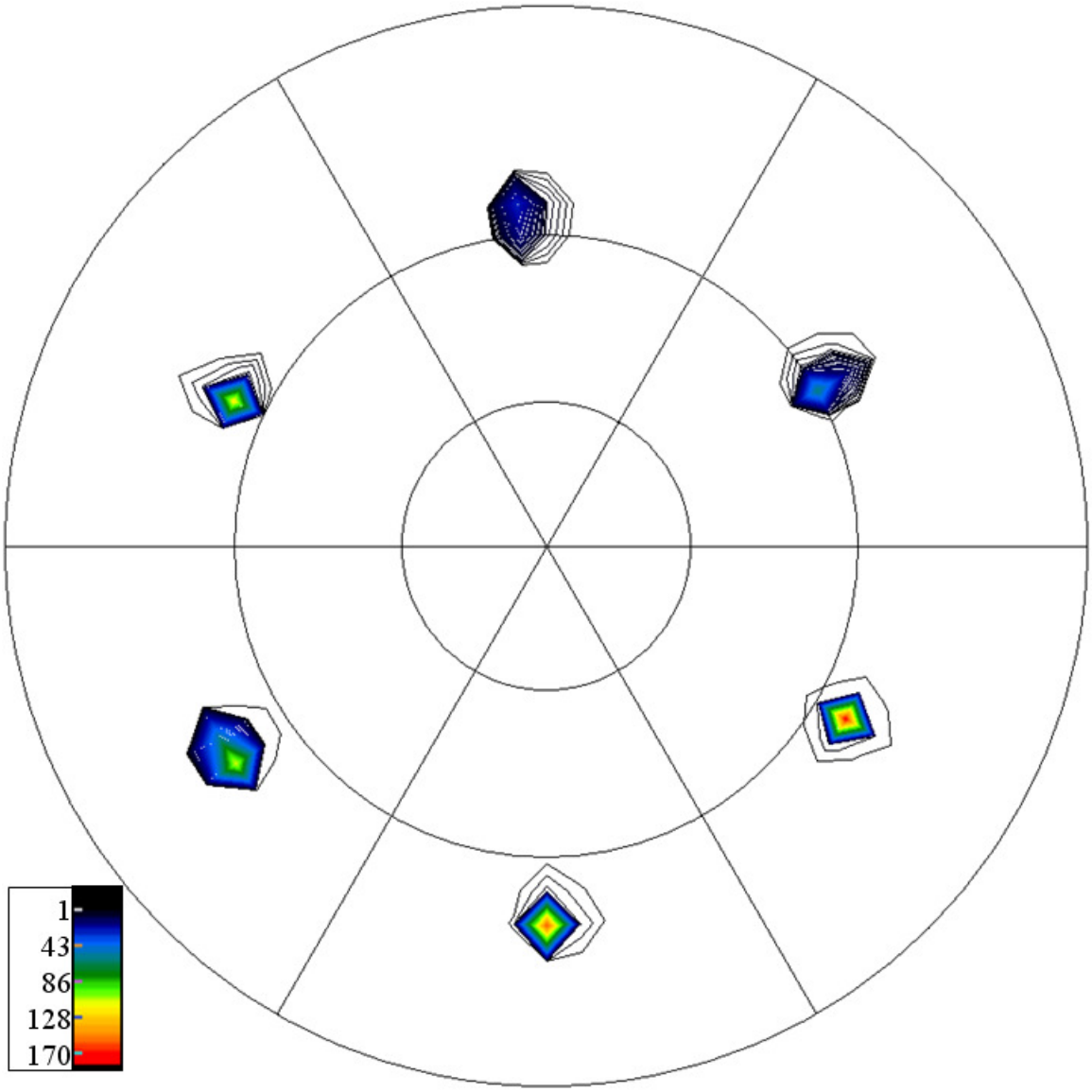

Figure B.3 $(11\bar{2}3)$ pole figure for the Fe_2O_3 phase.

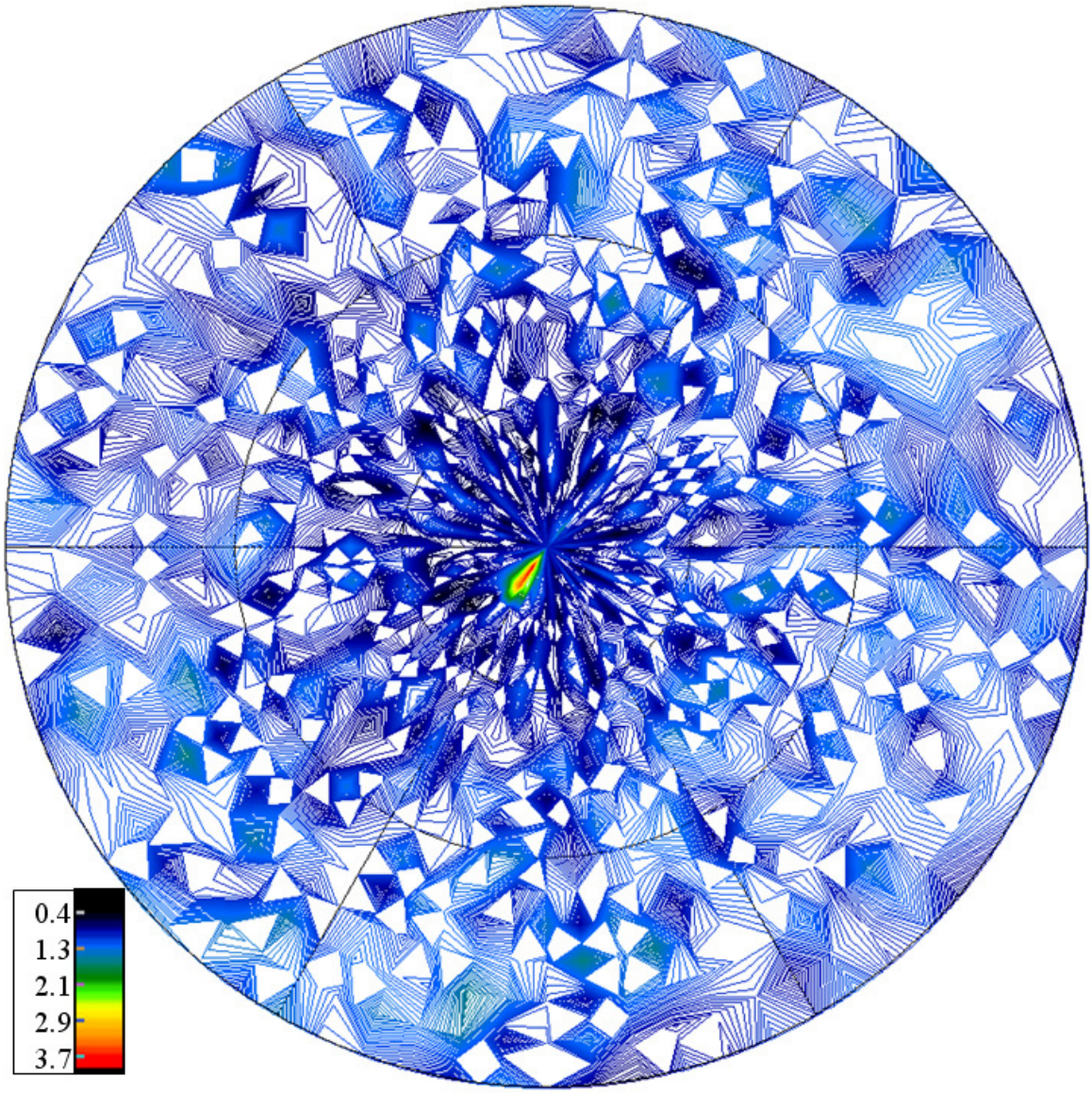

Figure B.4 (111) pole figure for the Fe_3O_4 phase.

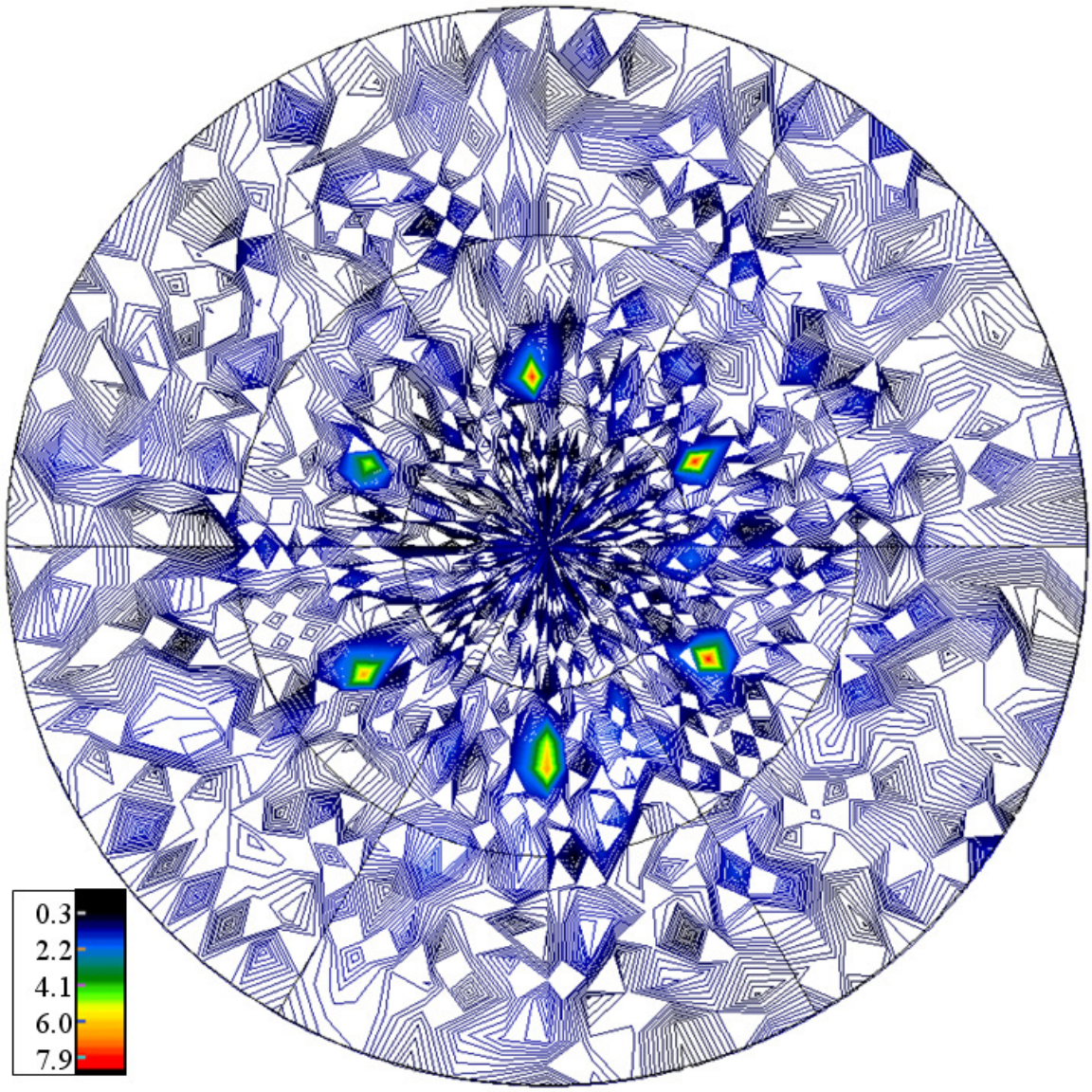

Figure B.5 (220) pole figure for the Fe_3O_4 phase.